HZDR-120

LASER-PROTON ACCELERATION IN THE NEAR-CRITICAL REGIME USING DENSITY TAILORED CRYOGENIC HYDROGEN JETS

Martin Rehwald

Wissenschaftlich-Technische Berichte
HZDR-120 · 2022 · ISSN 2191-8708

WISSENSCHAFTLICH-
TECHNISCHE BERICHTE

HZDR
HELMHOLTZ ZENTRUM
DRESDEN ROSSENDORF

Wissenschaftlich-Technische Berichte
HZDR-120

Martin Rehwald

LASER-PROTON ACCELERATION IN THE NEAR-CRITICAL REGIME USING DENSITY TAILORED CRYOGENIC HYDROGEN JETS

HELMHOLTZ ZENTRUM
DRESDEN ROSSENDORF

Druckausgabe: ISSN 2191-8708

Elektronische Ausgabe: ISSN 2191-8716

Die elektronische Ausgabe erscheint unter Creative Commons License (CC BY 4.0):

https://www.hzdr.de/publications/Publ-34409

urn:nbn:de:bsz:d120-qucosa2-786267

Die vorliegende Arbeit wurde sowohl als Dissertation an der Fakultät Mathematik und Naturwissenschaften der Technischen Universität Dresden sowie als Wissenschaftlich-Technischer Bericht des Helmholtz-Zentrum Dresden – Rossendorf mit der Berichtsnummer **HZDR-120** veröffentlicht.

2022

Herausgegeben vom

Helmholtz-Zentrum Dresden - Rossendorf

Bautzner Landstraße 400

01328 Dresden

Germany

TECHNISCHE UNIVERSITÄT DRESDEN

HZDR
HELMHOLTZ ZENTRUM DRESDEN ROSSENDORF

Bereich Mathematik und Naturwissenschaften Fachrichtung Physik, Institut für Strahlenphysik

Laser-proton acceleration in the near-critical regime using density tailored cryogenic hydrogen jets

Martin Rehwald, M. Sc.

Geboren am: 12.02.1991 in Freiberg

Dissertation

zur Erlangung des akademischen Grades

Doctor rerum naturalium (Dr. rer. nat.)

Gutachter

Prof. Dr. Ulrich Schramm
Prof. Dr. Thomas E. Cowan
Prof. Dr. Siegfried H. Glenzer

Betreuer

Dr. Karl Zeil

Eingereicht am: 09.12.2021
Verteidigt am: 17.03.2022

DRESDEN concept
Exzellenz aus Wissenschaft und Kultur

Abstract

Modern particle accelerators are a key component of today's research landscape and indispensable in industry and medicine. In special application areas, the portfolio of these facilities will be expanded by laser-driven compact plasma accelerators that generate short, high-intensity pulses of ions with unique beam properties. Though intensely explored by the community, scaling the maximum beam energies of laser-driven ion accelerators to the required level is one of the most significant challenges of this field. This endeavor is inherently linked to a fundamental understanding of the underlying acceleration processes. The prospect to efficiently increase the beam energy relies on the ability to control the accelerating field structures beyond the well-established acceleration from the stationary target rear side. However, manipulating the interaction in such micrometer-sized accelerators proves to be challenging due to the transient nature of the plasma fields and requires precise tuning of the temporal laser pulse shape and the volumetric density distribution of the plasma target to a level that could so far not be achieved.

This thesis investigates laser-proton acceleration using a cryogenic hydrogen target that combines the capabilities of predictive three-dimensional simulation and the in-situ real-time monitoring of the density distribution in the experiment to explore the fundamental physical principles of plasma based acceleration mechanisms. The corresponding experiments were performed at the DRACO laser facility at the Helmholtz-Zentrum Dresden-Rossendorf. The key to the success of these studies was the advancement of the cryogenic target system that generates a self-replenishing pure hydrogen jet. Using a mechanical chopping device, which protects the target system from the disruptive influence originating from the high-intensity interaction, allowed, for the first time, systematic experiments with a large number of laser shots in the harsh environment of the ultra-short pulse DRACO petawatt laser. The performance of a cylindrical hydrogen jet can be substantially optimized by a flexible all-optical tailoring of the target profile. Guided by real-time multi-color probing, the target density, the decisive parameter of the interaction, was scanned over two orders of magnitude allowing the exploration of different advanced acceleration regimes in a controlled manner. This approach led to the experimental realization of proton beams with energies up to 80 MeV and application relevant high particle yield from advanced acceleration mechanisms occurring in near-critical density plasmas, a regime so far mostly investigated in numerical studies. Besides cylindrical jets, the formation of thin hydrogen sheets was studied to gain insight into the fluid and crystallization dynamics that can be used to tailor the target shape for laser-proton acceleration. Using these jets, the onset of target transparency was explored, a regime that promises increased proton energies when optimized. Furthermore, after irradiation of the hydrogen jet with a high-intensity laser pulse, an unexpected axial modulation in the plasma density distribution was observed that can play a role in structuring the proton beam profile. This modulation is caused by instabilities that originate from the laser-plasma interaction, for example due to laser-driven return currents or the plasma expansion dynamics.

Publications by the author

- J. Metzkes, K. Zeil, S. D. Kraft, M. Rehwald, T. E. Cowan and U. Schramm. "Reflective optical probing of laser-driven plasmas at solid target surfaces." *Plasma Physics and Controlled Fusion* **58** (2016), p. 034012.
  DOI: 10.1088/0741-3335/58/3/034012

- J. Metzkes, K. Zeil, S. D. Kraft, L. Karsch, M. Sobiella, M. Rehwald, L. Obst, H.-P. Schlenvoigt and U. Schramm. "An online, energy-resolving beam profile detector for laser-driven proton beams." *Review of Scientific Instruments* **87** (2016), p. 083310.
  DOI: 10.1063/1.4961576

- U. Schramm, M. Bussmann, A. Irman, M. Siebold, K. Zeil, D. Albach, C. Bernert, S. Bock, F. Brack, J. Branco, J. P. Couperus, T. E. Cowan, A. Debus, C. Eisenmann, M. Garten, R. Gebhardt, S. Grams, U. Helbig, A. Huebl, T. Kluge, A. Köhler, J. M. Krämer, S. D. Kraft, F. Kroll, M. Kuntzsch, U. Lehnert, M. Loeser, J. Metzkes, P. Michel, L. Obst, R. Pausch, M. Rehwald, R. Sauerbrey, H.-P. Schlenvoigt, K. Steiniger and O. Zarini. "First results with the novel petawatt laser acceleration facility in Dresden." *Journal of Physics: Conference Series* **874** (2017), p. 012028.
  DOI: 10.1088/1742-6596/874/1/012028

- M. Gauthier, C. B. Curry, S. Göde, F.-E. Brack, J. B. Kim, M. J. MacDonald, J. Metzkes, L. Obst, M. Rehwald, C. Rödel, H.-P. Schlenvoigt, W. Schumaker, U. Schramm, K. Zeil, and S. H. Glenzer. "High repetition rate, multi-MeV proton source from cryogenic hydrogen jets." *Applied Physics Letters* **111** (2017), p. 114102.
  DOI: 10.1063/1.4990487

- S. Göde, C. Rödel, K. Zeil, R. Mishra, M. Gauthier, F.-E. Brack, T. Kluge, M. J. MacDonald, J. Metzkes, L. Obst, M. Rehwald, C. Ruyer, H.-P. Schlenvoigt, W. Schumaker, P. Sommer, T. E. Cowan, U. Schramm, S. Glenzer, and F. Fiuza. "Relativistic electron streaming instabilities modulate proton beams accelerated in laser-plasma interactions." *Physical Review Letters* **118** (2017), p. 194801.
  DOI: 10.1103/PhysRevLett.118.194801

- L. Obst, S. Göde, M. Rehwald, F.-E. Brack, J. Branco, S. Bock, M. Bussmann, T. E. Cowan, C. B. Curry, F. Fiuza, M. Gauthier, R. Gebhardt, U. Helbig, A. Huebl, U. Hübner, A. Irman, L. Kazak, J. B. Kim, T. Kluge, S. D. Kraft, M. Loeser, J. Metzkes, R. Mishra, C. Rödel, H.-P. Schlenvoigt, M. Siebold, J. Tiggesbäumker, S. Wolter, T. Ziegler, U. Schramm, S. H. Glenzer and K. Zeil. "Efficient laser-driven proton acceleration from cylindrical and planar cryogenic hydrogen jets." *Scientific Reports* **7** (2017), p. 10248.
  DOI: 10.1038/s41598-017-10589-3

- P. Sommer, J. Metzkes-Ng, F.-E. Brack, T. E. Cowan, S. D. Kraft, L. Obst, M. Rehwald, H.-P. Schlenvoigt, U. Schramm and K. Zeil. "Laser-ablation-based ion source characterization and manipulation for laser-driven ion acceleration." *Plasma Physics and Controlled Fusion* **60** (2018), p. 054002.
  DOI: 10.1088/1361-6587/aab21e

- T. Ziegler, M. Rehwald, L. Obst, C. Bernert, F.-E. Brack, C. B. Curry, M. Gauthier, S. H. Glenzer, S. Göde, L. Kazak, S. D. Kraft, M. Kuntzsch, M. Loeser, J. Metzkes-Ng, C. Rödel, H.-P. Schlenvoigt, U. Schramm, M. Siebold, J. Tiggesbäumker, S. Wolter and K. Zeil. "Optical probing of high intensity laser interaction with micron-sized cryogenic hydrogen jets." *Plasma Physics and Controlled Fusion* **60** (2018), p. 074003.
  DOI: 10.1088/1361-6587/aabf4f

- L. Obst, J. Metzkes-Ng, S. Bock, G. E. Cochran, T. E. Cowan, T. Oksenhendler, P. L. Poole, I. Prencipe, M. Rehwald, C. Rödel, H.-P. Schlenvoigt, U. Schramm, D. W. Schumacher, T. Ziegler and K. Zeil. "On-shot characterization of single plasma mirror temporal contrast improvement." *Plasma Physics and Controlled Fusion* **60** (2018), p. 054007.
  DOI: 10.1088/1361-6587/aab3bb

- T. Kluge, M. Rödel, J. Metzkes-Ng, A. Pelka, A. Laso Garcia, I. Prencipe, M. Rehwald, M. Nakatsutsumi, E. E. McBride, T. Schönherr, M. Garten, N. J. Hartley, M. Zacharias, J. Grenzer, A. Erbe, Y. M. Georgiev, E. Galtier, I. Nam, H. J. Lee, S. H. Glenzer, M. Bussmann, C. Gutt, K. Zeil, C. Rödel, U. Hübner, U. Schramm and T. E. Cowan. "Observation of ultrafast solid-density plasma dynamics using femtosecond x-ray pulses from a free-electron laser." *Physical Review X* **8** (2018),p. 31068.
  DOI: 10.1103/PhysRevX.8.031068

- L. Obst-Huebl, T. Ziegler, F.-E. Brack, J. Branco, M. Bussmann, T. E. Cowan, C. B. Curry, F. Fiuza, M. Garten, M. Gauthier, S. Göde, S. H. Glenzer, A. Huebl, A. Irman, J. B. Kim, T. Kluge, S. D. Kraft, F. Kroll, J. Metzkes-Ng, R. Pausch, I. Prencipe, M. Rehwald, C. Roedel, H.-P. Schlenvoigt, U. Schramm and K. Zeil. "All-optical structuring of laser-driven proton beam profiles." *Nature Communications* **9** (2018), p. 5292.
  DOI: 10.1038/s41467-018-07756-z

- G. A Becker, M. B. Schwab, R. Lötzsch, S. Tietze, D. Klöpfel, M. Rehwald, H.-P. Schlenvoigt, A. Sävert, U. Schramm, M. Zepf and M. C. Kaluza. "Characterization of laser-driven proton acceleration from water microdroplets."
  Scientific Reports **9** (2019), p. 17169.
  DOI: 10.1038/s41598-019-53587-3

- C. B. Curry, C. Schoenwaelder, S. Goede, J. B. Kim, M. Rehwald, F. Treffert, K. Zeil, S. H. Glenzer and M. Gauthier. "Cryogenic liquid jets for high repetition rate discovery science." *Journal of Visualized Experiments* **159** (2020), p. e61130.
  DOI: 10.3791/61130

- A. Huebl, M. Rehwald, L. Obst-Huebl, T. Ziegler, M. Garten, R. Widera, K. Zeil, T. Cowan, Thomas, M. Bussmann, U. Schramm and T. Kluge. "Spectral control via multi-species effects in PW-class laser-ion acceleration." *Plasma Physics and Controlled Fusion* **62** (2020), p. 124003.
  DOI: 10.1088/1361-6587/abbe33

- F.-E. Brack, F. Kroll, L. Gaus, C. Bernert, E. Beyreuther, T. E. Cowan, L. Karsch, S. Kraft, L. A. Kunz-Schughart, E. Lessmann, J. Metzkes-Ng, L. Obst-Huebl, J. Pawelke, M. Rehwald, H.-P. Schlenvoigt, U. Schramm, M. Sobiella, E. R. Szabó, T. Ziegler and K. Zeil. "Spectral and spatial shaping of laser-driven proton beams using a pulsed high-field magnet beamline." *Scientific Reports* **10** (2020), p. 9118.
  DOI: 10.1038/s41598-020-65775-7

- D. Levy, C. Bernert, M. Rehwald, I. A. Andriyash, S. Assenbaum, T. Kluge, E. Kroupp, L. Obst-Huebl, R. Pausch, A. Schulze-Makuch, K. Zeil, U. Schramm and V. Malka. "Laser-plasma proton acceleration with a combined gas-foil target". *New Journal of Physics* **22** (2020), p. 103068.
  DOI: 10.1088/1367-2630/abbf6d

- T. Ziegler, D. Albach, C. Bernert, S. Bock, F.-E. Brack, T. E. Cowan, N. P. Dover, M. Garten, L. Gaus, R. Gebhardt, U. Helbig, A. Irman, H. Kiriyama, T. Kluge, A. Kon, S. Kraft, F. Kroll, m. Loeser, J. Metzkes-Ng, N. Nishiuchi, L. Obst-Huebl, T. Püschel, M. Rehwald, H.-P. Schlenvoigt, U. Schramm and K. Zeil. "Proton beam quality enhancement by spectral phase control of a PW-class laser system." *Scientific Reports* **11** (2021), p. 7338.
  DOI: 10.1038/s41598-021-86547-x

- F. Kroll, F.-E. Brack, C. Bernert, S. Bock, E. Bodenstein, K. Brüchner, T. E. Cowan, L. Gaus, R. Gebhardt, U. Helbig, L. Karsch, T. Kluge, S. Kraft, M. Krause, E. Lessmann, U. Masood, S. Meister, J. Metzkes-Ng, Alexej N., J. Pawelke, J. Pietzsch, T. Püschel, M. Reimold, M. Rehwald, C. Richter, H.-P. Schlenvoigt, U. Schramm, M. E. P. Umlandt, T. Ziegler, K. Zeil and E. Beyreuther. "Tumor irradiation in mice with a laser-accelerated proton beam." Under review in: *Nature Physics*

- M. Rehwald, J. B. Kim, F. Yang, C. Bernert, C. B. Curry, M. Gauthier, U. Huebner, C. Schoenwaelder, U. Schramm, U. Zastrau, K. Zeil, S. H. Glenzer and S. Göde. "Ultra-fast ice formation induced sheet preservation in liquid hydrogen jets". *(in preparation)*

- M. Rehwald, C. Bernert, F.-E. Brack, M. Bussmann, T. E. Cowan, C. B. Curry, F. Fiuza, M. Garten, L. Gaus, M. Gauthier, S. Göde, I. Goethel, S. H. Glenzer, L. Huang, A. Huebl, J. B. Kim, T. Kluge, S. Kraft, F. Kroll, J. Metzkes-Ng, M. Loeser, L. Obst-Huebl, M. Reimold, H.-P. Schlenvoigt, C. Schoenwaelder, U. Schramm, M. Siebold, F. Treffert, L. Yang, T. Ziegler and K. Zeil. "Ultra-short pulse laser-driven acceleration of protons to 80 MeV from density tailored cryogenic hydrogen jets." *(in preparation)*

Contents

1 Introduction 1
1.1 Motivation . . . 1
1.2 Content of this thesis . . . 3

2 Theory of laser-matter interaction in different density regimes 7
2.1 Laser-proton acceleration from solid targets . . . 8
2.1.1 Plasma formation . . . 10
2.1.2 Propagation of electromagnetic waves in plasmas . . . 11
2.1.3 Laser energy absorption into electrons . . . 12
2.2 Underdense and near-critical density plasmas . . . 15
2.2.1 Laser-proton acceleration in the near-critical regime . . . 16
2.2.2 Target concepts and their experimental realization . . . 21

3 Development of cryogenic jets as high repetition rate targets for laser-driven ion accelerators 25
3.1 Generation of micrometer-sized cryogenic jets . . . 27
3.2 Technical realization of the jet delivery system . . . 28
3.3 Imaging setup for jet characterization . . . 32
3.4 Cylindrical jets . . . 33
3.5 Hydrogen sheet jets . . . 36
3.5.1 Characterization of sheet jets under different operation conditions . . . 38
3.5.2 Fluid dynamics . . . 39
3.6 Implementation in a laser-plasma experiment . . . 43
3.6.1 Characterization of the jet stability . . . 43
3.6.2 Shielding of the jet source for improved stability . . . 46
3.6.3 Vacuum system requirements . . . 49
3.7 Slit aperture optimization for laser-proton acceleration experiments . . . 51
3.8 Conclusion . . . 52

4 Laser-driven proton acceleration with cryogenic hydrogen jets in the petawatt regime 53
4.1 The high-intensity laser system DRACO 56
4.2 On-target laser contrast characterization using optical probing 59
4.3 Setup of particle and optical diagnostics 62
4.4 Proton acceleration in the transparency regime using sheet jets 65
4.5 Cylindrical jets at different laser contrast conditions 70
4.6 Tailoring the plasma density distribution 73
4.6.1 Setup for generating a controlled pre-pulse 73
4.6.2 Enhanced proton acceleration through target pre-expansion 74
4.6.3 Characterization of the target density distribution 78
4.6.4 Interpretation of the experimental results using numerical simulations 83
4.7 Conclusion 92

5 Investigation of picosecond plasma dynamics using optical probe pulses 97
5.1 Pump-probe experiments at DRACO 150 TW 99
5.2 Magneto-hydrodynamic instability hypothesis 104
5.3 Weibel-induced filamentation hypothesis 107
5.4 Discussion based on numerical simulations 108
5.5 Conclusion 113

6 Summary and outlook 115

7 Appendix 119
7.1 A: Thomson parabola spectrometer calibration method 119
7.2 B: Methods to determine central hits 121

Bibliography 123

1 Introduction

1.1 Motivation

Modern particle accelerators are engines of fundamental research and key components for the development of new methods in industry and medicine. High-power laser-driven compact plasma accelerators represent an actively studied scientific field all over the world that will expand the portfolio of conventional machines in special application areas. The interest originates from the electric field gradients on the order of GV/m to TV/m that are significantly larger than from RF-cavity based conventional accelerators (< 100 MV/m). This allows a substantial reduction of the necessary accelerator lengths leading to higher availability of such particle sources. Establishing the necessary high field gradients requires the generation of a relativistic plasma by irradiating matter with a laser pulse exceeding intensities of 10^{18}W/cm^2. These intensities can be provided by utilizing the technique of chirped pulse amplification (CPA) [1] which allows generating laser powers on the order of several petawatts. For this purpose, the laser energy is delivered in an ultra-short pulse with a duration of a few 10 fs and focused to a spot size in the order of micrometers. Laser-based particle accelerators can be used to generate electron beams from gas targets in a scheme called laser wakefield acceleration (LWFA) [2] with up to GeV energies [3, 4] or to produce MeV proton and ion beams. The best-studied physical mechanism underlying laser-ion acceleration is target normal sheath acceleration (TNSA) introduced by Wilks et al. [5]. A laser pulse, irradiating a micrometer thick foil, ionizes the target front side and generates a population of hot electrons that travel to the rear side, escape into the vacuum and thereby establish a sheath field strong enough to accelerate ions sufficiently. The emitted ion beams provide an exponential energy spectrum with a characteristic cut-off energy, a micrometer source size [6, 7], a beam divergence of about ± 10-20 ° [8, 9], high particle numbers per bunch [10] and an initially short bunch duration. These beam properties are useful for a number of applications ranging from ultrafast electromagnetic field probes [11, 12, 13] and high flux neutron converter for material radiography [14] through isochoric heating of warm dense matter [15] and inertial confinement fusion [16] to injection sources for conventional accelerator structures [17]. In particular important is the potential for medical applications in the form of laser-driven sources for radiation therapy [18, 19, 20, 21]. The preparation and optimization of the proton beam for radiobiological experiments is one of the key topics at the Dresden laser acceleration source (DRACO) at the Helmholtz-Zentrum Dresden-Rossendorf (HZDR), where this thesis was carried out. This involves the optimization of the laser-matter interaction, the implementation of a tunable beam delivery system based on pulsed solenoids [22] as well as the execution of the irradiation studies of cell samples or small animal tumors [23]. Reaching the medically relevant regime requires for protons at least 200 MeV [24] which has not been demonstrated so far. For comparison, the highest published proton energies are currently at 94 MeV by Higgenson et al. [25]. Slightly lower energies were also reported by Wagner et al. [26]. Increasing the available proton and ion energy is thus one of the most significant challenges of this field.

While scaling to higher proton energies is primarily accomplished by increasing the laser energy on target, optimizing the accelerator for applications by controlling the desired kinetic energy, particle number or beam profile requires a fundamental understanding of the underlying mechanisms that govern the acceleration dynamics. A better understanding could allow improving the acceleration schemes not only in the TNSA case but also for alternative mechanisms like radiation pressure acceleration (RPA) [27, 28, 29, 30, 31], relativistic induced transparency (RIT) [25, 32, 33, 34, 35, 36], collisionless shock acceleration (CSA) [37, 38, 39], hole-boring (HB) acceleration [27, 31, 30], synchronized acceleration by slow light (SASL) [40, 41] or magnetic vortex acceleration (MVA) [42, 43, 44, 45, 46, 47, 48, 49, 50, 51]. However, the compactness of the interaction region in the order of the laser spot size (typically a few micrometers) as well as the temporal laser intensity profile, which includes pedestals and pre-pulses that precede the main high-intensity pulse, poses a major difficulty in determining a detailed microscopic picture of the temporal evolution of the plasma dynamics. This is further complicated by the usually overdense and optically opaque plasma originating from the solid target material. Direct observation of the bulk dynamics is therefore only possible at X-ray free electron lasers that can penetrate these plasmas. While the potential of this approach was already shown in [52], the small number of worldwide available X-ray free electron lasers[*] limits the access to a few experimental campaigns. As a consequence, experimental efforts often deduce understanding from temporally and spatially integrating diagnostics of particle beams or secondary radiation. Simulations then provide an instrument to gain insights into the complex plasma processes and link the experimental observations to the microscopic dynamics. However, simplifications and assumptions are necessary for the simulations, due to the finite computational resources. This involves for example the limitation of the size of the simulation area or the reduction of the material density. Furthermore, the exact target shape and temporal laser profile is often simplified, since the influence of the nanosecond radiation background prior to the peak intensity is not included in the simulation. The necessary accurate experimental input for predictive simulations is often not feasible and therefore relies on best knowledge.

---

[*] There are three X-ray free electron lasers (XFEL) in operation: the European XFEL in Hamburg, the Linac Coherent Light Source at the SLAC National Accelerator Laboratory and SACLA XFEL in Japan.

Another major challenge is the realization of a sufficient high repetition rate that is required to achieve application-relevant particle yields. In order to take advantage of repetition rates in the order of 1-10 Hz delivered by upcoming petawatt-class laser facilities [53], the laser operation, target delivery and alignment processes, as well as the online diagnostic suite must be efficiently managed. Currently, all aspects that are necessary for stable long-term operation with a high number of shots (> 1000 per hour) are discussed (e.g. in [54]). This includes, among other things, debris related limitations as well as the target manufacturing processes. The usage of higher repetition rate laser-matter interactions is furthermore beneficial for the understanding of the acceleration process since it enables more systematic studies based on statistical evaluations where a much larger number of parameters can be scanned and shot-to-shot fluctuations can be mitigated.

1.2 Content of this thesis

The presented thesis addresses the current challenges in laser-driven ion acceleration by investigating a continuous cryogenic hydrogen jet technology as an alternative target approach that can provide insight into the plasma dynamics by establishing a link between the accelerated particles, a temporally resolved observation of the target evolution and numerical simulations. The usage of a solid hydrogen (wire-like) jet is motivated by its low solid density which is typically an order of magnitude below the density of plastic or metal foil targets and the free standing arrangement allowing for on-shot optical probing of the plasma evolution. The low density of hydrogen enables investigation of various alternative acceleration schemes (e.g. SASL, RIT, MVA) and facilitates numerical simulations since a lower degree of spatial resolution is required, reducing the computational costs. Simulations are further simplified by the less complex ionization physics of hydrogen and the single-species target material. From an application point of view, the hydrogen target is debris-free and enables long-term operation at >1 Hz repetition rate. This target system was already utilized in a number of different laser-plasma experiments, in particular in two experimental campaigns [55, 56, 57, 58, 59] at the 150 TW arm of DRACO laser system. The experimental work of this thesis concentrates on the scaling to the petawatt level, which became recently available with the DRACO laser upgrade, and on the exploration of advanced acceleration schemes.

Despite the many advantages, the cryogenic target is technologically very demanding and requires an extensive infrastructure to operate in a harsh laser-plasma environment. Based on the results at the 150 TW arm of DRACO [57], two aspects were identified which are crucial for the successful application of the jet target at a petawatt-class laser system. Following an introduction to the target system, these are addressed in Chapter 3. The first aspect concerns the spatial overlap between jet and laser focus defining the stability of the acceleration performance. The practical solution of shooting close to the fragile nozzle aperture, where the fluctuation of the jet position is reduced, is not applicable with petawatt laser powers, because the aperture is damaged by the interaction. This leads to the design and the implementation of a novel chopper devise that prevents damaging the target system and therefore enables systematic studies at the DRACO petawatt arm. Second, the fluid dynamics and thermodynamic processes involved in the generation of sheet like jets are investigated. The planar geometry is more favorable in comparison to cylindrical jets due to the more collimated proton emission [57] as well as the larger target width and therefore better spatial overlap with the high-intensity laser pulse. The studies enable insights into the generation of well-defined and controllable solid hydrogen targets of optimized shapes and stability.

In chapter 4 the cryogenic hydrogen jet target is then used to investigate proton acceleration at the DRACO petawatt laser. A primary task is the identification and the investigation of different acceleration regimes with thin and near-critical density targets. Scaling the pulse power to the petawatt regime involves an increase in laser background radiation which can tremendously change the target evolution during the interaction. Controlling the temporal laser pulse intensity profile (referred to as *laser contrast*) is therefore a key requirement when extending the proton energy scaling from the DRACO 150 TW to the petawatt level. When using a plasma mirror device to enhance the laser contrast, the proton performance from cylindrical and planar jet targets is comparable to foil targets of equivalent thickness. However, the proton performance from a cylindrical jet can be substantially optimized by an all-optical tailoring of the target density profile. This approach leads to the experimental realization of proton beams with energies up to 80 MeV and application-relevant particle yields when using pre-expanded targets with reduced plasma density. Interpretation of the experiments is assisted by realistic numerical simulations where the initial target configuration, characterized by optical probing, is applied as an input. The simulation results indicate that the pre-expansion induces a transition between different acceleration mechanisms. In this best performing configurations, the laser pulse either penetrate the relativistic transparent plasma giving rise to magnetic vortex acceleration at the rear side or accelerates protons in the bulk of the target. The generation of proton beams with kinetic energies up to 80 MeV with a target system that is in principle capable of providing high repetition rate delivery of a renewable pure hydrogen jet marks an important step towards applications of laser-driven particle sources and allows the exploration of advanced acceleration regimes in a controlled manner.

The final part of this thesis in chapter 5 describes the observation of axial density modulation occurring in the expanding hydrogen jet plasma after irradiation with a high-intensity laser pulse. Such a modulation may give rise to perturbations of the target surface which could influence the spatial uniformity of the ion beam, similar to what was shown for example with structures targets [6, 8]. Concerning applications, a spatial variation of the beam profile is often detrimental and must therefore be avoided which requires an understanding of the underlying processes [55, 60, 61, 62, 63, 58]. Based on previous work [64, 65], two possible mechanisms (either magneto-hydrodynamic instabilities or Weibel-induced filamentations) are identified that may cause the observed modulation. According to numerical studies, both effects may contribute to the growth of the plasma modulations. This could influence the laser-matter interaction in particular when an early pre-expansion, caused by the rising slope of the temporal laser profile, is triggered.

2 Theory of laser-matter interaction in different density regimes

The central task for building a particle accelerator by means of a strong laser system is to convert the energy of the ultra-short laser pulse into directed particle momentum. In contrast to electrons, this energy transfer cannot be obtained directly for ions, because the high rest mass prevents an efficient acceleration at available laser intensities. For example, in the case of protons, intensities larger than $5 \cdot 10^{24}$ W/cm^2 [66] would be required which is at least two orders of magnitude above the intensities achieved with state-of-the-art laser systems. Because of this, laser-ion acceleration represent a secondary process that relies on the establishment of quasi-static electric fields through a population of energetic electrons. The generation of these electric fields can be achieved by several mechanisms studied in experiments and simulations. All have the same goal, to optimize the conversion efficiency of the available laser energy into kinetic energy and yield of the ion beam.

This chapter explains the essential physical processes and introduces the most important mechanisms that are relevant for laser-driven ion acceleration and that are the basis for the experiments discussed in this thesis. The first part conceptually describes target normal sheath acceleration (TNSA), the most extensively studied laser-based acceleration mechanism, outlining central aspects of laser-matter interaction that are relevant for this thesis. This includes the plasma generation via ionization, the optical properties of plasmas and the transfer of laser energy to fast electrons. Motivated by scaling studies with low-density cryogenic jet targets, the second part of this chapter is dedicated to the importance of laser interactions with plasmas whose densities are much lower than those of typical solid targets. Beneficial effects in such plasmas are discussed for the case when a low-density front side layer is combined with a solid foil and when the initial target turns transparent during the interaction with the high-intensity pulse. Moreover, laser-ion acceleration by the magnetic vortex acceleration (MVA) mechanism will be introduced. The chapter closes with an overview of target systems that are used to investigate this low-density regime providing the context in which the hydrogen jet target system is discussed. Since the experimental studies presented in this thesis are mainly relevant to proton beam generation (due to the pure hydrogen target content), this chapter primarily focuses on laser-proton acceleration. Nevertheless, the same effects and mechanisms can also be applied to other ion species.

2.1 Laser-proton acceleration from solid targets

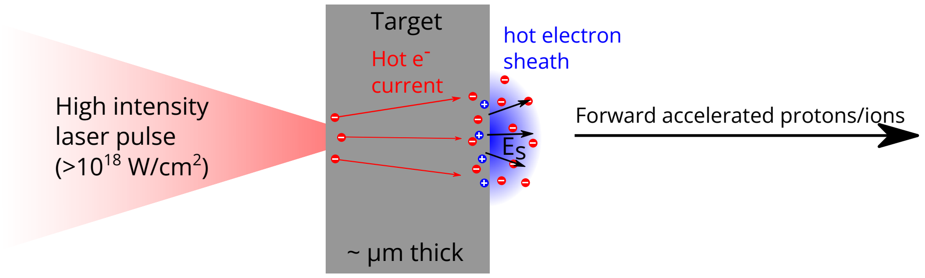

Figure 2.1: Schematic of the TNSA acceleration mechanism. An intense ($I_L > 10^{18}$ W/cm^2) laser pulse ionizes the front side of the micrometer thick solid density target and accelerates electrons in the process. At the target rear side, these electrons form a quasi-static electric sheath field that accelerates protons and ions from a thin surface layer.

Laser-driven proton acceleration is a secondary process that relies on the establishment of an electric field through the interaction of a high-intensity pulse with a dense target. An often investigated and robust mechanism that yields proton beams with energies of up to several 10 MeV [67, 68, 9] is target normal sheath acceleration (TNSA) [5]. The conceptual scenario for TNSA is illustrated in figure 2.1 and will be explained briefly. A micrometer thick solid density target is irradiated with an intense laser pulse ($I_L > 10^{18}$ W/cm^2) that ionizes the target front side and generates a hot electron current of temperature T_e penetrating the bulk. As the electrons reach the rear side and attempt to escape into the vacuum, a quasi-static charge-separation field of strength E_s is established that accelerates ions and protons from a thin surface layer. This field can be estimated by [5]

$$E_s = \frac{k_B T_e}{e L_s} \tag{2.1}$$

with k_B the Boltzmann constant and e the elementary charge. For a steep interface at the target rear side, the spatial extension of the sheath L_s is given by the Debye length

$$\lambda_D = \sqrt{\frac{\varepsilon_0 k_B T_e}{n_e e^2}} \tag{2.2}$$

that depends on the plasma density n_e. λ_D is a characteristic length over which the electric potential is reduced to $1/e_N$ (Euler's number) due to the screening by the surrounding plasma. E_s typically reaches field strengths in the order of TV/m [33], which is enough to accelerate protons to multi-MeV energies at the target rear side. More extensive analytical models for laser-driven ion acceleration can for example be found in the publications by Mora et al. [69] or Schreiber et al. [70].

Other acceleration mechanisms

While TNSA represents one widely known process for the generation of laser-driven proton beams, several other mechanisms were investigated with the goal of identifying the most efficient regime to transfer the available laser energy into kinetic energy of the protons. A summary of the principle ideas behind some of those mechanisms is presented here. The reviews from Macchi et al. [33] and Daido et al. [66] provide a more comprehensive description.

One can imagine that an increase in kinetic energies of laser-driven protons requires either a stronger electric field or an increase in the duration for which the acceleration can be maintained. The latter can be realized by a comoving electric field that, in comparison to the TNSA case, does not remain stationary. This basic idea is embedded for example in the radiation pressure acceleration (RPA) [28] mechanism. In this process, a high-intensity laser pulse pushes the electrons at the surface of an opaque target inwards due to the ponderomotive force (section 2.1.3). An electrostatic field forms, because of the slower response of the more massive ions, which acts on the ions and leads to their acceleration. For an ultra-thin target, in the so-called *light sail* regime, all target electrons are accelerated forward, forming a relativistic plasma mirror. While being reflected off the electron layer, the laser pulse pushes the electrons further and the ions are accelerated by the comoving electric field. RPA light sail acceleration is experimentally [29, 62] very challenging since the thin targets must remain dense enough during the interaction and thus pre-expansion and heating needs to be completely prevented. This can be realized with an ultra-high laser contrast and a circularly polarized pulse [71]. An additional complexity represents the Rayleigh-Taylor (RT) instability that occurs during the radiation pressure acceleration [62] and causes rippling and at some point breakups of the interfaces.

Even if the initial target is much thicker and not all electrons experience the radiation pressure of the laser pulse, the plasma is still pushed inwards at the front side. This process is named hole boring [27] as the finite laser spot size leads to a parabolic deformation of the surface allowing the pulse to penetrate the target with a velocity v_{HB}. The resulting electrostatic potential can be the source of a shock propagating with v_{sh} into the target if the hole-boring velocity is larger than the ion sound speed [72]. This process is termed collisionless shock acceleration [37] and was studied experimentally in e.g. [38] or [73]. Background ions are accelerated by or, in other words, are reflected at the electric potential, which originates either from the hole-boring process or the shock, producing a population of energetic protons with on average twice the velocity of v_{HB} or v_{sh}.

Coulomb explosion, as the last process that should be mentioned here, is a collective mechanism of ion acceleration where almost all electrons are expelled from the irradiated target [74, 75, 76, 77]. The remaining ion core explodes due to the repulsive positive electric charge and ions are accelerated in the electrostatic potential which is formed by the ejected electrons. Coulomb explosion can be realized by e.g. irradiating nanometer-sized cluster targets [78, 79, 80].

This rather phenomenological description of the different ion acceleration mechanisms conceptually illustrates the scenario of the energy transfer to ions and protons through a population of laser-driven electrons. In order to explain how the electrons gain their kinetic energy in the first place, the basics of laser-matter interaction must be discussed in advance starting with the generation of plasmas.

2.1.1 Plasma formation

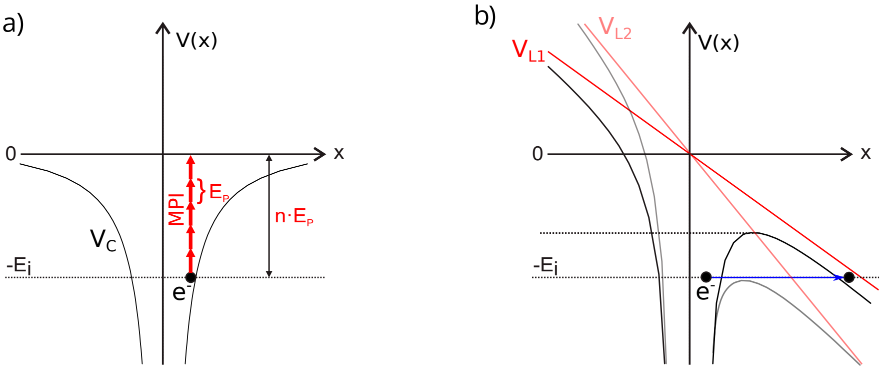

Figure 2.2: Ionization mechanisms and the Coulomb potential (V_C) in a single atom. a): Multi-photon ionization (MPI). b): Tunneling ionization (solid lines like V_{L1}) and barrier suppression ionization (BSI, illustrated by transparent lines).

Before any laser energy can be transferred into kinetic energy of particles, electrons must be freed from the attracting coulomb potential of their nucleus. This ionization process transforms the irradiated material into a plasma state. While photoionization of the atoms by single photons with the wavelength λ_L and energy $E_p = \frac{2\pi\hbar}{\lambda_L}$ ($\hbar$: Planck constant) cannot be directly achieved for most substances, since E_p is too small to overcome the ionization energy E_i[*], for the intensities available with short pulse lasers other ionization mechanisms become relevant.

Multi-photon ionization (MPI), as one example, is the transition of the electron to an unbound state by simultaneous absorption of at least n photons with a total energy $n \cdot E_p > E_i$ (displayed in figure 2.2a). MPI requires e.g. $n \geq 10$ photons with a wavelength of 800 nm to ionize hydrogen atoms that feature an ionization energy of 13.6 eV. If the incident laser is intense enough, then the associated electric field ($E_f \propto \sqrt{I_L}$) is able to alter the coulomb potential to such an extent that electrons can tunnel through the remaining potential barrier with a certain probability. This tunnel ionization process is shown in figure 2.2b for the laser field potential V_{L1}. A further increase of the laser field strength lowers the potential barrier below the energy level of the electron and leads to instantaneous ionization (barrier-suppression ionization). The threshold intensity for this process is given for the charge state Z of the relevant atom by [81]

$$I_{BSI} = E_i^4 \frac{\pi^2 c \varepsilon_0^3}{2Z^2 e^6} \quad . \tag{2.3}$$

c, ε_0 and e denote the speed of light, the vacuum permittivity and the elementary charge. Barrier-suppression ionization is e.g. expected at laser intensities above $1.37 \cdot 10^{14}$ W/cm^2

---

[*] For example near-infrared laser photons with λ_L = 800 nm yielding E_p of 1.5 eV are not energetic enough to ionize most materials. For comparison, hydrogen features a ground state potential of 13.6 eV.

for hydrogen. Since the peak intensities for proton acceleration ($I_L > 10^{18}$ W/cm^2) are several orders of magnitude above I_{BSI}, most materials can be expected to become fully ionized. Moreover, ionization typically begins in the rising edge of the pulse and as a result, the highest intensities interact with the generated plasma. The transition from the solid state to a plasma state substantially changes the optical properties of the material and therefore the propagation of the electromagnetic wave.

2.1.2 Propagation of electromagnetic waves in plasmas

Consider a fully ionized plasma consisting of electrons and ions that are in local thermal equilibrium. Due to their higher mass, the movement of the ions is neglected in comparison to the lighter electrons. Hence, the electron population can oscillate with respect to the static ion background with the plasma frequency [82]

$$\omega_P = \sqrt{\frac{n_e \cdot e^2}{\varepsilon_0 \cdot m_e}} \tag{2.4}$$

where m_e and n_e describe the electron mass and the electron density, respectively. An external plane wave consisting of an electric field described by $\vec{E}(\vec{r},t) = \vec{E_0}(\vec{r})cos(\omega_L t)$, with an amplitude $\vec{E_0}$ and an angular frequency $\omega_L = 2\pi c/\lambda_L$, disturbs the plasma by shifting the electrons against the ion background. The system response to the disturbance is given by the dielectric function

$$\varepsilon = \eta^2 = 1 - (\omega_P/\omega_L)^2 \quad . \tag{2.5}$$

From this, the refractive index η can be derived as a key parameter for the propagation of electromagnetic waves in a plasma*.

In the case of $\omega_L > \omega_P$, which is equal to $0 < \eta < 1$, light penetrates the plasma and is deflected in this process. In contrast to transparent media with $\eta > 1$ (like optical components made of glass) where a convex shape leads to focusing effect, a plasma with $\eta < 1$ defocuses a plane wave. For low-frequency light ($\omega_L < \omega_P$) the refractive index is purely imaginary and the plasma therefore opaque. Nevertheless, an evanescent wave can still penetrate the plasma over a characteristic length denoted by the skin depth $l_s = c/\omega_p$. Thereby, the amplitude decreases exponentially with the penetration depth.

The density at which $\omega_L = \omega_P$ applies or, in other words, at which the plasma changes from transparent to opaque for a given light wavelength, is the critical density n_c. Analogous to equation 2.4, n_c is given by

$$n_c = \frac{\omega_L^2 \cdot \varepsilon_0 \cdot m_e}{e^2} \quad . \tag{2.6}$$

Plasmas with densities above n_c are called overdense. Underdense plasmas, on the other hand, are characterized by $n_e < n_c$. By combining equation 2.5 and 2.4 the refractive index can be expressed using the plasma density

---

*This approach ignores the influence of the magnetic component of the wave. This is justified as long as the disturbance of the plasma electrons by the electric field leads to electron velocities far below the speed of light.

$$\eta = \sqrt{1 - \frac{n_e}{n_c}} \quad . \tag{2.7}$$

For example, laser light with 800 nm wavelength originating from near-infrared laser systems can penetrate plasmas up to the critical density of $n_{c,800\mathrm{nm}} = 1.74 \cdot 10^{21}\ \mathrm{cm}^{-3}$. As a comparison, the electron density for fully ionized materials can be calculated using $n_e \approx N_e/M \cdot N_A \cdot \rho$, with the number of electrons N_e and the molar mass M in each molecule, the Avogadro constant N_A and the mass density ρ. If materials consist of several molecular compounds, an additional summation of the relative contributions is required. Solids used as targets for laser-ion acceleration feature much higher densities than $n_{c,800\mathrm{nm}}$ and act therefore as overcritical plasmas (e.g. titanium with $n_e = 1.24 \cdot 10^{24}\ \mathrm{cm}^{-3} \approx 700\, n_{c,800\mathrm{nm}}$ or formvar [83], a typical plastic to fabricate thin films, with $n_e = 4.1 \cdot 10^{23}\ \mathrm{cm}^{-3} \approx 235\, n_{c,800\mathrm{nm}}$). Even solid hydrogen, the material with the lowest solid density, is characterized by an overcritical plasma density of $n_e = 5.1 \cdot 10^{22}\ \mathrm{cm}^{-3}$, which is about 30 times higher than $n_{c,800\mathrm{nm}}$.

Note on relativistic effects

The propagation of electromagnetic waves in plasmas discussed so far is only valid until the acceleration of electrons in the electric field results in velocities that are comparable to the speed of light. Higher field amplitudes cause a relativistic mass increase $m_e = \langle\gamma\rangle \cdot m_{e0}$ with the time-averaged relativistic factor $\langle\gamma\rangle$. The increased electron mass lowers the plasma frequency, since $\omega_P \propto m_e^{-1/2}$, and hence modifies the refraction index calculation from equation 2.7 to

$$\eta_{rel} = \sqrt{1 - \frac{n_e}{\langle\gamma\rangle \cdot n_c}} \quad . \tag{2.8}$$

As a result, intense laser pulses can penetrate targets with up to $\approx \langle\gamma\rangle \cdot n_c$ and thus can enter plasmas with densities above the (non-relativistic) critical density. This effect is known as relativistic transparency. In reality, however, the density threshold for transparency is much more complex because the electromagnetic wave compresses the electron density through the ponderomotive force (see next section). This counteracts the laser penetration [84]. The higher electron mass increase additionally leads to an increase in skin depth to $l_{s,rel} = \sqrt{\langle\gamma\rangle} \cdot c/\omega_p$, which results in a larger penetration depth of the evanescent wave.

2.1.3 Laser energy absorption into electrons

In order to understand how the energy of the laser pulse is converted into kinetic energy of the plasma electrons, first, the energy gain by a single electron in a vacuum will be discussed. Assume a plane electromagnetic wave with amplitudes $\vec{E_0}$ and $\vec{B_0}$ for the electric and magnetic field components and an angular frequency ω_L: $\vec{E}(\vec{r},t) = \vec{E_0}(\vec{r})cos(\omega_L t)$, $\vec{B}(\vec{r},t) = \vec{B_0}(\vec{r})cos(\omega_L t)$. In this field, an electron with the charge q_e is accelerated due to the

Lorentz force

$$\vec{F}_L = q_e\vec{E} + q_e\vec{v} \times \vec{B} \tag{2.9}$$

and the resulting motion caused by the electric field component is described by an oscillation with the starting point at the center. The Lorentz force term originating from the magnetic field can be neglected as long as the electron velocity $\vec{v}$ is much smaller than the speed of light. Due to the periodic nature of the electric field, the electron does not gain any net kinetic energy after one oscillation. However, adding a spatial gradient to the electromagnetic wave, as it is present in a focused laser beam, leads to a gain in the electron momentum. The initial acceleration shifts the electron to a region with a lower amplitude and, thus, a weaker restoring force. The yield averaged over one oscillation becomes non-zero and is expressed by the time-averaged, non-relativistic ponderomotive force $\vec{F}_p^{nrel}$ [85]

$$\vec{F}_p^{nrel} = -\frac{q_e^2}{4m_e \cdot \omega_L^2}\nabla(\vec{E}_0^2) \propto -\nabla I_L \quad . \tag{2.10}$$

As a result, particles are pushed to regions of lower field amplitudes or rather lower laser intensities I_L gaining momentum in this process.
With the increase of the electric field amplitude, the electron velocity approaches the speed of light and the effect of the magnetic field cannot be neglected anymore. Derivation of the relativistic equation of the ponderomotive force requires a mathematical approach which is presented in e.g. [86]. This leads to the expression

$$F_p^{rel} = -m_e c^2 \nabla\langle\gamma\rangle \tag{2.11}$$

where the time-averaged relativistic factor $\langle\gamma\rangle$ can be estimated by [33]

$$\langle\gamma\rangle \approx \sqrt{1 + a_0^2/2} \quad . \tag{2.12}$$

$a_0 = \frac{eE_0}{m_e c\omega_L}$ denotes the normalized vector potential which is equal to the ratio of the electron momentum gained from the accelerating field and $m_{e0}c$. a_0 can be calculated based on the laser intensity I_L and wavelength in micrometer $\lambda_{\mu m}$ by [33]

$$a_0 = 0.85\sqrt{\frac{I_L\lambda_{\mu m}^2}{10^{18}\mathrm{Wcm}^{-2}}} \quad . \tag{2.13}$$

Relativistic effects become relevant for near-infrared laser pulses at $I_L \gtrapprox 10^{18}$ W/cm^2 ($a_0 > 1$), at so-called relativistic laser intensities. For comparison, nowadays available laser pulses, as e.g. from the DRACO system with peak intensities up to $5 \cdot 10^{21}$ W/cm^2 at 800 nm wavelength (see chapter 4), correspond to $a_0 \approx 48$ and $\gamma \approx 34$. For simplicity, γ (without the brackets) refers to the time-averaged Lorentz factor throughout the rest of this thesis. Note that the expression for γ only serves as an estimate for a free electron, the energy transfer to collective responding electrons would be overestimated. According to Kluge et al. [87], in this case, a weighted average of the kinetic energy of an ensemble of electrons must be considered to find the time-averaged relativistic factor.

In the section up to this point, it was explained how a single electron is accelerated by an electromagnetic wave. However, mechanisms that are responsible for the laser energy absorption in a plasma are vastly different because now a large number of electrons, which are coupled to the heavy ions background, are present. The following part summarizes the most relevant mechanisms. A more extensive description is given, for example, by Wilks et al. [88].

Absorption of laser energy and conversion into kinetic energy of the electrons is in general a very complex process that depends on several laser parameters as irradiance, wavelength and polarization as well as target properties such as density and pre-plasma scale length. Moreover, since the intensity levels of real laser pulses span over several magnitudes, a multitude of absorption mechanisms could play an important role. The following part concentrates on the most significant mechanisms. For this purpose an overdense plasma is assumed, which is irradiated by an ultra-short laser pulse with a peak intensity $I_L \gg 10^{18}\,\mathrm{W/cm^2}$. The initial target is fully ionized and at the vacuum interface the plasma density decreases exponentially with a finite scale length L_p. This scenario is usually caused by the background radiation that interacts with the target front before the peak intensity arrives. According to the optical plasma properties, the pulse penetrates the underdense part of the plasma and is reflected latest at the relativistic critical density γn_c while an evanescent wave enters the overdense plasma. The most significant absorption mechanism in this scenario is the relativistic $\vec{J} \times \vec{B}$ heating, as discussed by Kruer and Estabrook [89]. In a simplified picture and for a normal laser incidence, electrons are accelerated parallel to the surface by the electric field component of the laser pulse. The electron motion combined with the magnetic field component results in a Lorentz force perpendicular to the surface that acts on the electrons and accelerates them into the overdense plasma. Since the laser pulse can only penetrate up to the characteristic skin depth, the electrons will be screened from the restoring Lorentz force gaining kinetic energy in this process.

While $\vec{J} \times \vec{B}$ heating becomes dominant at relativistic intensities, a similar conversion from laser energy into electron momentum becomes relevant at sub-relativistic conditions making only use of the electric field as proposed by Brunel [90]. This requires an oblique laser incidence in order to provide an electric field component normal to the target surface. This field accelerates electrons into the overdense plasma beyond the critical density that attenuates the restoring force. Electrons gain kinetic energy in this process similar to the $\vec{J} \times \vec{B}$ effect.

While both mechanisms explain an energy transfer in a thin layer at the critical density, focusing a high-intensity laser pulse onto a (relativistically) underdense plasma can also lead to an efficient energy conversion into electrons, however, at different interaction dynamics. This results from the fact that the laser pulse can propagate through a plasma that is classically ($n_e < n_c$) or even relativistically transparent ($n_e < \gamma n_c$). While in solids the pulse interacts mainly with a thin surface layer of sub-micrometer thickness, in the case of underdense plasma targets the pulse can propagate over distances of at least several micrometers within the material. Electrons gain energy from the laser pulse and thus are expelled from the laser propagation axis under the action of the ponderomotive force. This results in the formation of a channel with a low electron density. The laser pulse is focused in such a channel since light rays are bent to regions of higher refractive index which is equal to smaller plasma density (see equation 2.7). Another contribution to the self-focusing effect arises from the relativistic mass increase of the plasma electrons. Electrons that experience higher laser intensities also reach higher energies which leads to a larger relativistic γ factor and thus to a larger refractive index (equation 2.8). The threshold power for relativistic self-focusing at a certain plasma density is given by [91, 92]

$$P_c \approx 17 \frac{n_c}{n_e} \mathrm{GW} \quad . \tag{2.14}$$

Laser powers above the critical P_c result in a relativistic self-guiding of the pulse confining the laser beam in a small spot size over several times the Rayleigh length. Since the immobile plasma ions remain stationary, their restoring electrostatic potential can lead to the development of an accelerating plasma cavity. For lower density plasmas (10^{17}–10^{19} cm^{-3}), these cavities are exploited in laser-driven wakefield accelerators (LWFA) to generate GeV electron beams with a small energy spread [2]. The transfer from laser energy to the electrons results in depletion of the laser pulse. For the LWFA regime the depletion length $L_d \approx (n_c/n_e)c\tau_L$ [93], with τ_L the laser pulse duration, is in the range of millimeters. Despite the complex absorption processes [94] for plasma densities in the vicinity of the critical density, depletion lengths can be described by similar equations [95]. As a consequence, it is expected that the energy of an ultra-short laser pulse is absorbed within a few micrometers to a few tens of micrometers. This scenario can be utilized for enhancing laser-ion acceleration, as will be discussed in the next section.

2.2 The role of underdense and near-critical density plasmas for laser-proton acceleration

Laser-ion acceleration is often associated with the interaction of a high-intensity laser pulse with a solid target that has a density significantly above γn_c. However, under experimental conditions, there is almost always an additional interaction with an underdense plasma region (e.g. on the irradiated target surface) that could be beneficial for the acceleration process. Moreover, the interaction of the laser pulse with a lower density target can even lead to an efficient ion acceleration. In contrast to solid density plasmas where the interaction is limited to a thin surface layer in the order of the skin depth, the laser pulse can penetrate transparent plasmas transferring its energy to electrons in the entire target volume which potentially leads to higher hot electron densities and thus stronger accelerating fields. However, establishing a substantial energy transfer requires a much thicker target. According to the depletion length (previous section 2.1.3), an ultra-short laser pulse of 30 fs can penetrate a plasma with a density in the vicinity of n_c on a length of several micrometers.

The beneficial usage of underdense plasmas in the context of laser-ion acceleration is often related to plasmas with densities in the same order as n_c ($\sim$ 0.1-10 n_c) that are termed near-critical density plasmas. Several ion acceleration mechanisms are discussed in this regime, ranging from relativistic transparency enhanced TNSA [32, 34, 36, 96] and synchronized acceleration by slow light (SASL) [40] to collisionless shock acceleration [37, 39] and magnetic vortex acceleration [43, 44, 47, 51]. In the following, a few scenarios are discussed in which the usage of near-critical density plasmas can be beneficial for ion acceleration. This involves layered targets, with a near-critical density front side layer, the relativistic transparency regime, where the target turns transparent during the interaction, as well as magnetic vortex acceleration. The latter two will become relevant in the experimental studies in chapter 4.

An additional remark concerning the future role of near-critical density targets should be added. With the progress in laser technology [53] and thus an increase in available peak intensities in the foreseeable future, the pulse can relativistically penetrate much higher plasma densities which could render near-solid targets transparent. This increases the importance of understanding the laser interaction with near-critical density plasmas. As an example, based on the optimistic peak intensities of next generation laser systems reaching up to 10^{23} W/cm^2 (e.g. at ELI-Beamlines [97]), the laser pulse is expected to relativistically penetrate densities up to $\approx 200 n_c$ which is already in the range of the density found in typical plastic targets.

2.2.1 Laser-proton acceleration in the near-critical regime

Near-critical density front-side layers

One beneficial application of near-critical density materials in ion acceleration studies is their usage in double-layer target configurations, where a n_c layer is attached to a solid foil. Several effects that can improve the yield of laser-driven protons were identified in numerical and experimental studies. First, according to particle-in-cell simulations [98, 99, 100, 101] more laser energy is converted into kinetic energy of the electrons because less light is reflected in comparison to the mirror-like, bare foil. The higher absorption results in an enhancement of proton energies. A near-critical front side layer is further expected to improve the laser beam quality by realistic self-focusing and pulse steepening [102] before interacting with the solid foil. The former is based on a variation in refractive index inside the plasma channel acting as a focusing lens that potentially reduces the laser spot size and thus leads to an increase in intensity that interacts with the foil. Since self-focusing sets in for laser powers above the critical value P_c, lower powers at the leading edge of the pulse (e.g. laser pre-pulses) might not experience the focusing effect reducing their relative intensity when they reach the foil. Moreover, the pulse contrast can further be enhanced due to depletion of the leading pulse edge during the propagation through the plasma. Lastly, a reported beneficial effect of the near-critical density layer is the generation of superponderomotive electrons that enhance the sheath field at the target rear side [103, 104, 105].

Experimental studies utilize nanoscopic substances made of carbon foam coatings [106] or carbon nanotube films [103] for the n_c layer. Most experiments found an improvement of proton and carbon energies, which is explained by a number of the processes from above. Note that some of the beneficial effects require not necessarily a near-critical plasma. Even a dense gas jet in front of a solid foil can be used to study the beam cleaning and self-focusing properties [107]. This was investigated as a project within the WHELMI[*] collaboration.

Relativistic induced transparency

In a plasma of solid density the pulse interacts only with a small layer on the irradiated target side that has a thickness on the scale of the relativistic skin depth $l_{s,rel}$ (section 2.1.2). A decrease of the target thickness to $l_{s,rel}$ results in a volumetric interaction with the entire target interior. Volumetric heating can enhance, for example, the acceleration performance in the TNSA regime. However, in order to reach this regime, targets have to be manufactured in a rather thin layer. For example, the relativistic skin depth for a plastic foil which is made of formvar ($n_{CH} = 235\, n_{c,800\mathrm{nm}}$) is about 46 nm assuming a petawatt-class laser pulse with $a_0 = 42$. Even for solid hydrogen ($n_{H2} = 30\, n_{c,800\mathrm{nm}}$), the element with the lowest solid density, $l_{s,rel}$ corresponds to about 127 nm. Such thin targets are typically subject to pre-expansion caused by heating due to the laser background radiation or ultimately the rising edge of the laser pulse. The expansion leads to a decrease in bulk density turning the target transparent during the interaction and the remaining laser pulse can penetrate the now (relativistically) underdense plasma. The combined effects of plasma expansion and a relativistic increase in the electron mass (see section 2.1.2) is termed relativistic induced transparency (RIT) [108, 25, 34, 36, 109]. Hence, RIT represents a scenario where the laser pulse interacts at least partially with a transparent plasma. According to Vshivkov et al. [36], RIT occurs when the target thickness d satisfies the condition

$$d \ll \frac{2a_0 c\omega_L}{\omega_p^2} \quad . \tag{2.15}$$

For example, a formvar foil thinner than 45 nm or a hydrogen target thinner than 350 nm satisfy this criterion ($a_0 = 42$).

RIT can strongly affect ion acceleration. It is most beneficial if the onset of transparency occurs at the moment when the peak intensity of the pulse reaches the target, which maximizes the transfer of laser energy into kinetic energy of protons and ions [108]. Based on this condition, Mishra et al. [35] proposed an analytic model that determines the optimal target thickness and density for ion acceleration. This model assumes a step-like overdense profile and a Gaussian laser pulse. The model also includes the target expansion and a corresponding reduction of the core density due to heating of the plasma. Mishra et al. found for the optimal areal density

---

[*] Weizmann-Helmholtz Laboratory for Laser Matter Interaction

$$\frac{n_e}{n_c} d \approx 0.59 \cdot c\tau_L \sqrt{a_0^3 \frac{m_e}{m_i}} \tag{2.16}$$

with the pulse duration τ_L and the electron/ion mass m_e/m_i. Assuming again $a_0 = 42$ and τ_L =30 fs for the laser beam, the optimal thickness d equals 1.25 µm for a pure hydrogen target and about 160 nm for formvar. Similarly, for a Gaussian laser pulse of intensity a_0 a simulation study by Esirkepov et al. [32] reported the optimal normalized areal density $\sigma = n_e/n_c \cdot d/\lambda_L$. The highest proton energies are obtained when the following condition is fulfilled

$$\sigma_{opt} \approx 3 + 0.4 \cdot a_0 \quad . \tag{2.17}$$

For the examples from above ($a_0 = 42$), the best performing thickness from equation 2.17 is expected at 0.56 µm for solid hydrogen and 70 nm for formvar.

The models from Mishra et al., Esirkepov et al., Vshivkov et al. as well as the relativistic skin depth can be used to estimate the required target thickness (for a known density) at which RIT is supposed to occur and thus ion acceleration can be improved. However, the best performing target thickness under experimental conditions [110, 111, 96, 25, 112, 108, 113, 114, 115, 116, 117, 118, 26, 119, 120, 121] often depends on the temporal laser intensity profile. A large amount of background radiation and strong laser pre-pulses can lead to an earlier pre-expansion and thus to an already transparent plasma before the peak intensity reaches the target. If the laser contrast level can be sufficiently suppressed, for example by implementing a plasma mirror device, an increase of maximum proton energies at the optimum thickness can be expected [96]. While proton acceleration in the TNSA regime may become ineffective when the target turns transparent at earlier times, other mechanisms could benefit and potentially leads to the generation of high energetic ion beams. One of those mechanisms is the so-called *break-out afterburner* (BOA) [122, 123, 108, 117]. BOA sets in when the expanded target becomes transparent. The penetrating part of the laser pulse pushes the electrons, which are expected to transfer their kinetic energy to the ions through the Buneman-type instability.

Magnetic vortex acceleration

Contrary to the previous two examples where in transparent plasma proton acceleration can be enhance by front-side effects or relativistic induced transparency, laser-proton acceleration can also originate directly from a near-critical density target. The best studied mechanism in this regime is the so-called magnetic vortex acceleration (MVA) that is schematically illustrated in figure 2.3. The central element is the existence of a magnetic field structure at the target rear side that can be explained as follows: The laser pulse penetrates the near-critical plasma, forms a channel and accelerates a thin electron filament along its propagation direction. A return current is formed at the channel walls that leads together with the hot electrons to the generation of a toroidal quasi-static magnetic field

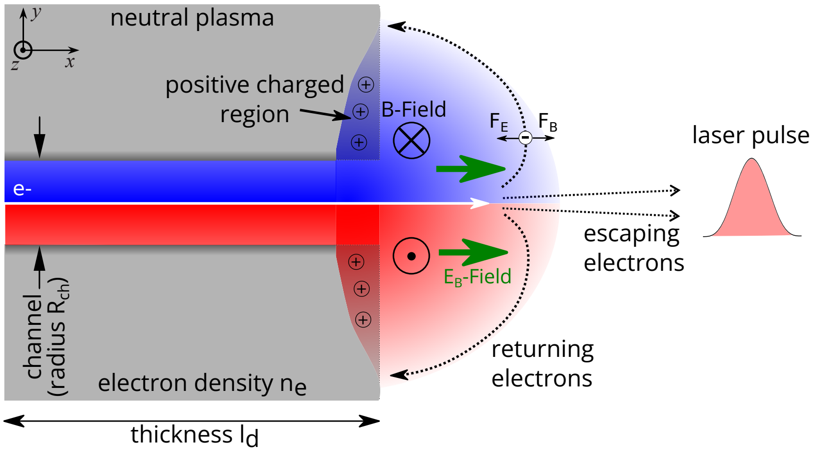

Figure 2.3: Based on [124]. Sketch of the magnetic vortex acceleration at the rear side of an underdense or near-critical density plasma irradiated by an intense pulse. A laser-generated electron current inside the low-density channel creates a toroidal magnetic field that expands from the rear side into the vacuum and induces an electric field E_B which is capable of accelerating plasma ions.

inside the channel with a typical strength in the order of $B \sim m_e c\omega_p/e \approx 10\,\text{kT}$ [66]. Following the laser pulse, the electron current exits the plasma region at the rear side resulting in an expansion of the magnetic field into the vacuum where it forms a vortex structure. Parts of the fast electrons return to the target due to the positive charged rear side and by that perform a vortical motion that helps to sustain the magnetic field after the laser pulse has passed [125]. Simulation studies of MVA [47, 48, 42, 126, 75, 43, 44, 125] proposed several physical processes that could lead to proton acceleration. All have in common that the magnetic field at the rear side plays a decisive role. The most straightforward process is based on the induction of an electric field. During the expansion of the magnetic field, the magnetic flux changes in time leading, according to Faraday's law, to the generation of an electric field that opposes its cause (the electron current) and therefore accelerates ions in the laser propagation direction. Note that the escaping electrons generate an additional charge separation field that contributes also to the final proton energies. While a detailed discussion about the relative contributions of the charge separation and induced electric field has not been reported so far, Willingale et al. [127] calculated for their example (with a pulse duration of 500 fs) that proton acceleration due to the magnetic field has a smaller effect than the charge separation field. However, for ultra-short pulses, the induced electric field could become more significant. As another example, Lemos et al. [128] found comparable contributions.

Beside the accelerating component, another beneficial characteristic of the induced electric field is a collimating transverse component that reduces the divergence of the proton beam [47]. The transverse field component is caused by the displacement of surface electrons on the rear side and thus the generation of positively charged regions (see figure 2.3) while the negative charge is concentrated around the central axis. As a result, narrow divergence angles below 8° (not commonly found in solid target experiments [8]) are predicted from numerical simulations for proton energies above 30% of the maximum energy [47].

The magnetic field further helps to sustain the electric field at the rear side for a longer time by preventing electrons from returning to the positive charged region on the rear side [129]. The effect is exemplified in figure 2.3 for an electron that returns to the rear side because it had not sufficient kinetic energy to escape from the target region. While this electron experiences an attractive Coulomb force $\vec{F_E}$ (in negative x-direction) due to the positive charged region, its movement under the influence of the magnetic field results in a counteracting force $\vec{F_B}$. Assuming $\vec{F_E} = \vec{F_B}$ allows to derive an estimator for the electric field that can be sustained by the magnetic vortex field $\vec{B}$. Consider a charge distribution $\rho = q_e n_e$ instead of a single electron in order to formulate the Lorentz force as $\vec{J} \times \vec{B}$ where $\vec{J}$ denotes the current density. $\vec{J}$ can be expressed with Ampere's law as $\nabla \times \vec{B} = \mu_0 \vec{J}$ [85] (neglecting time-varying $\vec{E}$-fields) which results in

$$\vec{F_E} = \vec{F_B} \tag{2.18}$$

$$\vec{E} q_e n_e = \frac{1}{\mu_0} (\nabla \times \vec{B}) \times \vec{B} \tag{2.19}$$

$$= \nabla \left(\frac{\vec{B}^2}{2\mu_0} \right) + \frac{1}{\mu_0} (\vec{B} \cdot \nabla) \vec{B} \quad . \tag{2.20}$$

The transformation from the second to the third line is the result of rearrangements by means of vector calculus identities, as shown in e.g. [85]. The term in equation 2.20 consists of a first component due to the magnetic pressure ($\frac{\vec{B}^2}{2\mu_0}$) and the magnetic tension force as the second term. The latter can be neglected in this estimation since $\vec{B_z}$ consists only of a component in z-direction that does not vary along z. As a result, the electron component of the plasma experiences a force due to the $\vec{B}$-field that is proportional to the gradient of the magnetic pressure. By rearranging equation 2.20 an electric field strength of $E \sim \nabla B^2/(2\mu_0 q n_e)$ can be derived*. This expression is often used to describe the electric field strength [124, 66, 126], which can be maintained by a toroidal magnetic field on the target rear side.

MVA can result in energetic proton beams when a uniform slab target with densities between 1.6 n_c to 10 n_c is considered [43]. However, MVA is sensitive to the rear side gradient. If the gradient is steep, the magnetic vortex expands perpendicular to the gradient, while a more gentle plasma gradient leads to a movement of the magnetic field along the channel axis. Nakamura et al. [44] found a proton acceleration optimum for a profiled target of a few 10 µm thickness surrounded by a lower density plasma region and a corresponding density ramp. The magnetic vortex expands in this case along the channel axis with a velocity on the order of the Alfvén velocity. The induced electric field reflects background ions, located ahead of it, to velocities twice the magnetic vortex expansion speed.

Generally speaking, in order to maximize the contribution of MVA under experimental conditions, as much laser energy as possible has to be transferred into the magnetic field structure. Two main conditions concerning the laser pulse and the target need to be satisfied for optimal energy transfer. First, the focal spot at the target front side should match the laser channel size inside the plasma, which is formed due to relativistic self-focusing. The radius of the channel R_{ch} for the employed laser with a power P_L and the wavelength λ is given by [130, 47]

---

*For comparison, the same expression in cgs units is given by: $E \sim \nabla B^2/(8\pi e n_e)$

$$R_{ch} = \frac{\lambda}{\pi} \left(\frac{n_c}{n_e}\right)^{1/3} \left(\frac{2P}{KP_{cr}}\right)^{1/6} \quad . \tag{2.21}$$

$K = 0.074$ denotes a geometry factor and P_{cr} is the characteristic power for self focusing that is 17 GW from equation 2.14. A laser spot size that is too small will lead to filamentation in multiple channels and a spot size that is too large will result in decreased energy transfer. Second, for an optimal energy transfer into electrons, the laser energy should be depleted on the target rear side. Thus, the depletion length [130, 47]

$$L_d = 2^{1/3} K^{2/3} c\tau_L \left(\frac{n_c}{n_e}\right)^{2/3} \left(\frac{P}{P_{cr}}\right)^{1/3} \tag{2.22}$$

should match the target thickness. Here the result depends on the laser pulse duration (τ_L). Proton energies become maximized if both conditions are satisfied. According to the simulations reported by Bulanov et al. [43], a 1 PW laser pulse interacting with a 50 λ thick and 3 n_c dense target could produce proton beams with energies up to 1.3 GeV . While MVA promises efficient laser-proton acceleration based on numerical studies, there are only a few experimental publications [45, 127, 131, 132, 46, 51, 128] that claim the observation of this mechanism. However, improvements of accelerated proton beams (regarding maximum energies, beam quality and yield) in comparison to TNSA acceleration with the same laser pulse from typical foil targets have not been reported to far.

As a final remark, it should be noted that near-critical density targets can also be beneficial for a number of acceleration mechanisms that are described for overdense plasmas. As an example concerning hole boring acceleration, the velocity v_{HB} [30, 33, 133]

$$\frac{v_{HB}}{c} = \frac{\Xi^{1/2}}{1 + \Xi^{1/2}}, \quad \Xi = \frac{ZI_L}{Am_p n_e c^3} \tag{2.23}$$

depends on the plasma density as $\propto 1/\sqrt{n_e}$ (in the non-relativistic limit [30]) and, thus, higher ion energies are supposed to be achieved for lower plasma densities. In fact, the highest proton energies from hole-boring are expected for targets that are barely opaque to the laser pulse [134]. Whereby due to steeping of the plasma density by the laser pulse [84], the initial plasma density can also be considerably lower than γn_c. Similarly, a comparable benefit for ion acceleration using lower plasma densities is also found for collisionless shock acceleration [72].

2.2.2 Near-critical density target concepts and their experimental realization

Understanding of the positive effects that are associated with near-critical density plasmas for example in double-layer targets, scenarios of RIT or magnetic vortex acceleration relies mostly on simulations. Experimental studies that isolate the contributions from the interaction with the near-critical density are limited due to the availability of such densities. This is because target materials with a density equivalent to n_c for near-infrared wavelengths cannot easily be fabricate. Solid (and liquid) materials are in general too dense (n_e is at least a few 100 n_c) while gases at ambient conditions are characterized by plasma densities in the sub-percent range of the critical density. As such, target systems attempting to reach the near-critical regime can be structured in three categories: high-density gas jets (1), expanding solid targets (2) or non-homogeneous nanostructured materials (3). Based on the published literature, an overview of these three attempts follows, highlighting their respective capabilities and limitations.

1) Gas nozzle designs, for example from Sylla et al. [49], operate at high pressures (up to 1000 bars) to produce gas jets with densities up to $\sim n_c$. Those jets were employed in a number of experiment [50, 135, 136, 137, 45, 138, 139, 140] where the high repetition rate capabilities and the operation with single ion species gases are advantageous. Most acceleration results reported on proton beams with maximum energies at the MeV level were explained either by Coulomb explosion or collisionless shock acceleration. In contrast, Willingale et al. [45] reported on helium ions with up to 40 MeV in a collimated beam in the laser propagation direction. Further analysis indicated a contribution from an accelerating electric field caused by a time-varying magnetic vortex field at the rear side [127]. Besides ion acceleration, high-density gas jets were also employed to study the permanence and stability of toroidal magnetic fields [141] and to investigate the collapse of laser pulses in near-critical plasmas [137]. The advantage of gas jets in this context is that they allow optical probing to be carried out, enabling the temporal and spatial interaction dynamics to be observed. Until now, high-density gas jets are characterized by a Gaussian-shaped density profile with an intrinsically long density ramp and are therefore not useful whenever a very sharp gradient is required. Moreover, at critical densities, ultra-short laser pulses deplete already within a few 10 µm and cannot penetrate the bulk of the gas to generate efficient magnetic vortex structures at the rear side that are required to study e.g. MVA under optimized conditions. A promising approach to reduce the length of the ramps and to increase the plasma density was reported by Helle et al. [51]. This approach is based on introducing strong hydrodynamic shock waves into a gas jet using nanosecond laser pulses.
While the production of gas targets with critical density for ~1 µm wavelength laser systems is technologically challenging, reaching the same conditions with infrared CO_2 lasers at 10 µm wavelength is less demanding due to the factor 100 lower critical density ($n_c \sim 1/\lambda^2$, refer to equation 2.4) that can be realized at much lower gas pressures. Under those conditions, the experiments from Palmer et al. [73] and Haberberger et al. [38] reported on monoenergetic proton beams that were accelerated by radiation pressure-driven shocks.

2) Contrary to gas jets where a low-density gas is compressed to reach plasma densities of n_c, exploded foil targets utilize the expansion of a solid material until the core density drops to the near-critical regime. The expansion is usually induced by irradiation with an additional laser beam or a laser pre-pulse [131, 132, 142, 143, 144]. Proton and ion acceleration from exploded foils is explained either by MVA [131, 132] or collisionless shocks

[143, 144]. This approach enables studies of various plasma density profiles by varying the intensity and time delay of the additional laser beam. However, the exact configuration at the arrival time of the high-intensity pulse can only be inferred in detail using numerical magneto-hydro dynamic studies (e.g. [131]) that simulate the expansion over a time span of several tens of picoseconds to nanoseconds. Experimental measurements of the exploded target profile can only resolve relatively low-density regions [143] or require more sophisticated methods, like x-rays probes, that penetrate and resolve the high plasma density regions.

3) An alternative strategy to reduce the plasma density of solids is to utilize materials that are not homogeneous on a micrometer to nanometer scale but feature an average density close to n_c. Low-density carbon foams [106, 145, 146] or carbon nanotube films [102, 103] are two examples for such materials. Foam targets can be manufactured with various densities and thicknesses offering a near-critical density target with sharp gradients that can be utilized to characterize the propagation of high-intensity laser pulses through n_c plasmas [95, 147]. As pointed out in the previous section, an improved laser absorption in comparison to a bare foil is expected when the foam is combined with a solid density foil to a double layer configuration. As a result, an enhancement in proton beam performance can be demonstrated in various experiments (e.g. [106, 103]). However, foam targets have the disadvantage that effects of the n_c plasma cannot be isolated because inherently effects from the nanoscopic structure are always included. This structure can cause, for example, increased laser absorption similar to surface modifications on the front side of the target [148, 149, 150]. A recent numerical study by Fedeli et al. [99] demonstrated that a nanostructure in a near-critical foam target shows a significantly increased absorption compared to a homogeneous one.
Cluster gas jets are another non-homogeneous approach to explore the regime of near-critical density. The target consists of a cloud of solid-density sub-micrometer-sized clusters embedded in a background gas. Fukuda et al. [46] reported that the cluster evaporates under the action of a laser pre-pulse forming an underdense plasma with $n_e \sim 0.02 n_c$. Ions with energies of 10-20 MeV per nucleon were detected in the laser propagation direction and, based on numerical simulations, explained by the formation of strong dipole vortex structures. Contrary, the Coulomb explosion mechanism explains the ion acceleration from other cluster target experiments [78, 80, 151].

The hydrogen jet target system, which will be introduced in the next chapter, can be transformed into a near-critical density plasma. This follows the approach of an exploding target, but with an important variation. The target material is solid hydrogen with a density equal to 30 $n_{c,800\text{nm}}$ which is about one order of magnitude less dense than a typical solid foil made from metal or plastic. As such the hydrogen material is only slightly too dense to become relativistically transparent for petawatt-class laser pulses in an experiment [*]. Thus, to access the near-critical density regime, only a small expansion is required, which facilitates conserving sharp density gradients at the interfaces. In combination with optical probing methods, this simplifies a density scan ranging from underdense to opaque plasma, as it will be carried out in chapter 4, and thus enables the exploration of the various laser-plasma processes and acceleration regimes mentioned in this chapter.

---

[*] As described in section 2.1.2, plasmas up to a density of 30 $n_{c,800\text{nm}}$ can theoretically be penetrated at a laser amplitude of $a_0 = 42$.

In summary, the introduction of the different target concepts and the variety of effects that occur during irradiation of near-critical density plasmas provide the background for the experimental studies in the following chapters. Based on recent publications, it can be suspected that the major benefit of near-critical plasmas for laser-ion acceleration is given by hybrid scenarios, as shown by Higginson et al. [25], or as an additional layer in front of a solid foil [103]. Whereby, especially the possibilities of proton acceleration in transparent plasma seem to be insufficiently explored experimentally. However, the processes leading to the improvement of the maximum energy of the proton beams could often only be derived from corresponding numerical simulations, since experimental diagnostics usually only records time-integrated signals and thus cannot resolve the ultra-fast dynamics. Furthermore, the contribution of near-critical plasmas is often difficult to derive experimentally. As such, in particular near-critical targets, that allow for optical probing methods, can be utilized to spatially and temporally resolve plasma and field characteristics in isolated scenarios and thus provide insight into the ultra-fast dynamics which might be useful as an input for numerical studies that ultimately could lead to an optimization of the different acceleration schemes.

3 Development of cryogenic jets as high repetition rate targets for laser-driven ion accelerators

Cryogenic liquids are a key technology for cooling systems in medical and scientific applications such as superconductor infrastructure, rocket fuel injectors, fusion energy and energy storage. In recent years, cryogenic liquids have attracted growing attention as targets in relativistic laser-plasma experiments [55, 57, 58, 152, 153, 154, 155]. They provide the unique capability to generate ultra-pure solid density materials using chemical elements that under ambient conditions exist in the gas phase. Thus, a large variety of different types of cryogenic targets such as jets/filaments [156, 157, 158], ribbons [159], free-standing foil-like targets [160] or clusters [80, 46] were already applied.

Jets in particular are boundary-free, renewable and debris-free micrometer-sized targets of single species content or well-defined mixtures. These properties are beneficial for the following aspects in a laser-plasma experiment. First, the renewable and self-aligning property enables the availability of a large number of targets without any further preparation that is in particular interesting when higher repetition rate applications are considered [54]. Current fabrication approaches and operation procedures of commonly used target concepts (e.g. foils, micro-structured targets) could likely become a limiting factor [54] at repetition rates of 1-10 Hz since 3600-36,000 targets would be required per hour and a new target needs to be inserted and aligned with micrometer precision for every shot as the high-intensity laser irradiation usually destroys the material. Second, the usage of jets mitigates the production of debris because the cryogenic content is gaseous at ambient temperatures and therefore removed by the vacuum system. In the case of metal and plastic targets, debris is permanently deposited on the surfaces of large (and expensive) optics, degrading their optical properties. Third, the small lateral size of cryogenic jets and the free-standing arrangement facilitates pump-probe configurations, as no support structure of the target is needed in the vicinity of the interaction region. This simplifies precise alignment and characterization of the filament and allows to determine the evolution of the irradiated target using optical probing methods (e.g. [55] or chapter 4). Lastly, the controllable target content of single-species or well-defined mixtures enables a variety of different experiments concerning the generation of pure proton beams or the investigation of different ion species interacting during the expansion of non-uniformly composed target systems (multi-species effects [161]).

In an early stage of this thesis, the cryogenic jet technology was implemented and used in a series of laser-proton acceleration experiments at the 150 TW DRACO laser facility. The generation of pure multi-MeV proton beams at 1 Hz repetition rate [56] was demonstrated with cylindrical jets of 2 to 10 micrometers in diameter and the angular proton beam emission distribution was investigated for cylindrical and planar jet geometries [57]. As expected, the curved jet surface of a cylindrical jet emits protons isotropically in the plane perpendicular to the jet axis while the proton angular emission distribution is significantly narrowed for the planar shaped jets resulting in a three to four times higher particle flux along the target normal direction. Based on these findings, two key aspects for improving the jet target concept were derived that need to be addressed in order to apply the jet in an experiment with increased peak intensities (e.g. DRACO petawatt). First, the exact shape of planar jets, in particular the sheet thickness, was not completely clear which complicated the correct modeling of the target. Moreover, width and thickness of the jet could not be controlled which prevented further optimization of the accelerator performance. The second aspect concerns the spatial overlap between jet and laser focus defining the stability of the proton beam performance. Larger jet cross sections would of course compensate for laser and target jitter but are limited by the pumping speed of the vacuum system. The only practical solution is to shoot the laser very close to the target system where the fluctuation of the jet position is reduced. However, shifting the high-intensity laser interaction too close to the cryogenic source may damage the fragile aperture. This yields distortions of the laminar flow that will degrade the jet stability or, in the worst case, lead to the complete failure of the target system.

The studies presented in this chapter address these two aspects by investigating the formation of planar jets and by performing technological improvements of the target system. The first part introduces the working principle of the cryogenic jet generation (section 3.1) and presents the technical realization of the cryostat system in section 3.2. Afterwards, an optical probing setup for detailed characterization of the jet shape and dimensions is presented which is based on imaging shadowgraphy and interferometry and which uses stroboscopic back-illumination with short laser pulses (section 3.3). The morphology and fluid dynamics of cylindrical and, in particular, sheet-like targets are discussed in section 3.4 and section 3.5, respectively. Detailed experimental characterizations of planar jets, which were generated with slit apertures, provide novel insights into the formation of such targets. These results are essential to better control the generated shape and to optimize the target for the application in the experiment by e.g. tuning the sheet thickness. Section 3.6 focuses on the aspects of target implementation into the harsh laser-plasma environment. Constraints regarding the vacuum conditions were identified and addressed by a differential pumping approach. The characterization of the spatial stability for different jets is discussed with respect to the impact on the laser-proton acceleration. Two methods for increasing the target stability by (optical or mechanical) shielding the cryogenic target system were developed. These mitigate potential damage to the aperture and thus enable systematic studies with the DRACO petawatt laser. Based on the obtained knowledge of jet stability and fluid dynamics, the final part of this chapter summarizes the results by discussing the optimal aperture shape for applications at high-intensity laser systems.

3.1 Generation of micrometer-sized cryogenic jets

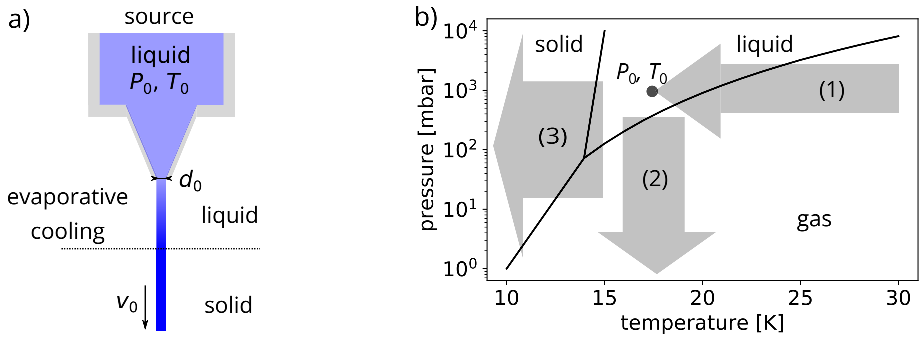

Figure 3.1: a): Schematic of the generation of cryogenic jets in a vacuum. P_0 and T_0 describe temperature and pressure of the liquid inside the source. d_0 denotes the size of the aperture and v_0 the flow velocity. b): Simplified phase diagram of hydrogen [162]. Arrows indicate the relevant processes for solid jet generation: (1) Cooling down and liquefaction inside the source, (2) evaporation of surface molecules during extrusion into the vacuum, (3) bulk solidification due to evaporative cooling.

The basic principle of generating a cryogenic jet is illustrated in figure 3.1a. A liquid is continuously pressed through a nozzle with an aperture of size d_0 (e.g. $d_0 = 5\,\mu\text{m}$ in diameter) and forms a filament at appropriate conditions of inlet backing pressure P_0 and source temperature T_0 that have to be within the liquid phase of the applied substance. For hydrogen, as an example, typical source operation conditions of 18 K and 4 bar can be acquired from the simplified phase diagram in figure 3.1b. Due to the constant backing pressure, a stream of liquid travels with a flow velocity v_0 that is described by the Bernoulli principle (assuming an incompressible fluid)

$$\frac{v_0^2}{2} = gz + \frac{P_0}{\rho} \tag{3.1}$$

where $g = 9.81\,\text{m}/s^2$ describes the acceleration due to gravity and z denotes the vertical elevation above a reference point. The density ρ can be found in table 3.1 besides other properties of para-hydrogen*. For typical source arrangements z is a few centimeters and thus the influence of gravity can be neglected: $gz \approx 0.1\,\text{m}^2/\text{s}^2 \ll P_0/\rho \approx 5500\,\text{m}^2/\text{s}^2$ for $z = 1$ cm. During the extrusion process, the static backing pressure P_0 therefore results in

---

*Hydrogen consists of the two spin isomeric forms: para-hydrogen (antiparallel nuclear spins) and ortho-hydrogen (parallel spins). Due to the lower energetic state, para-hydrogen is the dominant fraction in the liquid phase e.g. at 20 K accounting for a ratio of about 99.8%.

property	value	reference
saturated liquid		
triple point	13.95 K, 72 mbar	Henning et al. [163]
density	ρ = 0.073 g/cm^3	Stewart et al. [164]
surface tension	γ = 2.5e-3 N/m	Grigorev et al. [165], Blagoi et al. [166]
viscosity	$\eta = 1.59 \cdot 10^{-5} Pa \cdot s$	Keesom et al. [167]
solid phase		
density	ρ = 0.086 g/cm^3	Stewart et al. [164]
refractive index	1.135 (for 800 nm)	Perera et al. [168]

Table 3.1: Key properties of saturated liquid para-hydrogen at a temperature of 18 K, if not stated otherwise, and solid hydrogen at 6 K. A collection of additional properties of liquid and solid hydrogen can be found in [169].

a flow velocity v_0 described by

$$v_0 = C_D \cdot \sqrt{\frac{2 \cdot P_0}{\rho}} \tag{3.2}$$

with the additional experimentally determined discharge coefficient [170] C_D that accounts for natural losses due to friction in the nozzle ($C_D < 1$). As an example, Kim et al. [171] compared calculations based on the Bernoulli principle with flow velocity measurements by double-pulse illumination in Methane/Argon jets and found about 10% lower speeds than from equation 3.2, which is equal to $C_D \approx 0.9$. Since there is no further friction after exiting the source assembly, the hydrogen jet travels with a constant flow velocity that is typically in the order of 100 m/s in the applied backing pressure range of a few bars.

Once the liquid jet enters the vacuum chamber, the surrounding pressure decreases rapidly, as indicated by the arrow (2) in figure 3.1b. This results in an endpoint within the gas phase region. At the vacuum interface, energetic hydrogen molecules evaporate and escape from the jet lowering the temperature of the remaining liquid (arrow (3) in figure 3.1b). Once T drops below the sublimation curve, solidification sets in and thus the jet target freezes into a solid filament with a fixed shape. The combination of solidification and deformation by surface tension plays an important role in the shape formation of cylindrical (section 3.4) and planar jets (section 3.5). In liquid hydrogen, the typical timescale for this crystallization process is on the order of microseconds [172]. Within this period, the jet moves less than one millimeter ($v_0 \sim 100$ m/s) which is much smaller than the distances used in typical source arrangements. In a laser-plasma experiment, the jet target is thus already frozen and accordingly consists of solid hydrogen.

3.2 Technical realization of the jet delivery system

Within this thesis, a cryogenic delivery system was realized that is capable of generating a jet as a target for laser-proton acceleration. The system is similar to that described by Kim et al. [156] which was derived from a design used for laser heating experiments at FLASH [173]. The assembly consists of four main components: 1) gas delivery system, 2)

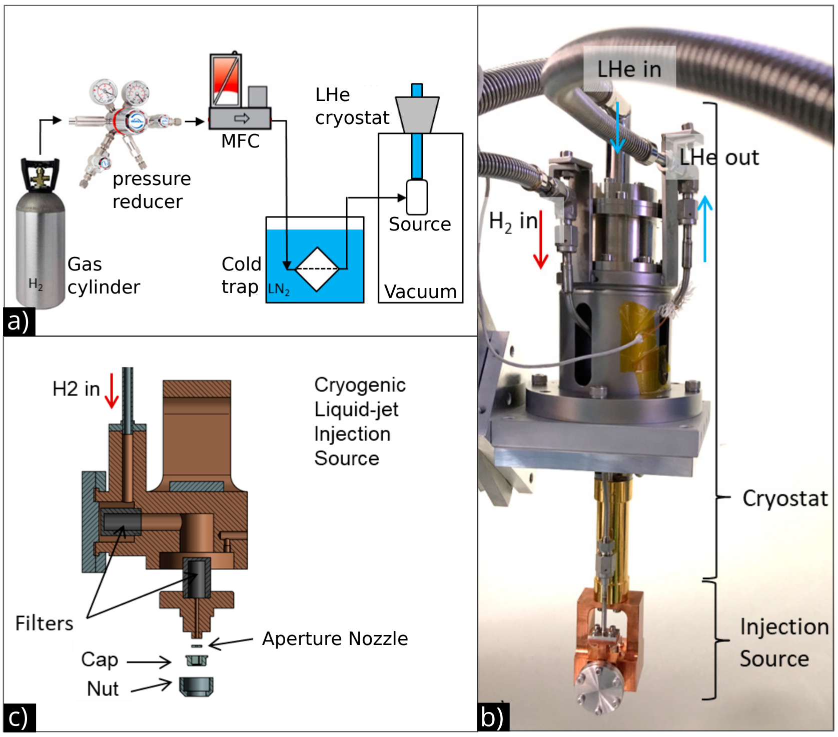

Figure 3.2: Components of the cryogenic target system. a) A gas delivery system including backing pressure and mass flow controllers (MFC) as well as the liquid nitrogen cryo-purification stage. b) Picture of the in-vacuum cryostat with flexible supply lines for the liquid helium input (LHe in), the consumed helium gas output (LHe out) and the hydrogen process gas (H_2 in). The injection source assembly is mounted to the cold tip while the cryostat is temperature stabilized at e.g. $T = 18$ K with millikelvin precision. c) Cross section of the source assembly and exploded view of the nozzle-spout.

in-vacuum cryostat, 3) source module and 4) aperture nozzle, each described briefly in the following. For further technical documentation and a step-by-step operation guide of such a system, refer to [174].

1) The process gas supply system delivers the content of the target and has to fulfill high-purity standards to obtain nucleation free liquids, which would otherwise cause clogging of the micrometer-sized nozzle. A schematic of the full gas supply system is presented in figure 3.2a. Hydrogen from a gas cylinder, specified with $\geq 99.9999\%$ H_2, is further purified using a liquid nitrogen cold trap in which remaining impurities, e.g. water, carbon dioxide and hydrocarbons, are captured on the inside of the cold tube. The gas backing pressure is regulated via a two-stage membrane pressure reducer in a range of 0-15 bar and with a precision in the order of 0.1 bar. The gas throughput can be controlled with a mass flow controller mounted in line (Bronkhorst EL-FLOW Select F-201CV). In this setup, adjustable gas flow precision is typically in the order of one percent of the full range, e.g. about 3 sccm (standard cubic centimeters per minute). During operation, the controller is usually in a monitoring state while the flow is determined by the aperture cross section and the applied backing pressure. For comparison, typical flow rates during extrusion of a cryogenic jet are 100-400 sccm.

2) Cooling to cryogenic temperatures is achieved with a gas flow type cryostat (pictured in figure 3.2b) supplied with liquid Helium (LHe) from an external tank. The system was customized development by *CryoVac*[*] and features unique flexible supply lines for the liquid helium cooling circuit and the gas supply. The construction mechanically decouples the cryostat module from the vacuum chamber walls and hence minimizes potential vibrations originating in particular from the turbomolecular pumps. Target positioning on a micrometer scale is achieved with three motorized linear translation stages in an XYZ-configuration. More than 4 W cooling power is specified at a temperature of 4.2 K that is sufficient for the liquefaction of all relevant gases including helium. A specific heat exchanger in the LHe return line of the cryostat allows pre-cooling of process gases to temperatures of about 30 K. The temperature of the cold tip, whereto the source is mounted, is measured with a calibrated silicon diode (Lake Shore DT-670) and adjusted to the set temperature with a precision of 1 mK by controlling the output of an integrated heater element using a PID (proportional-integral-derivative) loop.

3) Cooling and liquefaction of the process gas occur inside the source that is mounted to the cold tip of the cryostat and that is built from oxygen-free copper for high thermal conductivity. All interfaces are sealed with indium to ensure proper thermal contact and tightness at cryogenic temperatures. The purified gas from the delivery system enters pre-cooled and passes a sintered steel filter with a nominal pore size of 0.5 µm before it accumulates inside the source, as it is shown in the cross section of the module in figure 3.2c. Remaining impurities (e.g. nitrogen) freeze inside the filter, which prevents clogging at the aperture. The adjusted temperature of the source assembly causes the gas to liquefy before it exits through the last filter element and the aperture into the vacuum chamber of the experiment. With this source, typical operation conditions for hydrogen are temperatures in the range of 15-22 K and backing pressures of 1 – 6 bar. The interchangeable nozzle-spout allows for fast replacements of apertures in case of clogging, laser damage or when using a different target geometry.

4) The shape of the extruded jet is mainly determined by the form and dimensions of the aperture. Robust circular aperture nozzles manufactured from a platin/iridium compound (figure 3.3a) are available with diameters larger than two micrometers. Depending on the initial source conditions, either a solid cylindrical jet or a chain of equidistantly spaced droplets can be formed ([175, 156] or section 3.4). Rectangular shaped slit aperture nozzles, which are used to generate sheet-like jets, are fabricated in a customized process developed at the IPHT Jena[†]. Electron beam lithography and dry etching techniques are applied to 1 mm thick silicon wafers. One wafer layout contains up to 150 small 3x3 mm^2 nozzle plates of different nominal aperture sizes, e.g. $W = 0.5, 1, 2, 4$ and 8 µm in width and $L = 20$ µm in length. Two different aperture types, shown in figure 3.3b and c, have been produced and tested. The 'straight slit nozzle' is rectangular shaped with rounded corners and about parallel aperture walls in the final 2 µm thick slit layer (as illustrated in

---

[*] CryoVac GmbH & Co. KG, Troisdorf, Germany

[†] Leibnitz institute of photonic technology

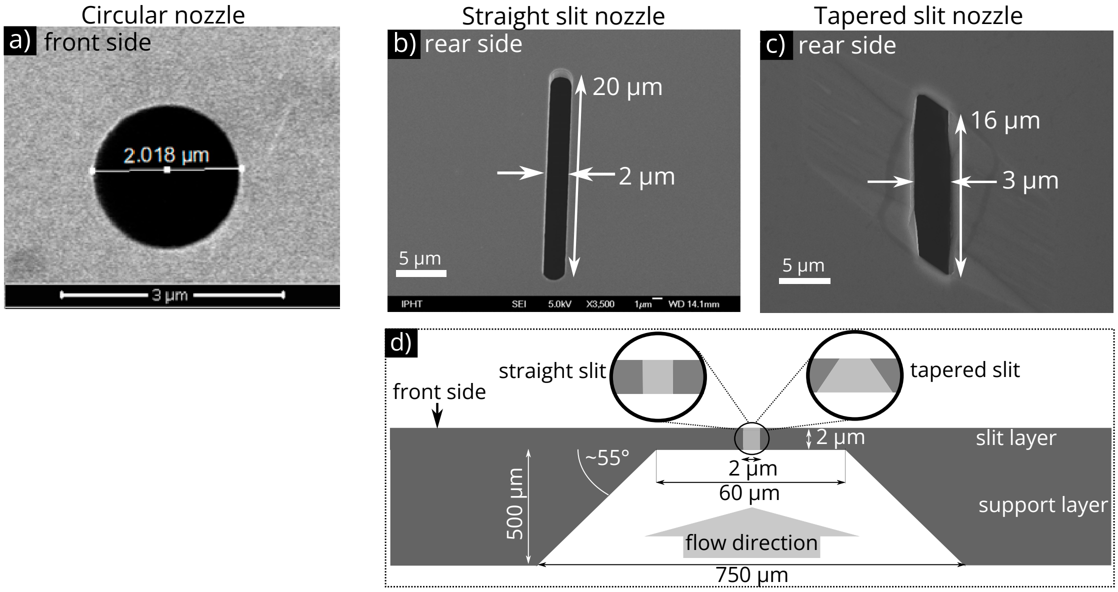
Circular nozzle
a) front side
2.018 µm
3 µm
Straight slit nozzle
b) rear side
20 µm
2 µm
5 µm
IPHT SEI 5.0kV X3,500 1µm WD 14.1mm
Tapered slit nozzle
c) rear side
16 µm
3 µm
5 µm
d)
straight slit
tapered slit
front side
2 µm
slit layer
~55°
2 µm
60 µm
500 µm
support layer
flow direction
750 µm

Figure 3.3: SEM (scanning electron microscope) images of a circular nozzle with a 2 µm diameter aperture (a), a 'straight slit nozzle' with a nominal 2x20 µm^2 aperture (b) and a 'tapered slit nozzle' featuring a non-symmetric aperture footprint and the tapered sidewalls (c). d) Sketch of the slit aperture cross section (not to scale). The micrometer thick slit layer contains either a straight or tapered slit aperture.

figure 3.3d. This aperture provides a uniform flow distribution. A second aperture type, referred to as 'tapered slit nozzle', features beveled walls in the slit layer that originate from the applied etching process and was utilized to investigate the influence of non-uniform flow distributions introduced by the slit shape onto the jet generation. Most prominent in the scanning electron microscope images of figure 3.3c is the rhomboidal cross section with angled facets on the major and minor slit axis (as schematically illustrated for e.g. the major axis in figure 3.3d). Note that the cross section of the tapered nozzle in figure 3.3c differs slightly from the design value of 2x20 µm^2.

The dimensions of selected jets generated by different circular and slit apertures, which

aperture	jet dimensions		H_2 gas flow [sccm]
cylindrical aperture	jet diameter		
5 µm @ 16-20K, 1-4bar	$\sim$ 5 µm		80-120
10 µm @ 16-20K, 1-4bar	$\sim$ 10 µm		320-480
straight slit aperture	sheet thickness	sheet width	
1x20 µm^2 @ 16-19K, 1-3bar	0.6 µm	10-15 µm	70-120
2x20 µm^2 @ 16-18K 1.3-4bar	1.2 µm	15-20 µm	140-250
2x20 µm^2 @ 16.8K, 7bar		50 µm	
4x20 µm^2 @ 18K, 4bar		17 µm	320-430
4x20 µm^2 @ 18K, 8bar	0.4 µm	40 µm	
tapered slit aperture	sheet thickness	sheet width	
1x20 µm^2 @ 22.5K, 5.5 bar	0.23 µm	50 µm	70-140
2x20 µm^2 @ 17K, 5 bar	0.35-0.45 µm	42-60 µm	150-230

Table 3.2: Overview of jet dimensions and hydrogen flow conditions for various nozzle types (slit and cylindrical) at different source temperature and backing pressure conditions that were tested in the context of this work.

were investigated in the context of this work, are summarized in table 3.2. Cylindrical jets typically have the same size as the circular aperture while slit nozzles generate sheet-like jets of various dimensions that partially differ substantially from the slit cross section. The underlying fluid dynamics is in detail investigated and discussed in section 3.5 for two 2x20 μm^2 nozzles, one with a straight slit and one with a tapered aperture, while qualitatively comparable characteristics were found for the other tested apertures as well.

3.3 Imaging setup for jet characterization

The characterization and optimization of cylindrical and planar jets as a function of the operation parameters as well as on-shot measurements during a high-intensity laser-plasma interaction (in chapter 4 and 5) represent a significant part of this work. For that, an imaging setup to characterize the target with sufficient temporal and spatial resolution was developed and applied in various configurations. The general arrangement is shown in figure 3.4a, it consists of two high resolution imaging systems for simultaneous observation of the xz and yz target plane (z is the extrusion direction of the jet). For the studies reported in this chapter, an imaging system with a spatial resolution better than 2 micrometers was used. Due to the jet flow velocity of about 100 m/s, a stroboscopic back illumination with a pulse duration shorter than 10 ns corresponding to a jet movement less than 1 micrometer is required to preserve the image quality. A short pulse laser system (e.g. Titanium:Sapphire-based with 800 nm wavelength) was used for back-illumination of the filament to satisfy the temporal requirements.

An interferometric method was employed in one of the imaging arms that allowed jet thickness measurements for the first time. Due to its simple alignment, the small number of required components and intrinsic temporal synchronization of the two replicas, a Nomarski interferometry setup [176] was chosen. In the most basic configuration, it consists of a Wollaston prism placed in between the imaging objective and the camera and a polarizer in front of the CCD (see figure 3.4b). The Wollaston prism made from quartz splits the laser pulse into two beams of the same intensity and orthogonal polarization and separates them with a divergence angle of one degree. The polarizer is oriented such that two beams of equal polarization and intensity (therefore two images of the same object) interfere in the image plane. Due to the spatial separation, the image of the phase object from one beam overlaps on the CCD with an undisturbed region of the other beam and vice versa (figure 3.4b). An additional polarizer or waveplate in front of the object allows manipulating the polarization of the illumination. Using these components, the aim of the alignment is to achieve maximum separation of the objects in real space and at the same time to optimize the distribution of DC an AC components in the Fourier space with the appropriate orientation of the interference fringes with respect to the object as well as the fringe contrast.

The deformation of the interference fringes by the object corresponds to a phase shift $\Delta\varphi$ equivalent to an optical path difference $\Delta L = \Delta\varphi/(2\pi) \cdot \lambda$ for the illumination wavelength λ.

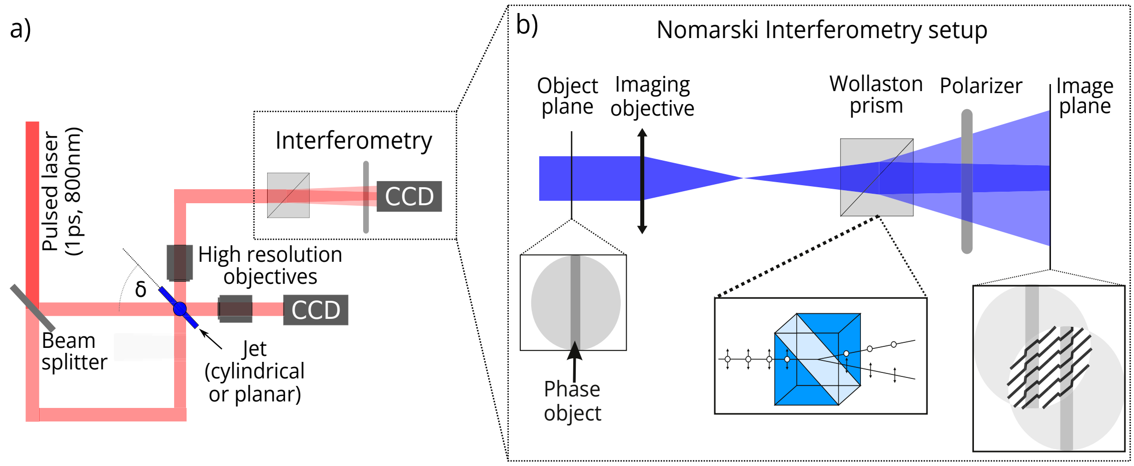

Figure 3.4: a) Experimental imaging setup for target characterization. The hydrogen jet is illuminated by a short pulse laser and imaged from two different angles with high resolution. δ describes the orientation angle in the case of a planar jet. One imaging axis is equipped with a Nomarski interferometer, which is schematically illustrated in b).

ΔL is caused by the slower speed of light in the material in comparison to that in the surrounding vacuum and is described by the refractive index n and the thickness of the object d. This allows calculating the thickness d based on the phase shift by

$$d = \frac{\Delta\varphi}{2\pi} \cdot \frac{\lambda}{n-1} \quad . \tag{3.3}$$

Before applying this setup for thickness measurements of solid hydrogen jets, the method was verified with a micro-strip of known geometry (few micrometers wide and about 1 μm thick) made from a transparent material.
The general concept of the setup described here, using two beams to probe the jet from different perspectives (one equipped with an interferometer if necessary), was implemented and adapted during the laser-plasma experiments presented throughout this thesis. In the following, the dynamics of cylindrical and planar hydrogen jets, that were characterized using this setup, are discussed.

3.4 Cylindrical jets

The fluid dynamics of cryogenic hydrogen jets ejected from circular nozzles was investigated in various works [177, 175, 172, 156]. In general, under laminar flow conditions, a cylindrical column of solid density establishes due to evaporative cooling before the surface tension reshapes the jet into a chain of well-separated droplets. Exemplary microscopic images of extruded jets from circular apertures of 2 μm, 5 μm and 10 μm in diameter, shown in figure 3.5a-c, allow studying the shape and morphology of the hydrogen filament. Since the jet is basically a transparent column, transmitted light from the back-illumination is focused similarly to a tiny cylindrical lens in a distance that is within the depth of field of the objective leading to a brighter region in the center while the target-vacuum interface appears darker [178]. This effect is most prominent for the ø 5 μm jet in figure 3.5b.

Deviations from the cylindrical form are often caused by local turbulences due to nanoscopic dents or spikes imprinted in the aperture or generated by frozen contamination pieces. A criterion for laminar flow conditions during the extrusion process is a Reynolds number Re below $Re_{crit} \approx 2000$. The Reynolds number depends on the density, flow velocity and viscosity η of the fluid as well as the nozzle diameter

$$Re = \frac{\rho \cdot v \cdot d_0}{\eta} \quad . \tag{3.4}$$

With the properties of liquid hydrogen in table 3.1, $v_0 = 100$ m/s and $d_0 = 5$ µm the Reynolds number is equal to about 2300 and therefore above the critical value of Re_{crit} at which turbulences start to occur. Since Re_{crit} is an approximation, laminar flow might be maintained at even higher Reynolds numbers. Experimental investigations, for example by Kim et al. [156], demonstrate laminar flow conditions for typical operation parameters of source temperatures between 16-20 K and backing pressures of 2-5 bar without determining a strong impact on the jet shape and stability. However, under such source conditions, it is expected that the roughness of the nozzle plays an important role in the onset of turbulences and the goal is to reduce features that disturb the laminar flow in order to maintain a stable jet. As such, the manufacturing process should prevent small dents or imperfections of the aperture and dust particles or frozen gas impurities need to be avoided as well. Proper chemical cleaning of the nozzle-spout in combination with a rigorous inspection of the aperture can further mitigate disturbances in the liquid flow and prevent derivations from the ideal cylindrical jet form.

The most obvious inhomogeneity is a droplet-like structure that appears along the axis and originates from the Plateau-Rayleigh instability. This is best visible in figure 3.5c. Although the instability grows sufficiently fast to have an impact on the jet shape, the hydrogen jet freezes before it is disrupted [156]. The estimated magnitude for the time scale on which

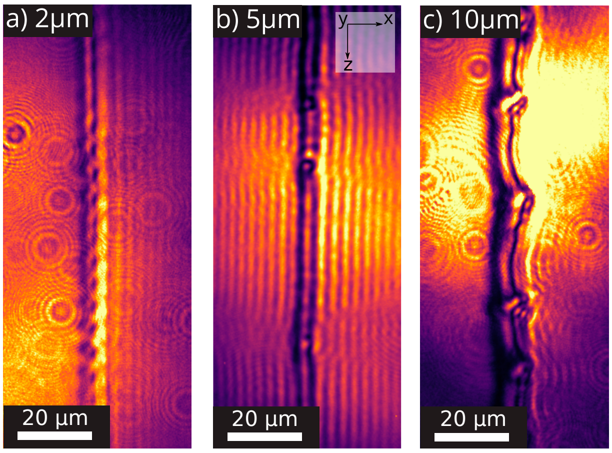

Figure 3.5: Microscopic shadowgraphy images of cylindrical hydrogen jets extruded from ø 2 µm (a), ø 5 µm (b) and ø 10 µm (c) circular apertures. Due to the resolution limit of the imaging system, the ø 2 µm jet cannot be resolved well.

a liquid stream breaks up into droplets is given by [179]

$$t_0 \sim \sqrt{\frac{d^3 \cdot \rho}{\gamma}} \quad . \tag{3.5}$$

Assuming a density of $\rho_{H2} = 0.073\,\text{g/cm}^3$, a surface tension of $\gamma_{H2} = 2.5\text{e-}3\,\text{N/m}$ (from table 3.1) and a jet diameter of 5 µm results in a time scale in the microsecond range and is therefore comparable to estimates for the solidification time from [172]. As a result, operation at lower source temperatures reduces the solidification time and can improve the uniformity of the cryogenic jet. For higher initial temperature, evaporative cooling takes longer and the jet begins to break into a stream of droplets.

Test of droplet chains and hydrogen-deuterium mixture-jets

By stimulating the Plateau-Rayleigh-Instability, the solidification process can be used to produce spatially synchronized mass limited targets that are interesting for laser-proton acceleration in the TNSA regime. Single microdroplets can reduce the electron spread due to the restricted volume and thus provide higher accelerating fields for the protons. This concept was investigated in a number of experiments with either liquid droplets [180, 181, 182, 183, 184, 185] or levitating spheres [186, 187].

In order to generate cryogenic droplets, the extruded jet is perturbed at a frequency close to the instability frequency. The wavelength λ_R at which the perturbation grows most rapidly depends linearly on the cylinder radius r_0 with $\lambda_R \approx 9r_0$ [179]. With the flow velocity of the jet v_0, one can calculate the perturbation frequency by $\nu_R \approx \frac{v_0}{9 \cdot r_0}$. Under typical operation conditions (r_0 = 2.5 µm, v_0 = 100 m/s), ν_R of about 4 MHz is required for triggering the Plateau-Rayleigh-Instability. This principle was experimentally demonstrated by [188] for liquid and by [157] for cryogenic jets. Technically, the perturbation can be achieved by adding a piezo actuator to the nozzle-spout as it is described by Kim et al. [171].

Figure 3.6 shows an example for cryogenic hydrogen droplets with a diameter of approximately 10 µm and a separation between two spheres of about 22 µm. This is consistent with the optimal perturbation wavelength $\lambda_R \approx 22$ µm of the Plateau-Rayleigh-Instability from a circular aperture with a radius of 2.5 µm. The diameter of the droplets is furthermore comparable to the size expected from mass conservation when transforming a 22 µm long piece of a 5 µm jet into a sphere of 9.5 µm in diameter.

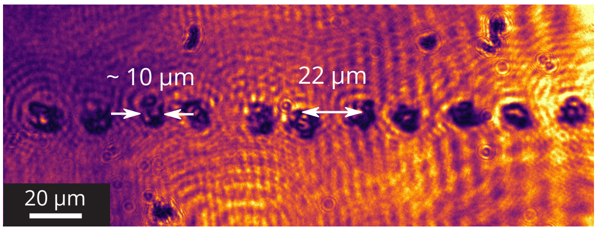

Figure 3.6: Microscopic shadowgraphy images of a chain of droplets generated from a 5 µm circular nozzle by stimulating the Plateau-Rayleigh-instability.

Another aspect of the TNSA acceleration mechanism namely the interaction of different target ion species within the sheath field distribution can be investigated with cryogenic jets. Besides hydrogen, which was primarily used throughout this thesis, mixtures of hydrogen and deuterium can be applied to study these so-called multi-species effects in a controlled environment, as proposed by Huebl et al. [161]. The morphology and the shape of these mixture-jets does not differ from those of pure hydrogen jets. In a first proof of concept experiment, mixture-jets were used in a laser-plasma experiment at the petawatt arm of the DRACO system (refer to chapter 4). Although accelerated deuterium ions were observed, the complete control over the gas mixture ratio and the stability of the jet was not yet sufficient to perform a detailed study.

In general, jet targets can be produced from various gases and mixtures. However, the morphology and characteristics of those targets might differ from the hydrogen case. For example, Kim et al. [171] investigated argon and methane jets. In the case of argon, solidification due to evaporative cooling results in a cylindrical target geometry, while methane jets remain liquid and breaks up into a stream of droplets.

3.5 Hydrogen sheet jets

Thin cryogenic sheet jets are novel targets with a planar geometry that were systematically characterized for the first time. The main goal was to understand the underlying fluid dynamics for optimizing the jet dimensions with regard to the application in a laser-plasma experiment. During this thesis, several different shapes of apertures were tested (table 3.2) and used in the different experimental campaigns (e.g. [57] and chapter 4). As mentioned in section 3.2, the most striking observation was that nominally identical slit cross sections resulted in substantially different jet geometries. Obviously, the microscopic shape of the aperture dominates the fluid dynamics (compare straight slit and tapered apertures), which will be discussed in this section. For this, a series of jet characterization experiments were conducted in a collaborative effort with the High Energy Density Science group of SLAC National Accelerator Laboratory to investigate the two different types of slit apertures (nominal size of 2x20 μm^2) with the optical probing setup introduced in section 3.3. This section first summarizes the experimental results before the involved fluid dynamics are discussed.

Microscopic example images of jets produced from straight and tapered slit nozzles are shown in figure 3.7a and b. Although the size of the jets differs considerably, the overall shape and morphology are similar. The cross-section is characterized by a thin flat part in the center and a cylindrically formed edge (rim) on each side. This results in a dumbbell-like shape with a sheet width w and a sheet thickness h, as illustrated in figure 3.7c. Jets generated by the straight slit aperture are about 15 µm wide while the tapered nozzle can generate sheets of more than 40 µm in width, which is much larger than the original slit length (20 µm) of the aperture.

The thickness of the sheet was calculated based on the interferogram in figure 3.7d using

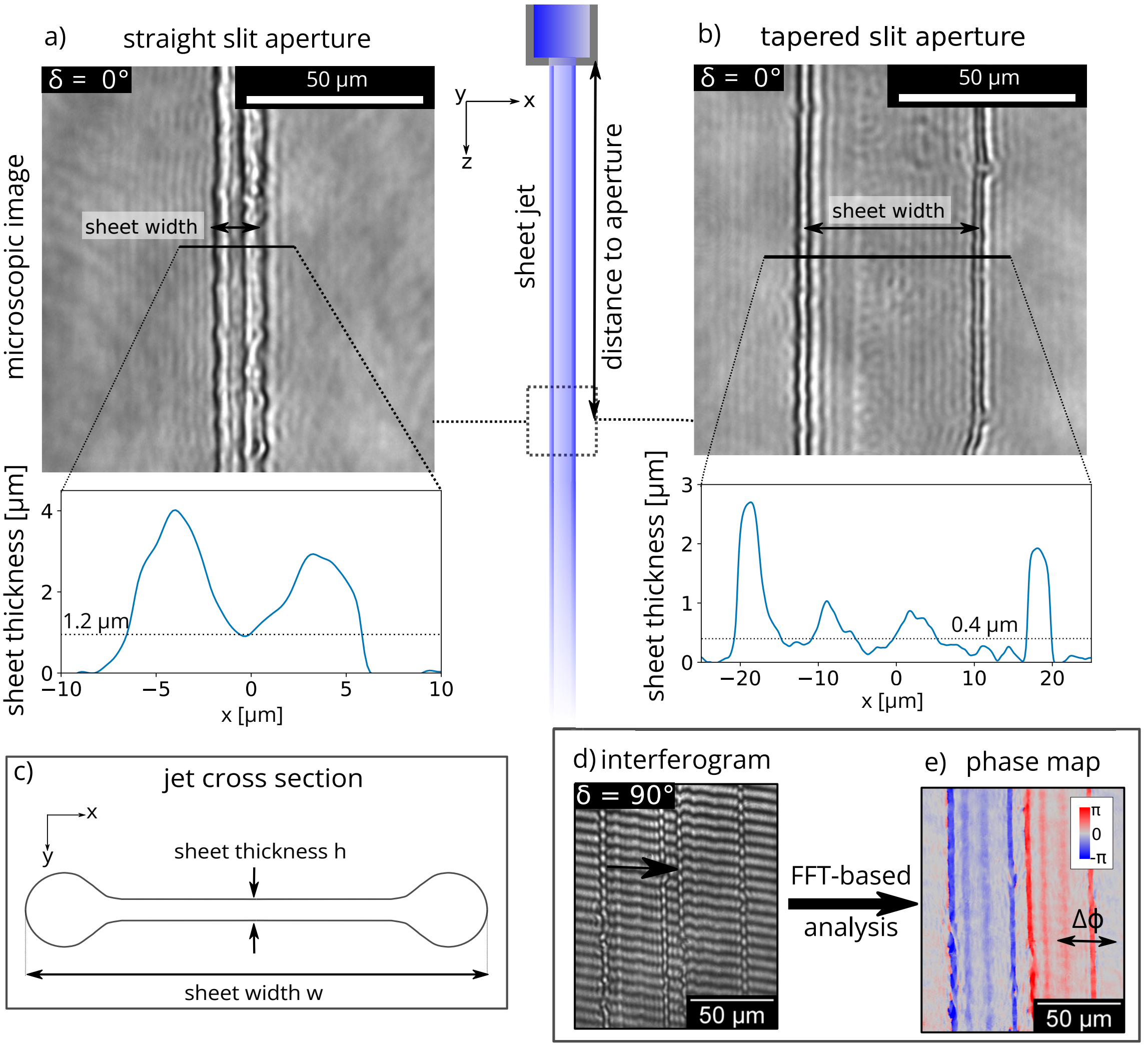

Figure 3.7: Shape and cross section of the sheet jet produced by a straight (left row) and tapered (right row) 2x20 µm^2 slit apertures. Microscopic images and the calculated cross sections from interferometry are displayed in a) and b). c) Schematic of the jet cross section consisting of an inner planar part and two cylindrical rims on the edges. d) and e): Example interferogram and the calculated phase map for a jet from the tapered slit aperture.

the phase shift difference between the inner part of the jet and the outer (undisturbed) vacuum region, as illustrated by $\Delta\varphi$ in figure 3.7e. Recorded interferograms contain two copies of the sheet since the Wollaston prism in the interferometry setup splits the laser pulse into two replicas. At the vacuum-jet interface, the interference fringes are not continuous due to the refraction occurring in the cylindrical rims. As a consequence, the number of 2π phase shifts cannot be inferred. From mass conservation considerations, however, an upper limit for the sheet thickness can be determined. A 40 µm wide sheet originating from an aperture cross section of 2x20 µm^2 results in an average thickness of 1 µm that is well below 5.7 µm which would be required for a 2π phase shift (c.f. equation 3.3 for λ =800 nm and $n_{H2} = 1.14$). As a result, additional phase jumps can be excluded and the measured phase shift in the center of the jet corresponds to the thickness given by equation 3.3. The accuracy of the phase shift measurement is limited by the contrast of the interference fringes and amounts to a value of 0.135 (in units of π). For solid hydrogen, this corresponds to an

accuracy of the thickness measurement of 150 nm. The spatial resolution of the evaluated thickness distribution is limited to about 5 µm due to the applied frequency filtering in the Fourier space as part of the analysis method for the interferograms. This complicates the measurements around the edges of the jet and small structures at the center might not be resolvable.
Exemplary lineouts of the determined sheet thickness are shown for both nozzle types below figure 3.7a and b. The jet from the tapered aperture features an average thickness of 400 nm in a wide planar part. Variations stem either from capillary waves [189] or from nanoscopic spikes and dents imprinted in the aperture slopes. In contrast to this, the sheet originating from the straight nozzle is characterized by a minimum thickness value of about 1.2 µm in the center and an increasing thickness towards the edges.

3.5.1 Characterization of sheet jets under different operation conditions

The images and results in figure 3.7 are representative for standard source operation conditions, e.g. $T_0 = 18$ K and $P_0 = 4$ bar. Depending on the nozzle type, it was found that the jet shape and dimensions show significant variations with the backing pressure.

Straight slit aperture

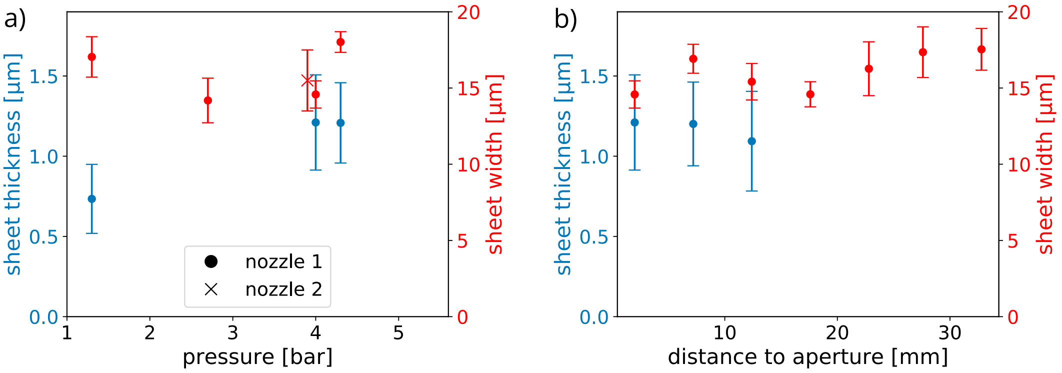

Figure 3.8: Straight slit nozzle results. Sheet width (red) and thickness at the jet center (blue) displayed as a function of backing pressure (a) at 18 K and 2 mm below the aperture. The same characteristics are shown as a function of the distance to the aperture (b) at 4 bar and 18 K. The 'x' data point in the left plot at 4 bar represents results from another aperture of the same type. Each data point consists of the measurements from 50 images, where the marker shows the average value and the error bar represents the standard deviation. Due to slight rotation of the sheet when increasing the distance to the aperture (b), interferograms and therefore thickness measurements could not be obtained above 12 mm. Also, due to design restrictions of the nozzle cap images cannot be obtained for distances below 0.5 mm (see ref. [174] for details).

The experimental investigation of the influence of the backing pressure and the distance to the aperture on a 2x20 μm^2 straight slit nozzle jet is shown in figure 3.8a and b. Within the measurement uncertainties, both parameter studies reveal that the dimensions of the jets are invariant against changes of the operation conditions with an average sheet width of 16 µm and a thickness at the jet center of about 1.2 µm.* Since the jet is characterized by a constant flow velocity of ~ 100 m/s, the distance scan in figure 3.8b practically illustrates the temporal evolution on a sub-millisecond scale with the result that the shape is not changing with time. Data for another aperture of the same type yields comparable sheet widths as indicated by the 'x'-shaped marker in figure 3.8a at 4 bar demonstrating the reproducibility of the presented results.

Tapered slit aperture

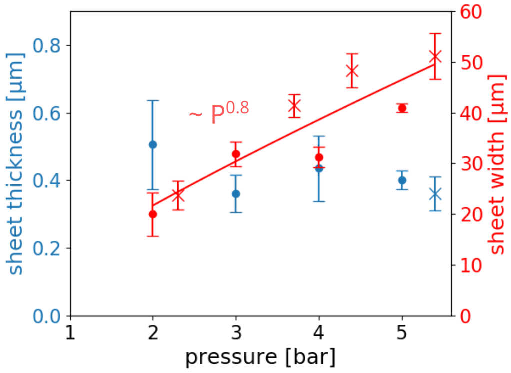

Figure 3.9: Tapered slit nozzle results. Sheet width (red) and average thickness of the planar part of the jet (blue) as a function of the backing pressure. The source temperature was 17 K and the distance to the nozzle was 2 mm. Full circles and 'x' markers represent data from two apertures of the same type. Each data point consists of the measurements from 50 images, where the markers show the average value and the error bars represent the standard deviation. A solid line provides a fitted power law of the form $A \cdot x^a$ for the sheet width measurements with $A = 12.2$ and $a = 0.83$.

The influence of the backing pressures on the sheet dimensions for a 2x20 µm^2 tapered aperture is shown in figure 3.9. The different markers (full circles and 'x') represent data from two apertures of the same type where the deviations that occur can be explained by small differences in the experimental conditions (e.g. exact temperature at the tip of the source). In contrast to the straight slit aperture, an increase in sheet width with the backing pressure is observed. The width is around 20 µm for 2 bar and therefore comparable to the size of the aperture, but increases for higher pressures to 40-50 µm. Generated sheets are therefore much wider than the slit length. With increasing backing pressure, the sheet thickness shows a decrease from 500 nm to about 350 nm, although statistically not significant.

3.5.2 Fluid dynamics of sheet jets

In the following, it will be discussed how the large differences of jet characteristics for the two aperture types can be explained with fluid dynamics of liquids and the onset of

---

*Retrospectively, the jet thickness measurements of a 2x20 µm^2 straight slit nozzle confirm the assumption in Obst et al. [57] about the target thickness of more than 1 µm.

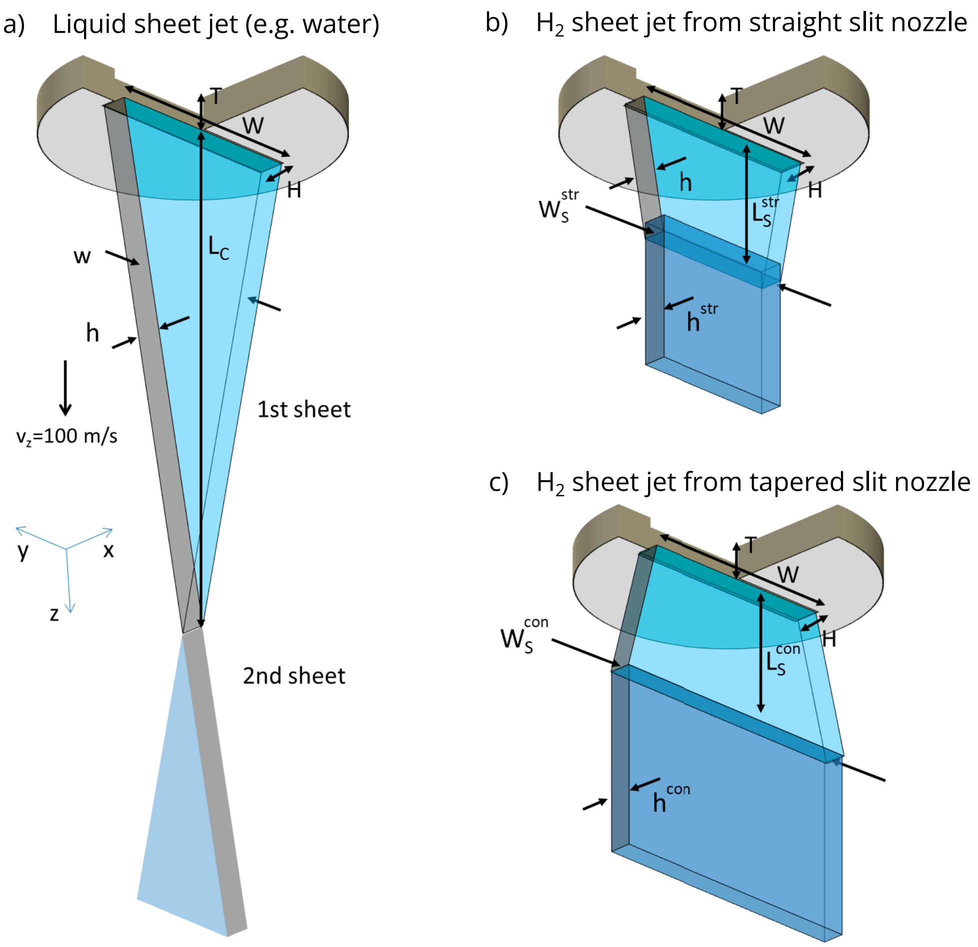
a) Liquid sheet jet (e.g. water)
T
W
H
L_C
w
h
v_z=100 m/s
y
x
z
1st sheet
2nd sheet
b) H_2 sheet jet from straight slit nozzle
T
W
H
h
W_S^{str}
L_S^{str}
h^{str}
c) H_2 sheet jet from tapered slit nozzle
T
W
H
W_S^{con}
L_S^{con}
h^{con}

Figure 3.10: Illustration of the jet fluid dynamics after extrusion of the liquid through a slit aperture nozzle. a) Driven by surface tension forces, a triangular shaped liquid sheet with a coalescence length L_C is established. b) Rapid crystallization of hydrogen causes the jet to solidify at a distance L_S^{str} after which the shape is conserved and characterized by a sheet width W_S^{str} and thickness h^{str}. c) Tapered slit apertures adding a lateral moment of inertia to the fluid motion that leads to an increased jet width and reduced thickness before freezing. The superscripts ^{str}, ^{con} refer to the straight and tapered aperture respectively, while a subscript $_S$ denotes a frozen jet.

solidification. While liquid sheets realized at ambient conditions by either slit apertures [190, 191, 192, 193, 189] or in impinging/colliding geometries [194, 195, 196, 197] were extensively studied, cryogenic sheets jets have not been examined so far. Similar to the Rayleigh-Taylor breakup into droplets (see section 3.4), surface tension governs the liquid flow extruded from rectangular slit nozzles [198] as illustrated in figure 3.10a. Behind the nozzle exit, surface tension starts to act on the sheet edges causing the generation of cylindrical rims that confine a flat sheet of thickness h and width w. The resulting jet shape resembles the dumb-bell cross section that was found in the experimental investigations in figure 3.7. As the liquid propagates further in the extrusion direction z, the rims move towards the center of the jet (in y-direction) with a velocity of [198]

$$u_e = \sqrt{\frac{2\gamma}{\rho \cdot h}} \quad . \tag{3.6}$$

Where γ and ρ denote the surface tension and density of the liquid, respectively. Since the gravitational force is negligible for sufficiently high flow velocities at the nozzle exit, as shown in section 3.1, a characteristic triangular sheet develops. The rims finally converge at the coalescence length L_C below the aperture, with [198]

$$L_C/W = \sqrt{We/8} = \sqrt{\frac{\rho h v_0^2}{8\gamma}} \propto v_0 \quad . \tag{3.7}$$

The coalescence length depends on the Weber number *We*, a dimensionless parameter describing the ratio between inertia and surface tension of a moving liquid. For the experimental conditions $v_0 \approx 100\,\mathrm{m/s}$ and the respective length of a 2x20 µm^2 slit nozzle, $L_C = 0.2\,\mathrm{mm}$ is calculated using $\gamma_{H2} = 2.5 \cdot 10^{-3}\,\mathrm{N/m}$ and $\rho_{LH2} = 73\,\mathrm{kg/m^3}$ from the table 3.1. As the jet moves farther downstream, momentum conservation causes the jet to widen again, which leads to the formation of a series of *n* alternating orthogonal sheets [199] with decreasing width and length due to natural losses caused by internal friction.
In contradiction to the classical fluid behavior, however, the measured images (figure 3.8) from cryogenic hydrogen jets do not indicate tendencies of coalescence or provide evidence that the sheet width *w* changes with the distance to the aperture. Instead, *w* is constant up to 50 times the length L_C, as shown in figure 3.8b. Similar to the suppression of the Rayleigh breakup into droplets for cylindrical jets, this indicates that the fluid dynamics of the liquid sheet is stopped. This solidification is not observable in the experiment due to the nozzle cap that prevents the acquisition of images within the first 0.5 mm below the aperture. However, with an expected $L_C = 0.2\,\mathrm{mm}$, it can be assumed that the fluid motion will be stopped at the latest after the first few sheets. Figure 3.10b illustrates this in the case where solidification occurs in the first sheet. As a consequence, the jet shape and width is maintained ($W_S^{str} = w(z > L_S^{str}) = \mathrm{const.}$) after a characteristic length $L_S^{str} = v_0 t_S$ at which a critical layer of solid hydrogen is established. Based on a flow velocity 100 m/s and the highest possible $L_S^{str} = 0.5\,\mathrm{mm}$ in the experiment, an upper limit for the formation time t_S of 5 µm can be calculated, which is in the same order of magnitude as the freezing time reported by [172]. Since both L_S^{str} and L_C (equation 3.7) scale linearly with v_0, the jet solidifies at the same point in its evolution. The width of the frozen sheet therefore remains independent of the flow velocity and hence the backing pressure P_0, which is consistent with the experimental observation shown in figure 3.8a for the straight slit nozzle.
The second nozzle type, the tapered slit nozzle, can generate jets that are wider than the nozzle dimensions (depending on the backing pressure P_0), as experimentally investigated (figure 3.9). Modeling the flow through the rather complex aperture geometry with a rhomboidal orifice and tapered aperture walls as well as additional slopes on the edges, as shown in figure 3.3d, is not trivial. Therefore, a phenomenological description of the sheet formation is given which follows the scaling analysis of liquid jets introduced by Ha et al. [192]. This assumes that the flow through tapered nozzles is governed by the same fluid dynamics as in the case of colliding jets. For now, solidification of the sheet should be ignored. Then, initially the jet width increases and, due to mass conservation, the sheet thickness is reduced. The thinner the sheet gets, the stronger the effect of the surface tension be-

comes, until a balance with the lateral inertia of the material is achieved. At this point, the stretch motion is reverted which ultimately results in the coalescence of both rims. The resulting form of the liquid jet resembles a chain of oval leafs, with the first leaf characterized by a maximum width $W_{\mathrm{max}}^{\mathrm{con}}$ and coalescence length $L_{\mathrm{C}}^{\mathrm{con}}$ which is larger than the slit length and L_C from a uniform flow velocity of a straight slit aperture, respectively. While the size of the first sheet is empirically determined by Ha et al. [192], for this phenomenological description and comparison to the experimental measurements, the dependency on the flow velocity is of interest and given by

$$\frac{L_{\mathrm{C}}^{\mathrm{con}}}{W} \propto v_0^{1.9} \tag{3.8}$$

and

$$\frac{W_{\mathrm{max}}^{\mathrm{con}}}{W} \propto v_0^{1.8} \quad . \tag{3.9}$$

Overall the length and width of the first leaf increase with v_0. As for the straight slit aperture, recorded sheet images from the tapered aperture do not indicate tendencies of coalescence and thus solidification of the jet already occurred within the first 0.5 mm from the nozzle. For illustration, the case for solidification in the first leaf is illustrated in figure 3.10c. Based on the measurements in sections 3.5, it can be expected that the fluid motion is stopped far from a coalescence point, as the measured jet width after freezing W_S^{con} is larger than the slit length. Moreover, the experimentally observed pressure dependence ($\sim P^{0.8} \sim v_0^{1.6}$) of the solidified jet width in figure 3.9 indicates a similar scaling as $W_{\mathrm{max}}^{\mathrm{con}}$ in equation 3.9. This suggests that solidification occurs within the vicinity of the maximum width of the first or second leaf. Note that with $L_C = 0.2\,\mathrm{mm}$ and $L_{\mathrm{C}}^{\mathrm{con}} > L_C$, at most two leafs are expected within the first 0.5 mm.

In order to fulfill mass conservation the sheet thickness h decreases as the jet widens. This explains the experimentally measured jet thickness that is several times thinner than the nominal slit width of 2 µm. This behavior is also supported by the empirical dependency found by Ha et al. [192]

$$h \propto \frac{1}{z} \quad . \tag{3.10}$$

h decreases with the distance to the nozzle z and depends otherwise only on the geometry of the aperture. Assuming again a similar fast formation of a critical solid layer in less than $t_S = 5\,\mu\mathrm{m}$, the lateral motion stops at a maximum $z = v_0 \cdot t_s$ resulting in $h \propto 1/v_0$ with equation 3.10. The general trend of this finding agrees with the experimental data in figure 3.9 where the sheet thickness h decreases with the flow velocity, although statistically not significant.

So far, the discussion of the fluid dynamics has focused on the shape of the slit layer, while the influence of the support layer was neglected. However, as illustrated in the cross section in figure 3.3d, an additional slope in the support layer walls is present and capable of introducing a further variation in the flow distribution that might affect the fluid dynamics as well. Moreover, the description of the flow is idealized and e.g. viscosity was neglected but is supposed to affect the fluid dynamics in particular near the slit [198]. A combination of these aspects likely causes differences between experimental observation and the fluid model description. For example, the experimentally determined sheet thickness of 1.2 μm from the straight slit nozzle is decreased in comparison to slit width of H = 2 μm.

In order to draw a more quantitative picture, detailed modeling of the flow field inside the nozzle together with the thermodynamics of the cooling and crystallization processes is needed, using advanced simulation tools such as computational fluid dynamics (CFD) and finite element methods (FEM). This approach is then complemented by a comprehensive experimental characterization of the liquid flow close to the nozzle. In addition, the spatio-temporal evolution of the crystallization pathway could be studied at x-ray free electron lasers using diffraction and imaging methods.

3.6 Implementation in the laser-plasma experiment at DRACO petawatt

Besides the characterization of the hydrogen jets and the derived understanding of the fluid dynamics, the aspect of implementation in a harsh laser-plasma environment is crucial for the successful application of the jet target system. With respect to the studies in the following chapter, the main interest is the implementation in the experimental environment for ion acceleration at the DRACO petawatt laser system. However, the aspects discussed here also apply more generally to all experiments where the jet is irradiated with high intensity laser pulses. The crucial point for a successful long-term application is to ensure a stable spatial overlap between the micrometer-sized jet and the micrometer-sized laser focus spot. For this purpose, first, the stability of the target is characterized and then strategies to significantly improve the spatial overlap are discussed.

3.6.1 Characterization of the jet stability

Up to this point, studies of the extruded jets were mostly based on measurements close to the aperture because evaporative cooling freezes the hydrogen within the first millimeter and no change of the morphology and shape was observed farther downstream. However, the jet is characterized by an inherent position and orientation fluctuation that typically increases with the distance to the aperture.

The distribution of the relative jet position transversely to the flow direction at a fixed 20 mm distance to the aperture is exemplified in figure 3.11a for a cylindrical hydrogen jet. The positioning jitter, which describes the standard deviation of this distribution, is $\sigma_x = 8.1$ μm and $\sigma_y = 9.7$ μm with respect to the x and y directions. With regard to the ejection direction at the nozzle, this corresponds to a pointing fluctuation of 0.41 mrad and 0.49 mrad, respectively, or a total pointing fluctuation of 0.63 mrad when combining both directions. The jet stability measured here is thus comparable with earlier results presented in [57] or [156]. The positioning jitter results in strong shot-to-shot fluctuations in a laser-plasma experiment. Assuming a 3 μm laser spot and a Gaussian distributed position fluctuation with a standard deviation of 9 μm (average of σ_x and σ_y), full hits (laser spot fully covered by

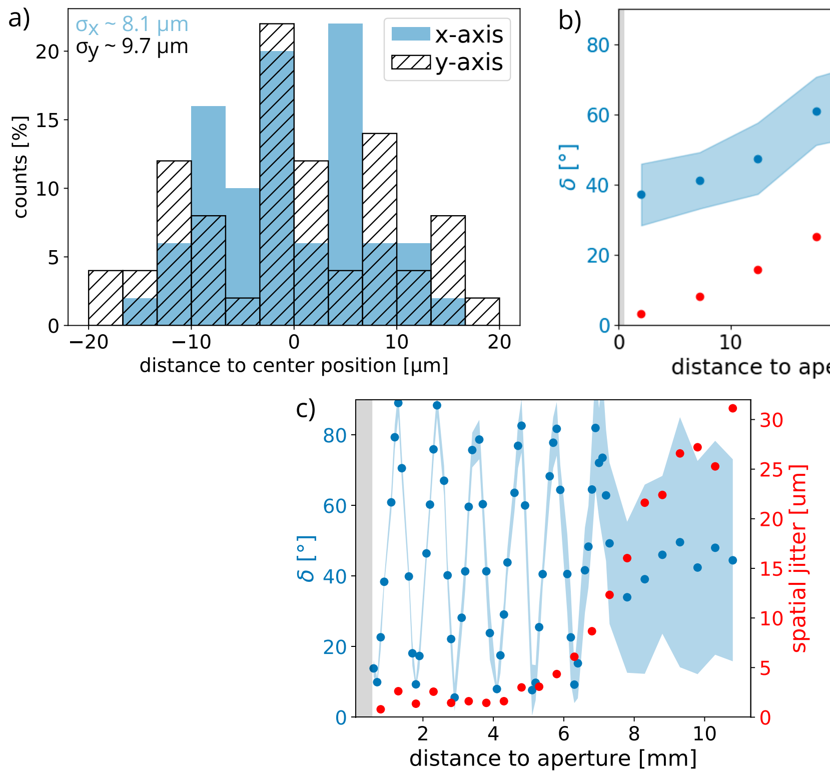

Figure 3.11: a) Relative lateral position of a ⌀ 5 µm cryogenic jet 20 mm below the nozzle obtained from 50 consecutive images recorded at 1 Hz. x and y-axis refer to the directions perpendicular to the extrusion direction. σ denotes the standard deviation for the respective distribution. Spatial jitter (standard deviation) and orientation angle δ (angle of the planar part in the x-y plane) with respect to the distance to the aperture in b) for a jet from a 2x20 µm^2 straight slit nozzle operated at 18 K and 4 bar and in c) for a sheet generated by a 1x20 µm^2 tapered nozzle at 5 bar and 16.5 K. The spatial jitter in b) and c) represents the combination of both σ in x and y-direction ($(\sigma_x^2+\sigma_y^2)^{1/2}$). Each data point is based on 50 measurements. The markers show average values. The error bars for δ contains 95% of the measurements. Distances to the aperture below 0.5 mm are not accessible due to restrictions of the nozzle cap (gray shaded area).

the 5 µm jet) are expected in less than 10% of the shots and complete misses (no overlap between the 3 µm laser spot and the jet) are expected in about 65% of the shots. The low hit probability demonstrates the need for wider targets, such as planar jets.

Figure 3.11b illustrated the stability of a sheet jet generated by a 2x20 µm^2 straight slit aperture as a function of the distance to the nozzle. The approximately linear increase of the spatial jitter with the distance to the aperture is explained by the fluctuation of the jet ejection direction at the nozzle. The average pointing fluctuation, calculated from dividing the spatial jitter by the distance to the nozzle, of 0.45 mrad is comparable with the 0.63 mrad achieved for the 5 µm cylindrical jets. Similarly, the expected stability for an overlap with a laser focal spot of 3 µm can be estimated at 20 mm distance to the aperture. At this position, the 16 µm wide sheet features a spatial jitter perpendicular to the laser axis of 6.5 µm ($1/\sqrt{2}$ of the value displayed in figure 3.11b). With a probability of 50%, the laser spot is completely covered by the jet, which represents an at least 5-fold increase compared to the cylindrical jet, making the planar jet a more reliable target in terms of shot-to-shot stability. While due to the planar geometry, sheet jets reduce the influence of the position jitter on the laser target overlap, they additionally introduce the importance of axial orientation.

The orientation angle δ (i.e. angle of the planar part in the x-y plane, see figure 3.4a for illustration) is also characterized by an inherent fluctuation that can e.g. alter the emission direction of laser-driven proton beam (refer to section 4.4). For the straight slit nozzle, δ is very stable for all distances to the aperture, as the measured fluctuation is less than 10° (indicated by the blue shaded area in figure 3.11b). This provides a sufficiently reproducible orientation for an application in a laser-plasma experiment. The orientation angle shows a weak dependence on the distance to the aperture, as a rotation of less than 35 ° occurs during the jet propagation of 30 mm. A possible reason for this slow rotation along the z-direction might be small imperfections or dust particles disturbing the uniform liquid flow and are likely to change from nozzle sample to nozzle sample. It is also important to note that the position jitter and the orientation of the planar jet are insensitive to the operation conditions of the target system (source temperature and backing pressure).

The characteristics of the jet stability change considerably for a 1x20 μm^2 tapered aperture, as displayed in figure 3.11c. The observed orientation changes rapidly compared to the straight slit aperture as a full rotation of the sheet is achieved in about 2 mm of propagation. The target shape along the z-direction can therefore be imaged as a double rim-helix spanning a thin sheet layer. This axial orientation depends not only on the distance to the aperture but also on the backing pressure and source temperature, which allows for precise alignment of the sheet. The responsible angular momentum in the liquid flow is introduced by the rhomboidal nozzle footprint with non-orthogonal tapered slit edges as illustrated in figure 3.3c. For a technical point of view, the unique opportunity to rotate and align the jet sheet with respect to laser or detector axis without mechanical intervention was found to be very useful in proton acceleration experiments to control proton beam pointing and was applied for the shots on planar jets in section 4.4. The fluctuation in the orientation of the jet (figure 3.11c) is small for short distances to the nozzle, however, increases rapidly above 6-7 mm as it is illustrated by the blue colored area. At even larger distances, this results in a mostly undefined alignment of the sheet and therefore explains the average orientation values of about 45 °. The spatial jitter further shows the same characteristics. It is smaller than 4 µm at short distances from the aperture, however at about 5 to 6 mm a fast increase is observed. This behavior cannot be explained by a fluctuation in the direction in which the jet is ejected into the vacuum, because this would require a linear increase of the spatial jitter starting from the nozzle. While understanding the cause requires further investigations, it is important to note that the distance at which the stability rapidly decreases can be significantly improved with the beneficial selection of the operation parameters. For example, a spatial jitter of 10 µm and a fluctuation in the orientation of $\sim$10° at a distance of 20 mm below the nozzle was achieved at a temperature of 22 K and a backing pressure of 6 bar for the same 1x20 μm^2 aperture. This demonstrates a comparable target stability with respect to the sheets from straight slit nozzles and cylindrical jets. However, this also indicates that, contrary to the straight slit nozzle, the sheet from a tapered aperture is more sensitive to the operation parameters used. Note that due to the 50 µm wide sheet (see table 3.2), full hits in a laser-plasma experiment are almost guaranteed (>99%) with tapered slit apertures under such stability conditions.

Independent of the utilized aperture as well as the experimental implementation [156, 57], the lowest spatial jitter is about 3-5 µm at 10 mm below the nozzle and increases farther downstream. Since this is already in the order of the focal spot size of a high-intensity laser pulse and can thus have a large influence on the laser-plasma interaction (in particular for cylindrical jet targets), the best option to achieve better shot-to-shot stability is to reduce the distance to the nozzle. However, it has been observed in experiments with high power lasers [57, 200] that the nozzle suffers from severe damage caused by the laser-matter interaction being too close. So far, the workaround was either to increase the distance to the nozzle and thus decrease the jet stability or to replace the aperture after each shot which extremely reduces the repetition rate. While the former approach was sufficient at the level of 150 TW laser systems, damaging becomes intuitively more severe for higher laser powers. A sufficient large distance to the aperture of at least 20 mm, that is required for long-term operation at petawatt laser powers, leads to a large spatial jitter and thus a hit probability that is too low for controlled laser-proton acceleration studies.

3.6.2 Improvement of target stability through shielding of the jet delivery system

A novel approach to increase the hit probability is to prevent damage to the sensitive aperture plate by providing an efficient protection from the laser-plasma interaction. One can differentiate the disruptive energy deposition inside the nozzle into energy transfers along the jet material (hydrogen in a solid or plasma state) and emission of radiation and charged particles (e.g. hot electrons) that travel through the vacuum. Examples for the first category are shock waves that are introduced by the compressing force of the laser, or return currents, which arise as a result of the charge imbalance in the interaction region (refer to [64] or chapter 5).

Two methods that are subjected to shield the aperture were implemented and tested. While laser cutting only disrupts the solid connection between the interaction point and the sensitive nozzle, mechanical cutting additionally blocks the line-of-sight.

Laser cutting

A cutting laser beam is introduced into the experimental setup (figure 3.12a) to study if disruption of the cryogenic jet can prevent damaging of the sensitive nozzle. The cutting pulse was generated from a portion of the high-intensity beam and focused to a spot size of 50 µm, large enough to account for the spatial jitter of the jet. Irradiation with pulse energies E_{cut} of at least 0.3 mJ is sufficient for ionization of the solid hydrogen because the peak intensity of the laser pulse is estimated to be in the order of 10^{14} to 10^{15} W/cm^2 (depending on E_{cut}) and thus larger than the barrier-suppression ionization threshold (see section 2.1.1) of $1.37 \cdot 10^{14}$ W/cm^2. After a duration of 10 ns the target material is vaporized

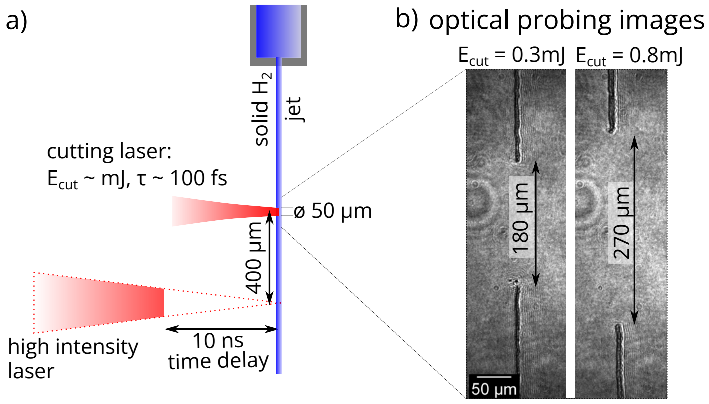

Figure 3.12: a) Arrangement of the cutting laser beam featuring an energy E_{cut} on the mJ-level, a pulse duration $\tau \approx 100$ fs and a focal spot size of 50 µm. With a time offset of 10 ns, the cutting beam hits the jet target 400 µm above the focus position of the high-intensity laser. Optical probing images (b) indicate 10 ns after the irradiation with the cutting pulse a few 100 µm wide gap in the hydrogen jet.

on 180 µm length (see left image in figure 3.12b) and a gap in the jet is formed which represents the introduced interruption. Note that the jet movement in this 10 ns time frame is on the order of 1 µm and can therefore be neglected. Intuitively, an increase in pulse energies to $E_{cut} = 0.8$ mJ (right image in figure 3.12b) leads to a larger size of the gap due to two aspects. On the one hand, the threshold for ionization is reached at a larger distance to the central spot and, on the other hand, more material can evaporate due to the higher amount of deposit energy. It is important to note that the laser cutting does not result in any observable modifications of the solid jet in the region where interaction with the high-intensity laser takes place (0.4 mm farther below).
Unfortunately, on-shot application of the laser cutting indicates a slightly, but not complete, reduction in damage to the aperture. From this, it can be concluded that radiation and charged particles (traveling through the vacuum) deposit a considerable amount of energy in the aperture plate. It is therefore essential to block the line-of-sight between the interaction point and the nozzle as well.
Nevertheless, laser cutting allows the precise and stable generation of gaps in the target. This enables the fabrication of jet sniplets of limited size by cutting the target above and below the interaction region, which presents a potential approach to generate mass reduced target for future studies.

Mechanical chopper

A second approach to mitigate the aperture damage is to utilize a mechanical cutting device, referred to as *mechanical chopper*, that intercepts the energy transfer along the jet and blocks the line-of-sight. The main challenge lies within the precise temporal synchronization of the position of the mechanical device to the laser shot, as laser shots without cutting must be prevented. The upper limit for the precision of the synchronization is defined by the time duration of about 10 µs that the jet (flow velocity of ≈ 100 m/s) needs to travel the distance of about 10 mm between the interaction point and the nozzle. A more

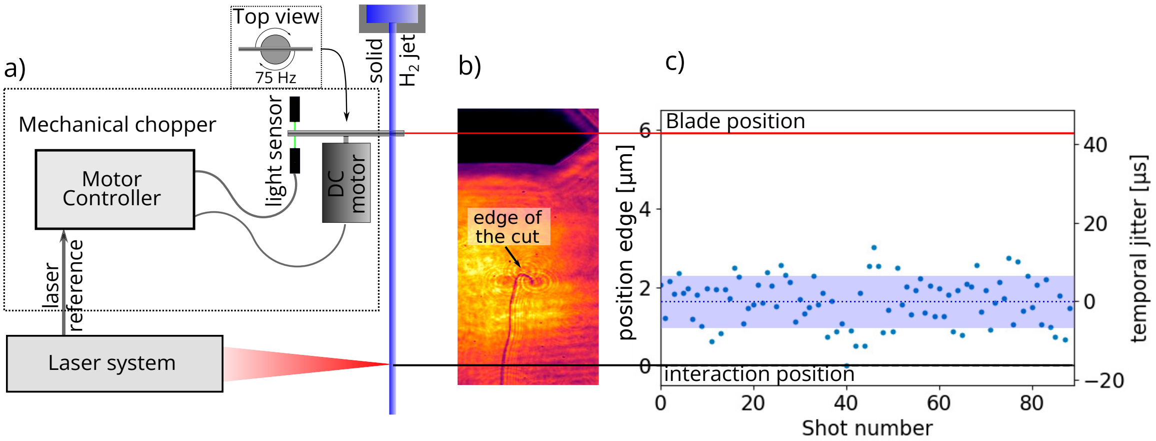

Figure 3.13: a) Schematic drawing of the components of the mechanical chopper (DC motor with a rotating blade, a light barrier, a motor controller and a laser reference signal). b) A shadowgraphy image generated by back-illumination with a sub-ps optical probe beam, that is synchronized to the high-intensity laser, shows the chopper blade (black bar in the top of the image), the cryogenic jet in the bottom of the image and the cutting edge. c) Characterization of the stability of the mechanical chopper. Red and black horizontal lines illustrate the position of the blade as well as the interaction point. Blue dots indicate the position of the jet edge obtained from probe images for about 90 consecutive images at 1 Hz. The blue shaded area illustrated the standard deviation interval.

accurate synchronization, of course, allows for a smaller distance to the nozzle and thus a lower spatial jitter.

For the implementation in the experiment, a fast spinning blade is used, which is inserted between the aperture and the interaction point and which is driven by a direct current electric motor. The rotation of the electric motor is synchronized to a 10 Hz laser trigger signal by a motor controller from an optical chopper system (Thorlabs MC2000B-EC) as illustrated in figure 3.13a. The actual blade rotation is further detected by a light sensor consisting of a laser diode and a photodiode. The light sensor provides feedback to the controller allowing to adjust the rotation speed in order to synchronize the blade position to the trigger signal.

The on-shot position of the blade is measured and adjusted with a low magnification imaging system to achieve the cutting prior to irradiation with the high-intensity laser pulse. The probe image in figure 3.13b illustrates the situation where the cut edge is positioned about 2 mm above the interaction point. Momentum transfer from the blade causes a small curl at the edge of the jet resulting in a deflection of the target within the first 0.5 mm below the cutting point. However, the jet stability is not affected farther below. A study concerning the temporal stability of the mechanical cutting is shown in figure 3.13c. The blue data points indicate the position of the edge of the cut (see probe image in figure 3.13b) for about 90 consecutive images at 1 Hz. The stability of the edge position can be characterized by a standard deviation of 0.6 mm while 1.6 mm marks the highest offset from the average. The jet edge is intentionally positioned at a larger distance to the blade to increase the safety margin for laser shots without cutting which could potentially damage the aperture. The resulting increased chance for shots without a target, where the jet edge is below the interaction point (e.g. at shot number 40) is especially acceptable in the case of high repetition rate operation. The implementation of the mechanical chopper in the laser-plasma experiment (see next chapter) showed that damage to the aperture was prevented at 10 mm distance between nozzle and interaction point. This reduction of the distance to the aperture by at least a factor of two and thus an increase in jet stability enables systematic studies of laser-plasma interactions at the petawatt level that are presented in the next chapter. It is expected that a more advanced electronic control system currently under development [201] that uses a pulse width modulation driven brushless DC motor will be able to improve the stability of the temporal synchronization by up to one order of magnitude. It should be noted that such a technical solution could also be of interest for other target systems used in high-power laser experiments where small apertures are applying to produce solid or liquid targets [153, 199, 197, 159].

3.6.3 Vacuum system requirements

Besides improving the hit probability, the employed vacuum system is essential for the implementation of cryogenic jet targets in a laser-plasma experiment. Firstly, the achieved vacuum chamber pressure is crucial for the long-term stability of the jet. Secondly, since the jet delivery system inserts a substantial gas load in the order of 100-400 sccm (see table 3.2 for typical amounts of hydrogen gas required for each nozzle type) into the target chamber, the available pumping speed hence limits the cross section of applicable apertures. For the stable long-term operation of the jet, a pressure in the vacuum chamber better than 10^{-3} mbar is required. For higher pressure, heating of the cryostat assembly due to conduction with residual gas becomes non-negligible and more cooling power is required for a given operation temperature. The heating power per surface area can be estimated using [174] $P_{\text{gas}}/A \approx 10.9 \cdot p_{\text{mbar}}$ [W/cm^2], where p_{mbar} denotes the vacuum pressure of the surrounding gas in mbar. A cold surface with the size $A \approx 100\,\text{cm}^2$ of the here presented cryogenic system results in P_{gas} of about 1.1 W for $p_{\text{mbar}} = 10^{-3}$ mbar. As the typical cooling power of the cryostat is less than 10 W at 18 K operation temperature, an upper limit in the order of 10^{-2} mbar can be estimated for short-term operation*. The jet generation is prevented at even higher vacuum pressures due to heating of the target system to temperatures where hydrogen evaporates inside the source. This leads to a rapid backing pressure increase in the gas supply line that can potentially damage in particular the sensitive aperture plate. An additional effect at vacuum pressures above 10^{-3} mbar is that residual particles tend to freeze more often close to the cold nozzle. This potentially results in a partial clogging of the aperture which can decrease the stability of the jet and is therefore only tolerable for a few minutes, e.g. during cooling down of the source assembly. It is additionally disadvantageous that the throughput of the typically used turbomolecular pumps is pressure-dependent and decreases significantly above 10^{-3} mbar. This makes the vacuum system less effective at higher chamber pressures so that increases in flow rate lead to a disproportionate increase of the chamber pressure.

As the vacuum system in a laser-plasma environment is only designed to reach medium-scale conditions (10^{-5} to 10^{-6} mbar) for preventing laser field-induced ionization and optics

---

*Note that the practical limit might be lower because other heat transfer processes are not considered and a remaining cooling power is required for a temperature-stabilized operation.

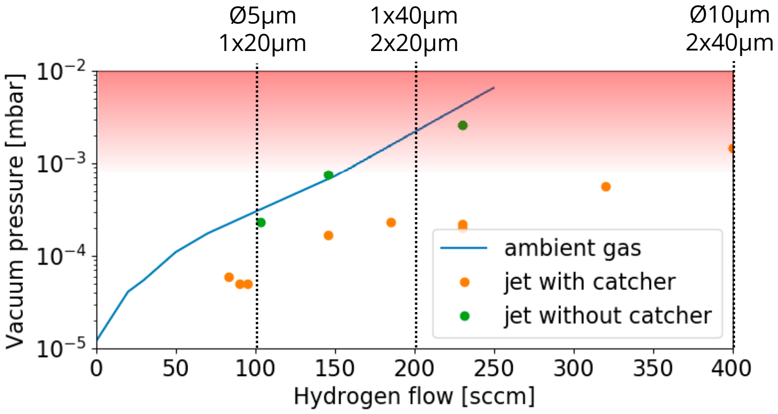

Figure 3.14: Vacuum chamber pressures for an applied pumping speed of 7000 l/s at various amounts of hydrogen gas loads (expressed in standard cubic centimeter per minute). Dots represent measurements with different jet geometries from table 3.2, which were performed either with a differential-pumped catcher (orange) or without one (green). For comparison, the blue line indicates the reaction of the vacuum system to the insertion of hydrogen gas at ambient conditions. The red area marks the region where a stable long-term operation is not recommended. Typical hydrogen flow values for different sizes and geometries of the aperture are illustrated by the dotted lines and are calculated by $v_0 \cdot A_0 \cdot \alpha$. A_0 is the aperture size (e.g. 40 μm^2 for a 2x20 μm^2 nozzle), v_0 is the flow velocity of the extruded jets and $\alpha \approx 812$ denotes the density ratio between liquid and gas phase (see table 3.1).

damages, installation of additional pumping power is required to accomplish vacuum pressure below 10^{-3} mbar for the typical aperture cross section. Figure 3.14 shows measurements of the vacuum pressure for various gas loads from cryogenic targets obtained during jet characterization runs at the target area for ion acceleration at the DRACO petawatt laser system (see chapter 4.3). A total of 4 high throughput turbomolecular pumps (*pfeiffer vacuum HiPace2300*) with a combined pumping speed of around 7000 l/s (for hydrogen) were installed at the chamber and backed by either scroll or side channel pumps. In order to determine the maximum cross section of applicable apertures, the response of the vacuum system to a gas load was characterized. For this purpose, hydrogen at ambient conditions was inserted into the target chamber (blue line in figure 3.14) which overlaps with example vacuum pressures measured during cryogenic jet operation. Already at about 150 sccm, a value smaller than the typical hydrogen flow through an aperture of 2x20 μm^2, 10^{-3} mbar is exceeded and jets with higher gas loads are limited in their long-term stability or might be restricted in their operation parameter, to e.g. reduced backing pressures.

However, the chamber pressure can be significantly reduced by utilizing the concept of differential pumping. For this purpose, the jet is captured in an individual pumped volume (catcher) with a round opening of 3 mm in diameter. This results in a reduction of the vacuum pressure in the target chamber by about one order of magnitude (orange dots in figure 3.14). The maximum hydrogen flow for long-term operation with the catcher is therefore increased to about 300-350 sccm. Although even larger cross sections (up to 4x20μm^2) were tested during jet characterization runs, as indicated by the orange dot at about 400 sccm, their implementation in a laser-ion acceleration experiment is not recommended. If the jet leaves the catcher for even a few seconds, a considerable gas load is introduced that cannot be handled by the vacuum system. The subsequent abrupt heating of the source interrupts the jet production so that a stable long-term operation is not practicable. In order to employ larger apertures in a laser-plasma experiment, one can further improve the vacuum system by using customized or specialized pumps for light elements, e.g. roots pumps, or by extending the catcher design to a two-stage approach.

3.7 Slit aperture optimization for laser-proton acceleration experiments

Based on the acquired knowledge of fluid dynamics and the target implementation studies, it is now possible to suggest nozzles of optimized shape for laser-proton acceleration studies. Successful application of planar hydrogen jets in a laser experiment requires three main target conditions to be fulfilled: stability, sheet width and thickness. While the first two determine the reproducibility and shot-to-shot fluctuations, the latter can substantially influence the proton acceleration performance.

To ensure a stable laser target overlap (>95% probability of full hits) a sheet width that is four times larger than the position jitter is required. From typical spatial jitter values (standard deviation) of ~5 μm at 10 mm below the aperture with the mechanical chopper (section 3.5.1), one can calculate a minimum width of about 20 μm. While sheet targets generated by a tapered aperture can be adjusted to the appropriate width, for jets from straight nozzles the slit length has to be chosen slightly above the required sheet width.

Secondly, a stability of the sheet orientation better than about 10° is required to ensure that the emission direction of the accelerated proton beam is smaller than the typical divergence angle of the accelerated proton beam. Straight aperture jets seem to be intrinsic stable in their orientation. However, for tapered apertures, one has to identify the best operation conditions for a reasonable stable orientation.

Finally, the sheet thickness has to be adjusted for optimized proton acceleration. For example, the experiments in the next chapter will suggest an optimal thickness at around 0.5-1 μm for the DRACO petawatt laser. An adjustment of the sheet thickness has to be accomplished by the choice of the slit width because the source conditions do only allow for smaller corrections by changing the backing pressure. Since the sheet thickness was experimentally found to be a factor of two or four lower than the nominal slit width referring to the straight and tapered aperture, respectively (see table 3.2), one should select an aperture with a slit width increased by that factor.

In summary for a future campaign at the DRACO petawatt laser either a 2x40 μm^2 straight slit aperture or a 4x20 μm^2 tapered aperture are suggested. Both nozzle types are expected to deliver more than a 20 μm wide and about 1 μm thick sheet jet.

Further target optimization could benefit greatly from computational tools that allow the aperture shape to be evaluated for the required sheet shape in preparation for an experimental campaign. Experimentally, new nozzle designs might in addition be benchmarked with millimeter-sized machined models of the same geometry. By selecting an appropriate fluid and flow velocity, the same dynamics (without the evaporative cooling) are expected when the dimensionless number (e.g. Reynolds or Weber number) are similar. This approach allows, as preparatory studies, the characterization of different aperture shapes under less demanding ambient conditions and at larger dimensions.

3.8 Conclusion

Experimental studies for optimizing cylindrical or thin planar jets of solid hydrogen as targets for laser-proton acceleration were presented. The vacuum system was improved to facilitate the implementation of more optimized (larger cross section) apertures in a laser-plasma environment. Moreover, the development of a mechanical chopper device led to increased target stability and demonstrated the protection of the sensitive aperture plate from disruptive influences originating from the interaction. This for the first time allowed the application of a large amounts (>100) of laser shots with the same slit nozzle without causing any damage and thus enabled experiments at the DRACO petawatt laser with a significantly enhanced hit probability. This will be demonstrated in the next chapter. A second version of the chopper system with a more accurate synchronization is under development [201] and will further improve the stability of the target system.

The fluid dynamics occurring in the planar jet geometry was investigated in order to identify the most favorable slit dimensions to generate optimized shaped sheet targets in the future. Upon ejection, the initial fluid contraction motion, governed by surface tension forces, stops at a characteristic length after which solidification of the hydrogen suppresses the fluid properties and consequently conserves the jet shape. Based on the investigations with slits of a nominal 2x20 μm^2 cross section, dimension and stability of the jets from straight apertures are independent of the applied source conditions for parameters ranging from 1-4 bar and 16-20 K. Depending on backing pressure, the sheets generated by tapered slit nozzle, on the other hand, are tunable and can become much wider and thinner than the initial nozzle width, while the stability seems to be sensitive to the operation parameters of the cryogenic system. The inherent axial rotation of hydrogen jets was found to be very useful to control the sheet orientation with respect to the incoming laser axis by adjusting the source operation parameters.

Besides cylindrical and planar jets, studies on either multi-species effects with mixtures of hydrogen and deuterium as proposed in [161] or cryogenic microdroplets as mass limited target produced by the stimulated Plateau-Rayleigh breakup or by laser cutting above and below the interaction region are promising for further investigations.

4 Laser-driven proton acceleration with cryogenic hydrogen jets in the petawatt regime

Potential applications of laser-driven ion sources depend on the ability to provide tunable distributions of particles with sufficient maximum energies. Scaling to higher ion energies is primarily achieved by raising the applied laser power. However, a higher laser power, in general, implies an increase of unwanted background radiation originating from pedestals and pre-pulses that were generated in the laser chain and that precede the main high-intensity pulse. This results in a premature transition of the initially cold target into a pre-plasma state which alters the interaction and therefore influences the acceleration performance to a great extent. In figure 4.1, the consequences of this can be observed in the scaling studies performed with the 150 TW arm of the DRACO laser system [67] that were extended to the petawatt level by the DRACO upgrade [203]. While the maximum proton energies obtained at the 150 TW arm with micrometer thick metal foils and intrinsic contrast (blank red stars from [67]) agree well with the theoretical prediction (gray line) from Kluge et al. [87], maximum energies measured at the DRACO petawatt (PW) arm with the same target remains below this curve (filled red stars). Note that the theoretical scaling assumes an overdense target, where the laser interacts with a surface layer that is thin in relation to the overall target thickness. The theoretical scaling therefore only serves as a comparison when other conditions dominate. The maximum proton energies can be increased, for example, by employing thinner targets and reducing the laser intensity level prior to the main pulse with a plasma mirror device [96] (empty blue diamond marker in figure 4.1). Additionally, the accelerator performance can be optimized by adjusting the temporal pulse shape [202] (filled blue diamond). Hence, for a given laser power, the primary task is to identify the ideal and technically realizable combination of laser pulse profile and target shape.

This optimization is inherently linked to the investigation of different acceleration processes, since generally multiple mechanism coexist. TNSA (section 2.1) as the best established

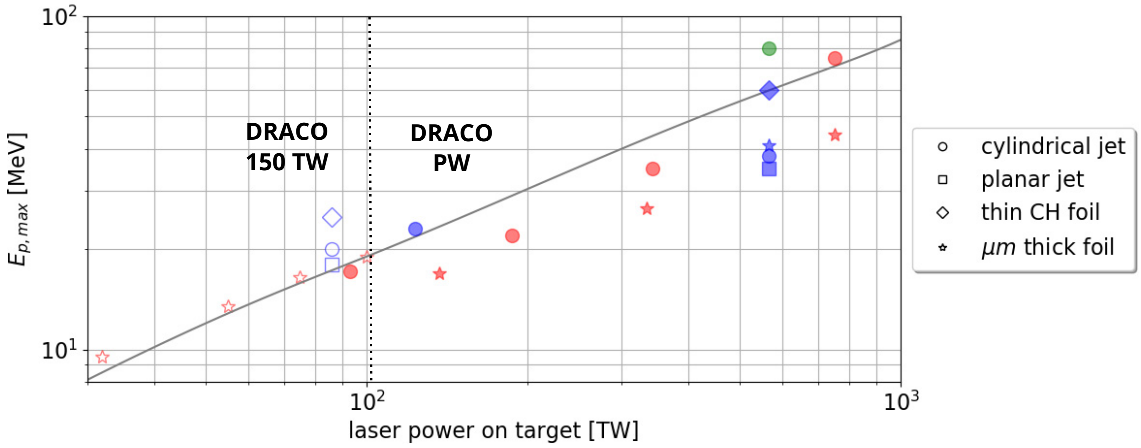

Figure 4.1: Maximum proton energies $E_{p,max}$ from the 150 TW (blank markers) and the petawatt arm (filled markers) of the DRACO laser system. The colors indicate the laser contrast condition. Red: intrinsic contrast, blue: plasma mirror (PM) enhanced contrast and green: PM contrast with optimized proton performance due to a pre-pulse induced artificial target pre-expansion. Blank red stars represent data from Zeil et al. [67] for foil shots and the blank blue dot/square were obtained with a cylindrical/planar cryogenic hydrogen jet in Obst et al. [57]. The empty blue diamond shows the highest measured proton energy at the 150 TW arm using a thin liquid crystal film target [96]. For the DRACO PW, the blue diamond indicates the best performing plastic target (formvar) with a thickness of 400 nm [202] and the blue star shows $E_{p,max}$ for a 2 µm thick titanium foil (filled star marker). Hydrogen jet targets irradiated at the DRACO PW arm in the frame of this thesis are represented by filled circles and squares. The gray line indicates a TNSA scaling for DRACO laser parameters and thick overdense targets [87].

mechanism is based on accelerating protons (and ions) from the target rear side due to a space charge field that is established by a population of hot electrons. For thin targets, proton acceleration can be enhanced by the onset of RIT (section 2.2.1) where the laser transfers its energy volumetrically to the electrons. Light pressure can push an entire thin foil that leads to proton acceleration by RPA (section 2.1) in the light-sail regime. Thick targets, on the other hand, are exposed to the same radiation pressure at the front side, which is referred to as hole-boring (section 2.1 and 2.2.1). For near-critical densities, ions can experience synchronized acceleration when the laser pulse penetrates the plasma (SASL) or magnetic vortex structures can be generated at the rear side which in turn drive a proton beam (MVA, section 2.2.1).

Several of those schemes have the potential to improve key aspects of the proton beam. For this, however, configurations must be found in which individual acceleration processes can first be identified and then optimized. In experiments, strategies to select a mechanism have proven to be most viable through target material and shape. Advanced acceleration schemes are therefore investigated by specialized target systems using ultra-thin overdense foils (e.g. [25, 96]) or near-critical density targets. The latter can be provided by exploded foils [143, 131, 72, 204], nanostructured materials [95, 106], low-density substances like solid hydrogen [152, 205, 57, 153] or high pressure gas jets [137, 105]. For details on the target systems, refer to section 2.2.2.

In this chapter, it is shown that cryogenic hydrogen jets are a beneficial target system to study aspects of different acceleration mechanisms in unprecedented detail in order to understand and optimize their individual contributions. This is facilitated by the low plasma

density and the small spatial scale of the target as well as the advantageous technical aspects of cryogenic hydrogen jets that were introduced in the previous chapter. The volumetric mass density of solid hydrogen when fully ionized is the equivalent of only 30 $n_{c,800\mathrm{nm}}$ and is therefore small in comparison to materials from typical foil targets (e.g. plastic targets: $\sim$230 $n_{c,800\mathrm{nm}}$ or titanium targets: $\sim$700 $n_{c,800\mathrm{nm}}$). Experimental studies investigating near-critical density targets are simplified by the usage of solid hydrogen, because the theoretical laser intensity for relativistic transparency, which is about $3.8 \cdot 10^{21}$ W/cm^2 (see section 2.1.2) at 800 nm wavelength, can already be reached or even be exceeded by available intensities of petawatt laser systems. Important to note is that the low density also facilitates numerical simulations because a reduced degree of spatial resolution is required in comparison to denser materials to resolve the plasma oscillation wavelength. Simulation complexity is further reduced by the relatively simple ionization physics of the pure hydrogen target content. According to numerical studies [205, 152], another advantage of pure hydrogen is a higher laser to proton conversion efficiency in comparison to standard plastic targets which is the result of a higher laser absorption due to the lower density and ion mass. Lastly, the cryogenic jet is a well-suited target for temporally resolved observations of femtosecond to multi-picosecond plasma dynamics due to the free-standing arrangement and the small spatial scale enabling optical probing from different observation angles. As a result, the cryogenic hydrogen jets are a key tool linking targetry, laser diagnostics, optical probing, acceleration dynamics and predictive simulation capabilities to resolve the microscopic picture of the interaction.
While two previous campaigns at the 150 TW arm of DRACO already demonstrated the capabilities of the cryogenic jet to investigate proton acceleration [55, 56, 57, 58, 59, 206], the experiments presented in this chapter represent the continuation of this endeavor and cover laser-plasma interaction studies using hydrogen jet targets irradiated with the DRACO PW system. The experiments were carried out in close collaboration with the High Energy Density Science group of SLAC National Accelerator Laboratory.

In this chapter, investigations of laser-driven proton acceleration from different target density distributions originating from cylindrical and sheet-like hydrogen jets are presented. After a brief introduction of the DRACO laser system, it will be demonstrated how optical probing of cylindrical jets can be used to characterize the laser contrast on target. This technique allows to exclude any pre-plasma expansion earlier than one picosecond prior to the main pulse arrival for plasma mirror cleaned contrast conditions (section 4.1). In figure 4.1, the results of the proton acceleration experiments are summarized and compared to those achieved with foil targets. The first part (section 4.4) focuses on experiments performed with a thin sheet jet of foil-like geometry and plasma mirror cleaned pulses. Based on the results obtained at the 150 TW arm of DRACO, the planar geometry is interesting due to the large jet width which enables a high hit probability and thus stable proton acceleration with energies of up to 34 MeV (filled blue square in figure 4.1). Although neither the sheet thickness nor the laser pulse shape was optimized so far, the acceleration performance is already comparable to that of foil targets irradiated under the same conditions.

Since the planar jet was found to be too thin for optimal performance and thicker hydrogen sheets were not yet available for implementation in a laser-plasma experiment, a cylindrical jet with 5 μm in diameter was utilized to study the performance of a thick hydrogen targets using the DRACO PW laser system. Proton acceleration from cylindrical jet targets is characterized by a higher shot-to-shot fluctuation and a more divergent emission due to the wire-like shape. However, the target has a more favorable radially symmetric geometry for optical probing. Therefore, cylindrical jets (section 4.5) were used to investigate the correlation of proton emission and plasma density evolution for different laser contrast conditions. While proton energies comparable to those of micrometer thick metal foils were found with plasma mirror cleaned contrast in the TNSA regime (compare filled blue circle and star markers in figure 4.1), the laser-plasma interaction at intrinsic laser contrast leads to much higher proton energies which were associated with a strong pre-expansion detected by optical probing.

In order to reproduce this increase in proton energies under controlled conditions, the influence of pre-expansion was investigated in the second part of the laser-plasma experiments. Based on plasma mirror enhanced laser contrast, which excludes any change of the target state before the last picosecond, the spatio-temporal target density distribution was manipulated by using an additionally introduced low intensity pre-pulse (section 4.6). This technique allows to study the acceleration performance in a plasma density scan over two orders of magnitude, ranging from overdense (30 $n_{c,800\mathrm{nm}}$) to underdense targets ($< n_{c,800\mathrm{nm}}$). Protons with kinetic energies of up to 80 MeV were detected when the core plasma densities were decreased to a few times $n_{c,800\mathrm{nm}}$. The interpretation of the experiments is assisted by realistic numerical simulations where the initial target configuration, characterized by optical probing, is applied as an input. The simulation results indicate that the target density sweep induces a transition between different acceleration mechanisms. TNSA prevails for unexpanded targets, while acceleration in the bulk dominates in an expanded near-critical density plasma. Magnetic vortex acceleration becomes the most efficient mechanism when the laser pulse penetrates the target.

4.1 The high-intensity laser system DRACO

The proton acceleration studies presented in this thesis were carried out at the high-power titanium:sapphire laser system DRACO (Dresden laser acceleration source) [203] which is located in the ELBE* center at the Helmholtz-Zentrum Dresden-Rossendorf (HZDR). This double CPA [1] laser system with a central wavelength of 800 nm and a pulse bandwidth of 60 nm is designed for either 45 J (Petawatt arm) or 6 J pulses (150 TW arm) individually compressed to a pulse duration of 30 fs (FWHM). The concept of the laser chain and the amplification stages is illustrated in figure 4.2. The principle of chirped pulse amplification is fundamental for the generation of high-intensity laser pulses and relies on temporal pulse stretching prior to the amplification in order to reduce the laser intensity below the

---

*Electron Linac for beams with high Brillance and low Emittance

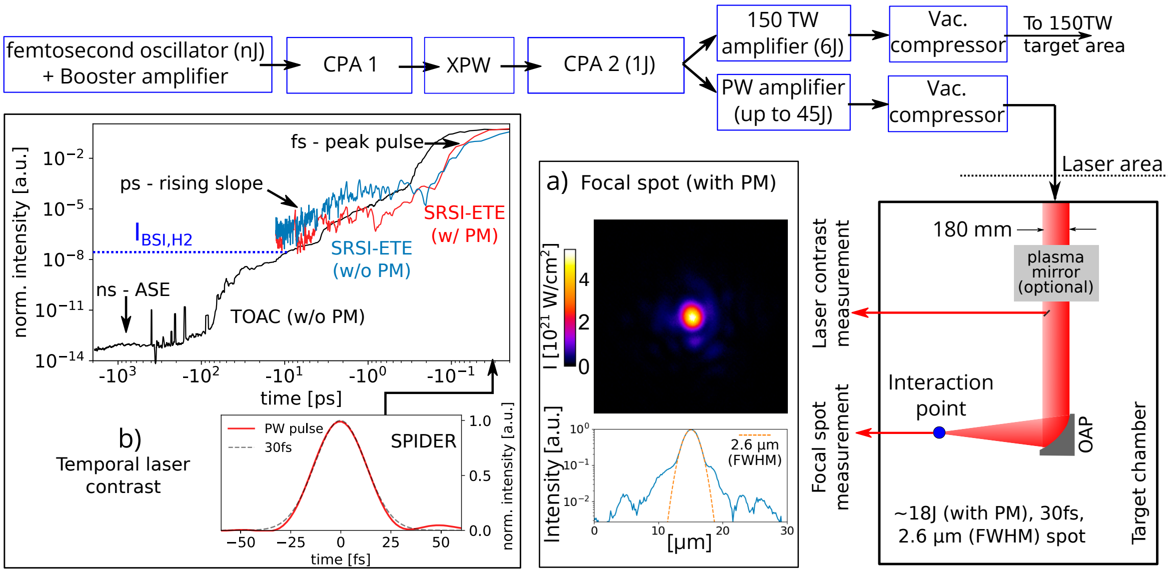
femtosecond oscillator (nJ)
+ Booster amplifier
CPA 1
XPW
CPA 2 (1J)
150 TW amplifier (6J)
Vac. compressor
To 150TW target area
PW amplifier (up to 45J)
Vac. compressor
Laser area
180 mm
plasma mirror (optional)
Laser contrast measurement
Interaction point
Focal spot measurement
OAP
Target chamber
~18J (with PM), 30fs,
2.6 µm (FWHM) spot
a) Focal spot (with PM)
I [10^{21} W/cm^2]
4
2
0
Intensity [a.u.]
10^0
10^{-1}
10^{-2}
2.6 µm (FWHM)
0
10
20
30
[µm]
norm. intensity [a.u.]
10^{-2}
10^{-5}
10^{-8}
10^{-11}
10^{-14}
fs - peak pulse
ps - rising slope
$I_{BSI,H2}$
SRSI-ETE (w/ PM)
SRSI-ETE (w/o PM)
ns - ASE
TOAC (w/o PM)
-10^3
-10^2
-10^1
-10^0
-10^{-1}
time [ps]
b)
Temporal laser contrast
PW pulse
30fs
SPIDER
1.0
0.5
0.0
norm. intensity [a.u.]
−50
−25
0
25
50
time [fs]

Figure 4.2: Sketch of the dual beam (150 TW/PW) laser chain of the DRACO system and the PW beam delivery to the laser ion target chamber. The pulse is generated in the front-end (oscillator and booster amplifier), amplified in a first CPA stage, cleaned in a XPW stage, further amplified in a second CPA stage and then distributed to the two final amplifiers with independent compressors. Focusing by an off-axis parabolic mirror to intensities on target of up to $5.6 \cdot 10^{21}$ W/cm^2 takes place in the target area. An additional plasma mirror (PM) device can be inserted for suppression of laser background radiation. a) An exemplary spatial laser intensity profile. At high intensities, the distribution agrees well with a Gaussian profile of 2.6,µm FWHM, as shown by the horizontal lineout below the image. b) shows the temporal laser intensity profile acquired from the SRSI-ETE and SPIDER measurements with and without the PM (see text for details). The black line shows smoothed measurements from a scanning TOAC to indicate the relative intensity level at earlier times.

damage threshold of the beamline optics and to prevent nonlinear effects. Temporal compression after the amplification stages provides the capability to reach ultra-high intensities at femtosecond pulse durations. The DRACO laser system features two CPA stages with a cross-polarized wave generation (XPW) [207] in between to improve the temporal laser contrast. XPW generation is a four-wave mixing process in an anisotropic crystal that has a cubic dependence on the intensity and thus results in suppression of low-intensity pulse parts. Splitting into the 150 TW and the PW arm is performed in the second CPA stage. The pulse is then amplified to a maximum energy of either 6 J or 45 J. Both beams are independently compressed to 30 fs and are delivered to separate target areas dedicated to proton or electron acceleration experiments using solid or underdense (gaseous) targets, respectively. The fact that the two independent amplifier beamlines contain the same pre-amplification enables e.g. pump-probe experiments with a laser-driven proton probe (proton radiography as in [208]) or laser cutting as it is demonstrated in section 3.6.2.

In the laser ion target area, the beamline is equipped with a recollimating single plasma mirror (PM) device just before the final focusing optics as a contrast cleaning tool. It can be added on-demand to study laser-matter interaction in the ultra-high contrast regime. The PM is an intensity-dependent filter in which laser light is mostly transmitted through a substrate, as long as the impinging intensity is below the ionization threshold. The surface turns into a plasma once the ionization threshold is exceeded and thus reflects the subsequent laser pulse. As a consequence, background radiation is suppressed by about two orders of magnitude up to the trigger point that typically occurs a few 100 fs before the peak of the laser pulse [209]. The plasma mirror device further protects the laser system from potentially destructive back reflections that could otherwise damage expensive optics. Throughout the rest of this thesis, the enhanced laser contrast achieved by using the plasma mirror device is referred to as *PM-cleaned contrast*, while the configuration without PM will be termed *intrinsic contrast*.

The laser pulse characterization is schematically shown for the PW arm in figure 4.2. The most relevant beam parameters for the laser-driven ion acceleration are the laser energy on target, the focal spot size and the temporal intensity profile, which includes the duration of the ultra-high intensity peak. The laser pulse energy is measured with a full aperture energy sensor in the laser area behind the final amplification stage and reaches 32-33 J* in the here presented experimental work. The range indicates the difference between experimental days. Losses during beam transport to the interaction point ($\sim 30\%$) result in an energy on target of about 23 J. Adding the plasma mirror device further reduces the energy on target to 18 J (80% reflectivity of the plasma mirror). Focusing the 180 mm diameter laser beam with an off-axis parabolic mirror of 400 mm focal length results in a micrometer-sized spot that is imaged on a CCD sensor by an aberration-corrected microscope objective and optimized by the usage of adaptive optics (e.g. deformable mirror). In order to prevent damage to the imaging arrangement, alignment and optimization are done with an attenuated laser beam. The intensity distribution of the focal spot is shown in figure 4.2a, yielding a peak intensity of $I_p = 4.2 \cdot 10^{21}\,\mathrm{W/cm^2}$ when applying the plasma mirror and $I_p = 5.6 \cdot 10^{21}\,\mathrm{W/cm^2}$ at intrinsic laser contrast. This assumes a pulse duration of 30 fs that can be verified on-shot with an in-vacuum 2nd-order autocorrelator. The spatial full width at half maximum (FWHM) value describes the focal spot size and is used in this thesis if not stated otherwise. From the lineout in figure 4.2a, a Gaussian distribution with a FWHM of 2.6 µm is found to characterize the central spot. About 30% of the pulse energy is contained within the FWHM that equals an average intensity of $I_{FWHM} = 3.4 \cdot 10^{21}\,\mathrm{W/cm^2}$ with PM and $I_{FWHM} = 4.4 \cdot 10^{21}\,\mathrm{W/cm^2}$ without.

For laser-driven ion acceleration the temporal intensity profile is one of the key characteristics of the pulse. While the ultra-high intensity peak covers only a temporal window of a few 10 fs, background radiation spans over several nanoseconds. This includes a ns-pedestal that is generated by incoherent amplified spontaneous emission and a rising main pulse edge. Additionally, distinct pre-pulses can originate from uncontrolled shortcuts of scattered light in the laser system or conversion of post-pulses into pre-pulses by non-linear processes associated with the accumulated B-integral in the laser chain [210]. The combination of all background radiation features acts on the initial cold target and results in a transition into an often unknown plasma state prior to the arrival of the main pulse. Figure 4.2b displays the temporal laser contrast of the DRACO PW arm determined with different devices and for different conditions (with and without plasma mirror). The laser contrast was studied by means of self-referenced spectral interferometry at extended time excursion (SRSI-ETE) [211]. This device features a temporal window of 18 ps with a resolution of 18 fs and an effective dynamic range of almost 10^7 in a single shot [202]. The recorded temporal intensity profile shows the central peak and an increasing slope on the picosecond level similar to the contrast measurements at the 150 TW arm, which can be found in [209]. Comparison of the PM-enhanced (red line in figure 4.2b) and intrinsic contrast (blue line) indicate a suppression by one to two orders of magnitude in intensity at around 1 ps prior to the main pulse. Limited by the dynamic range of the measurement device, differences between both contrast settings are not resolvable at earlier times. According to the measurements, it is expected that the intensity level for ionizing the target material was exceeded between 10 ps and 1 ps before the arrival of the main peak. This is exemplarily demonstrated by the barrier suppression ionization threshold of hydrogen (section 2.1.1) that is displayed as a blue line in figure 4.2b at a relative intensity level $\sim 3 \cdot 10^{-8}$ when assuming a peak intensity of $I_p = 5.6 \cdot 10^{21}\,\mathrm{W/cm^2}$. Additionally, on the nanosecond time scale amplified spontaneous emission (ASE) defines the background level, as indicated by the third order autocorrelator (TOAC) measurements (shown by the black line). Note that the TOAC signal was smoothed to indicate the relative intensity levels more clearly. As discussed by [202], the visible pre-pulse-like signatures between -500 ps and -100 ps can partially be identified as measurement artifacts. It should also be noted that the differences between TOAC and SRSI-ETE curves may be due to the different measuring methods. These differences are investigated in more detail in the thesis of T. Ziegler [212]. For completeness, a SPIDER* measurement of the main laser peak shows a profile that is well described by a Gaussian shape with 30 fs pulse duration (FWHM) (inset in figure 4.2b).

---

*The PW amplifier was not fully pumped causing the lower pulse energy in comparison to the design value of 45 J.

4.2 On-target laser contrast characterization using optical probing

The temporal evolution of the target under the action of the impinging laser pulse is a rather complex process because the interaction covers several orders of magnitude in laser intensity and time leading to several possible mechanisms of ionization (e.g. multi-photon ionization or barrier suppression ionization, see section 2.1.1) and of laser energy transfer into electrons (section 2.1.3). While laser contrast diagnostic tools allow to quantify the laser intensity level at a given point in time, deriving the accumulated effect of the temporal laser profile on-target is challenging. As will be briefly shown in the following, the hydrogen jet target can be used to characterize this accumulated effect. This is facilitated by the free-standing target arrangement that enables unrestricted optical probing from different angles and supported by the high repetition rate capability allowing to scan the temporal evolution with a large number of measurements. Moreover, the relative simple ionization dynamics of hydrogen enables estimations of the required intensity thresholds for a com-

---

*The technique *spectral phase interferometry for direct electric-field reconstruction* (SPIDER) measures the interference between a pair of replica of the input beam [213] and reconstructs the pulse.

parison with the temporal laser intensity profile.

The setup for on-shot characterization with a cylindrical hydrogen jet target is shown in figure 4.3a. It utilizes two optical probe beams (arranged as shown in the schematic) which are provided by a stand-alone probe laser system (pulse duration 160 fs) synchronized to the high-intensity laser with an accuracy of 50 fs. The setup is comparable to that used for the jet characterization described in section 3.3. In order to mitigate the effect of the disturbing plasma self emission [59] which often complicates the measurements, an off-harmonic central wavelength of 515 nm (frequency-doubled) in one probe arm and 1030 nm in the other arm were chosen. In comparison to the previously conducted 150 TW experiment [57], a new probe laser system was installed, achieving higher output energy. This allows a further suppression of the strong plasma self emission from the laser-target interaction. Imaging systems with a verified spatial resolution limit of 2 μm were implemented for on-shot target characterization. The high dynamic range imaging sensors were filtered by narrow interference filters blocking all wavelengths outside a 10 nm (FWHM) transmission window around the probe wavelength by several orders of magnitude. For details on the off-harmonic probe laser system including synchronization schemes and beam parameters, refer to [59, 214].

Figure 4.3b-e shows back-illuminated shadowgraphy images of 5 μm cylindrical jets measured with the 515 nm probe arm at different times before t_0, the arrival time of the peak intensity of the PW pulse. To allow comparability, only shots with central irradiation of the high-intensity beam, filtered by the target position, were selected for this study. While the target remains completely transparent at 1.1 ps before t_0, as indicated by the bright line along the jet center axis*, a first opaque region in the vicinity of the focal spot appears at 0.7 ps. This region grows when approaching t_0, as indicated by the horizontal white lines in figure 4.3c-e. The transition from transparency to opacity is caused by the ionization of the hydrogen jet, which generates an overdense plasma that cannot be penetrated by the probe beam anymore. Note that this does not necessarily require a fully ionized jet. A thin plasma layer on the surface with a thickness on the order of the skin depth (10-100 nm, refer to section 2.1.2) and a plasma density above the critical density (for the corresponding probe wavelength) is already sufficient to make the target opaque for the probe pulse. As a result, an ionized thin layer cannot be differentiated from a fully ionized target by means of optical probing.

When comparing the shadowgraphy images for laser shots with PM-cleaned and intrinsic contrast (in figure 4.3f), two major differences become apparent. Firstly, a much stronger plasma self-emission is present in the intrinsic contrast case which saturates the imaging CCD in the central part. Similar to the observation during experiments at the 150 TW arm [59], the overexposure is due to plasma self-emission at the same wavelength as the probe pulse but can be substantially mitigated by applying the PM configuration. Secondly, the diameter of the opaque region, which will be called *shadow diameter* throughout this chapter, is strongly expanded in figure 4.3f to about 15 μm or about three times the initial jet size indicating vastly different target conditions at the arrival of the peak intensity. The on-

---

*The bright line represents a line focus which is caused by the refraction of the back-illumination in the cylindrical jet.

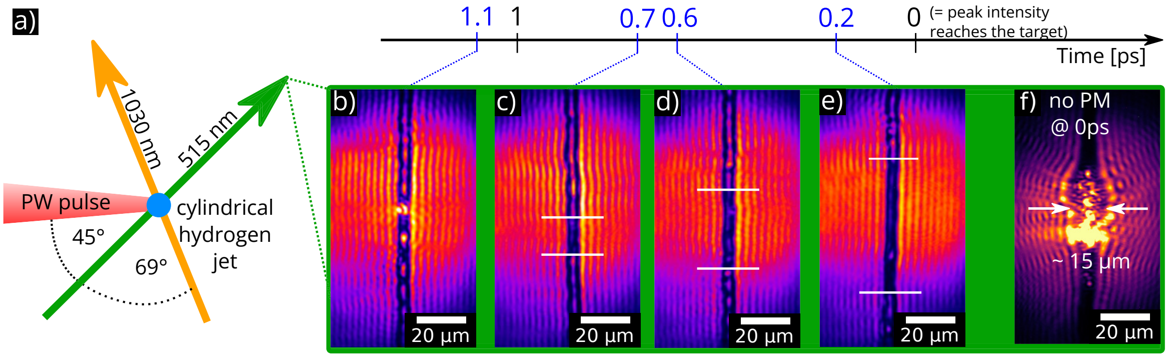

Figure 4.3: On-shot probing of a 5 µm cylindrical hydrogen jet with a 515 nm beam at different time delays with respect to the arrival of the plasma mirror cleaned high-intensity laser pulse. a) Experimental arrangements. b-e) Optical probe images from 1.1 ps–0.2 ps prior to the arrival of the peak intensity indicating the transition from a transparent to an opaque target. The white lines in c-e) indicate the extension of the opaque region. f) shows for comparison, a shot without plasma mirror at 0 ps.

shot probing images thus illustrate the much cleaner conditions when utilizing the PM to improve the temporal laser contrast. In this case, an expansion prior to the arrival of the peak intensity is limited to the level below the resolution of the optical probing and the high-intensity pulse therefore interacts with a practically unchanged plasma density distribution. In the course of this chapter, the defined target conditions with the PM-cleaned contrast provide a realistic input for simulation studies and are the basis for an intentional manipulation of the density profile by an introduced pre-pulse (section 4.6).

Since with PM-cleaned contrast the threshold for darkening was exceeded on-target at about 0.7 ps before t_0, an intensity on the order of the barrier-suppression ionization intensity would be expected, which is given for hydrogen by $1.37 \cdot 10^{14}$ W/cm^2 according to equation 2.3. However, based on the SRSI-ETE measurement in figure 4.2b, this intensity threshold is exceeded a few picoseconds earlier. Additionally, at 0.7 ps before t_0 intensities on the order of $10^{-6}\, I_{max} \approx 4.2 \cdot 10^{15}$ W/cm^2 are already reached. The reasons for the disagreement of probing data and the SRSI-ETE measurements are related to several aspects that go beyond the scope of this work and will be discussed as part of other theses by S. Assenbaum [201], C. Bernert [215] and T. Ziegler [212]. Preliminary results indicate that with a cylindrical jet target, early stages of ionization cannot be resolved very well. This can be significantly improved if sheet jets with a planar geometry are used. The first visible effect of ionization then already appear about 2 ps before t_0. To understand the accumulated effect of laser intensity on the target, it is also necessary to determine the pulse duration dependent intensity required for ionization. While for 30 fs pulses (i.e. laser pre-pulses) the intensity threshold is well described by barrier suppression ionization, for pulses of several picoseconds duration (i.e. the main pulse edge) the required intensities are about two orders of magnitude lower. Furthermore, to compare the ionization threshold of hydrogen with absolute laser intensity levels, the different contrast measurement techniques have to be considered and compared. Nevertheless, this study demonstrates the capability of on-shot optical probing of jet targets that can complement the typical laser contrast metrology.

4.3 Setup of particle and optical diagnostics

For the laser-proton acceleration studies presented in this chapter, the experimental arrangements consisting of optical and particle diagnostics are sketched in figure 4.4. The setup is based on the earlier cryogenic jet experiments at the 150 TW arm of DRACO and marks the ongoing improvement in particular with respect to the target implementation (damage protection of the nozzle with the chopper system and vacuum infrastructure improvements, see section 3.4 and 3.2) and the optical probe laser system to cope with the challenges imposed by the increased laser input energy. The in-vacuum cryogenic source, introduced in the last chapter, injects a continuous liquid jet into the vacuum chamber, which freezes due to evaporation cooling and thereby forms the solid target. Cylindrical and planar jet geometries were generated by applying nozzles with a 5 μm circular hole or a 2x20 μm^2 tapered slit aperture, respectively. The cryogenic source is completely integrated and can be positioned with respect to the laser focus using XYZ-translation stages. Using the optical probe beams to image the target (see section 4.2), the hydrogen jet can then be precisely aligned in terms of position and rotation. Inset (a) in figure 4.4 shows shadowgrams for jets generated by the cylindrical (left) and the planar aperture (right). The employed hydrogen sheet is characterized by a width of about 50 μm and a thickness of 200 nm±100 nm that was measured by the same method as described in section 3.3 using interferometry implemented in the 515 nm probe arm.

The detector system for accelerated particles consists of two Thomson parabola spectrometers (TPS), which allow online measurements of proton spectra. One TPS is aligned to the drive laser axis and the other is placed at a 45° angle. At the entrance of the TPS, protons are spatially filtered by a pinhole of 1 mm diameter that covers a solid angle of about 1 μsr. Afterwards, protons are deflected in the horizontal plane by a magnetic field (930 mT, 200 mm length) and in the vertical direction by an adjustable electric field. The latter is usually required to separate the traces of different ion species. However, due to the single-species target content in this experiment, the electric field is only used for a few shots to verify the acceleration of a pure proton beam. After a drift distance of 53 mm (behind the end of the magnetic field), the particle tracks are detected by a microchannel plate, which is equipped with a phosphor screen on the rear side. The screen is then imaged using a CCD camera. The TPS is sensitive to protons with energies above 4 MeV (limited by the size of the MCP). The energy resolution ΔE is dominantly defined by the projected size of the pinhole on the MCP. For e.g. 10 MeV protons, ΔE amounts to $\pm 2\,\%$ and increases to $\Delta E = \pm 4.5\,\%$ at 80 MeV. The analysis of the proton tracks includes a relativistic correction because the associated increase in proton mass (e.g. about $\gamma = 1.085$ for 80 MeV) leads to a systematic error of up to 20% in kinetic energy if relativistic effects are not considered. The deflection of particles in the electric and magnetic field was simulated using the software package COMSOL multiphysics. This serves as the input for the processing of the raw data into particle spectra. A high accuracy of the deduced particle energy is accomplished

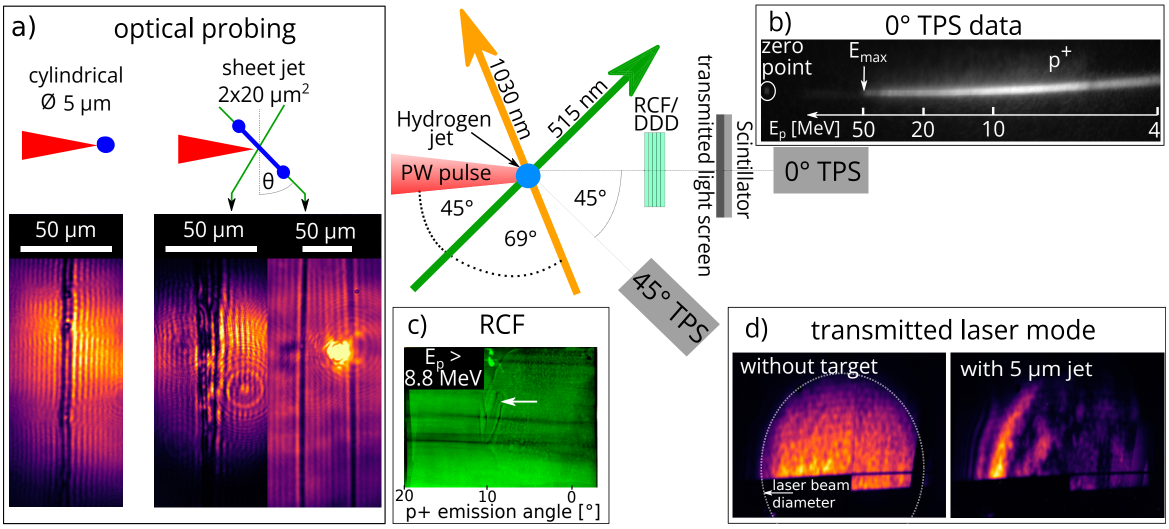
a) optical probing
cylindrical
Ø 5 µm
sheet jet
2x20 µm²
θ
50 µm
50 µm
50 µm
1030 nm
515 nm
Hydrogen jet
PW pulse
45°
69°
45°
RCF/
DDD
transmitted light screen
Scintillator
0° TPS
45° TPS
b) 0° TPS data
zero point
E_max
p+
E_p [MeV] 50 20 10 4
c) RCF
E_p > 8.8 MeV
20 10 0
p+ emission angle [°]
d) transmitted laser mode
without target
with 5 µm jet
laser beam diameter

Figure 4.4: A sketch of the experimental setup illustrating the arrangement of the optical and particle diagnostics. Insets show exemplary diagnostics results: a) On-shot optical probing images of a cylindrical jet (left) and a sheet jet (right). Note that the spatial scale differs for the shadowgrams. b) TPS raw image in laser forward direction indicating a single proton trace with a maximum proton energy $E_{p,max}$ of about 50 MeV. c) A RCF (radio-chromic film) recorded for a laser shot on a cylindrical jet. Protons below 8.8 MeV were stopped in layers prior to this film. The white arrow points towards the imprint in the proton beam profile caused by a pick-off mirror in the laser beamline. d) Transmitted light distribution captured 45 cm behind the interaction for a shot without target and one with a 5 µm cylindrical jet.

by benchmarking the particle-tracing simulations in an experimental campaign at a conventional accelerator [216] with an energy and charge calibrated beam. Figure 4.4b shows a TPS raw image detected for a high power laser shot onto a cylindrical hydrogen jet target. The single trace demonstrates the acceleration of a pure proton beam with a maximum energy of about 50 MeV. The hydrogen target content simplifies the analysis of the images significantly since an overlap of the traces from different particles, as it is typical for the case of multi-species targets, is intrinsically prevented.

Radio-chromic film (RCF) stacks were placed on a single shot basis 12 cm behind the target in laser propagation direction to diagnose the proton numbers and beam profiles. The stacks consist of several absolute dose-calibrated GafChromic EBT3 [217] layers with metal sheets as absorbers in between. Since protons are stopped in different layers, depending on their initial energy, an absolute spectrum can be reconstructed. Figure 4.4c pictures an example film that is sensitive to protons with energies above 8.8 MeV showing two typical features in the proton beam profile of an irradiated cylindrical hydrogen jet. First, the beam profile reveals stripes originating from the isotropic proton emission in the horizontal plane (perpendicular to the jet extrusion direction). This beam characteristic is due to the curved jet surface [57] and resembles that obtained from wire targets [56, 218, 82]. Second, small-scale modulations and the imprint of a pickoff mirror (white arrow), that is positioned in the collimated laser beam before the final focusing, are visible. These structures are imprinted on the proton beam by the laser light that propagates around the jet and that causes the formation of quasi-static electric fields in the beam path by ionization of the residual gas [58].

Unfortunately, measurements with RCFs could only be obtained for a few shots because the number of available stacks was limited during one day of experiments (typically less than 10). To account for this, two online scintillator-based detectors were used to record information about the beam profile on all other shots. A depth dose detector (DDD) was positioned slightly below the main laser axis for resolving a horizontal cross section of the angular proton depth dose profile. The measurements are evaluated in the context of the directionality of the proton beam in section 4.6. Moreover, a second scintillator that detects the proton beam profile similar to an RCF was placed 45 cm behind the target. The scintillator detects protons with energies above 12 MeV and was imaged by an in-vacuum camera, similar to the device described in [219]. A 1 mm thick glass ceramic plate, made of MACOR, stacked in front of the scintillator further captured the transmitted laser beam mode and was imaged by a filtered CCD with either an 800 nm (40 nm FWHM) bandpass filter or a longpass filter with a cut-on wavelength of 645 nm (RG645 Schott). Based on the integrated camera signal, the fraction of transmitted light of the main laser wavelength can be determined. Transmission is caused either by transparency in the case of the thin planar sheet or by a part of the laser pulse that propagates around the cylindrical jet without interacting.

Before presenting the measurements from the DRACO PW laser, the proton performance results from the preceding experimental study at the 150 TW arm of DRACO [57] will be briefly summarized. Irradiating the cryogenic jet targets resulted in proton energies of up to 20 MeV for intrinsic as well as PM-cleaned contrast. The obtained maximum proton energies were comparable for different geometries (cylindrical and planar) and similar to metal foils while TNSA was identified to be the dominant acceleration mechanism. When comparing the proton numbers, it was found that the particle emission per solid angle from the planar jet was about 3.5 times higher than for the cylindrical jet and comparable to the proton flux from 2 μm thick titanium foils. While the wire-like jet emits protons almost isotropically in the horizontal plane, a better collimated component in target normal direction is observed for the planar targets. Furthermore, the planar shape is more favorable due to the wider jet since it has a lower sensitivity to the positioning jitter and thus leads to higher shot-to-shot stability of the accelerated proton beam.
The novel targetry developments introduced within this work, e.g. the mechanical chopper (section 3.6.2), now enable systematic studies in the PW regime in particular for the more sensitive planar slit apertures. During the course of the experimental campaign, more than 1500 laser pulses of different intensities were focused on cryogenic jets. Cylindrical and planar jets are characterized by their performance in terms of proton acceleration and will be compared to foil targets. The following analysis focuses mainly on the maximum proton energies as a characteristic parameter based on which the influence of different target shapes and laser contrast conditions is investigated to identify regimes with the best performance.

4.4 Proton acceleration in the transparency regime using sheet jets

A sheet-like hydrogen jet was chosen as the first target shape to study the laser-plasma interaction in the PW regime. Based on the results obtained at the 150 TW arm of DRACO, the combination of higher hit rates and higher proton numbers renders the planar jet the more favorable geometry for potential applications. For the investigations at the PW arm of DRACO a significantly wider jet of 50 μm was chosen to further improve the shot-to-shot stability. The resulting reduction in jet thickness to about 200 nm (c.f. the tapered slit aperture in section 3.5) is additionally interesting to study acceleration mechanisms proposed for thin targets (like RIT, RPA). To prevent the thin sheet from being strongly expanded even before the actual main pulse, the jets were irradiated with PM-cleaned contrast conditions. In this section, the acceleration performance from this planar jet is investigated and compared to that of plastic foil targets.

Figure 4.5a displays the maximum proton energies detected in laser forward direction and in 45° as a function of the orientation angle θ of the planar jet*. For example, $\theta = 0°$ describes the laser incidence along the target normal direction as it is shown schematically in the lower part of figure 4.5a. The sheet was rotated by manipulating the operation parameters of the cryogenic system (e.g. backing pressure and source temperature) as described in chapter 3.5. Due to the fluctuation in the orientation of the planar jet, on-shot values of θ were calculated from the sheet width in the simultaneously acquired probe images with an accuracy of about $\pm 5°$. To ensure comparable amounts of deposited laser energies in figure 4.5a, the shots were filtered by the laser-target overlap. For this purpose, a fixed position was assumed for the laser focus and the jet position was determined from the probing images. All shots where the laser spot (2.6 μm FWHM) was not fully covered by the sheet were excluded. However, since the 50 μm width of the jet is several times larger than the 5 μm spatial jitter (see section 3.6.1), only a few shots at high θ had to be excluded.

Protons with the highest energy were detected when the target normal direction of the sheet was aligned with the corresponding TPS axis. For example, protons with highest $E_{p,max}$ were detected in the 0° TPS for normal laser incidence ($\theta \approx 0°$). Similarly, $\theta \approx 45°$ yielded proton energies of up to 30 MeV measured in the 45° TPS. However, maximum proton energies between 10 MeV and 20 MeV were detected in laser forward direction for the same $\theta \approx 45°$ orientation. The cause for the still strong proton emission in laser forward direction is likely explained by the isotropic emission that originates from the cylindrical edges of the sheet. Using PIC simulations, this effect was already shown in figure 5 in the publication by Obst et al. [57]. This explanation is further confirmed by the $E_{p,max}$ measurements for orientation angles at about 70°, where the maximum proton energy becomes comparable in laser forward direction and in 45°. The isotropic emission from the edges superimposes the proton acceleration signature and thus complicates conclusions about the emission originating from the planar part of the jet. An even wider sheet could reduce the emission from the rims sufficiently. Nevertheless, this shows that planar jets can be

---

*θ describes the orientation angle in the horizontal plane, as shown in figure 4.4a

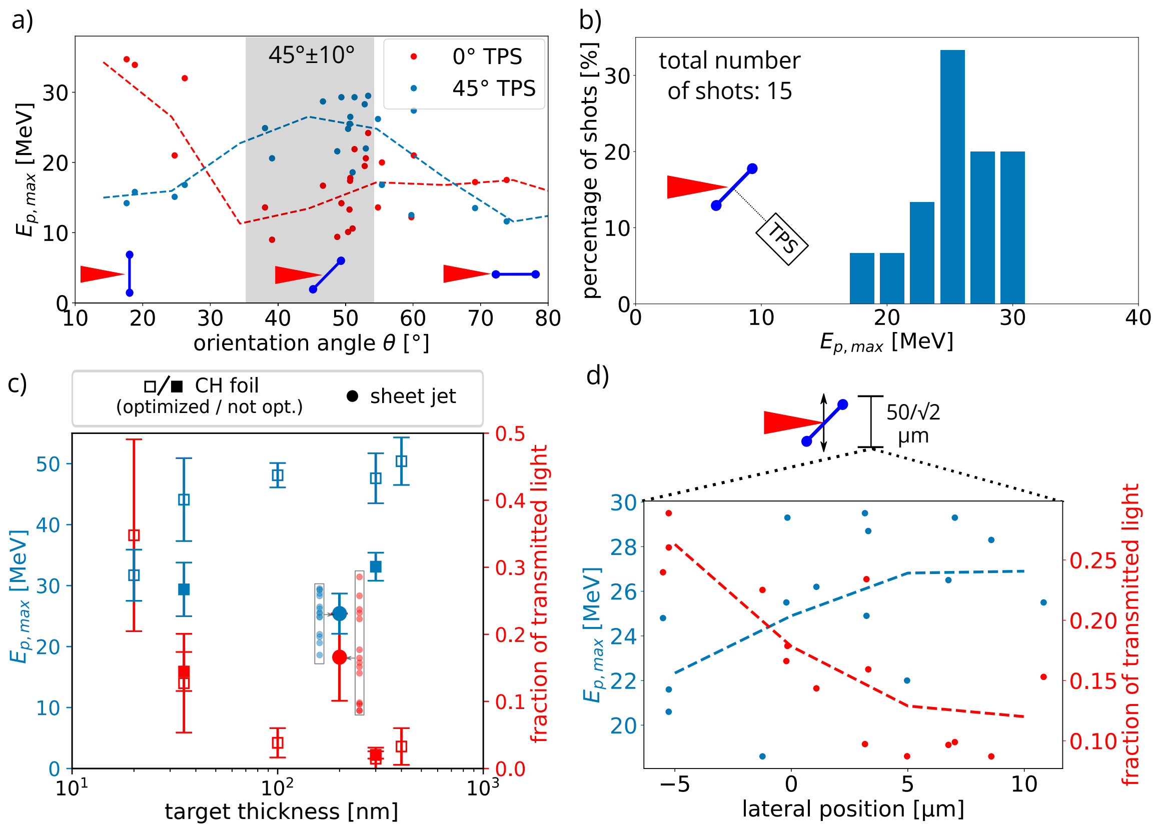

Figure 4.5: Proton acceleration performance obtained from a 50 µm wide and 200±100 nm thin planar hydrogen jet that was irradiated by an 18 J laser pulse with PM-cleaned contrast. a) Maximum proton energies $E_{p,max}$ detected in laser forward direction (red) and under 45° (blue) for different orientation angles θ of the planar jet (see pictogram in the lower part). Each dot indicates a single shot while lines show the average (in a 5° bin) as a guide for the eye. The measurement uncertainty of the orientation angle is 5° for each data point. The subset with $\theta = 45° \pm 10°$ (gray shaded area) is used for the other plots. b) The distribution of $E_{p,max}$ as measured in the 45° TPS for this subset (15 shots). c) $E_{p,max}$ and fraction of transmitted light measured for shots with the sheet jet and in comparison with plastic (formvar) targets of different thicknesses. Markers display the average of 5-20 shots. The error bars represent the standard deviation as an indication for the shot-to-shot fluctuation. Uncertainties in thickness are about 10% for the plastic targets. Filled squares represent shots with an optimized pulse shape while empty squares show shots obtained for a Fourier transform limited pulse (see text for details). d) $E_{p,max}$ and fraction of transmitted light as a function of the lateral target position. The zero position indicates the jet center. Dots are single measurements and lines indicate the average values within a 5 µm bin as a guide for the eye.

operated reliably at a PW laser system for a large number of shots and the direction of the proton beams can be adjusted by rotating the sheet.

However, the maximum proton energies (up to 34 MeV) are not yet fully optimized. To identify possible scenarios for improvement, the performance of the proton acceleration from the thin planar hydrogen jet is being evaluated. A key factor in the behavior of thin targets under the influence of intense laser pulses is the onset of transparency during the interaction. The reason for this is that heating the target causes an expansion and thus a decrease of the core density, which in turn renders the plasma (relativistically) transparent for the laser pulse (see section 2.2 and 2.1.2). If the onset of transparency occurs at the moment when the peak intensity of the pulse reaches the target, an increase in proton energies is expected [108]. An earlier onset, on the other hand, is often detrimental for proton acceleration. However, since this point in time is not accessible in experiments with the often time-integrating diagnostics, a scan of different target thicknesses is carried out, as shown by e.g. Poole et al. [96] or in the thesis of L. Obst [206]. A significant transmission value thereby provides an indication that the target becomes transparent during the interaction. Crucial for the target thickness at which the transparency occurs during the interaction are the laser contrast conditions. With a high-contrast laser pulse, transmission of laser light can only be detected for thin foil targets (e.g. < 40 nm in [96]). Such targets are subject to the onset of relativistic induced transparency (RIT, refer to section 2.2). The laser light can thereby penetrate the target bulk and thus interact volumetrically. In the context of TNSA, this can lead to an increase in proton energies. This enhancement in acceleration performance is one of the reasons for using targets of a few tens of nanometers thickness. To determine the best performance for the hydrogen jet using a thickness scan, various slit aperture dimensions would be required. However, in particular larger apertures could not be used at the time of the measurements due to the vacuum limitations (see section 3.6). In order to evaluate the performance of the hydrogen jet nevertheless, a comparison is carried out with plastic (formvar) foils of different thicknesses. For these foils it was found that the highest proton energies are not achieved for the best compressed laser pulse (referred to as *Fourier transform limited pulse shape*), but by manipulating the temporal shape of the laser pulse (referred to as *optimized pulse shape*) through the spectral phase terms group velocity dispersion and third order dispersion [202]. The underlying mechanism that causes the increase in maximum proton energies by a factor of almost two is currently under investigation and part of another thesis prepared by T. Ziegler [212].

In the following, the proton emission from the hydrogen jet is compared to that of plastic foil targets. To achieve equivalent laser pulse conditions, the foils were irradiated with a laser incidence angle of 45° and in the case of the hydrogen sheet only shots with θ between 35° and 55° were used (gray shaded area in figure 4.5a)*. Furthermore, only the maximum proton energies measured with the 45° TPS (target normal direction) are evaluated for this comparison. The distribution of maximum proton energies measured with the sheet jet for $\theta = 35^\circ - 55^\circ$ (15 shots in total) is shown in figure 4.5b. The average $E_{p,max}$ for this subset is 25 MeV, with single shots ranging from 18 MeV to 30 MeV†.

Figure 4.5c compares the target normal performance in terms of maximum proton energy of sheet jets to plastic foils made from formvar. The foil thickness was varied from 20 nm to about 400 nm. Since the pulse shape optimization was not yet applied to the hydrogen jet, both contrast settings are shown for formvar to give a comprehensive picture. Filled squares represent the Fourier transform limited pulse shape configuration that was also applied to the planar jet. The open squares show the optimized pulse shape. The formvar foil data points are taken from [202]. Additionally, the integrated transmitted light signal was measured, which provides an indication whether the target becomes transparent during the interaction. The absolute transmission value should be treated with caution since the bandpass filter (central wavelength 800 nm with a 40 nm FWHM) limits the detectable wavelength range. This adds a systematic error due to potential spectral broadening during the transmission of the laser pulse through the plasma [206]. However, general tendencies are representative.

---

*Note that ± 10° is a realistic assumption for the stability of the jet orientation (see section 3.6.1).

†Compared to previous results [57] at the 150 TW arm of DRACO, the stability of the maximum proton energies from a planar jet is further improved due to the wider jet target and therefore lower shot-to-shot fluctuation in laser target overlap.

Considering first the formvar foils with optimized pulse shape, thick targets ($\geq$ 100 nm) show only low laser light transmission (< 5%), whereby maximum proton energies are approximately constant with respect to the thickness. For thin formvar foils (<100 nm) on the other hand, an increase in transmitted light was observed and for the thinnest foil of 20 nm even a reduction of $E_{p,max}$ compared to thick films was measured. In the case of the Fourier transform limited pulse shape, fractions of transmitted light are comparable to the optimal pulse shape, while maximum proton energies are significantly lower. The 200 nm thick hydrogen sheet jet performs in terms of maximum proton energies slightly worse than the formvar foils irradiated with the Fourier transform limited pulse (filled squares). Concerning the transmitted light, however, a significant transmission is measured for the jet, which in the case of plastic foils is only achieved at a much lower thickness.

The large amount of transmitted light (either for <100 nm foils or the hydrogen sheet) indicates the onset of transparency during the interaction since other contributions to the transmitted light signal can only account for a small portion. Examples of these contributions are the laser background radiation that penetrates the initial transparent target before ionization occurs, light passing around the hydrogen sheet (less than 2% is estimated from focal spot measurements in figure 4.2a) and classical transparency via a penetrating evanescent wave. For the latter, a significant contribution would only be expected for thicknesses near the characteristic skin depth (25 nm for hydrogen and 8.5 nm for formvar). For foils, a significant transmission value for thicknesses < 100 nm suggest that the target becomes partly transparent during the interaction. At these thicknesses, the maximum proton energies (see figure 4.5c) already decrease slightly compared to thicker foils. It can thus be assumed that under the experimental conditions the onset of transparency occurs for targets that are too thick to achieve an increase in proton performance due to RIT. To examine at which target thicknesses the onset of RIT is actually expected, four models are considered (see table 4.1). These models are (1) the relativistic skin depth, (2) the onset of relativistic induced transparency according to Vshivkov et al., (3) the best proton performance deduced from multi-parametric PIC-simulations by Esirkepov et al. [32] and (4) the analytic model for the best proton performance described by Mishra et al. [35]. Refer to section 2.2 for a more detailed introduction of each model. The relevant thickness for plastic foils is in the range of a few 10 nm. However, shots on the 35 nm thick foil, which best matches this thickness range, show no improvement in performance. Instead, it even shows a slight reduction of the maximum proton energies, which is probably explained by the onset of transparency being too early.

The aim now is to determine to which foil thickness the jet behaves equivalently. Based on the transmitted light measurements, it can be assumed that the jet already becomes partly transparent and thus behaves similar to a 20-35 nm thick foil. According to the table 4.1, the

Model/Criteria	Thickness [nm] for 45° laser incident	
	Formvar foil	Hydrogen jet
Relativistic skin depth (section 2.1.2)	31	91
Vshivkov et al. [36] (equation 2.15)	<28	<222
Esirkepov et al. [32] (equation 2.17)	42	353
Mishra et al. [35] (equation 2.16)	86	672

Table 4.1: Target thicknesses of formvar foils and hydrogen jets that fulfill the different criteria for the onset of relativistic induced transparency. For the calculations a laser intensity of $a_0 = 37$, a wavelength of 800 nm and plasma densities of 30 $n_{c,800\mathrm{nm}}$ for the hydrogen jet and 235 $n_{c,800\mathrm{nm}}$ for the formvar foil were used. Note that for the calculations in this table, the 45° laser incident angle was taken into account for both a_0 and the projected thickness.

relevant thickness for the onset of RIT for the hydrogen jet is between 90 nm and 670 nm and therefore significantly higher than the thickness value for the plastic foil. The reason for this is the lower density of hydrogen ($30n_{c,800nm}$) compared to formvar ($235n_{c,800nm}$). Apart from the relativistic skin depth, the other three models actually specify an areal density for a given laser pulse. As such, the equivalent thickness of the low-density hydrogen jet is $n_{CH}/n_{H2} = 235n_c/30n_c \approx 7.8$ times the thickness of the formvar foil. This means that the 200 nm thick hydrogen jet should behave comparable to a 25 nm thick foil, which is in good agreement with the estimation based on the transmitted light. However, based on the results for formvar, this also means that the jet probably becomes transparent too early and one might expect higher $E_{p,max}$ for a thicker sheet.

Although no direct thickness scan was performed with the hydrogen sheet, the change in thickness along the lateral jet position (see section 3.5) can be exploited. This is the case because the planar sheet is in general not homogeneous due to small dents and spikes in the nozzle aperture. Figure 4.5d shows the 15 shots on the hydrogen sheet sorted by their on-shot lateral position. This shows a dependence of the maximum proton energies and transmission values on the lateral position. The higher average maximum proton energy and lower transmitted light at a lateral position between 5 to 10 µm is likely associated with a thicker region while a thinner part of the sheet can explain the lower $E_{p,max}$ and higher transparency at a position of -5 µm. However, because the probing setup was optimized for on-shot operation, the capabilities of target characterization were limited and thus the actual thickness profile of the sheet jet could not be measured. Regardless, the results from figure 4.5d provide further evidence that the hydrogen sheet becomes transparent too early, worsening proton acceleration, and that better performance in terms of maximum proton energy is expected for thicker jets.

In summary, the planar jet was successfully utilized for a large number of shots (> 100) to generate proton beams at a petawatt laser system. With the sheet target, which provides high repetition rate and debris-free operation, the same performance was achieved (in terms of maximum energy and shot-to-shot stability) as with foil targets under comparable laser conditions. Based on the improvements in proton acceleration for plastic foils, it can be assumed that for planar jets a significant increase in maximum proton energies is likewise possible by a similar optimization of the laser pulse shape [202]. Additionally, a thicker jet (about 0.5 µm) could improve the proton acceleration performance. Whereby the optimum can be achieved by thickness scans, e.g. by varying the operation parameters of the target system in future studies.

4.5 Cylindrical jets at different laser contrast conditions

Besides the usage of thin sheets, the main interest in the hydrogen jet is motivated by its low solid density, which facilitates the investigations of different acceleration mechanisms in the near-critical density regime. Since the 200 nm thick planar jet becomes already transparent under PM-cleaned contrast conditions, significantly thicker targets are more suited to study different laser contrast conditions. As thick and wide sheet jets were not available during the laser-plasma experiments in this thesis (mainly due to vacuum restrictions), cylindrical jets with 5 µm diameter were used to investigate the effect of different target density distributions.

Contrary to the planar geometry, a typical spatial stability of the cylindrical jet at 10 mm below the nozzle of about 5 µm, as derived from the characterization in section 3.6.1, is comparable to the target diameter. This leads to significant shot-to-shot fluctuation due to the non-perfect overlap of the laser focus spot and the target. Maximum proton energies for high-intensity laser shots are therefore distributed over a wide energy range, which is exemplarily shown in figure 4.6a. The jitter parallel to the propagation of the drive laser has a negligible effect for laser-proton acceleration since it is well within the $\sim$ 20 µm Rayleigh length of the laser focus. However, as expected a strong influence on the maximum proton energies is observed for the lateral jitter (displayed in figure 4.6b). The best performance was obtained for central hits, while in general a larger distance to the central position is associated with lower maximum proton energies caused by the reduced overlap. Although the focal spot size is only 2.6 µm, $E_{p,max}$ of several MeV can still be measured for shots with a lateral distance of 10 µm. This can be explained by the spatial distribution of the focal spot from figure 4.2a indicating that about 10 µm away from the central peak the intensity level still amounts to around 10^{19} – 10^{20} W/cm^2 which is sufficient to accelerate protons to energies of a few MeV. Although the spatial jitter leads to strong shot-to-shot fluctuations, for at least 90% of the interactions with the cylindrical jet protons with energies above 4 MeV, the lower energy threshold of the TPS, were detected. This marks a significant improvement of the hit probability in comparison to the 150 TW campaign, where only about 50% of the total shots resulted in a detectable proton signal, and can be directly attributed to the reduction in distance to the nozzle made possible by the implementation of the new chopper device (section 3.4).

Simultaneously transmitted light measurements (figure 4.6b) on a screen behind the target in laser forward direction show a clear dependence on the lateral jet position as well. Shots at a large lateral distance lead to a small laser target overlap and thus to a higher amount of transmission. A good overlap, on the other hand, blocks a large fraction of the laser beam. Example images for both cases are shown in figure 4.4d. As a consequence, transmitted light measurements can serve as a criterion for laser target overlap in particular when on-shot position determination with the probe beam is not possible e.g. due to

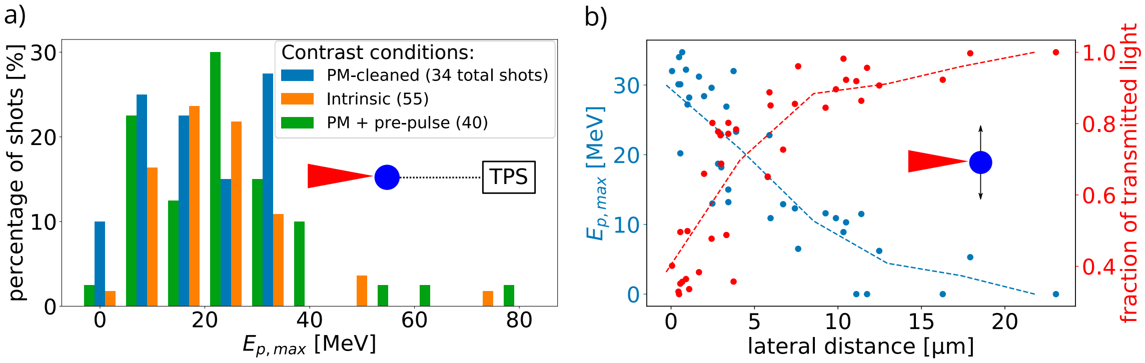

Figure 4.6: a) Maximum proton energy distribution in laser forward direction for shots 10 mm below the aperture and for different laser contrast conditions: Intrinsic laser contrast (23 J on target, 55 total shots), PM-cleaned contrast (18 J on target, 34 shots) and PM-cleaned contrast with an additionally introduced pre-pulse (18 J on target, 40 shots, section 4.6 for details). b) Maximum proton energy and fraction of transmitted light compared to the lateral position of the jet for PM cleaned shots on target with 18 J. A lateral distance of 0 μm corresponds to the best laser and target overlap. Dashed lines indicate the trend as a guide for the eye.

strong self emission. Contrary to the planar jet, light penetrating the bulk by relativistic induced transparency is assumed to be negligible due to a thickness of several micrometers. This is further supported by the fact that the lowest detected fraction of transmitted light (for the best laser target overlap) of about 30% roughly matches the 25% of laser energy which is obtained by integrating the focal spot image (figure 4.2a) when assuming the 5 μm jet would cover the central region as a vertical bar.

Despite the inherent fluctuations in maximum proton energies, the influence of different laser contrast settings can be studied by analyzing the best performing shots. For this purpose, figure 4.7 shows for two shots with different laser contrast configurations the proton spectra in addition to the maximum proton energies. For comparison, proton spectra of two shots on foil targets are shown as well. In order to ensure comparable conditions (similar peak intensities) for the two types of targets, protons were detected in laser forward direction and the foil targets were shot under normal incidence. Proton numbers from irradiated foils were deduced from calibrated RCF stacks, displayed by the filled circles in figure 4.7. Recorded TPS spectra, displayed as solid lines, were scaled to match the number of particles from the RCFs. Since RCF and TPS measurements could not be obtained for the same shot for the case of the cryogenic jet, a more complex method based on the calibration of the MCP signal was used to obtain absolute proton spectra. This method is described in appendix A.

For the plasma mirror cleaned configuration, the highest recorded $E_{p,max}$ amounts to 38 MeV and is therefore similar to shots on 2 μm thick titanium foil with cut-off energies of up to 42 MeV, as it is shown in figure 4.1. For a comparison of particle numbers in figure 4.7 shots with similar cut-off energies were chosen. Since both targets are a few micrometers thick and proton spectra are characterized by an exponential shape, the dominant acceleration mechanism is supposed to be TNSA (section 2.1). Particle numbers from the cryogenic jet are on average about 2-3 times lower than those of foils. This result is comparable to the factor of 3.5 that was found in the campaign at the 150 TW arm [57]. The lower proton

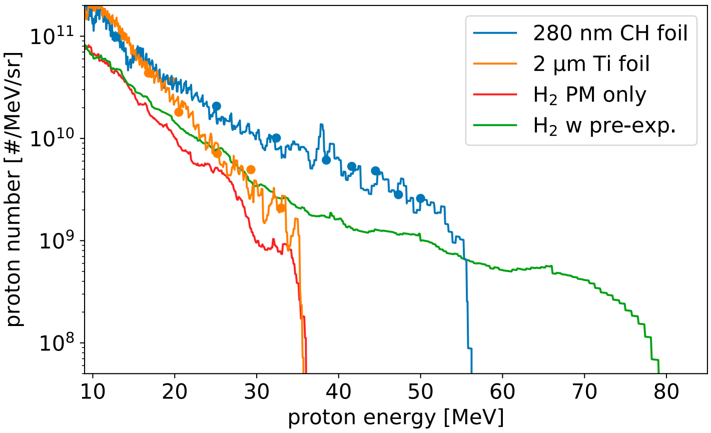

Figure 4.7: Measured absolute proton spectra from a 2 µm titanium foil (orange line), a 5 µm cylindrical hydrogen jet (red line) and a thickness and temporal pulse shape optimized 280 nm plastic foil [202] (blue line). The optimal jet performance was achieved with an artificially introduced pre-expansion (green line). The targets were irradiated with 18 J plasma mirror cleaned laser pulses under an incidence angle of 0° and the protons were detected by a TPS in laser forward direction. Radio-chromic film stacks were recorded simultaneously for foil shots and are displayed by filled circles.

numbers from the hydrogen jet are caused by the isotropic proton emission in the horizontal plane induced by the wire-like geometry.

With intrinsic laser contrast at full laser energy*, significantly higher maximum proton energies of up to 75 MeV were measured than with PM-cleaned contrast (figure 4.6a). The increase of laser energy on target by about 30% (corresponds to 5 J), that occurs when the plasma mirror is not used, cannot explain the doubling in $E_{p,max}$. Since the appearance of shots yielding such high proton energies is correlated to a significant target pre-expansion as it was obtained by the optical probing diagnostics (figure 4.3f, section 4.2), a dedicated experimental and numerical study was carried out to investigate the dominant process leading to this increase of $E_{p,max}$. In this study, the plasma pre-expansion is manipulated by a controlled pre-pulse before the PM-cleaned main pulse irradiates the target. This will be presented in the next section of this chapter.

Before doing so, the best performance of the cryogenic jet should be compared to optimized foil targets for the same laser pulse. Figure 4.7 shows the proton spectrum of the best shot with a cryogenic jet (green line) and with a formvar (CH) foil target (blue line). The formvar foil was irradiated with a PM-cleaned contrast pulse and was optimized in terms of thickness and temporal pulse shape [202]. This comparison illustrates the relevance of the high proton energies of up to 80 MeV. The performance from the hydrogen jet is substantially higher than from optimized foils and is achieved with a target system that allows high repetition rates and debris free operation. Interestingly, proton numbers from the cylindrical jet are again a factor of 2-4 lower than those from foils.

---

*At intrinsic contrast conditions, the repetition rate capability of the jet target in combination with the mechanical chopper was tested for potential applications, as the plasma mirror would otherwise limit the repetition rate of the laser system. At 23 J on target 0.1 Hz (limited by the safe operation of the laser system) was shown, whereas 1 Hz operation at reduced laser energy was additionally tested similar to the proton beam generation with 1 Hz in the DRACO 150 TW experiment published in [56].

4.6 Tailoring the plasma density distribution

A systematic study was conducted to investigate in great detail the proton accelerator performance as a function of the target pre-expansion. The aim is to reproduce under controlled conditions the increase of maximum proton energies as found in the intrinsic laser contrast case. The required level of control is achieved by ensuring that under PM-cleaned contrast conditions a change of the target state occurs only within the last picosecond before the arrival of the main pulse (see section 4.2). Therefore, the plasma density distribution can be precisely manipulated by applying a timed pre-pulse, which arrives a few tens of picoseconds before the main pulse. With the help of optical probing, the amount of pre-expansion can then be deduced and linked to the maximum proton energies.

4.6.1 Setup for generating a controlled pre-pulse

The setup in figure 4.8 extends the experimental arrangement in section 4.3 by an additional 1″ pick-off mirror in front of the last beamline mirror in order to generate an intentional pre-pulse that reaches the interaction point prior to the main pulse with a time difference τ_{pp}. By varying the distance l_{pp} between pre-pulse and beamline mirror, τ_{pp} can be adjusted. A small portion of the laser beam is reflected from the rear side of the pre-pulse mirror, as illustrated by the inset in figure 4.8a. This enables short time differences down to 0 ps, since reflection at the front side would limit τ_{pp} to a few tens of picoseconds (depending on the pre-pulse mirror thickness). Propagation through the glass substrate increases the pulse duration, due to the dispersive characteristics of the medium, and thus decreases the intensity. Longer wavelengths travel with a higher group velocity than shorter wavelengths leading to an increased pulse duration t' (FWHM) after transmission through the substrate that is given by

$$t' = t\sqrt{1 + \left(\frac{4\ln 2 \cdot D_\omega \cdot l}{t^2}\right)^2} \tag{4.1}$$

for a pulse with a Gaussian temporal profile. Using t the FWHM value of the initial pulse duration, D_ω the group velocity dispersion of 36.16 fs^2/mm (for fused silica glass [220]) and l the propagation length through the medium of about 13.6 mm*, t' calculates to 55 fs. t' should be treated as a lower estimation because nonlinear effects (e.g. self-phase modulation), that occur when the pulse travels through the substrate, are not taken into account. The pre-pulse is further focused to a spot size of 32 µm x 19 µm yielding a peak intensity of $I_{pp} = 5.8 \cdot 10^{17}$ W/cm^2 or about 7000 times lower than the main pulse intensity (see figure 4.8b,c). The elliptical shape of the focal spot is the result of the 45° laser incident angle on the pre-pulse mirror and the overall larger focal spot (in comparison to the high-intensity laser beam) is related to the small size of the pick-off mirror.

To determine the expansion of the cylindrical jet (see section 4.2) that is caused by the pre-

---

*l is calculated from the substrate thickness of 6 mm while the laser incident angle of 45° and the refraction at the interface between glass and vacuum is taken into account.

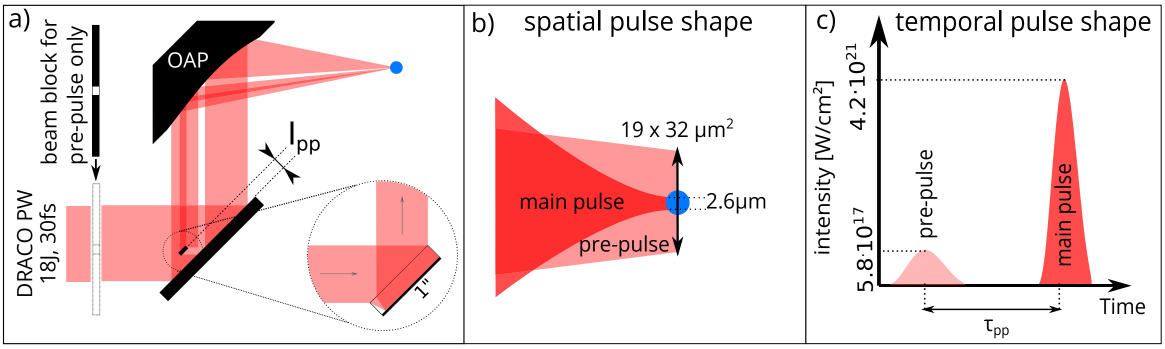

Figure 4.8: a) Experimental setup for laser-target interaction with a pre-expanded (exploded) cylindrical hydrogen jet target. The inset in a) shows the arrangement for producing an intentional pre-pulse by reflecting a small fraction of the full laser beam from the rear side of a ⌀1″ large and 6 mm thick pick-off mirror. The front surface of the pre-pulse mirror is coated with an anti-reflective layer to minimize additional reflections. Schematic representation of the spatial and temporal pulse shape of the pre-pulse in comparison to the main pulse are shown in b) and c). l_{pp} describes the distance between beamline and pre-pulse mirror and τ_{pp} denotes the time difference between the two pulses.

pulse, the shadow diameter $d_{515\text{nm}}$ was evaluated for each shot with the 515 nm probe arm. As in section 4.2, $d_{515\text{nm}}$ quantifies the size of the opaque plasma region. The expansion of the hydrogen jet was further characterized using the second probe arm (1030 nm wavelength). Based on this two color probing approach, a target expansion model was derived that serves as an input for numerical studies. Before this will be described in detail, obtained proton acceleration results are presented in the next section.

4.6.2 Enhanced proton acceleration through target pre-expansion

An extensive data set was collected with various plasma density distributions over the course of three experimental days which contains more than 350 full energy laser shots (18 J on target) while τ_{pp} was varied from 0 ps up to 170 ps. The major results of this study are summarized in figure 4.9. The most striking observations are proton beams with kinetic energies of up to 80 MeV. Proton spectra for different shadow diameters, shown in figure 4.9a, indicate this optimal performance at about 2-3 times the initial target size ($d_{515\text{nm}} = 11$µm). No pre-expansion ($d_{515\text{nm}} = 5$µm) or larger pre-expansion ($d_{515\text{nm}} = 28$µm) show lower maximum proton energies as well as a reduced particle yield. Independent of the target configuration, the proton number decreases monotonically with energy and no pronounced peaks or gaps are visible in the spectrum. A systematic scan over different pre-expansions is shown in figure 4.9b-d. Here, the maximum proton energies detected in laser forward direction (figure 4.9b) and in 45° (figure 4.9c) are displayed with respect to the shadow diameter $d_{515\text{nm}}$.

For the best shots (orange dots in figure 4.9b) in laser forward direction a two-fold energy increase is observed between $d = 11$ µm–17 µm with respect to the unexpanded jet. This is accompanied by increasing fluctuation towards higher energies as indicated by the blue and grey dots. For an even larger expansion, a subsequent decrease in energy is observed. The trend of maximum proton energies averaged over several shots is masked

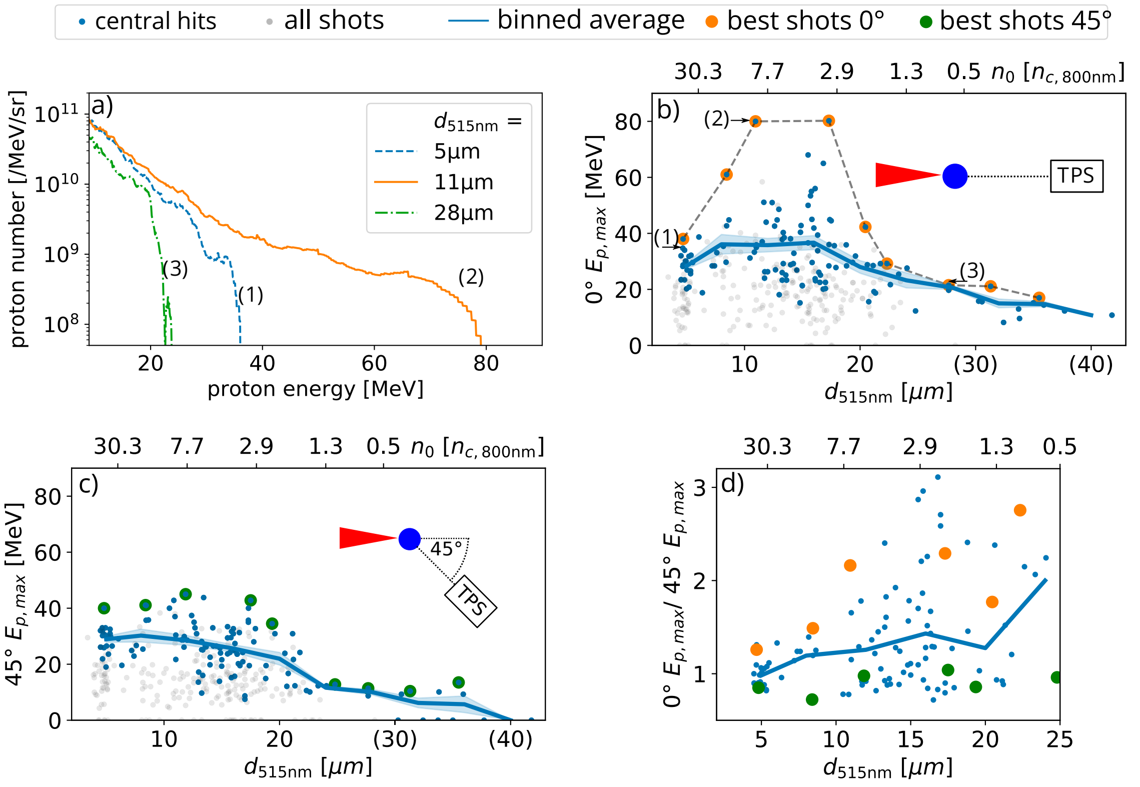

Figure 4.9: a) Example proton spectra in laser forward direction for different pre-expansion configurations covering the unexpanded case (blue), the best performance (orange) and a largely expanded jet (green). The corresponding shots are marked by (1) - (3) in b). Appendix 7.1A provides more details on the method for obtaining the absolute proton spectra. For all shots, the maximum proton energies $E_{p,max}$ detected in laser propagation direction (b) and in 45° (c) is shown as a function of the shadow diameter $d_{515\text{nm}}$ and the core density n_0 (displayed as top axis). n_0 is calculated from the expansion model introduced in the next section. Blue dots represent single shots with central hits accounting for one-third of all shots. Faint grey dots represent non-central hits. The blue line and the blue shaded area indicate the trend of the average $E_{p,max}$ and the corresponding standard error of the mean, respectively. The orange circles highlight best performing shots within 4 µm bins of the shadow diameter. d) shows the ratio between $E_{p,max}$ measured in 0° and 45° emission direction. The average of the individual ratios (blue line) can only be calculated reliably up to $d_{515\text{nm}}$ =25 µm because $E_{p,max}$ in 45° is below the detection threshold for a large fraction of shots at higher $d_{515\text{nm}}$. Parenthesized shadow diameters in b) and c) for values $\geq$ 30 µm (on the x-axis) indicating the onset of transmittivity of the target for the 515 nm probe beam and are therefore only an estimation.

by the shot-to-shot fluctuation of $E_{p,max}$ originating from the positioning jitter of the cryogenic jet as discussed in 4.5. Since the measurement of the on-shot jet position and the high power focus position was not sufficiently precise, the degree of laser target overlap was determined by integrating the laser light signal T (normalized to the signal without a jet) measured with a ceramic screen behind the target. For a central interaction, the target blocks a large part of the focus spot leading to reduced laser light signal (T close to 0) on the ceramic screen, whereas more light is recorded on the screen if the laser pulse only grazes along the jet surface or misses the target completely (T=1). We applied a threshold defining one third of all shots with the lowest laser light signal of a given subset, which contains same sized targets, as central hits. Although the fraction of 1/3 was obtained empirically, the trend of the increased maximum proton energies for a certain pre-expansion remains robust against changing this fraction, as it will be demonstrated in appendix B. However, shots with d > 25 µm were no longer filtered, as at these pre-expansions the core density drops below $n_{c,800\mathrm{nm}}$ and the target thus turns classically transparent for the high-intensity laser pulse. The result of the transmitted light filter is shown in figure 4.9b. Blue dots represent central hits with T below the threshold and faint grey dots indicate all other shots (with a weaker laser target overlap). Shots resulting in low or no detected $E_{p,max}$ are reliably marked as non-central hits, while most of those leading to high maximum proton energy are identified as central hits. The best distinction could be achieved for the unexpanded jet at 5 µm shadow diameter.

The average of $E_{p,max}$ for central hits in laser forward direction is indicated in figure 4.9b by the blue line with the respective standard error of the mean. While $E_{p,max}$ yields 29 MeV without any additional pre-pulse ($d_{515\mathrm{nm}} \approx 5$µm), an increase in the average proton cut-off energies to 36 MeV is found for shots with a shadow diameter of approximately 7 µm–17 µm. This agrees well with the trend found for the best shots.

In contrast, $E_{p,max}$ in 45° direction (figure 4.9c) shows a different characteristic. While the average value of the maximum proton energies decreases slightly with the shadow diameter, best shots with up to 40 MeV (highlighted by green circles) are achieved for shadow diameters of up to 20 µm. At even larger shadow diameters, no protons above 4 MeV (detection threshold) were detected in the 45° TPS in most cases.

As a further characteristic, the angular distribution of the proton emission for different pre-expansions was investigated. Due to the technical difficulties with RCF measurements (c.f. section 4.3), this investigation is based on data from the on-shot diagnostics (TPS and DDD). Figure 4.9d is dedicated to the investigation of the ratio of $E_{p,max}$ obtained from the 0° and 45° TPS. The ratio on a single shot basis indicates a strong fluctuation which is related to the centrality of the interaction. Represented by the blue line, the binned averages show an increase with shadow diameter. No pre-expansion ($d_{515\mathrm{nm}} = 5$ µm) yields a ratio close to unity which is consistent with isotropic proton emission within the horizontal plane, i.e. perpendicular to the jet axis. This is expected for the curved surfaces of cylindrically shaped jets [57] and wire targets [56, 218, 82]. With increasing diameter, the emission direction of the most energetic protons is shifted towards the laser forward direction. Again, for the subset of shots with the best performance in laser forward direction (orange dots), which likely feature a central laser target overlap, this trend is more pronounced. This means that in the case of a target pre-expansion the highest energetic component of the proton beam is no longer isotropically distributed but is predominantly peaked in laser forward direction. For ratios smaller than one, faster protons are deflected in the 45° direction likely due to a non-central hit. However, as $E_{p,max}$ in 45° is limited to 40 MeV (figure 4.9c) and never exceeds the kinetic energies obtained in the 0° by more than 30% (the lowest measured ratio is about 0.7), one can deduce that non-central hits are less efficient or the most energetic particles are never deflected by as much as 45°.

While figure 4.9 incorporates all data measured on the three measurement days, it is important to note, that the same characteristics can also be found for each day of the experiment individually which demonstrates the robustness of the presented results.

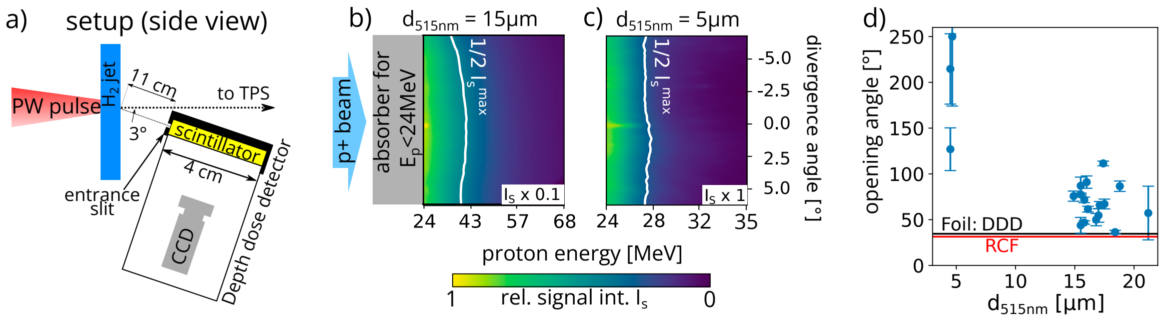

Figure 4.10: a) Side view sketch of the depth dose detector (DDD) implementation in the laser-plasma experiment (not to scale). The CCD camera unit is adopted from [219]. Example results of recorded scintillator images for b) a pre-expanded target with $E_{p,max} = 69$ MeV and for c) an unexpanded target with $E_{p,max} = 32$ MeV. Note the different energy scales. White contour lines indicate the curvature of the depth dose distribution by connecting points of equal signal intensity values. d) Opening angle calculated at half of $E_{p,max}$ of a Gaussian fit of the contour lines for different target pre-expansions. Errors on the y-axis are obtained by varying the signal level of the contour line. As illustrated by the horizontal lines, the opening angle from the DDD (black line) agrees for foil targets with measurements obtained by RCF-stacks (red line).

The observation of a proton beam peaked in laser forward direction for pre-expanded jets is further supported by measurements of the horizontal cross section of the angular proton depth dose profile with a scintillator-based detector that covers a divergence angle of ±7°. The working principle of this depth dose detector (DDD) is schematically shown in figure 4.10a. By placing the scintillator along the proton beam propagation direction, an energy resolution is achieved in one spatial direction while the other direction resolves the angular distribution. To prevent saturation and to block background radiation, a shielding surrounding the DDD stops residual light and prevents protons with energies below 24 MeV from reaching the sensitive area. Comparing a laser shot with pre-expansion and one without in figure 4.10b,c indicates a difference in angular distribution that is illustrated by white contour lines connecting points of equal signal intensity. While in figure 4.10c the dose distribution seems to be independent of the divergence angle that supports an isotropic proton emission in the horizontal plane, the contour line in figure 4.10b is curved which is caused by the angular distribution of the proton beam. More quantitatively, the curvature of the contour lines is analyzed in figure 4.10d for the available shots that were obtained with the DDD. By assuming that the shape of the contour lines can be described reasonably well by a Gaussian distribution, one can parameterize the curvature by calculating FWHM of this distribution that will be called opening angle. Although the opening angle can in general not directly be associated with a property of the proton beam, since the nonlinear energy deposition in the scintillator is not taken into account, it can still serve as an estimator to compare the envelope-divergence for different proton beams. This procedure was benchmarked for shots on foil targets that indicate an opening angle retrieved with the DDD that is comparable to the beam envelope-divergence obtained from irradiated RCF-Stacks (horizontal lines in figure 4.10d). Although the data set is limited, one can clearly distinguish between an isotropic proton emission given by a large opening angle for unexpanded jets ($d_{515\text{nm}} \approx 5$ µm) and a much smaller one for shadow diameters between 15-20 µm. This agrees qualitatively with the ratio of maximum proton energies obtained with the TPS and thereby supports the finding of a proton beam peaked in laser forward direction if the jet is pre-expanded.

4.6.3 Characterization of the target density distribution

To investigate the prevailing acceleration mechanisms, which lead to the highest proton energies, the experimental conditions were modeled in a series of three-dimensional particle-in-cell (PIC) simulations that will be discussed in the next section. Since 3D-PIC simulation can only cover a limited temporal window of the laser-matter interaction (typically less than 1 ps), a complete start-to-end simulation including the low intensity pre-pulse induced plasma expansion (tens of picoseconds) as well as the high-intensity main pulse is not feasible. However, by deriving the plasma density distribution as a function of the pre-expansion the simulation time can be reduced to a few hundred femtoseconds, the temporal window of the main pulse interaction. Based on experimental measurements with optical probe beams, a model of the density distribution is obtained here. This approach defines precise input parameters for the numerical studies. Any additional target manipulation due to the laser background is limited to the last picosecond by using the plasma mirror device (see section 4.2) and can thus be included in the PIC simulation. It should be noted that the combination of a PIC simulation of the pre-pulse interaction with the target and a hydrodynamic expansion study over tens of picoseconds can provide an alternative (numerical) approach to derive a density distribution.

The pre-pulse tailored target density profile was determined in a dedicated experiment run. For this, the entire beam was blocked and only a portion with the size of the pre-pulse was sent onto the jet. Shadowgrams for various τ_{pp} were collected with two-color probing, as shown in figure 4.11a, from which the shadow diameter is obtained and displayed in comparison to τ_{pp} in figure 4.11b. Probing with two colors allows determining the density gradient during expansion. Note that this study was conducted with a more intense pre-pulse ($\approx 2.65 \cdot 10^{18}\,\mathrm{W/cm^2}$) than the one utilized for the proton acceleration experiments ($I_{pp} = 5.8 \cdot 10^{17}\,\mathrm{W/cm^2}$) in order to resolve all details of the expansion dynamics. However, a similar scan obtained with the same pre-pulse intensity as in section 4.6.2 leads to comparable model results, only with an overall slower evolution. Investigations of the target expansion dynamics indicate a symmetrical increase of the shadow diameter with time whereby the shadow expands faster in the 1030 nm probe image (see figure 4.11a). On top of the overall expansion, an axial modulation of the plasma density is found whose origin and relevance for proton acceleration will be discussed in chapter 5.

For the first few 10 ps expansion time, the target bulk remains opaque, so that the density profile in the center is not yet accessible. However, in the case of the later time steps, transition into transparency can be observed. This occurs for the entire bulk at once. Together with the observed symmetric expansion, this motivates the assumption of a radial, top-hat-like density profile. In our constructed density model (see figure 4.11c), this is reflected by the constant core density n_0 with a certain radius R. The observation of different shadow diameters for the two different probe wavelengths in one shot is expressed by an additional exponential density slope with a scale length L_p. The plasma density distribution

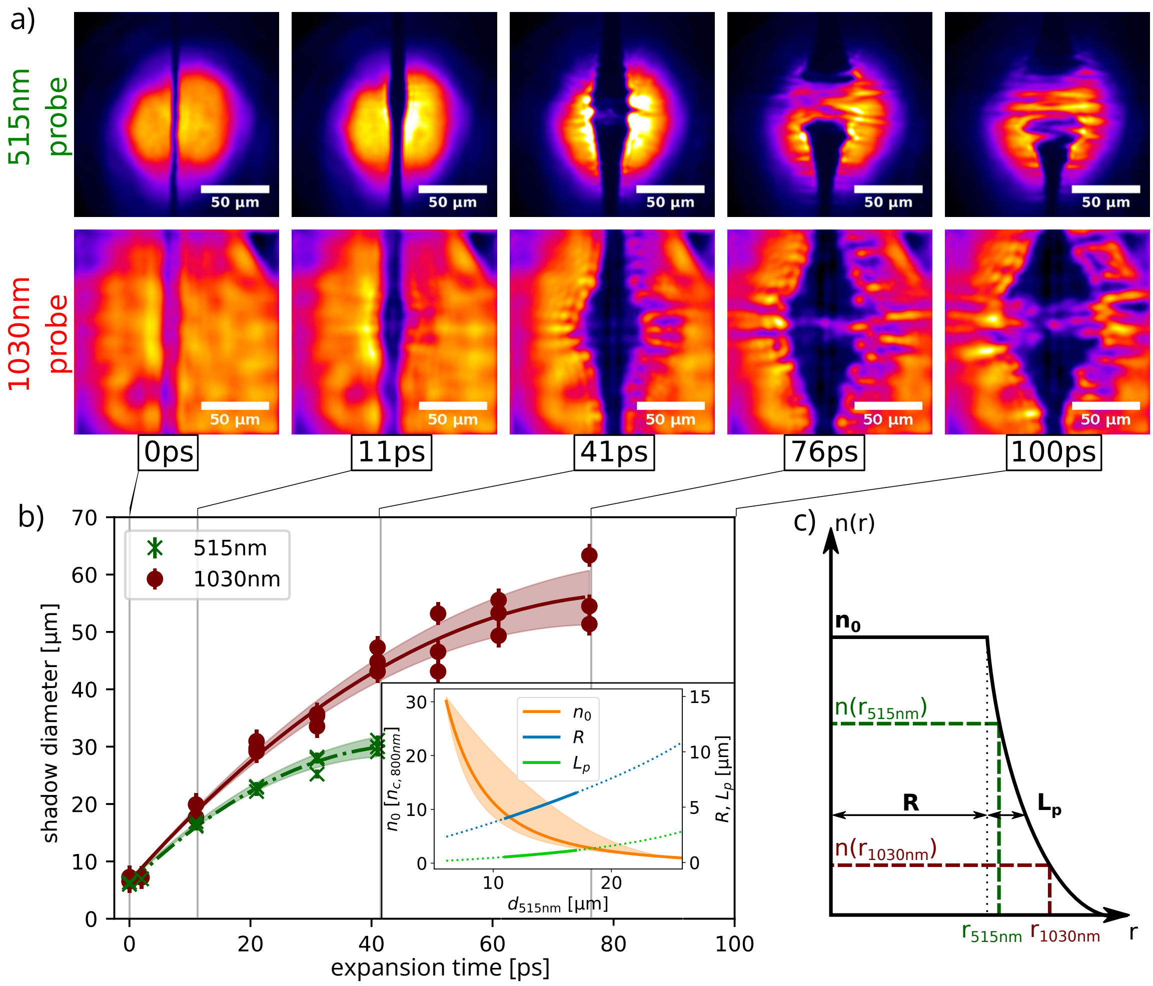

Figure 4.11: Characterization of the target expansion by imaging shadowgraphy with two colors. a) Temporal evolution of the jet due to a pre-pulse with an intensity of about $2.65 \cdot 10^{18}$ W/cm^2. For the 515 nm probe arm, the jet becomes transparent 41 ps after irradiation with the pre-pulse (for 1030 nm at 76 ps). b) Interpolation of extracted shadow diameters as a function of τ_{pp} for 515 nm and 1030 nm probe pulses. The error bars denote the resolution limit of the imaging system. Lines from polynomial fits are used to parameterize the shadow diameter at both probe wavelengths. c) Top-hat-like model of the target density distribution. The two colors probe different densities at different radii of the profile. The inset in b) shows the three model parameters as a function of the 515 nm shadow diameter. Uncertainties in the interpolation of the target diameter (shaded area in b) lead to the errors of the model parameters as exemplary shown for the core density (shaded regions) in the inset.

can thus be expressed by

$$n(r) = \begin{cases} n_0 & \text{for } r \leq R \\ n_0 \cdot e^{-\frac{r-R}{L_P}} & \text{for } r > R \quad . \end{cases} \tag{4.2}$$

The three parameters n_0, R and L_P can be determined by the following three boundary conditions for each shadow diameter. First, the particle number within the cross section A needs to be conserved. This can be described by $\int n(r)dA = N$. Where N, the line density, is determined by $N = \pi R_0^2 \cdot n_{H2}$ with the initial jet radius R_0 = 2.5 µm and the plasma density of solid hydrogen n_{H2} = 30 $n_{c,800nm}$. Second, L_P is derived from shadow diameters measured by the two color probe beams. Since both wavelengths address different critical plasma densities and n_c scales with the wavelength by $\sim 1/\lambda^2$ (refer to section 2.1.2), the transition in the probe image from transparent to opaque occurs at $n_{515\text{nm}} = 4 \cdot n_{1030\text{nm}}$. Combining this with the exponential slope in equation 4.2 and solving for L_P results in

$$L_P = \frac{0.5 \cdot (d_{1030\text{nm}} - d_{515\text{nm}})}{\ln 4} \tag{4.3}$$

where $d_{515\text{nm}}$ and $d_{1030\text{nm}}$ denote the shadow diameter in the 515 nm and 1030 nm probe image, respectively. The last condition is given by the plasma density n_{th} at which the transition from the opaque to the transparent plasma region occurs in the probe image and thus for which the shadow diameter is measured. Note that n_{th} is different for the two probe colors. Within the framework of this model, it is assumed that n_{th} is constant for all expansion times. It is further assumed that n_{th} equals the core density at the moment when the bulk of the target becomes transparent due to the decrease of n_0 by expansion. Optical probing images in figure 4.11a indicate that the bulk transparency for the 515 nm probe beam starts to appear after 41 ps and for a shadow diameter of 30 µm. Similar arguments can also be made for the 1030 nm probe beam whereby the plasma turns transparent at larger expansions and therefore smaller densities. n_{th} is obtained for the 515 nm probe beam by solving equation 4.3 and by conserving the particle number at a pre-pulse delay of 41 ps. This leads to $n_{th,515nm}$=0.45 $n_{c,800\text{nm}}$.

This result is somehow surprising because a threshold density corresponding to the critical plasma density (2.4 $n_{c,800\text{nm}}$ for 515 nm) would be expected (compare with section 2.1.2), whereas $n_{th,515\text{nm}}$ is less than 20% of 2.4 $n_{c,800\text{nm}}$. However, it can be shown that due to the deflection of the probe beam in the radially symmetrical underdense plasma region, the transition from opaque to transparent in the shadowgraphy image occurs at a density well below 2.4 $n_{c,800\text{nm}}$. For this purpose, a target density distribution as in the expansion model is considered in which the core density corresponds to the critical density for 515 nm wavelength and the core is therefore opaque. The underdense plasma outside the core

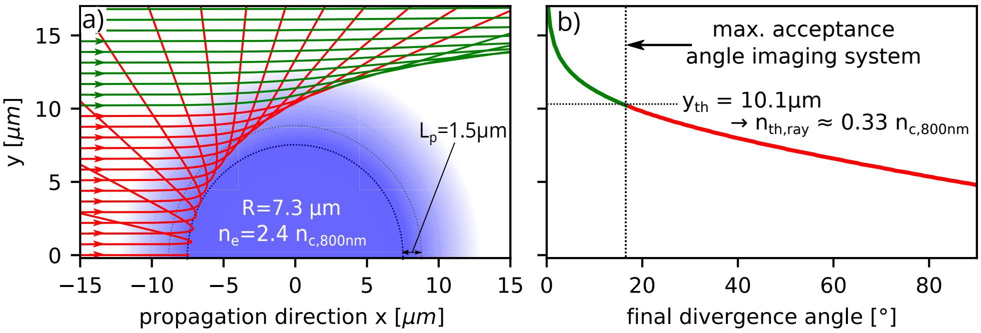

Figure 4.12: Traces of light rays deflected by a plasma density distribution that is characterized by a core of radius R and an exponential slope with a scale length L_p. a) Paths of light rays that initially propagate in the positive x-direction. b) Divergence angle after propagation through the plasma (0° marks the initial direction of the rays). Green (red) indicates light rays with a divergence angle smaller (larger) than the theoretical acceptance angle of the imaging system.

is transparent. In this scenario a shadow diameter of a size equal to the core diameter would be expected. However, deflection of the probe beam in an underdense plasma region leads to divergence angles that exceed the acceptance angle θ of the imaging system. Probe beam parts with a high divergence are not imaged on the camera sensor, resulting in a dark area that is larger than the nominal overdense plasma region and that matches the experimentally measured shadow diameter.

To demonstrate this, a simple ray-tracing calculation was conducted. Parallel light rays representing the 515 nm probe beam illuminate a radially symmetric density distribution (corresponding to that of the target expansion model) with a constant density core and an exponential slope. The path of the light rays is calculated by repeatedly advancing and refracting the rays through the density distribution in small discrete steps whereby the refractive index is determined by the plasma density according to equation 2.7. Figure 4.12a displays the path of light rays for a target shape with $n_0 = 2.4 n_{c,800\mathrm{nm}} = n_{c,515\mathrm{nm}}$, $R = 7.3\,\mu\mathrm{m}$ and $L_p = 1.5\,\mu\mathrm{m}$. The core remains therefore opaque while the outside plasma is transparent. The underdense plasma has a defocusing effect due to a refractive index $\eta < 1$. The angular redistribution after propagation is displayed with respect to the starting y-position in figure 4.12b and shows a rapid increase of the final divergence angle as the propagation path approaches the dense plasma region. For the utilized imaging system in the experimental studies, an acceptance angle $\theta = 17^\circ$ can be estimated based on the working distance of 80 mm and the aperture diameter of 50 mm. Light rays with divergence angles exceeding θ are not expected to contribute to the image recorded with the camera sensor and are marked as red lines in figure 4.12 while green indicates rays with lower divergent angles. The threshold, which separates green and red rays, equals an initial y-position $y_{th} = 10.1\,\mu\mathrm{m}$. Since y_{th} is almost 3 µm larger than R, the expected shadow diameter is also larger than the diameter of the overdense plasma region. This demonstrates that the size of the critical density region cannot be resolved. Instead, the threshold density $n_{th,ray}$ is obtained from the ray-tracing approach by $n_{th,ray} = n(x = 0, y = y_{th}) = 0.33 n_{c,800\mathrm{nm}}$. Although slightly lower, $n_{th,ray}$ reasonably resembles the threshold $n_{th} = 0.45\, n_{c,800\mathrm{nm}}$ that was calculated based on the onset of bulk transparency in the probe images. This shows that the about 5 fold reduction of n_{th} in comparison to the critical density of that particular wavelength can mostly be explained by refraction of the probe beam in the underdense plasma region and the limited acceptance angle of the imaging system. Although here the calculation was done for a wavelength of 515 nm, the same factor 5 is also approximately valid for other wavelengths, like the 1030 nm, which were used for the other probe arm. Running the ray-tracing calculation for different parameter sets of n_0, R and L_p within the relevant range (given by the target pre-expansion) results in similar n_{th} that differ only slightly. This supports the above mentioned assumption that for a given probe wavelength the transition from opaque to transparent in the shadowgraphy images occurs at a fixed density that is independent of the pre-expansion. Instead of considering only one density, the ray-tracing methods can be further extended to additionally including the imaging system and thus generating synthetic probe images for a given density distribution. Comparison of these images with the experimental measurements then allows an iterative approach to

determine the parameters of the distribution.
The results of the angular redistribution also imply a more general conclusion concerning the optical probing of plasma distributions. Not only does the wavelength play an important role with respect to the highest observable plasma density by optical probing, but also the imaging system can substantially limit the accessible plasma densities.

With n_{th} obtained by the onset of bulk transparency and supported by the ray-tracing calculation, the model from equation 4.2 can finally be solved for each pre-pulse delay. The resulting target parameters are presented as a function of the 515 nm shadow diameter in the inset of figure 4.11b. With increasing $d_{515\text{nm}}$, the core radius and scale length increase almost linearly while the core density decreases rapidly with $\sim 1/d_{515\text{nm}}^2$ *.
Based on this expansion study, for the on-shot measurement of the shadow diameter only one probe wavelength (515 nm) is sufficient to fully characterize the density profile in the full scale experiment and thus to derive the core density values displayed in the top x-axes of figure 4.9b-d. When applying the model on the acceleration performance measurements in figure 4.9, it follows that the most energetic proton beams (with up to 80 MeV) are obtained in laser forward direction at a core radius of about 3.5-5.5 µm, a scale length of 0.5-1 µm and a core density of 4-9 $n_{c,800nm}$. This means that the highest proton energies are achieved for near-critical density targets, with a performance that is significantly higher than in the case of solid-state density (30 $n_{c,800nm}$). In combination with the change in the angular distribution of the proton emission, this implies an acceleration mechanism that differs from TNSA. In order to investigate the acceleration mechanisms for near-critical density targets, simulations are required. These are presented in the following section. It should be noted that the target expansion model presented here is idealized, e.g., the transition from the core region to the exponential slope is simplistically assumed to be abrupt, whereas in reality a smoother transition is expected. As such, simulations employing this target density profile are primarily used to investigate the various acceleration mechanisms involved in the different target density regimes, while an accurate quantitative comparison with the experimental results is limited.
Lastly, it is interesting to note that a significant proton acceleration performance in laser forward direction with $E_{p,max}$ of up to 20 MeV is still measured at classically transparent core densities ($n_e < n_c$). This shows that the hydrogen jet can also be used to investigate laser-proton acceleration in underdense plasmas. Complementary to the otherwise often used high-pressure gas jets (e.g. [50, 135, 136, 137, 45, 138, 139, 140], refer to section 2.2.2), the cryogenic jet can be applied to study acceleration mechanism in a relatively thin (a few 10 µm) underdense plasma with still rather short plasma gradients.

---

*Due to the linear increase of the core radius with $d_{515\text{nm}}$ and a quadratic increase of the core area with R, the scaling of the core density with $\sim 1/d_{515\text{nm}}^2$ is expected.

4.6.4 Interpretation of the experimental results using numerical simulations

To examine the mechanisms governing the proton acceleration results, three-dimensional simulations were performed using the particle-in-cell code PIConGPU [221, 222]. The cylindrical target was modeled as a wire-like radially symmetric plasma density distribution with the jet axis along the z-direction. The input parameters for the target shape were derived from the expansion model (previous section). In a multitude of simulations, the core density n_0, the core radius R and the scale length L_p were varied at the same time according to the model. The low plasma density ($\leq 30 n_{c,800nm}$) enabled full three-dimensional simulations. The simulation box has a size of 28.8 µm in x-direction, 57.6 µm in y-direction and 14.4 µm in z-direction. The box contains 30 cells/µm and 5 particles per cell. The laser propagates in positive y-direction, is polarized in the x-direction and features a normalized peak vector potential a_0 of 33 with a spatial Gaussian-shaped distribution of 4.1 µm (FWHM). The intensity is slightly smaller than the peak intensity in the experiment ($a_0 \sim 45$) to cope with the imperfections during the measurements (e.g. systematic alignment differences between the jet position along the laser axis and the focal plane, shot-to-shot position fluctuations). Increasing the simulated a_0 to higher values showed qualitatively similar overall trends with slightly higher final proton energies.

Figure 4.13 illustrates the results obtained for several simulation runs with different target shapes. The presented results are: (1) the maximum proton energies $E_{p,max}$ (black crosses) reached at the end of the simulation, which serves as a comparison to the experimental data in figure 4.9. (2) the maximum plasma density n_{max} (blue triangles) along the laser propagation path (averaged over an area of 1 µm^2) within the simulation time step in which the peak of the pulse is supposed to reach the target center. n_{max} provides an indication whether the plasma is transparent for the laser pulse. (3) the ratio of laser energy converted into the kinetic energy integrated across all electrons and ions (yellow dots). The latter serves to estimate to what extent the change in laser absorption (due to the different core densities and scale lengths) can explain differences in the maximum proton energies. Based on the trend of $E_{p,max}$, three regions with clearly different proton acceleration performance can be identified. Region I ($n_0 > 25\, n_{c,800\text{nm}}$) shows moderate proton energies $E_{p,max} \approx 60$ MeV. A distinct peak with significantly higher $E_{p,max}$ of up to 200 MeV is observed in Region II ($n_0 = 12 – 14\, n_{c,800\text{nm}}$). Within this region the maximum on-axis density drops below the relativistically critical density $n_c^{rel} = \gamma n_{c,800\text{nm}}$ (blue dashed line). Proton energies decrease for lower initial core densities and increase again forming a secondary maximum with up to 80 MeV in Region III ($n_0 < 6\, n_{c,800\text{nm}}$) before dropping again for even higher densities.

Discussion of experimental and numerical results

Before the underlying mechanisms in the three regions will be discussed in detail, the following section gives an overview of how well the simulation reproduces the experimental results such as the increase in proton energies with pre-expansion and the transition of

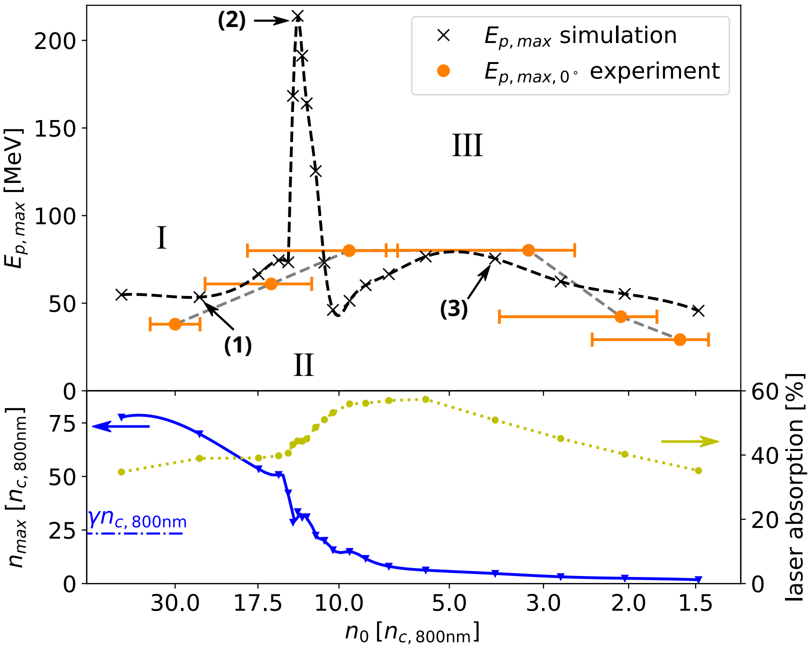

Figure 4.13: Results of several simulation runs using a laser pulse with a peak intensity of $a_0 = 33$. The target density distribution is varying according to the expansion model. Each individual simulation run is represented by its initial core density on the x-axis. Maximum proton energies $E_{p,max}$ (black crosses) at the simulation end, maximum on-axis density n_{max} (blue triangle, obtained at the time when the peak intensity is supposed to reach the target center) and the percentage of laser energy converted into kinetic energy of all particles (yellow dotted line) are displayed. The horizontal blue line indicates the theoretical threshold for relativistic transparency $\gamma n_{c,800nm}$ from equation 2.8. Roman numerals (I, II, III) identify three regions with different proton acceleration performance. (1) - (3) refer to individual simulation runs that are representative for the respective regions and which will be discussed later with figure 4.16 in detail. For comparison to the experiment, proton energies of the best performing shots (orange circles as in figure 4.9b) are included as well. Error bars combining uncertainties of the expansion model and the target diameter measurement are shown for these shots to discuss the assignment of the experimental data to the three regions.

the proton beam emission distribution from isotropic to more directed along the laser forward direction. For this purpose, maximum proton energies and angular distribution of emitted proton beams as well as the influences of non-central hits are investigated in the simulation and compared to the experimental results.

Maximum proton energies

Regarding the maximum proton energies, both experiments and simulations (orange dots compared to black crosses in figure 4.13) show an increased performance for the pre-expanded compared to the unexpanded target configuration. In agreement with the measured 38 MeV from an unexpanded jet, simulation results for core densities exceeding 25 $n_{c,800nm}$ (Region I) are characterized by relatively low maximum energies of 55 MeV that are rather stable against variations of the simulation input parameters (e.g. a change in core density has a negligible effect on $E_{p,max}$). The experiment shows one broad optimum of $E_{p,max}$ for a target density of 4-9 $n_{c,800nm}$ that, however, qualitatively differs from the simulation result indicating two proton energy maxima. One occurs in the region II at an initial core density of about 13 $n_{c,800nm}$ and one in the region III at about 5 $n_{c,800nm}$. Another difference is that in the region II the maximum proton energies in the simulation are considerably higher compared to the experimental measurements. A possible explanation for both disagreements is that due to the shot-to-shot fluctuations in the experiments, it can be assumed that region II is rarely reached in the experimental study. The rather small peak width ($n_0 = 12 – 14\, n_{c,800\mathrm{nm}}$) corresponds to a change in shadow diameter from 9-9.7 µm (refer to inset in figure 4.11b) which is below the resolution limit of our shadowgraphy imaging. Since only 7 shots were acquired within this shadow diameter interval, it may never have been possible to match the target conditions in region II and simultaneously providing a central irradiation. Additionally, near region II an unambiguous assignment of shots to a specific region is impossible due to the remaining experimental uncertainty of the density determination, as displayed by the error bars. Nevertheless, one cannot exclude that for shots like the experimental data point at $9.3\, n_{c,800\mathrm{nm}}$, the acceleration process in region II plays a role for the observed proton energy increase when comparing with unexpanded targets. Since $E_{p,max}$ in region III is less sensitive to the exact core density of the plasma distribution, it is experimentally easier to tune the target to the desired conditions. Exemplary, with the same argument as above, the experimental data point at about $3.2\, n_{c,800\mathrm{nm}}$ can be assigned to region III. Lastly, the simulation performed with the lowest core density ($2.7\, n_{c,800\mathrm{nm}}$) indicates a decrease in performance that agrees well with the reduction of $E_{p,max}$ for $n_0 < 3\, n_{c,800\mathrm{nm}}$ in the experimental studies.

Generally speaking, quantitative differences of $E_{p,max}$ between experiments and even three-dimensional simulations in figure 4.13 can be explained due to several reasons. Different local thicknesses and shapes of the jet (see section 3.4) as well as fluctuations of the pre-pulse intensity cause changes in the target density distribution from shot-to-shot and day-to-day. Furthermore, the assumed target shape simplifies the actual plasma density distribution excluding all non-radial modifications (e.g. transverse density modulations), the spike-like axial plasma density modulation (refer to chapter 5) or the background hydrogen gas content [153], which originates from evaporation at the target-vacuum interface. Those modifications were neglected for the simulation input but can result, for example, in filamentation of the laser pulse causing a reduced acceleration performance. Moreover, the idealized assumption of a constant core density could lead to unrealistically high proton energies in region II. Preliminary simulation results using a slowly varying core density indicate a decrease of $E_{p,max}$ while the region II extents over a larger density range.

Angular distribution of the emitted proton beam

Besides the maximum energies, the angular distribution of the proton beam is another characteristic that can be compared to the experimental results. Figure 4.14 shows angularly resolved proton spectra for three simulation runs, marked by (1) - (3), which represent the typical behavior in each of the regions I - III. Simulation run (1) in figure 4.14a features an isotropic proton emission with almost uniform distribution of $E_{p,max}$. This is comparable to the experimental results obtained for an unexpanded jet. Simulation run (2) and (3), on the contrary, result in a more directed proton beam in which the proton energy

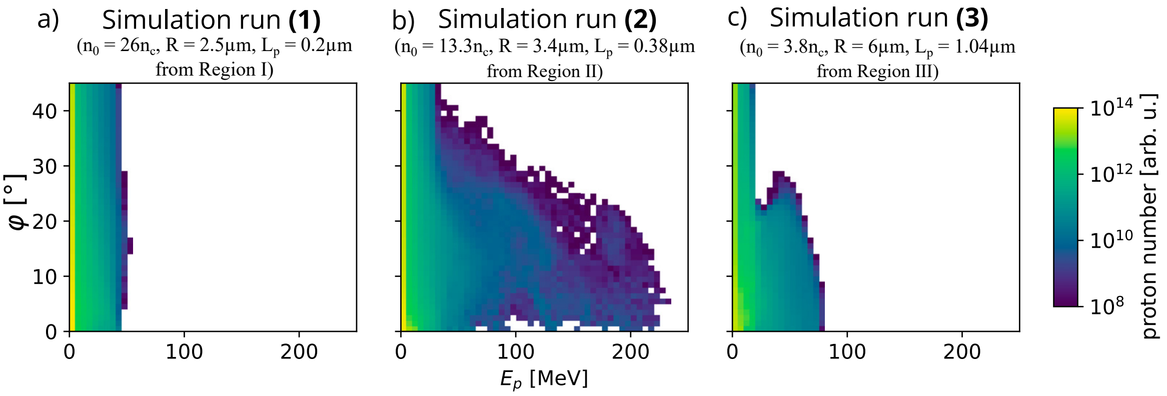

Figure 4.14: Simulation results showing the calculated (at 240 fs after t_0) angular proton energy E_p spectra in the xy-plane for three simulations that are representative for their regions. (1) - (3) refer to the simulation in figure 4.13. The angle φ denotes the emission direction perpendicular to the jet axis. $\varphi = 0°$ indicates the laser forward direction.

at larger emission angles φ is reduced in comparison to the laser forward direction. This qualitatively agrees with a more directed proton beam along the laser forward direction that is obtained for a pre-expanded target by TPS and DDD measurements from figure 4.9 and figure 4.10. The differences in the angular distribution of the emitted proton beams in simulation run (2) and simulation run (3) are probably too insignificant to be resolved experimentally. Thus, region II and region III cannot be distinguished based on the experimental measurements.

Non-central hits

While numerical studies have so far only considered central laser-target interactions, non-central irradiation is unavoidable in experiments due to the position jitter of the cryogenic jet. To check whether the shot-to-shot fluctuations in the experimental results (especially for the ratio $0°E_{p,max}/45°E_{p,max}$) can be reproduced, further simulations were dedicated to investigate the influence of non-central hits on the proton emission distribution. The numerical studies were performed by varying the lateral position of a fixed target ($n_0 = 3.5\,n_{c,800\mathrm{nm}}$, R=7 µm and L_P=0.2 µm) which is assigned to region III. A region III scenario was chosen because it is expected from the experimental data that a change in the lateral target position will have a significant influence on the angular proton emission distribution (see figure 4.9). In comparison, a region I scenario is less suitable since the expected change in the emission characteristics of the proton beam is much smaller due to the isotropic emission. The laser pulse for this scan had a slightly higher peak intensity of $a_0 = 45$. However, this is not expected to affect the impact of non-central hits in qualitative terms.

Figure 4.15 shows the results for a variation of the lateral target position. α and $E_{p,max}$ display the emission direction of the fastest protons and the kinetic energies observed in 0° or 45° for various target x-positions ranging from central hits ($x_t = 0$) to $x_t = R$. $x_t = 0$ results in proton beams with the most energetic component being emitted at an angle $\alpha = 0°$. This is consistent with the experimental observation that states that with central irradiation the

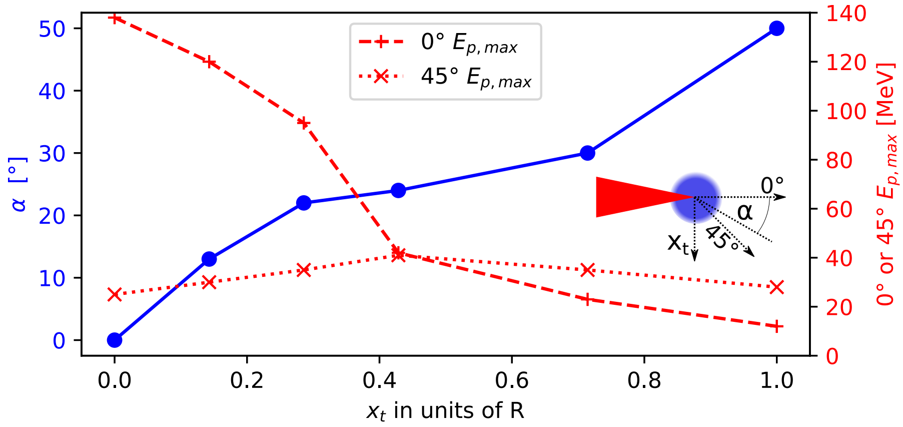

Figure 4.15: Simulation results shown for 240 fs after the peak intensity (a_0 = 45) reaches the center of a n_0= 3.5 $n_{c,800\mathrm{nm}}$, R=7 µm and L_P=0.2 µm target. The target center x-position x_t was varied between 0 (central hit) and R (peak intensity hits the edge of the plateau). α indicates the propagation direction of the protons with the highest kinetic energy and $E_{p,max}$.

highest energetic protons are accelerated in laser forward direction. However, as soon as x_t increases a deflection of the $E_{p,max}$ can be observed. The extreme case, when the laser grazes along the edge of the core region, leads to α above 45°. Consequentially, $E_{p,max}$ in 0° decreases when x_t is increased. $E_{p,max}$ in 0° reaches for example less than one-third of the value at central irradiation when the target position is more than 3 µm shifted laterally. In contrast, the proton emission in the direction of 45° is only weakly dependent on x_t and becomes more energetic than the component emitted in the direction of 0° for $x_t \gtrsim 0.4R$. The highest E_{max} in 45° is found in the vicinity of $x_t = 0.5 \cdot R$ and not when the laser hits the edge. This can be explained by an overall decrease in performance that occurs as soon as the interaction is not centered anymore. In general, protons emitted in the direction of 45° never reach the same maximum energies as protons emitted in laser forward direction for central hits. This agrees well with the experimental results from figure 4.9 where maximum proton energies detected in 45° direction were only about half as high as in laser forward direction.

For different lateral target positions, one can further investigate the ratio of maximum proton energies (0°$E_{p,max}$/45°$E_{p,max}$). For $x_t = 0$, $E_{p,max}$ in 0° is several times higher than 45° $E_{p,max}$ which agrees qualitatively with the experimentally obtained ratio of about 2-3 for centrals hits (orange dots) in figure 4.9d. The best proton performance at 45° (at about $x_t = 0.5R$) compares to only slightly higher $E_{p,max}$ at 45° than at 0° and therefore to a ratio marginally below one which resembles the lowest experimental measured ratio values in figure 4.9d (green dots) reasonably well. These two scenarios (central hit and best proton performance emitted at 45°) represent the cases for the highest and lowest ratios of proton energies. Other target alignments result mostly in ratios between these two cases. Overall, the ratio of 0°$E_{p,max}$/45°$E_{p,max}$ achieved by variation in the lateral target position thus agrees well with the experimentally measured ratio.

Discussion of the involved acceleration mechanisms

The central question arising from the experimental results in figure 4.9 is which physical process drives the increase of the proton energy to up to 80 MeV when reducing the target density. PIC simulations are the only available technique to assess the microscopic physics at these densities and thus to identify potential mechanisms that occur under the conditions in the experiment. The dominant acceleration scheme in each of the three identified regions is discussed with figure 4.16 using representative sample simulation runs, which are labeled (1) - (3). For comparison, these three simulation runs are marked with the same number in figure 4.13. Figure 4.16 shows longitudinal proton phase spaces with the on-axis electric field in the y-direction and the magnetic field component in z-direction for two different time steps. Additionally, for later times the cross section of the ion density distribution in the xy-plane is displayed in the third row.

Region I: Isotropic proton emission in the TNSA regime from an overdense plasma

In simulation run (1) the initial core density ($26\,n_{c,800\mathrm{nm}}$) is larger than the theoretical threshold for relativistic transparency $\gamma n_{c,800\mathrm{nm}}$ (about $23\,n_{c,800\mathrm{nm}}$). Additional steepening of the plasma caused by the compression of the electron fluid due to the ponderomotive forces leads to maximum on-axis densities significantly above the initial density (figure 4.13). As a result, the target is dense enough to be opaque for the laser pulse, as shown by the non-penetrating magnetic field component of the pulse in figure 4.16a,d. Fast electrons, that are generated at the irradiated interface, build up a quasi-static electric sheath field at the target rear side (demonstrated by the E_y component in figure 4.16a) which accelerates protons within the well-known TNSA regime. Due to the curved surface, high energetic protons (highlighted in red in figure 4.16g) are emitted isotropically in the xy-plane as it was already presented in figure 4.14. While the TNSA process forms a momentum spike at the target rear side in the proton phase space (figure 4.16d), a second spike originates from an electric field peak at the target front. This acceleration regime is regularly observed in numerical studies (see [57, 161, 205, 72]) and will be further discussed in region II. In the case of the simulation run (1), front side acceleration leads to similarly high proton energies as the TNSA mechanisms at the rear side. Protons accelerated at the front side can be injected into the rear side fields for post acceleration, a scenario often discussed in the literature (e.g. [205, 223]).

Region II: Directed proton emission by acceleration in the target bulk from near-critical density plasmas

For the target configuration in region II, the electric field peak at the front side becomes much stronger and proton acceleration becomes more efficient, resulting in increased proton energies. For the best performing plasma density distribution in simulation run (2) (second column in figure 4.16) with $n_0 = 13.3\,n_{c,800\mathrm{nm}}$, protons are predominantly accelerated by the electric field at $y \approx -1.5\mu\mathrm{m}$ in figure 4.16b, that is several times stronger than the rear side TNSA field. The process that leads to the strong electric field can be described as follows: Electrons are pushed inward by the ponderomotive force which leads to a steep-

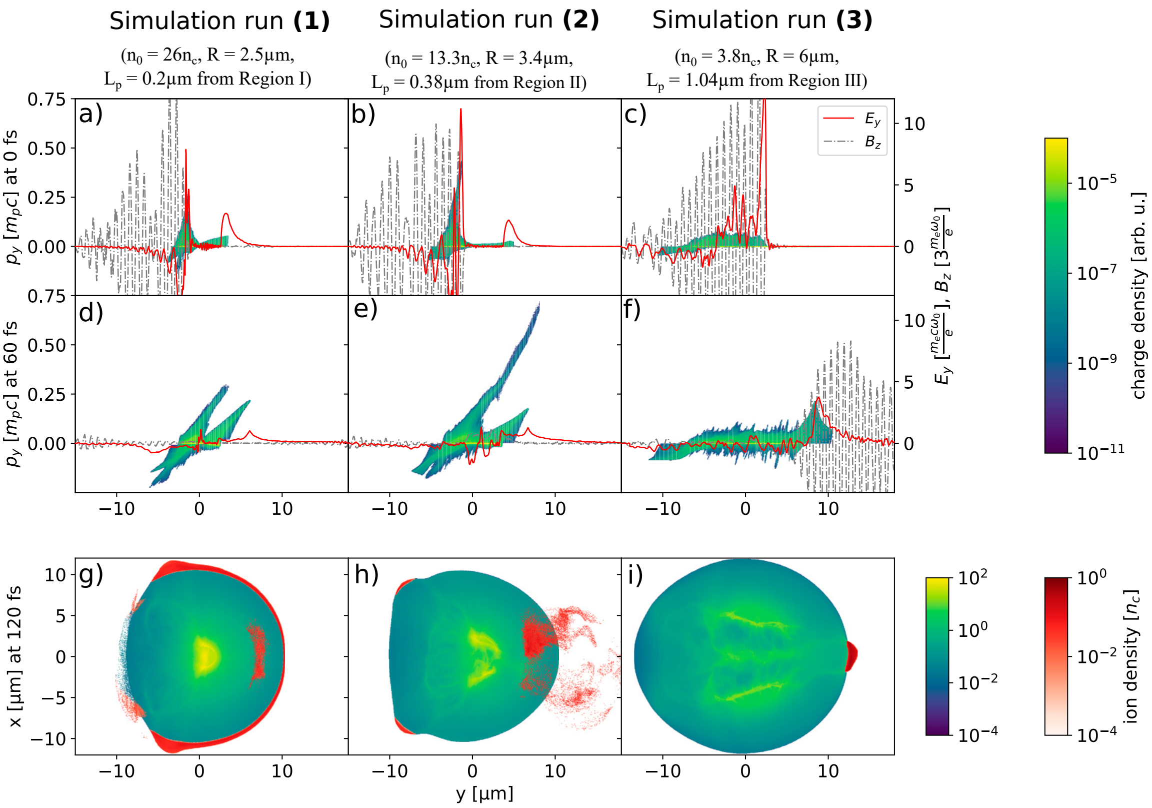

Figure 4.16: Longitudinal proton phase spaces and proton density distributions in the xy-plane (averaged over 1 µm in z-direction) for sample simulation runs in the different regions (I, II, III) that are presented in separated columns (left, middle, right). The first (second) row shows the simulation time when the peak intensity is supposed to reach the target center (+60 fs). On-axis electric (E_y) and magnetic (B_z) field components (averaged over a 1 µm^2 cross section) are overlaid to demonstrate the accelerating filed structure and the strength of the pulse, respectively. When displaying the proton density (third row), the distribution of protons with kinetic energies above 90% of $E_{p,max}$ is indicated by an additional red color scale.

ing of the plasma density. At the position of the leading laser edge, that is illustrated by the magnetic field component B_z in figure 4.16b, a charge separation layer forms which gives rise to an electrostatic field, that co-propagates with the laser pulse into the target. Due to the continuously impinging pulse, E_y penetrates the plasma with a velocity v_{E_y}. By evaluating the y-position of the E_y peak for several time steps spanning from -15 fs to 15 fs (the pulse duration centered at 0 fs), an average velocity of about $v_{E_y} \approx 8 \cdot 10^7$ m/s can be obtained. Protons are accelerated by the forward moving electric field and reach a kinetic energy of up to ∼185 MeV. This is the dominant contribution in relation to the final proton energy of 220 MeV. Compared to the electric field moving with v_{E_y}, the velocity of 185 MeV protons is about twice as high as v_{E_y}. After penetrating the bulk of the target, the energetic protons are then injected into the TNSA structure for post acceleration (similar to [205]).

The highest proton energies in region II are reached for an initial plasma density of about $0.6 \cdot y n_{c,800\mathrm{nm}}$ in simulation run (2) which agrees roughly with the numerical studies presented by [72]. According to Stockem et al., $0.5 \cdot y n_{c,800\mathrm{nm}}$ marks a characteristic density for a (gradual) transition from a target that remains overdense to the pulse due to compression by radiation pressure to a scenario where the plasma is transparent and the laser beam starts to propagate through the bulk.

A minor additional effect is a slightly higher laser absorption (yellow line in figure 4.13) in region II compared to region I. The pulse can, at least partially, transmit the target which leads to a more volumetric and a more efficient laser energy transfer to electrons.

The underlying acceleration mechanism has been discussed in several theoretical works [205, 72, 40] under slightly different perspectives. Therefore, possible explanations are briefly considered here. The scenario in the simulation run (2) closely resembles the process of hole-boring [31, 30]. However, analytic expressions for hole-boring [30] arrive at $v_{HB} = 2.8 \cdot 10^7$ m/s (equation 2.23) for our simulation conditions ($a_0 = 33$, $n_0 = 13.3\, n_{c,800\text{nm}}$) and therefore significantly underestimate v_{E_y}. This mismatch is potentially caused by the fact that the hole-boring model in equation 2.23 requires $n_e \gtrsim a_0 n_c$ [66] and is therefore not be applicable in this scenario. While compression of the electron fluid due to the strong laser pulse [84] to approximately $30\, n_{c,800\text{nm}}$ (based on n_{max} in figure 4.13) allows hole-boring to occur at initial plasma densities smaller than $a_0 n_c$, maximum kinetic energies of accelerated protons can be significantly higher [134] than the prediction from equation 2.23. According to Psikal et al. [205], an additional effect is self-focusing of the narrow laser beam inside the plasma, as a higher a_0 results in a linear increase of v_{HB}. Another potential explanation for the dominant proton acceleration in simulation run (2) is collisionless shock acceleration (CSA) [37, 39]. As discussed by Stockem Novo et al. [72], under the right laser and target conditions the shock velocity can exceed the hole-boring speed, making CSA the dominant process for proton acceleration. However, a clear shock front that detaches from the leading laser edge due to the higher propagation speed is not visible in the simulation results in figure 4.16.

A third potential explanation is synchronized acceleration by slow light (SASL) [40, 41]. In this scheme, a laser pulse that penetrates into a near-critical density plasma generates a ponderomotive electric sheath by pushing the electrons, which in turn accelerates ions. The laser pulse then increases its group velocity so that it corresponds to the ion velocity, causing the ions to experience synchronized acceleration. For the simulation run (2), the current status of the evaluation indicates that proton acceleration by slow light is the most likely explanation. However, preliminary results show that this mechanism is not optimized in this case since the velocity of the laser front increases only at early times synchronized with the proton velocities. Nevertheless, a detailed comparison of hole-boring, shock acceleration and proton acceleration by slow light is beyond the scope of this thesis and will be investigated elsewhere.

Region III: Magnetic vortex acceleration in a (relativistically) transparent plasma.

For the target configuration in region III, the pulse penetrates the entire target. For simulation run (3), this is shown by the resulting channel formation in figure 4.16i and additionally by the magnetic field component in figure 4.16f. Furthermore, the initial core density is clearly below the theoretical threshold for relativistic transparency and the steeping by the laser pulse increases the on-axis density only slightly (see n_{max} in figure 4.13).

Similar to simulation run (2), a strong electric field is generated at the laser front in simulation run (3), as displayed in figure 4.16c. With a velocity of $\approx 2 \cdot 10^8$ m/s, v_{E_y} is higher than in

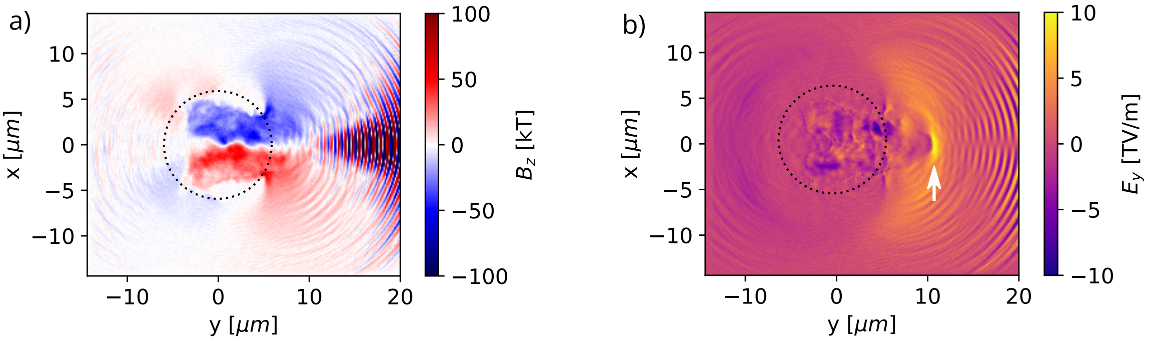

Figure 4.17: Distribution of a) magnetic field B_z and b) electric field E_y component in the xy-plane for the simulation run (3) (initial target conditions: $n_0 = 3.8\,n_{c,800\mathrm{nm}}$, $R = 6\mu\mathrm{m}$, $L_p = 1.04\mu\mathrm{m}$). The results are shown for a simulation time of 80 fs. The oscillating structure for y > 10 μm refers to the laser pulse. The black dotted circle illustrates the initial position of the core and a white arrow points to the area with the spatially limited electric field component in b).

the simulation run (2). The laser front now moves too fast to efficiently accelerate protons in the bulk, as indicated by the relatively small absolute momenta in the proton population behind the laser front in figure 4.16f. However, at later times (figure 4.16f) an additional electric field is observed at the target rear side, which leads to an efficient acceleration of protons. The underlying mechanism can be explained by magnetic vortex acceleration (MVA). By penetrating the plasma, the laser beam forms a channel (figure 4.16i) and exits at the rear side. The pulse accelerates electrons inside the channel in laser propagation direction probably due to a non-linear wake-field structure. The electron current leads to the formation of a toroidal magnetic field with a magnitude in the order of several 10 kT as shown by the B_z component in figure 4.17a. The magnetic field pinches electrons and ions leading to a larger density in the center of the channel (figure 4.16i). B_z further exits the plasma on the rear side and extents a few micrometers outside the initial target shape (figure 4.17a). This structure in the magnetic field is often associated with the onset of a magnetic vortex that induces an electric field at the target rear side, which accelerates protons. This mechanism was introduced in section 2.2.1. For simulation run (3), E_y is on the order of several TV/m, as displayed in figure 4.16f and protons are accelerated to energies beyond the TNSA performance in simulation run (1). Moreover, the strongest electric field is transversely limited in size (white arrow in figure 4.17b) which leads to the directed proton beam that was discussed using figure 4.14.

In contrast to acceleration in region II, where a strong dependence on the plasma density distribution is observed (see figure 4.13), MVA is less sensitive to the exact density distribution (refer to section 4.6.4). Since it is therefore possible to generate stable proton beams with maximum energies that are higher than in the TNSA case, studying the MVA regime is particularly interesting for future experiments with the cylindrical jet target. Accordingly, it is important to determine how the target shape can be optimized for MVA. In general, two conditions must be considered. First, the laser spot size should match the channel diameter given by relativistic self focusing. Second, the target thickness should be selected such that the laser pulse is fully depleted at the rear side (see section 2.2.1 for detailed information). The optimum for the second condition can be determined using the model from Bulanov et al. [43]. This model allows estimating the matching laser and target conditions under which the pulse is depleted when reaching the target rear side and thus is efficiently converted into kinetic energy of the plasma particles. With constant laser parameters, the optimal target would satisfy the condition given by equation 2.22. For our numerical (as well as experimental) pulse parameters with a laser power of ≈ 600 TW and a pulse duration of 30 fs, one arrives at $(n_e/n_{c,800\text{nm}})^{2/3} \cdot l_d \approx 65\,\mu\text{m}$. At a core density of $3.8\,n_{c,800\text{nm}}$, as in simulation run (3), the target would have to be about 27 µm thick for the laser pulse to be completely depleted. Since the target is only half as thick (about 12 µm) in simulation run (3), a large fraction of the laser pulse penetrates the plasma without getting absorbed. Based on equation 2.22 and the pre-expansion target characterization, for an initial 5 µm solid hydrogen jet the transfer of laser energy into kinetic energy of the plasma particles is supposed to be more efficient for a less pre-expanded target with a higher core density. This is due to the fact that a linear reduction in thickness results in a quadratic increase in core density due to the radial symmetry of the expansion dynamic. The expression $(n_e/n_{c,800\text{nm}})^{2/3} \cdot l_d$ is larger for a less pre-expanded target and thus closer to the optimum of 65 µm. At least the three simulation runs with the lowest core density in figure 4.13 confirm the assumption of better absorption of the laser energy for a higher core density, as shown by the yellow line.

To satisfy the condition of matching the laser spot size with the channel diameter, the required plasma density for a channel size equal to the simulated laser spot size (4.1 µm) can be calculated using equation 2.21. This results in $n_e \approx 2\,n_{c,800\text{nm}}$ for the employed pulse of 600 TW. While matching the channel and laser spot size seems to favor lower plasma densities, the optimal absorption prefers higher densities. When combining both conditions it is likely that the best performance in terms of maximum proton energies is reached at intermediate densities of about $5\,n_{c,800\text{nm}}$ as indicated by the simulation results in figure 4.13.

Based on this discussion, a better proton performance is expected for an initially thicker jet target. For the experimental studies a 10 µm cylindrical hydrogen jet is probably most interesting. Pre-expansion to 24 µm reduces the density to $4.4\,n_{c,800\text{nm}}$ accounting for a scale length of 1.04 µm as in region III. A PIC-simulation of these conditions predicts proton energies exceeding 120 MeV when using the same laser pulse. This already demonstrates the potential gain in performance with a more optimized target configuration. Additional PIC simulation runs examining slightly different profiles can be used to further optimize the target conditions and thus improve the acceleration contribution of MVA in future experimental studies.

4.7 Conclusion

Proton acceleration studies at the high-intensity laser system DRACO with cylindrical and planar cryogenic hydrogen jet targets were presented. Those studies serve as the continuation of a series of experimental campaigns [55, 57]. The successful implementation and long-term operation of the jet target in the harsh laser-plasma environment demonstrate the suitability for debris-free generation of single-species ion beams even under the increased demands of multi-10 J interactions. Moreover, due to the developments of a mechanical chopper system that prevent damage to the source nozzle, the stability of the laser target overlap and therefore the hit probability was significantly improved compared to earlier campaigns.

The jet was found to be a useful tool to determine the temporal target evolution by optical probing when irradiated with a laser pulse. The intensity threshold for turning opaque allows investigating the ionization processes and provides an independent measurement that can complement the typical laser contrast metrology. Furthermore, cylindrical and planar jets were recently deployed in a campaign with much lower intensities that aims to rigorously determine the threshold for ionization. Results of this are currently evaluated [201, 215].

The studies with the planar jets demonstrate that these targets can be implemented at a PW laser system and are particularly interesting when it comes to high repetition rates and debris-free operation at optimized performance. For comparable laser contrast conditions and target thicknesses (same areal density), the achieved proton beam performance from sheet-like hydrogen targets is comparable to non-renewable thin plastic foils with respect to maximum proton energies and even shot-to-shot stability. Although the acceleration performance is significantly lower than that of optimized plastic foils, it was shown that similarly high proton energies are expected from planar jets about twice as thick (0.5 µm) when the temporal pulse shape is adjusted. Therefore, nozzles with larger apertures are recommended for future campaigns. Moreover, by adjusting the operating conditions of the cryogenic source, it would be possible to systematically manipulate the sheet thickness and thus optimize the acceleration performance.

The target density, the decisive parameter defining which ion acceleration mechanism occurs, was tailored in another experimental run using cylindrical jets with 5 µm diameter. Under PM-cleaned laser contrast conditions, proton acceleration from these jets is dominated by TNSA, reaching maximum energies comparable to those of micrometer-thick foil targets. Proton numbers are about 2-3 times lower due to the curved geometry of the cylindrical jet. This agrees well with the experimental results from earlier experimental campaigns [57]. The manipulation of the plasma density distribution by pre-expansion due to an artificially introduced pre-pulse led to a significant increase of the maximum proton energies by up to a factor of two. The angular distribution of the proton emission is additionally influenced by the pre-expansion. The isotropic proton emission in the plane perpendicular to the jet axis in the unexpanded case is shifted towards a more directed proton beam in laser forward direction when the jet is pre-expanded. The generation of proton beams with kinetic energies up to 80 MeV with a target system that is in principle capable of providing high repetition rate delivery of a renewable pure hydrogen jet marks an important step towards applications of laser-driven particle sources. While under well-controlled pre-expansion conditions the number of shots is limited by the plasma mirror device, at intrinsic contrast protons with similar maximum energies can be produced with virtually no limit on the number of shots and a repetition rate only restricted by the laser system.

The pre-pulse essentially varies the target density by more than two orders of magnitude, ranging from an overdense target to a classically transparent plasma. Optical probing provides a detailed target expansion model that serves as a precise input for numerical studies. 3D-PIC simulations are in good agreement with the experimental results regarding the increase in maximum proton energy for a reduced core density and the divergence of the emitted particle beam. The simulations reveal the existence of two regions where proton acceleration is more efficient than TNSA from an unexpanded target. Under idealized conditions, acceleration in the bulk at near-critical densities by presumably SASL predicts the highest proton energies of more than 200 MeV, though experimentally very challenging to reach with the cylindrical jet. The dominant acceleration mechanism for slightly lower plasma densities is identified to be magnetic vortex acceleration. Although MVA is less efficient, it is experimentally more stable to achieve. The experimental observation of an increase in maximum proton energy from 40 MeV to 80 MeV with decreasing density could thus be identified as a transition from TNSA at solid density to enhanced acceleration in the near-critical density regime. Thereby, potentially both MVA and SASL contribute to the enhanced performance. Recent numerical studies to further investigate the contribution of these acceleration mechanisms in a less idealized scenario are currently analyzed. For this purpose, PIC simulations of the pre-pulse target interaction are combined with hydrodynamic expansion studies over a few tens of picoseconds and another PIC simulation that not only includes the Gaussian temporal shape of the high intensity pulse but also models the intensity slope in a few 100 ps before the peak. Preliminary results indicate that the acceleration in the region of the experimentally observed increase in maximum proton energy is dominated by SASL, while the influence of MVA is reduced due to the extended scale lengths on the rear side.

The experimental control and different plasma-based acceleration mechanisms made it possible to demonstrate high-energy proton beams from an advanced high repetition rate target system. A number of mechanisms (TNSA, MVA, RIT, SASL) are identified that can be addressed and further optimized in terms of their performance using the cryogenic jet target. With the help of numerical studies, the most beneficial plasma density distribution can be identified in each of the different regimes while differently sized and shaped jets can be adapted to meet the requirements. Complementary experiments to investigate e.g. the target pre-expansion with an ultraviolet probe beam, that is capable of sub-micrometer resolution, are currently analyzed [201, 215] and will further refine the simulation input. In order to reliably achieve the conditions for SASL in future experiments, the target must especially provide a precise core density. To keep the shot-to-shot fluctuations small, a planar geometry should therefore be used as the target, whereby besides the sheet jet, foils are also suitable. In the MVA regime, there is the potential to robustly accelerate protons to energies that are higher than in the TNSA regime. To optimize MVA and to limit the amount of hydrogen, an increase of the cryogenic jet diameter to about 10 µm is proposed instead of a planar geometry. The target shape obtained by pre-expansion (reduction of the core density to a few times n_c) is expected to feature a more efficient laser energy absorption and thus an enhanced acceleration performance. In the case of PM-cleaned contrast conditions, a sheet thickness of several hundreds of nanometers seems to be optimal for planar jets to provide a foil-like accelerator with debris-free operation at high repetition rates. Additionally, the possibilities to study the interaction in underdense plasmas with a strongly expanded jet shall be pointed out. Although the proton energy is lower, optical probes can be used to penetrate the plasma and potentially study microscopic processes of the acceleration.

Finally, all these opportunities for further studies of different acceleration mechanisms illustrate the need to be able to provide stable jets of different sizes and shapes. This motivates the further development of the target system and the demand for a detailed understanding of the involved fluid dynamics and solidification processes that shape the jet.

5 Investigation of picosecond plasma dynamics using optical probe pulses

The low-density and renewable hydrogen jet target is an attractive source for laser-driven proton beams, as presented in the previous chapters. In the best performing configuration, the target shape was optimized by a pre-expansion over a period of few tens of picoseconds. During this pre-expansion, prominent structures appear on the surface of the plasma, as it was pointed out in figure 4.11. More pronounced, the same structures can be observed on a time scale of tens of picosecond after irradiation of the hydrogen jet with an high-intensity laser pulse. Figure 5.1 displays a prominent example of this observation featuring characteristic "spikes" that appear radially in the target shadow. Although observed at several tens of picoseconds after the interaction with the intense laser pulse, those structures in the plasma density originate from the time when the high-intensity laser pulse irradiates the target. This raises the question if the proton acceleration, that occurs within the first picosecond, is affected by these perturbations at the target surface, as it is the case for other known modulations and instabilities studied in literature. For example, the homogeneity and reproducibility of the proton beam was found to be influenced by Rayleigh-Taylor or Weibel-like instabilities [55, 62, 224, 63, 225] or electromagnetic instabilities [60, 61]. Moreover, other potential causes for a modulated beam profile are structured or roughened target rear sides [218, 6, 8] that lead to a microfocusing phenomenon [226] or the imprint of laser near-field features into the proton bunch due to ionization of the residual gas content [58].

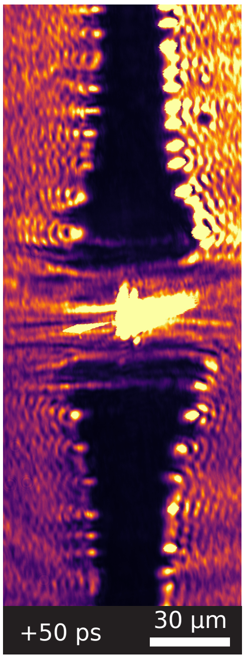

Figure 5.1: The shadowgram (recorded 50 ps after irradiation) shows characteristic spike-like structures at the observed target surface.

Understanding and potentially controlling the characteristic spikes in figure 5.1 is important since the usage of laser-driven accelerators for application requires, besides the adjusted proton energy, a high beam quality and reproducibility. This is in particular related to the uniformity of the spatial beam profile which is often desirable in e.g. medical application in order to deliver a uniform dose distribution [22, 24], as an injector into conventional accelerator structures [17] or for proton radiography [11, 12, 13].

The experimental studies in this chapter thus aim to investigate the evolution of the axial plasma density modulations in figure 5.1 and understand their cause. During two runs at the 150 TW arm of the DRACO laser system the modulations are characterized at different pump pulse intensities and target configurations using an optical probe beam. Two potential mechanisms, magneto-hydrodynamic instabilities and Weibel-induced filamentations are discussed as causes of the plasma density modulation due to their structural similarities as well as previous publications with comparable experimental conditions.

Laser-generated magneto-hydrodynamic (MHD) instabilities [64] are the result of return currents that generate large magnetic fields, which in turn radially compresses a wire-like target. This phenomenon has been extensively studied with pulsed power generators (Z-Pinches) in experiments [227, 228, 229] and with hydrodynamic codes [230, 231, 232, 233, 234, 235, 236]. Laser-produced return currents are a promising candidate for studying MHD instabilities on a time scale of picoseconds instead of the nanosecond time scales, which are usually achieved with pulsed power generators. The multi-MA [64] picosecond current pulses can have current rise times significantly shorter than the growth times of MHD instabilities, mitigating instabilities during the pinching process and potentially reach extremely over-critical density regions, as shown in simulations [237]. Moreover, laser-generated MHD instabilities can be used to model certain astrophysical phenomena on a laboratory scale, as for example the explosion of supernovas [238] or the origin of filaments in the Crab Nebula [239]. Although the temporal and spatial scales differ by several orders of magnitude, the same dynamics occur if the corresponding dimensionless numbers [234, 240], e.g. the Reynolds number, are of the same scale. The second hypothesis, the thermal anisotropy Weibel instability (TAWI) is attributed to the lower radial temperature compared to the axial and azimuthal temperature in an expanding wire-like plasma and was investigated by Quinn et al. [65] with proton radiography. Similar to the MHD instabilities, the interest in TAWI is motivated in an astrophysical context by the amplification of magnetic fields and their influence on phenomena such as energetic electromagnetic emission from gamma ray bursts [65] or the foreshocks of supernova remnants [241].

This chapter is structured as follows. Section 5.1 presents the experimental results. The two hypotheses are then introduced in section 5.2 (MHD instability) and section 5.3 (TAWI). In section 5.4, both hypotheses are discussed with the help of particle-in-cell simulations and compared with the experimental measurements. Simulations support the investigations of both hypotheses by studying the driving mechanism, the return current distribution and the temperature anisotropy, revealing that either instability possibly contributes to the development of the observed plasma density modulations.

5.1 Pump-probe experiments at DRACO 150 TW

The systematic experimental investigation of the plasma density modulations was performed in two runs during the first campaigns with the cryogenic jet target at the 150 TW arm of the DRACO laser system. The main objective in the first run was to investigate relativistic electron streaming instabilities [55] and to demonstrate a stable 1 Hz proton source [56]. The second run was performed during the campaign in which laser-proton acceleration from hydrogen jet with optimized laser conditions was studied [57]. Modulations in the plasma density distribution were observed during all experiments with the cryogenic jet target, even at low intensities in the pre-pulse expansion studies (chapter 4.6.3). However, this data analysis focuses on the runs at the 150 TW since they provide the most systematic scan of several laser and target parameters. The experimental setup is comparable to chapter 4 with respect to the arrangements and setup of diagnostics but differs in experimental parameters due to the earlier stage in the development. Thus, diagnostic methods were not as advanced as in the studies at the DRACO petawatt arm.

A schematic overview of the arrangement is given in figure 5.2a. Differences between the two runs with respect to laser and target parameters are described in the table in figure 5.2b. The 150 TW arm of DRACO produces laser pulses with energies of up to 3 J on target and durations of 30 fs (FWHM). By using an off-axis parabolic mirror (OAP) with f/2.5, laser pulses were focused to a spot size of 3 µm (FWHM) resulting in peak intensities of up to $5 \cdot 10^{20}$ W/cm^2. The hydrogen jet target, introduced in section 3.2, was extruded through cylindrical apertures with diameters of 2, 5 or 10 µm. If ionized, the solid density of hydrogen corresponds to an opaque plasma with an electron density of 30 times the critical density at 800 nm ($n_e = 5.1 \cdot 10^{22}\,\mathrm{cm}^{-3}$). An optical probe beam was used for the characterization of the laser target interaction perpendicular to the DRACO laser axis (see figure 5.2a). In the first run, a frequency-doubled leakage (∼mJ pulse energy) of the DRACO laser pulse with a duration of about 0.5 ps and a wavelength of $\lambda_p = 400$ nm was used. An independent probe beam produced by a frequency-doubled Yb:YAG laser system with a central wavelength of $\lambda_p = 515$ nm and a pulse duration of about 1.8 ps was utilized in the second run. The 515 nm probe pulse was synchronized to the DRACO pump beam [59] and has the advantage that the probe wavelength is not a harmonic of the pump laser pulse. Shadowgraphy images of the target were recorded on each laser shot by using a long working distance objective with a numerical aperture of f/1.6, yielding a spatial resolution of about 2 µm and a temporal resolution on the picosecond level given by the pulse duration of the probe laser. The laser target interaction point was defined 10 mm to 15 mm below the jet nozzle in order to prevent potential damage to the source. (The mechanical chopper system was not yet available.) For the second experimental run, a single plasma mirror (PM) setup [209] was used to enhance the laser contrast and thus to reduce pre-expansion in comparison to the experiments in run I at intrinsic contrast. Since the pointing jitter of the jet results in shot-to-shot fluctuations of the laser target overlap, as discussed in section 4.5, proton spectra detected by a Thomson parabola spectrometer (TPS) in laser direction were used to filter the shots on the basis of their maximum proton

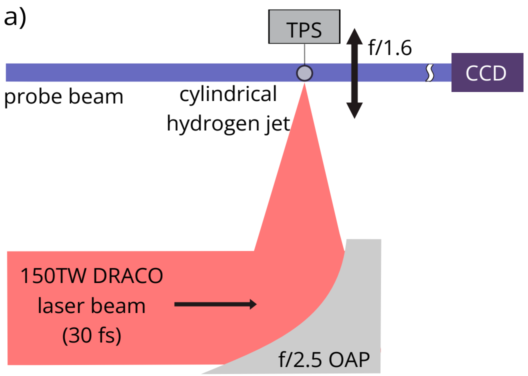

b)	probe beam	target size	laser energy
run I inherent laser contrast	400 nm 0.5 ps	⌀ 2 µm	2.2 J
		⌀ 5 µm	3 J
		⌀ 10 µm	0.6 J
run II PM enhanced contrast	515 nm 1.5 ps	⌀ 5 µm	2.4 J

Figure 5.2: a) Schematic of the experimental setup: Laser pulses (up to 3 J, 30 fs) are focused on a cryogenic hydrogen jet target. The probe beam (400 nm or 515 nm configuration) is used for spatially and temporally resolved imaging of the picosecond plasma dynamics. Proton spectra are recorded with a Thomson parabola ion spectrometer (TPS) in laser forward direction. b) Configurations of target sizes, laser energies, laser contrast conditions and properties of the probe beam for both experimental runs.

energies. Only shots with proton cut-off energies above $2/3 \cdot E_{p,max}$ were considered for the analysis presented in this chapter, where $E_{p,max}$ is the highest measured proton cut-off energy for the corresponding configuration. This filtering guarantees that only shots with sufficient laser-target overlap are considered, enabling systematic studies of the plasma dynamics.

The evolution of the irradiated target density distribution was characterized by delaying the probe beam up to 100 ps with respect to t_0, where t_0 is the time when the peak intensity of the pump beam arrives at the hydrogen jet. Three time series of single-shot shadowgraphy images are shown in figure 5.3 for different target and laser parameters. The vicinity of the central part of the recorded images is saturated by plasma self emission that is much stronger than the probe beam illumination. Compared to run I, the reduction of self emission in run II is due to the implementation of the plasma mirror and the off-harmonic probe beam [59]. The dark region in the center of all probe images corresponds to an opaque plasma that is formed by the ionized hydrogen jet. In shadowgraphy, the plasma dynamics can primarily be derived from the evolution of the interface between transparent and opaque regions. It can be estimated that the threshold density n_{th} at this interface corresponds to a plasma density on the order of the critical density for the given probe wavelength (n_{c,λ_p}). However, the exact value of the density, where the transition occurs, is supposed to be several times lower, since refraction in the near-critical plasma can deflect beamlets of the probe light to angles exceeding the acceptance of the imaging system. As an example, for the similar configuration of a pre-expanded target in chapter 4.6.3 it was estimated that the transition from opaque to transparent takes place at a plasma density that is about five times lower than the critical density. At later times, the expansion of the irradiated target results in a decrease of the plasma density below the critical density and thus in a transparent plasma. This effect is observed in the case of the 5 µm hydrogen jet in the area near the interaction region for delays starting at 50 ps (figure 5.3l and m). Note that the shadow reaches a width of about 45 µm before turning transparent, which is larger

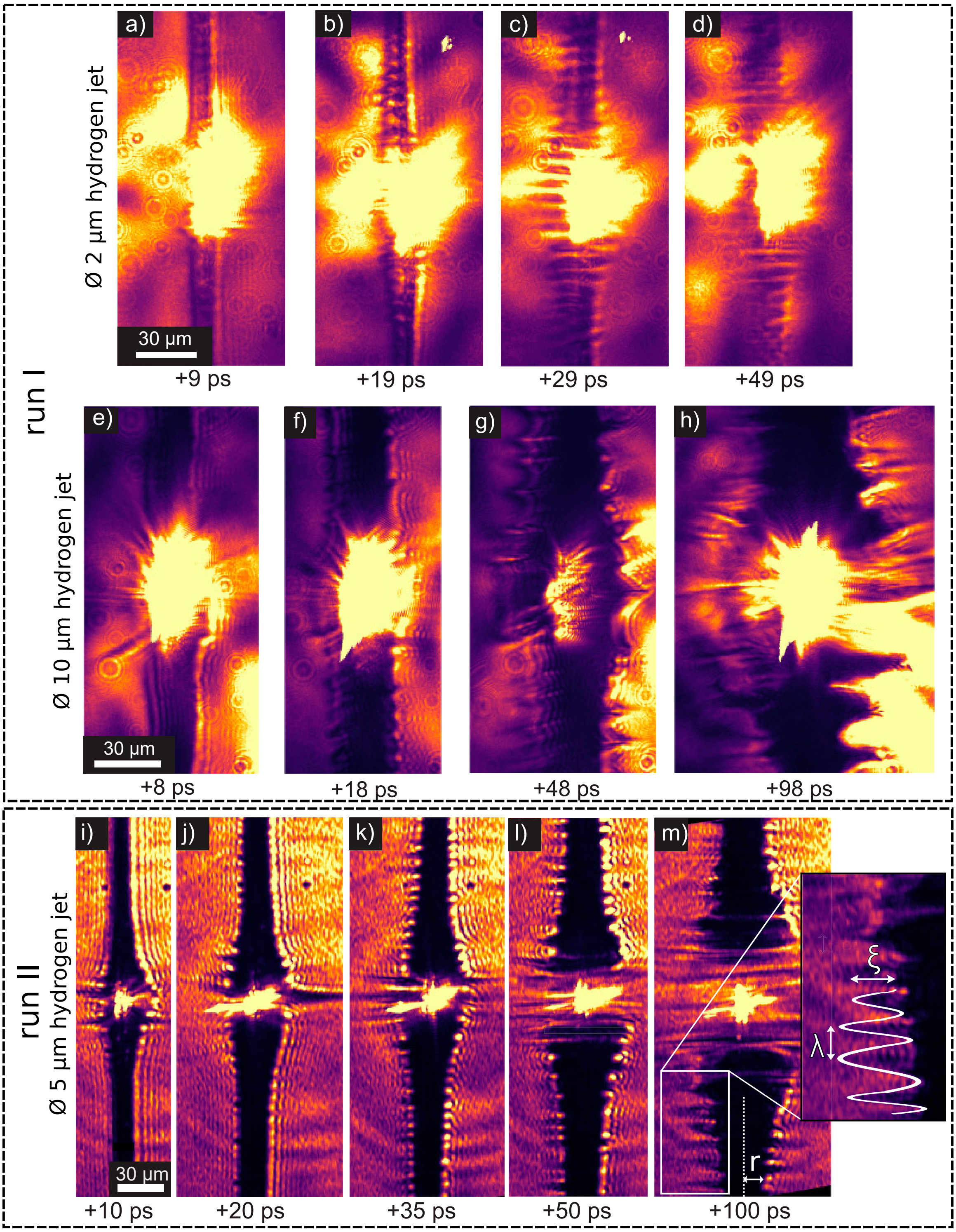
run I
Ø 2 µm hydrogen jet
a)
b)
c)
d)
30 µm
+9 ps
+19 ps
+29 ps
+49 ps
Ø 10 µm hydrogen jet
e)
f)
g)
h)
30 µm
+8 ps
+18 ps
+48 ps
+98 ps
run II
Ø 5 µm hydrogen jet
i)
j)
k)
l)
m)
30 µm
ξ
λ
r
+10 ps
+20 ps
+35 ps
+50 ps
+100 ps

Figure 5.3: Experimentally recorded shadowgraphy images (presented in false-color) of the laser-irradiated hydrogen jet for different probe delays (displayed below the image) in comparison to t_0. The pump beam incidences from left to right. The experimental conditions for each run and target are presented in figure 5.2b. The inset in m) illustrates the parameterization of the density modulation: amplitude ξ, wavelength λ and radius r.

than the 30 µm found in chapter 4.6 for the target pre-expansion studies. This difference can likely be explained by the implementation of the imaging system in run II that utilized spectral filtering using a reflective grating in the Fourier plane of a 4f-imaging system [59] in order to mitigate the plasma emission. The filtering reduced the acceptance angle of the imaging system and therefore the maximum divergence of deflected beamlets that are imaged to the CCD. As described by the ray-tracing calculations in section 4.6.3, this shifts the transition from an opaque to a transparent plasma to lower densities that are present at larger plasma expansions. Based on the procedure in section 4.6.3, the threshold density in this case can be estimated to be about one order of magnitude below the critical density for the given probe wavelength. This corresponds to about $0.1\, n_{c,515\text{nm}} \approx 0.25\, n_{c,800\text{nm}}$. The transition to a fully transparent plasma for the probe beam is further found for the 10 µm jet in the last observed time step (figure 5.3h) and for the 2 µm jet case between 20 ps and 30 ps (figure 5.3c and d).

The picosecond evolution of the interface between transparency and opacity in figure 5.3 features an overall radial expansion superimposed by an axial modulation of the plasma density. Three parameters are used to quantify the temporal evolution for the different laser and target conditions, shown in figure 5.4. Δr characterizes the radial expansion of the interface in comparison to the initial target radius. Since the axial plasma density modulation shows a wave-like pattern (inset in figure 5.3m) it is therefore described by a wavelength λ (axial distance from peak to peak) and an amplitude ξ (radial peak to valley distance). The region more than 50 µm above and below the interaction point was chosen for studying the evolution of these three parameters in order to avoid the plasma self emission.

Since shot-to-shot fluctuations and the optical resolution limit of 2 µm limit the significance of single measurements of ξ, λ and Δr, the values obtained are averaged from 3-5 images at

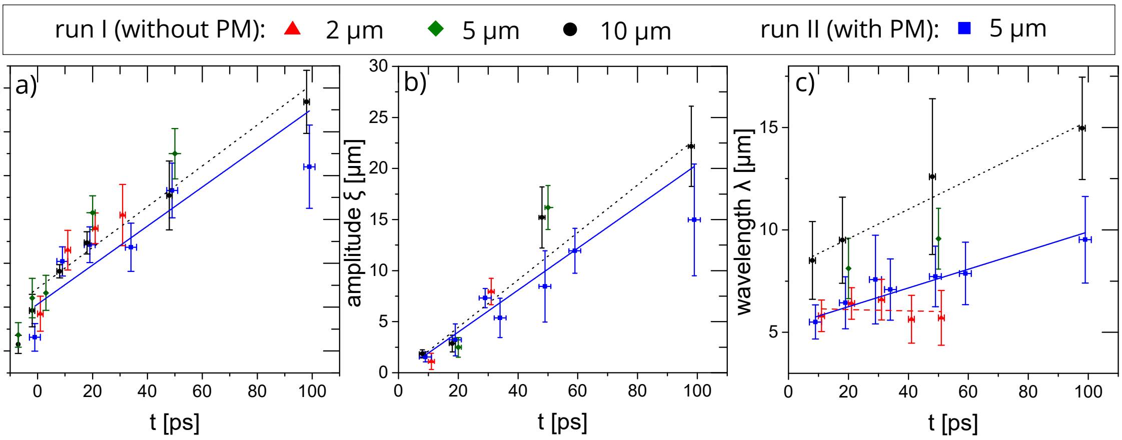

Figure 5.4: Radial expansion Δr (a), amplitude ξ (b) and wavelength λ (c) as a function of time for different experimental conditions (see table in figure 5.2). One data point represents the average values from 3-5 images recorded under the same experimental conditions. The error bars on the y-axis indicate the standard deviation and thus quantify the variation in the data set. Uncertainties on the time axis are determined by the probe pulse duration and the synchronization jitter. Linear regressions are shown in for two configurations (with the same color) to guide the eyes. The time on the x-axis is given relative to t_0.

nominally the same laser and target conditions. Furthermore, the following analysis of the temporal evolution of the three parameters in figure 5.4 is based on the general trends. The plasma radius in figure 5.4a shows a linear increase with time at an approximated velocity of $1 \cdot 10^5$ m/s. Surprisingly, Δr develops comparable for all experimental configurations and therefore seems to be mostly independent of the employed laser and target parameters. This demonstrates in particular that the difference in pulse energy (see figure 5.2b) has only a limited effect on the plasma expansion for the region more than 50 µm above and below the interaction point. Compared to a pre-expansion of about 2 µm in run I, the usage of the plasma mirror device in run II prevents the radial expansion prior to t_0, as shown at $t \approx 0$ ps in figure 5.4a (blue data points in comparison to green, red or black data points).

The amplitude of the plasma density modulation in figure 5.4b also shows a nearly linear monotone increase for all configurations. ξ reaches up to 20 µm at 100 ps. The density modulation cannot be investigated for times earlier than 10 ps due to the insufficient spatial resolution of the probe system preventing observations of structures smaller than 2 µm. However, extrapolating ξ to t_0 suggests that the modulation starts to grow at about the arrival of the peak intensity. The second parameter of the density modulations, the wavelength, is shown in figure 5.3c. λ increases with time for most of the experimental configurations. Only for the 2 µm jet case no significant change of λ is found for times between 10 ps and 50 ps. This might be linked to the reduction of the density below n_c that turns the plasma transparent and thus prevents further observation of the same structure with optical probing. Comparing λ for the different jet diameters suggests a dependence on the plasma radius where larger target diameters are accompanied by lower density modulation frequencies ($\lambda/r \approx$ const.).

In summary, on a time scale of tens of picosecond after the irradiation of the hydrogen jet target, a modulation in the plasma density was observed which features an increase in amplitude and wavelength with time while the overall plasma expands. This indicates that as a result of the laser-plasma interaction, a process is triggered that causes the modulation of the plasma density. Two hypotheses for such a process are introduced and discussed in the following sections. Before doing so, the relevant time scale for the growth of the density modulation should be critically discussed on the basis of the experimental data. Since an increase in amplitude and wavelength is observed over time, one might assume that the plasma modulation grows on a time scale of several 10 ps. However, it is equally possible that the modulation is imprinted into the plasma density at early times (<10 ps) and become observable as the plasma expands. During evolution, the density is reduced by the expansion of the plasma. However, as the observed threshold density is about constant, different regions of the plasma with potentially different amplitudes and wavelengths are then probed for different delays. Based on the experimental data, it is therefore impossible to determine whether the plasma density is still subject to active changes after some 10 ps or whether a pure expansion reveals earlier imprints.

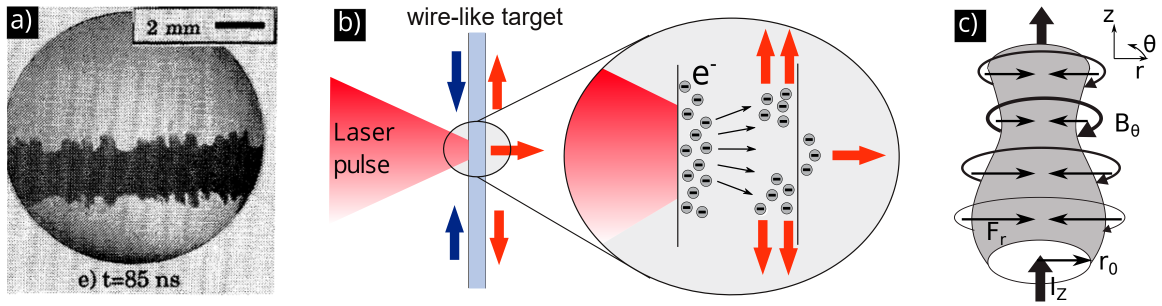

Figure 5.5: a) From Kalantar et al. [230]. A schlieren image of an aluminum wire (initial diameter of 100 µm) recorded at the peak of a 350 kA current pulse of ~ 100 ns duration shows modulations in the target diameter due to MHD instabilities. Note the much longer temporal and much larger spatial scale in comparison to the experimental results in figure 5.3. b) Model of the femtosecond dynamic of the irradiated wire-like target. Laser accelerated hot electrons (red arrow) leaving the interaction region are compensated by cold (blue arrow) return currents. c) Scheme of the m=0 MHD instabilities formation due to a pinching magnetic field generated by a current flow along the wire axis.

5.2 Magneto-hydrodynamic instability hypothesis

The first hypothesis that provides an explanation for the axial density modulations is based on magneto-hydrodynamic (MHD) instability signatures that are typically investigated in Z-pinch experiments (e.g. [230, 231, 232, 236, 233, 242, 243, 235, 227]). This hypothesis is motivated by a qualitatively similar structure when comparing the probing results from figure 5.3 with Z-pinch measurements. An example of such a measurement (from Kalantar et al. [221]) is shown in figure 5.5a. An additional motivation for this hypothesis is the work from Beg et al. [64], which claims the observation of an MHD instability in a laser-irradiated wire target experiment.

The key criteria for the onset of the MHD instability is a current flow that generates a magnetic field. In the Z-pinch experiments, this current is applied as a nanosecond pulse produced by an external pulse power generator. The origin of strong return currents as a potential driver for MHD instabilities in laser-driven plasmas on a picosecond timescale was first introduced by Beg et al. [64] and is illustrated in figure 5.5b. In this process, an intense laser pulse ionizes the target front side and transfers energy to the electron population in a thin surface layer. The hot electrons are able to leave the interaction region either by escaping from the rear side into the vacuum (only possible for the most energetic electrons) or by moving along the jet. This create a large electrostatic potential. A cold current in the opposite direction is then necessary to compensate for the resulting charge imbalance. Such return currents generated by irradiating solid targets with high-intensity laser pulses can reach values in the order of MA [64, 244].

The scheme in figure 5.5c demonstrates how the current flow in a wire-like (Z-Pinch) configuration leads to MHD instabilities. A current I_Z is sent through a cylindrical plasma in the z-direction. The resulting azimuthal magnetic field B_θ interacts with the particle flow associated with I_Z and generates an inwards direction Lorentz force F_r compressing (pinching) the plasma. While an internal pressure caused by joule heating of the plasma and the consequential thermal expansion can counteract F_r, this configuration is generally unstable and susceptible to the growth of MHD instabilities that amplify small perturbations on the surface of the wire-like target. In the case of the hydrogen jet, the initial perturbation can for example originate from inhomogeneities (small spikes or dents) in the liquid filament, as discussed in section 3.4.

It follows a discussion of the relevant MHD instability mechanisms in order to derive scaling laws that allow a quantitative comparison with the observed plasma density modulations. While this section focuses only on the important aspects of MHD instabilities for this work, a more extensive description can be found in the review from Haines [234], Ryutov et al. [233] or in the book from Liberman et al. [245]. In the linear stability analysis [234] of the Z-Pinch configuration, MHD instabilities are categorized into modes, where m=0 and m=1 are usually unstable and grow exponentially. Since m=1 refers to a transverse displacement of the plasma column from the z-axis (often termed kink instability), it differs from the axial symmetric experimental observation made here and is therefore negligible. The m=0 mode, on the other hand, is characterized by an axial symmetric signature and a target diameter that changes along the wire (in z-direction) which resembles the plasma density modulations observed here. While several mechanisms can lead to m=0 type signatures, the sausage and the magneto Rayleigh-Taylor (MRT) instability are the two dominant ones.

Sausage instability

The sausage instability arises as a direct consequence of the pinching Lorentz force originating from the interaction of the magnetic field and the current along the z-axis ($F_r \propto I_z \cdot B_\theta$). Assuming that the plasma column has a radius r_0 and the magnetic field B_θ is given by ampere's law

$$B_\theta = \frac{\mu_0 \cdot I_z}{2\pi \cdot r} \tag{5.1}$$

with μ_0 is the vacuum permeability and r is the radial distance from the wire axis, as illustrated in figure 5.5c. The compressing force associated with the magnetic field is further balanced for r_0 by an internal pressure p_i. This represents a simple form of the Bennett relation [246] that describes a pressure balance in a Z-pinch configuration. A reduction in radius ($r < r_0$) leads to an increase in magnetic field strength, since $B_\theta \propto r^{-1}$, and therefore to a stronger Lorentz force that overcomes p_i and thus results in a further decrease of r. Accordingly, a slightly higher initial r leads to further expansion. As a result, small perturbations in the radius are amplified. This scheme is referred to as sausage instability.

MRT instability

The magneto Rayleigh-Taylor (MRT) was introduced by [247] and further studied by e.g. [242, 243, 248, 235, 227]. In contrast to the sausage mode, MRT requires a dynamic configuration that features an acceleration of the plasma-vacuum interface. The concept is similar to the classical Rayleigh-Taylor instability [249, 250], where a heavy incompressible fluid is supported against gravity by a lighter one. Since the two fluids seek to reduce their combined potential energy, a perturbation at the interface will release potential energy when the heavier fluid is falling and the lighter fluid is rising. The same result is achieved when the system is accelerated upwards instead of gravity acting downwards. The lighter fluid can be considered as the magnetic field in the case of the MRT instability, while the heavy fluid is associated with the plasma cylinder. Here the MRT instability arises at the plasma-vacuum interface, where the magnetic pressure pushes the plasma.

The distinction between the sausage and the MRT instability is often not feasible in experiments because both require the same magnetic field as a driver. A purely MRT mode is present if, for example, there is no internal pressure, as is typically achieved with hollow thin walls cylinders (so-called cylindrical liners e.g. [235]). When the acceleration of the plasma-vacuum interface is zero, which is the case when the internal pressure balances the pinching force, then the interface becomes MRT stable and the sausage instability dominates. In the experimental observations presented here, the radial expansion velocity is about constant within the uncertainties and therefore the acceleration is close to zero. However, in particular, at earlier times (<10 ps) and at higher densities, where the plasma dynamics are not resolvable, accelerations different from zero may be present and an influence of MRT can thus not be excluded. Consequentially the MHD hypothesis will be further investigated assuming that both, the sausage and the MRT instability might be involved while using the term "(m=0) MHD instabilities" for their combined mode.

Both instabilities feature scaling laws for the characteristic growth time and the most dominant wavenumber that differ only slightly [228] as long as the wavelength of the instability is in the same order of magnitude as the plasma radius [245]. The first relevant characteristic of the MHD instability is the typical growth time τ that is defined as the inverse of the instability growth rate. In general, the order of magnitude of τ is given by [229, 228, 234]

$$\frac{1}{\tau} \approx \sqrt{\frac{B_\theta^2}{\mu_0} \frac{1}{\rho \cdot r_0^2}} \tag{5.2}$$

for the case of a wire-like target. Here, τ describes the time for the amplitude to grow by a factor of e_N, where e_N is Euler's number. μ_0 is the vacuum permeability, r_0 the initial radius of the solid wire, ρ the solid density of the target material and B_θ is the azimuthal magnetic field strength that can further be expressed with I_Z through equation 5.1. Calculating τ and comparing the result with the measurements in section 5.1 requires the knowledge of B_θ, which will be obtained by numerical simulation in section 5.4.

Secondly, scaling of the characteristic wave number of m=0 MHD instabilities was studied by e.g. [230, 251, 236]. These publications show that the plasma radius and the dominant wavelength λ_{MHD} are in the same order of magnitude. Moreover, a detailed examination [234, 236] further indicates that the product $2\pi/\lambda_{MHD} \cdot r$ stays about constant during the growth of the instability, potentially due to the transition to a nonlinear mode that leads to an increase of the dominant wavelength during the evolution. This correlation agrees with the experimental results from section 5.1 as the measured plasma radius and the modulation wavelength are both on a micrometer scale and increase at a similar rate over time.

5.3 Weibel-induced filamentation hypothesis

An alternative physical origin that could explain the experimental observations in section 5.1 is the thermal anisotropy-driven Weibel instability (TAWI) of the electron population. The hypothesis is motivated by the publication from Quinn et al. [65], where the observation of tube-like filamentary structures in an expanding plasma was attributed to TAWI. In that study, solid-density wire targets (50-100 µm) were irradiated with a high-intensity laser pulse (250-350 J, 700 fs) while the electromagnetic field structure was probed with protons on a time scale of several tens of picoseconds after the interaction. Figure 5.6a shows proton radiography results for three time steps between 10 ps and 50 ps after the interaction. This reveals structures that are comparable in spatial and temporal scale to the plasma density modulations observed in this work (see section 5.1). Although the proton probing diagnostic only resolves electromagnetic fields, it can be assumed that the tube-like filamentary structures are imprinted into the plasma density distribution that is visible with optical probing methods. Moreover, Quinn et al. also commented on similar structures that have been observed with optical shadowgraphy [65]. A schematic model of the current filaments is illustrated in figure 5.6b. It consists of a series of magnetic field tubes perpendicular to the surface of the wire with a superimposed electric field along the tube radii.

The origin of the electromagnetic field structure is a thermal anisotropy of the electron population that is attributed to the lower radial temperature (T_r) (in a wire geometry) in comparison to the azimuthal and axial temperature (T_θ, $T_z > T_r$). The reason for this probably stems from the radial charge separating field that accelerates ions and slows down electrons. The anisotropy $A = T_z/T_r - 1 > 0$ drives the thermal Weibel instability during the plasma expansion which was studied with numerical tools in e.g. [241, 252, 253, 254]. As a result, the magnetic field energy grows exponentially with a characteristics growth rate

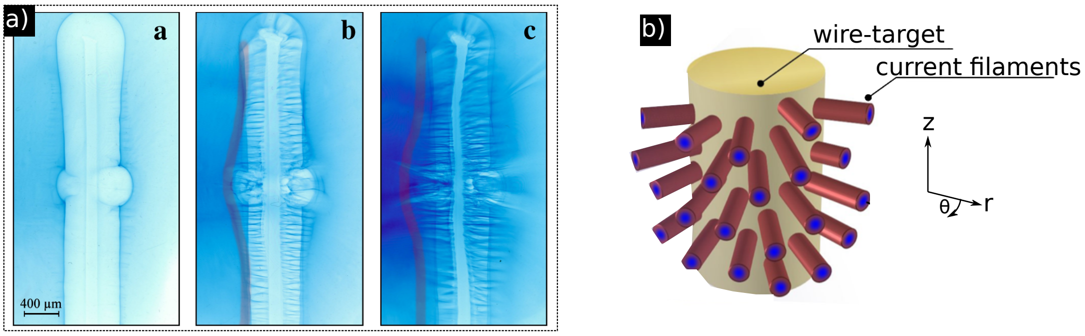

Figure 5.6: Both parts of the figure are adopted from Quinn et al. [65]. a) Proton radiography measurements, captured with RCF stacks, showing the electromagnetic field structure at ∼10 ps (left), ∼30 ps (middle) and ∼50 ps (right) after irradiation of the wire target. b) Schematic of the current filaments originating from the wire surface.

γ_{TAWI} given by [254]

$$\gamma_{TAWI} = k_{TAWI} \left(\frac{T_r}{m_e} \frac{A - c^2 k_{TAWI}^2/\omega_p^2}{1 + c^2 k_{TAWI}^2/\omega_p^2} \right)^{1/2} \tag{5.3}$$

that depends on the wave vector k_{TAWI}, the anisotropy A, the electron mass m_e, the plasma frequency ω_p (section 2.1.2) and the temperature perpendicular to the plasma surface T_r. Unstable modes, which are characterized by the fact that γ_{TAWI} is a real number, are required to fulfill: $A > c^2 k_{TAWI}^2/\omega_p^2$. The plasma system is therefore unstable for wave numbers in the range $0 < k_{TAWI} < k_{TAWI}^{max}$ where

$$k_{TAWI}^{max} = \sqrt{A} \cdot (\omega_p/c) \tag{5.4}$$

is the largest unstable wave vector. The fastest growing mode with the highest γ_{TAWI} is expected for a k_{TAWI} that is lower than k_{TAWI}^{max}.
For the TAWI hypothesis, the expected values of A can be estimated for the experimentally observed plasma density modulations in section 5.1. For this purpose, the plasma frequency and the wave number must be determined. Since the modulation of plasma density was observed at the transition between transparent and opaque plasma and thus at a plasma density of about $0.25\, n_{c,800\mathrm{nm}}$ (see section 5.1), a corresponding plasma frequency of $\omega_p = 1.16 \cdot 10^{15} \mathrm{s}^{-1}$ can be estimated. Assuming that the highest unstable wave vector of TAWI equals the typical wavelength of the plasma density modulation of about 5 µm from figure 5.4, $A = 0.1$ can be calculated based on equation 5.4. However, the estimate for A gives only the minimal anisotropy that explains the experimental modulations. Faster growth at the same wave number requires higher values of A. On the other hand, if TAWI occurs at higher plasma densities, the required anisotropy becomes lower. Despite the uncertainties in the estimations of A, a thermal anisotropy of approximately 10% seems reasonable in comparison to the results from Quinn et al. [65], where the radial electron temperature was found to be almost half of the azimuthal temperature. However, to determine whether such a thermal anisotropy occurs in the electron temperature, numerical studies are required.

5.4 Discussion based on numerical simulations

Numerical particle-in-cell (PIC) simulations were performed to further investigate if the two hypotheses (MHD or TAWI) provides a reasonable explanation of the experimentally observed plasma density modulations. However, simulating in a single PIC run the complete dynamics of laser-matter interaction in three dimensions on a spatial scale of several tens of micrometers and, most challenging, a temporal scale of tens of picoseconds is computationally too expensive and would exceed even the available resources of state-of-the-art supercomputers. However, restricting the numerical study to two spatial dimensions allows a large simulation area, which is comparable in size to the experimentally observed area. Although a very long simulation time of 4.5 ps can be achieved, the time at which plasma modulations were observed in the experiments (at least 10 ps) cannot be reached. Due to the spatial and temporal limitations of the simulations, a direct comparison with the experimental data is therefore not possible. As a consequence, the simulation is utilized to investigate the driver of the MHD (return currents) and TAWI (temperature anisotropy) hypothesis in the first few picoseconds to estimate characteristic time scales and wave numbers that are then compared with the measurements from section 5.1.

PIC simulations using the PICLS2D code [255] were performed for parameters corresponding to the experimental conditions. The simulation box has a size of 20.736 µm (=1296 cells in y-direction) and 122.68 µm (=7680 cells in z-direction), while each cell contains 200 ions and 200 electrons. The laser pulse is modeled as a Gaussian temporal profile with a full width at half maximum of 30 fs, a spatial Gaussian-shaped spot size of 3 µm and a peak intensity of $8 \cdot 10^{20}$ W/cm^2. The laser pulse propagates from left to right (in y-direction). In the two-dimensional geometry of the simulation, the jet target is modeled as a $d = 5\,\mu\text{m}$ wide (Extension in y-direction) rectangular shape with a height (z-direction) equal to the simulation box size. This corresponds to the side-view of the laser-plasma interaction. The target density $n_0 = 19.2\, n_{c,800\text{nm}}$ is only slightly below the density of solid hydrogen ($n_0 = 30\, n_{c,800\text{nm}}$). The low collisionality and low density of the hydrogen plasma facilitate the modeling by PIC simulations. Simulation results of current densities, magnetic fields, electron densities and temperatures are shown in figure 5.7.

Investigating the MHD hypothesis

The obtained simulation results will be discussed in the context of the two approaches, starting with the MHD hypothesis. Thus, the current flow that generates a magnetic field and therefore drives the instability is investigated. Figure 5.7a shows the distribution of the current density j in z-direction (along the wire) at 38 fs after t_0. The image indicates strong net currents with j_{peak} = 160 kA/µm^2 which are contained in a thin surface layer of about $\delta = 50$ nm (FWHM) while the bulk of the target only contains much smaller current densities (<1% of j_{peak}). The net current represents an electron flow towards the interaction point* caused by the charge imbalance originating from hot electrons escaping the interaction region. This simulation result agrees with the concept illustrated earlier (figure 5.5b).

The total return current I_A can be estimated by assuming that j is distributed on the ring-shaped surface with an outer radius r, which corresponds to half of the 5 µm target size. This approach assumes that the current densities from the 2D simulation are comparable to a 3D case. With an average $\bar{j}$ = 123 kA/µm^2 in the surface layer of thickness δ, the total current results in $I_A = \bar{j} \cdot \pi(r^2 - (r - \delta)^2) \approx 96$ kA. This value is comparable to reported laser-driven currents ranging from $\sim$10 kA [13, 256] to $\sim$ MA [64, 244].

While j is only present in a range of 30 µm above and below the interaction point at 38 fs, surface currents along the entire target are observed at later times, e.g. displayed for 500 fs after t_0 in figure 5.7b. However, j_{peak} dropped significantly in the first 500 fs to about

---

*The current density below (above) the interaction point flows in the positive (negative) z-direction and thus upwards (downwards).

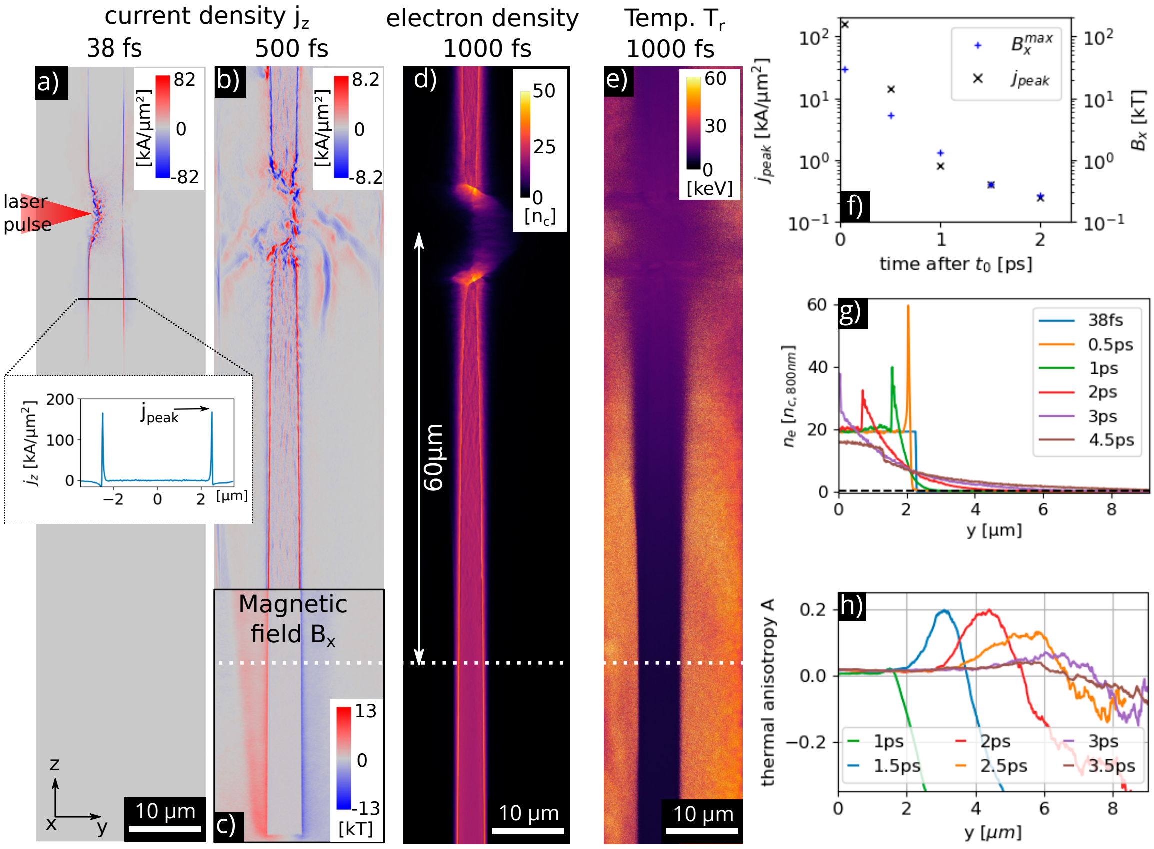

Figure 5.7: 2D PIC simulation results. a,b): Distribution of electron current densities in z-direction for 38 fs and 500 fs after the highest intensity reached the target (t_0). Red (blue) color indicates an upwards (downwards) directed current. Note that the color scale changes between a) and b). The inset in a) shows a lineout of the current density with the peak value j_{peak} of 160 kA/µm^2 located in a thin surface layer. c) Magnetic field in x-direction at 500 fs after t_0. Electron density distribution and radial electron temperature are shown for the 1 ps time step in d) and e), respectively. The dashed white line marks a distance of 60 µm below the interaction point and indicates the position for the lineouts in f)-h). f) The evolution of the peak current density (black 'x' marker) and the magnetic field strength at the target edge (blue crosses) both indicate a rapid decrease (by two orders of magnitude) over the course of 2 ps. Note that the value at 38 fs is taken from the inset in a) which is closer to the interaction region. g) Evolution of the rear side plasma density profile up to 4.5 ps. y=0 marks the target center and the black dotted line indicates 0.25 $n_{c,800\text{nm}}$. h) Thermal anisotropy *A* at the target rear side.

14 kA/μm^2 which is less than 10% of the peak current density at 38 fs. As shown in figure 5.7f, the current density decreases further at later times. The surface current drives a magnetic field B_x in x-direction outside the dense plasma region, which is exemplarily shown in figure 5.7c for 500 fs after t_0. The strongest fields of about 5.3 kT are present at the edge of the target. The field strength decreases for larger distances from the dense plasma region. Even higher magnetic fields were obtained at 38 fs after t_0 with up to $B_x^{max} = 30$ kT (not shown for brevity). Since B and j are proportional to each other, the temporal evolution of B_x^{max} indicates the same trend as the current density (see figure 5.7f). Advancing from 38 fs to 500 fs in the simulation, the spatial distribution of j (figure 5.7b) indicates a compression of the current-carrying surface layer. This compression is more clearly visible in the electron density distribution, which is displayed in figure 5.7d at the time of 1 ps after t_0. In addition, figure 5.7g shows the density profile at a fixed vertical position 60 μm below the interaction point for different time steps. 38 fs after t_0, the density distribution is still comparable to the initial target shape. 500 fs after t_0, however, a layer of higher density develops at the surface, which moves inwards in the following time steps and finally reaches the center at about 3 ps. Consequently, the plasma density rises to almost two times n_0. This can potentially be explained by the inwards and outwards expansion of the hot surface layer that is heated by the return current flows. Moreover, the pinching effect of the Lorentz force, where the current-carrying surface is accelerated inwards by the magnetic field, leads to an additional compression and therefore to an increase in density. For comparison, Kaymak et al. [237] found with numerical simulations in a more optimized scenario where the laser impinges at normal incidence on a carbon nanowire that the electron densities can reach values 1000 times larger than the critical density, due to the compressing force. The initial sharp transition in plasma density between target and vacuum becomes more diffuse over the same period of time as the plasma expands. The velocity of this plasma expansion can be estimated and compared with experimental measurements. For the threshold density of about 0.25 $n_{c,800\text{nm}}$, which was determined for the 515 nm probe beam (see section 5.1), the plasma expands in the simulation by about 4.7 μm in 3 ps which corresponds to a velocity $v_{PIC} \approx$ of $1.6 \cdot 10^6$ m/s. This reveals that v_{PIC} is several times faster than the velocities ($1 \cdot 10^5$ m/s) obtained in the experiments. The following two effects might contribute to this difference. First, since the measurement of radial expansion is based on a constant density, it can be assumed that after a few 10 ps the velocity will have decreased to some extent. Second, the PIC simulation overestimates the velocity due to the 2D geometry.

The results from the PIC simulations show that the driver (current and magnetic field) for an m=0 MHD instability are present for our experimental conditions. By applying equation 5.2 from section 5.2, the characteristic growth time τ of m=0 MHD instabilities can be estimated from the magnetic fields of the PIC simulation results. With r_0 = 2.5 μm the target radius, $\rho = 0.086$ g/cm^3 for hydrogen and a peak magnetic field strength of ≈ 30 kT results in a growth time $\tau \approx 1$ ps. However, the rapidly decrease of the magnetic field strength with time (see figure 5.7f) results in a fast increase in τ. For example at the simulation time

of 1000 fs, τ yields about 20 ps for a magnetic field strength of $\approx$ 1.5 kT.
Since the time scale on which a strong current and a magnetic field exists is smaller than the growth time, only a slight growth of m=0 MHD instabilities is expected [245]. However, analogous to the experiments, the lifetime of j and B in the simulation also need to be discussed. The rate of rise of the return current is related to the target inductance L [64, 257]. Since L typically increases with the wire length and the simulation covers only a relatively small area (∼100 μm) in comparison to the experimental arrangements (∼ centimeters), the duration of the return current might be underestimated. Furthermore, lifetime measurements of magnetic fields and transient electric charge from laser irradiated targets published in [256, 258, 257, 208, 259, 260, 13] consistently report on durations of a few tens of picoseconds. In particular, the results presented in [256] obtained with a comparable laser system (30 fs pulse duration and 3 J laser energy) indicate durations of the current pulse of 20 ps and therefore at least one order of magnitude longer than the result from the simulations presented here. However, the increased time duration in e.g. [256] is accompanied by a significantly reduced peak current, which is likely due to the larger distance of the measurement from the interaction point.
Addressing the question of time scales consequentially exceeds the scope of this thesis. Three-dimensional PIC simulations can be used to investigate the current density and the plasma expansions in a more realistic scenario on the sub-picosecond timescale. The transition to the experimentally observed time scales (tens of picoseconds) can presumably only be achieved by a subsequent MHD simulation and by considering the target system as an electric circuit that describes the time-varying current distribution. Some of these aspects will be discussed as part of the thesis by Y. Long [261].

Investigating the TAWI hypothesis

The thermal anisotropy Weibel instability, as the second hypothesis to explain the experimental observations in section 5.1, is driven by an anisotropy in the electron temperature. While, the thermal anisotropy is also expected to result in a growth of magnetic field structures, as shown by Quinn et al. [65], a clear distinction from the magnetic fields originating from the surface current cannot be easily accomplished. The following analysis therefore focused on the thermal anisotropy. Figure 5.7e shows the electron temperature in y-direction representing the radial component T_r that is obtained from the average electron momentum in each cell at 1000 fs after t_0. Note that in order to discuss our results in relation to the TAWI hypothesis, here we use the term "temperature" as a synonym for average kinetic energy. T_r is observed to be much larger in the surrounding plasma (about 40 keV) than in the center of the target (about 1 keV). Fast electrons leaving the target are predominant in the low-density plasma, so the temperature is high. In contrast, the target bulk is mainly occupied by cold electrons, which leads to a lower average temperature. As introduced in section 5.3, the thermal anisotropy A can be calculated by comparing T_r with the temperature component along the wire axis (in z-direction): $A = T_z/T_r - 1$. An $A > 0$ is expected to drive a thermal Weibel instability [65]. The resulting anisotropy is shown at a position 60 µm below the interaction point in figure 5.7h. Independent of the time step, A is observed to differ insignificantly from zero in the center of the plasma (y < 2µm) since the low-temperature electron population transfer only a neglectable momentum to the ion population and, thus, the temperature remains isotropic. For larger distances from the target center (y > 2µm) and for times at least 1.5 ps after t_0, a thermal anisotropy is observed in figure 5.7h, where temperatures in the radial direction are up to 20% lower than in axial direction. This allows for the growth of the thermal Weibel instability. At even larger distances from the center (e.g. y > 3.5µm at 1.5 ps) the anisotropy becomes negative suppressing the growth of unstable modes.

The expected TAWI wave numbers can be estimated as a comparison to the experimentally observed density modulation wavelengths (figure 5.4). By taking the highest A of 0.2 from the 2 ps time step in figure 5.7h and the plasma density of 0.5 $n_{c,800\mathrm{nm}}$ at the same y-position and time step from figure 5.7g, which corresponds to a plasma frequency of $1.65 \cdot 10^{15}\,\mathrm{s}^{-1}$, a maximum unstable wave number k_{TAWI}^{max} of about 2.5 µm^{-1} is calculated with equation 5.4. While k_{TAWI}^{max} is equivalent to a wavelength of $2\pi/k_{TAWI}^{max} = 2.5$ µm, the fastest growing unstable mode is expected at lower wave numbers and therefore at higher wavelengths. Independent of the exact value of the most unstable k_{TAWI}, the wavelengths of a possible Weibel instability is at least on the same order of magnitude as the wavelength measured in the experiment (5-10 µm in section 5.1).

Following the simulation results to later times indicates a decrease in thermal anisotropy. The lifetime of the thermal anisotropy is therefore only a few picoseconds and thus shorter than the experimentally observed density modulations. However, similar to the MHD hypothesis, comparing the time scales of the simulation and experiment exceeds the scope of this thesis.

5.5 Conclusion

In conclusion, this chapter reported on axial plasma density modulations that were observed on a time scale of tens of picosecond after the interaction of an ultra-short high-intensity laser with a cylindrical hydrogen jet target. The evolution of the micrometer-sized signature was determined by optical probing methods. An increase of wavelength and amplitude of the modulation with time was observed while the plasma expanded. Two hypotheses that explain the observation were investigated. First, a model based on magneto-hydrodynamic instabilities was presented, where laser-driven return current and resulting azimuthal magnetic fields drive a pinching instability. The second hypothesis is based on the thermal anisotropy-driven Weibel instability originating from a temperature anisotropy in an expanding plasma. Using a PIC study, which simulated several picoseconds, the drivers of both hypotheses were investigated. For the MHD instability, the simulation confirmed a return current along the wire-like plasma and the resulting azimuthal magnetic field. The fields are sufficiently strong to drive instabilities on a picosecond time scale. Moreover, the measured wavelength of the density modulation matches the expectation from the MHD instability hypothesis. The temperature anisotropy that causes the thermal

Weibel instability is also observed in the simulation. The wave numbers estimated from the thermal anisotropy are consistent with the experimental measurements. As a result, both hypotheses are plausible and can contribute to the observed signatures. However, for either model the duration, at which the driver was strong enough to amplify the corresponding instability, is on the order of picoseconds and therefore much shorter than the experimentally observed time scale of 10-100 ps. Two possible approaches were considered that can explain the plasma density modulations despite the different time scales. On the one hand, the lifetimes of the magnetic field and the thermal anisotropy are underestimated in the simulations, presumably due to the computational limitations, while the driver potentially exists for a longer duration in the experiment. On the other hand, it is also possible that the relevant instability growth occurs in the first few picoseconds imprinting a structure into the plasma that becomes more pronounced and therefore observable during the 10-100 ps expansion. As an outlook, preliminary results from the thesis of Y. Long [261] indicate that initially invisible perturbations can lead to significant modulations of the plasma density after a few tens of picoseconds of hydrodynamic expansion.

Since neither of the two hypotheses can be excluded and thus both could contribute to the experimentally observed density modulation, finding the dominant mechanism remains unsolved. Both hypotheses can be further investigated by an adapted numerical study that combine a long-running (several 10 ps) dedicated simulation with the input from a PIC simulation of the laser target interaction. While for the MHD model a subsequent magneto-hydrodynamic simulation with the current flows as an input parameter can be utilized, for TAWI a numerical study of the plasma expansion similar to Quinn et al. [65] with the plasma temperature as an input is a possible approach for future investigations. From an experimental point of view, a more detailed picture of the evolution can be obtained by resolving the magnetic field dynamics using more sophisticated probing methods e.g. Faraday rotation as in [259, 251] or proton radiography [13, 256].

Independent of the process that generates the plasma density modulations, the simulation shows that for both mechanism (MHD instability or TAWI) structures in the plasma density can only be expected after at least 1 ps. For the MHD instability, this is given by the growth time that is 1 ps for the highest magnetic field strength while in the case of TAWI the thermal anisotropy requires about 1.5 ps to develop. Since the laser-proton acceleration occurs within the first picosecond after t_0, it therefore seems unlikely that the two mechanisms discussed have a significant influence on the quality of the proton beam. However, the situation could change in the case of several picosecond (or even tens of picosecond) pre-expansions, that are triggered either by the picosecond rising slope of the temporal laser contrast (section 4.2) or by laser pre-pulses (section 4.6). A detailed consideration of both hypotheses for laser pulses, which are several orders of magnitudes lower in intensity, requires, however, further investigations that extend beyond this work.

6 Summary and outlook

In this thesis, the interaction of ultra-short, high-intensity laser pulses with solid hydrogen targets was investigated. Experiments were carried out to identify the most beneficial combination of laser pulse shape and target density distribution in order to examine potential paths towards the application of laser-driven proton and ion sources. This task is inherently linked to the study of various acceleration mechanisms. Due to its unique properties, the micrometer-sized cryogenic jet target can be used to link targetry, laser diagnostics, optical probing, acceleration dynamics and predictive simulation capabilities to resolve a microscopic picture of the laser-matter interaction for different acceleration mechanisms.
The first step was to study the fluid dynamics that govern the generation of solid hydrogen jets to produce optimally shaped targets. In particular, sheet-like jets were investigated which, due to their geometry, are particularly suitable for the debris-free production of stable proton beams at high repetition rates. Scans of the various operating parameters and two nozzle aperture types showed how the sheet width, the sheet thickness and the target stability could be tuned. By selecting the appropriate aperture geometries, planar jets with widths up to 40 µm and thicknesses ranging from a few 100 nm to micrometers can be generated and implemented as targets in a laser-plasma experiment. The target stability was further substantially increased by the introduction of a mechanical chopping device that protects the sensitive aperture plate from disruptive influences originating from the high-intensity interaction. Implementation of this device allowed for the first time a large amount (>100) of laser shots with the same nozzle (in particular with slit apertures) under jet stability conditions that enabled systematic experimental studies while scaling the pulse energy to the PW level.
In the second part of this thesis, these targetry developments were utilized to establish a self-replenishing cryogenic jet of pure hydrogen for proton acceleration studies in the harsh environment of the ultra-short pulse petawatt laser system DRACO. Different laser contrast conditions and target density distributions were investigated by implementing cylindrical and sheet jets. Although not optimized so far in terms of thickness and laser pulse profile, the achieved acceleration performance from hydrogen sheets is comparable to plastic foils with respect to maximum proton energies and shot-to-shot stability.

Using high contrast laser pulses, protons acceleration from cylindrical jets of 5 μm in diameter is dominated by TNSA, reaching maximum energies comparable to those from micrometer-thick metal targets. Tailoring of the spatio-temporal plasma density distribution by hydrodynamic pre-expansion with a timed pre-pulse provided a viable approach for the investigation of acceleration mechanisms in near-critical density plasmas. At optimal pre-expansion, proton beams with up to 80 MeV can be generated. These high proton energies from a target system that is in principle capable of delivering a pure hydrogen target with high repetition rate marks the most important experimental result of this work. According to three-dimensional particle-in-cell simulations, the best performance is achieved in the near-critical density regime by a combination of magnetic vortex acceleration and synchronized acceleration by slow light. Numerical studies coupling PIC and hydrodynamic simulations are currently conducted to further investigate the contribution of these acceleration mechanisms in a less idealized scenario and thus allow for a more accurate description of the interaction process. All those investigations confirm the capabilities of the hydrogen target to combine proton acceleration performance, optical probing and simulations in order to provide a fruitful system for optimizing the laser target interaction in further investigations.

In the final part of this thesis, the unique capabilities of the hydrogen jet were used to investigate the phenomena of axial plasma density modulation that appears several tens of picoseconds after the high-intensity laser pulse hits the target. Studying such modulations is motivated by the fact that they could represent a potential obstacle for generating a well-defined beam profile, as it is often required for applications. Regardless of the laser and target conditions used, the evolution of the micrometer-sized signature indicates an increase over time. Two hypotheses for explaining the observation were investigated that are based either on magneto-hydrodynamic instabilities or Weibel-induced filamentations. Numerical studies indicate that both hypotheses are plausible and can contribute to the observed density modulation. Although identifying the dominant mechanism remains therefore unsolved, both instabilities are generated on longer time scales than what is relevant for the proton acceleration. However, the density modulation could become more important in the case of several picosecond pre-expansions that are triggered by moderate laser contrast conditions.

Based on the successful characterization, implementation and irradiation of the cryogenic jet target at the DRACO PW laser system, the presented studies emphasize several potential routes to optimize the laser-plasma interaction in future campaigns. Proton acceleration studies in the near-critical density regime can be substantially extended by using optimized laser and target conditions. For example in the MVA regime, an increase of the initial jet diameter to about 10 μm is suggested for DRACO PW laser parameters. Pre-expansion reduces the core density then to a few times the critical density to optimize the laser energy transfer to the plasma electrons and thus to achieve higher proton energies. To keep the shot-to-shot fluctuations small, a thick hydrogen sheet could be used as an alternative target approach. In this regard, numerical studies can assist in determining the most beneficial plasma density distribution while different sized and shaped jets can be density tailored with controlled pre-pulses (in terms of intensity, pulse duration and delay) to meet the requirements. The jet with a planar geometry is also more favorable when a stable production of proton beams is required. For an optimized laser contrast and an optimized sheet thickness, maximum proton energies in the range of 60 MeV are expected. Regardless of the target geometry, a further improvement of the jet stability is crucial to investigate the different mechanisms systematically. This can be achieved with an optimized version of the mechanical chopper device, which features a more accurate synchronization [201]. In addition, the target system also enables future studies of multi-species effects [161] or the generation of pure particle beams of different ions (e.g.: helium, neon, argon). Besides the generation of foil-like and wire-like targets, cryogenic droplets can also be generated by either stimulating the Plateau-Rayleigh instability or by cropping a micrometer-sized fragment with an intense laser pulse. This allows studies with mass-limited targets.

In summary, all those mentioned paths provide various opportunities for future experimental studies that could finally lead to a better understanding of the fundamental physical principles that drive plasma-based proton accelerations and many other short pulse laser induced high field effects under controlled conditions.

7 Appendix

7.1 A: Thomson parabola spectrometer calibration method

Thomson parabola spectrometers (TPS) equipped with microchannel plate (MCP) detectors are a well-known diagnostic to characterize charged particle beams emitted from laser-plasma interactions. TPS are capable of high repetition rates and provide online measurements that are in particular important when strong shot-to-shot fluctuations are present, as it is the case for the irradiation of the cylindrical hydrogen jet target in chapter 4. To determine the absolute particle number contained in an ion beam, which is especially relevant for applications, an absolute calibration of the detector is required. However, several works [262, 263, 216, 264, 265] demonstrated that the calibration factor, which converts the output signal of the TPS into an absolute particle number, depends in general on the ion energy and scales non-linearly with the particle flux. The dependency on the ion energy is considered in the theoretical model from Prasad et al. [265] where the MCP response is described by $R_{MCP} \propto 1/cos(\theta)\,(dE/dx)\,g$. The gain g of the MCP is defined by the geometry of the micrometer-sized channels, the applied voltage and the particle penetration depth. (dE/dx) and θ describe the electronic stopping power of the projectile ions and the incidence angle with respect to the normal of the detector surface. Although all three parameters in the equation for R_{MCP} depend on the particle energy, the measurements of [265, 263] suggest that at energies where the penetration depth is larger than the thickness of the MCP, the MCP response will only depend weakly on the kinetic energy.

The second dependency regarding the particle flux can be explained as follows. Since the MCP is operated in a saturation mode, each microscopic channel that is triggered by an incoming proton becomes at least partially depleted. If another particle enters the same channel, less gain can be provided and the additional response is supposed to be weaker. This is because the time scale for restoring the same amplification is in the order of microseconds [266] and therefore several orders of magnitude longer than the duration of the proton pulse. As such, this saturation effect prevents in general a linear scaling of the signal strength with the particle number.

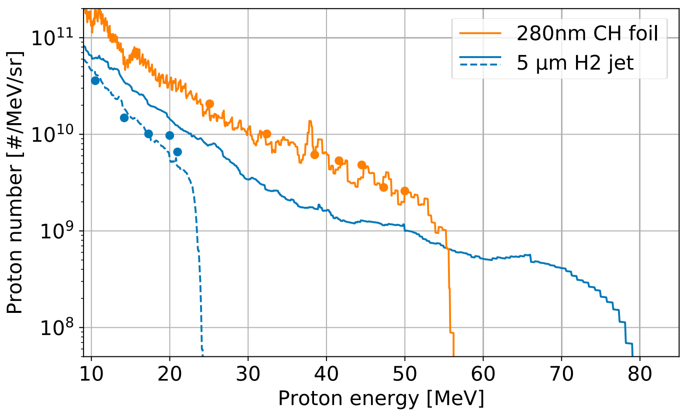

Figure 7.1: Absolute proton spectra obtained from a 280 nm thick formvar foil (orange) and a 5 µm cylindrical hydrogen jet (blue). The targets were shot under an incident angle of 0° and protons were detected by TPS (colored lines) and radio-chromic film stacks (filled circles) in laser forward direction. Two TPS measurements are shown for the cryogenic jet: one with comparable cut-off energy to a shot with a RCF-stack (dashed line) and another one showing the best performance with up to 80 MeV (solid line).

Despite these limitations, cross-calibration with e.g. radiochromic film (RCF) stacks can be performed to estimate absolute particle number from TPS measurements for at least a fraction of the spectrum where saturation has a small effect (generally at low particle numbers). This is exemplarily shown in figure 7.1 by the orange line (TPS) and orange circles (RCF) obtained for the same laser shot on a foil target. Here, the relative proton numbers obtained from the TPS data are scaled so that they overlap with the RCF determined absolute particle numbers. As described at the beginning of this section, the scaling factor generally depends on the ion energy and particle number and should therefore differ for each data point obtained from the RCF stack. However, for the energy range where both RCF and TPS data is available (25-50 MeV), this scaling factor is about constant within the measurement uncertainty. Thus, on this energy range of the proton spectrum, the saturation of the MCP has only a negligible influence. Note that at lower proton energies and thus higher particle numbers, saturation is likely to have a greater influence and particle numbers are thus underestimated. Applying now the same calibration to another TPS measurement where no RCF was irradiated is only possible if the spectra are reasonably comparable in terms of particle number and maximum proton energies. However, this is not the case for the experiments with the hydrogen jet (chapter 4). In order to be able to provide absolute particle numbers for the proton beams with up to 80 MeV, a calibration procedure was developed. This procedure is described here exemplary for the two proton spectra displayed by the blue lines in figure 7.1.

Since the maximum proton energy of 80 MeV differs significantly from the best performing shots recorded with RCF stacks under the same experimental conditions ($E_{p,max} \approx$ 21-25 MeV), one cannot directly compare both measurements. Instead, as an intermediate step, another TPS measurement (dashed blue line in figure 7.1) from a shot with the same nominal experimental settings and with maximum proton energy (around 24 MeV) similar to the RCF shot was scaled to the particle numbers from the stack (blue dots). Now, to obtain the calibration factor for the 80 MeV shot, the assumption is made that the same raw signal from two TPS measurements corresponds to the same particle density on the detector, even if the associated kinetic energies are not equal. This approach avoids limitations due to the unknown scaling of the calibration factor with the particle number, but also requires a negligible dependence of the MCP response on the particle energy, as discussed above. As an example, for the shot with up to 24 MeV (dashed line), the signal strength for protons with 21 MeV corresponds to approximately $n_p = 6.6 \cdot 10^9$ #/MeV/sr (according to the RCF measurement). The same TPS raw signal and therefore the same particle number, corrected by a geometry factor*, is found for the 80 MeV shot (solid line) for about 32 MeV protons. The calibration factor can thus be calculated for protons with 32 MeV. By repeating this method for all films of the RCF stack, a robust procedure for obtaining the calibration factor is found that allows to determine the absolute proton number for the 80 MeV proton beam and finally led to the spectra shown in fig. 4.7.

7.2 B: Methods to determine central hits

In order to discuss the influence of the applied filtering on the increase of average proton energies derived from the set of experimental data in section 4.6.2, three other procedures for data selection are tested and shown in figure 7.2a-c. While this comparison will focus on the maximum proton energies in laser direction, $E_{p,max}$ in 45° behaves similarly. First, the transmitted light threshold was chosen at a different level. Figure 7.2a shows $E_{p,max}$ in laser direction as a function of the target diameter, while only the 20% of shots with the lowest transmission were utilized for the binned average. Second, all shots without any further selection are shown in figure 7.2b. Finally, another method based on the spatial shape of the transmitted light instead of the total amount was implemented in figure 7.2c. While measured patterns of transmitted light from a shot which resulted in a high $E_{p,max}$ (in figure 7.2d), show mostly symmetric structures regarding the vertical axis, deviation from the central position leads to a more asymmetrical pattern which was separated manually. To comprehend the structure of transmitted light, a numerical calculation based on the diffraction propagation algorithms from the ray-tracing program OpticStudio from ZEMAX† was accomplished which allows simulating the optical system of the focusing off-axis parabola, the jet as a blocking obstacle and the ceramic screen for detection. Figure 7.2d shows the calculated upper half of the pattern originating from a circular Top Hat input beam. The jet acts as a spatial filter in the focus plane blocking the central 5 μm in the horizontal direction and everything in the vertical direction and therefore the largest part of the laser focus. Since high spatial frequencies, which originate from the edge of the top-hat beam, are separated from the central spot in the focus plane, they cannot be blocked by the obstacle. The light associated with the high spatial frequencies forms the ring structure in the detector plane that is comparable to the transmitted light measurement in figure 7.2d.

---

[*] The geometry factor accounts for the magnetic field deflection in the detector plane which scales with the proton energies approximately with $\sim E_{kin}^{-1/2}$ [264]. Less energetic particles are separated by a larger distance on the MCP than faster particles.

[†] Zemax LLC, Kirkland, Washington, USA

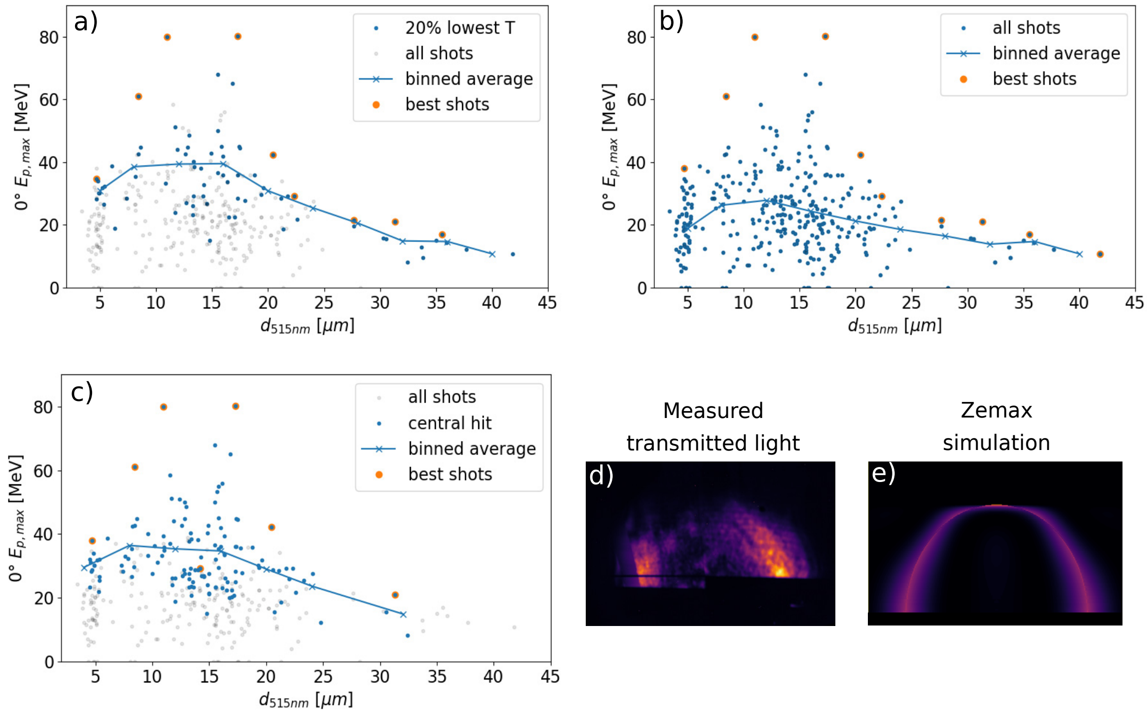

Figure 7.2: Effect of different filters on the average of $E_{p,max}$. a) 20% of shots with the lowest amount of transmitted light. b) Without any selection of shots. c) Manual filtering with respect to the transmitted light pattern. Comparison of the measured spatial distribution of transmitted light for a central shot (d) and the simulated pattern for the same scenario in (e).

Regardless of the different filtering methods, the general increase in $E_{p,max}$ for shadow diameters of 11 µm-16 µm and a subsequent decrease of proton energies for larger target diameter remains the same which demonstrates the robustness and significance of this result.

Bibliography

[1] D. Strickland and G. Mourou. “Compression of amplified chirped optical pulses.” *Optics Communications*, **56** (1985), pp. 219–221. doi:10.1016/0030-4018(85)90120-8.

[2] M. C. Downer et al. “Diagnostics for plasma-based electron accelerators.” *Reviews of Modern Physics*, **90** (2018), p. 35002. doi:10.1103/RevModPhys.90.035002.

[3] A. J. Gonsalves et al. “Petawatt Laser Guiding and Electron Beam Acceleration to 8 GeV in a Laser-Heated Capillary Discharge Waveguide.” *Physical Review Letters*, **122** (2019), p. 84801. doi:10.1103/PhysRevLett.122.084801.

[4] S. P. D. Mangles et al. “Monoenergetic beams of relativistic electrons from intense laser–plasma interactions.” *Nature*, **431** (2004), pp. 535–538. doi:10.1038/nature02939.

[5] S. C. Wilks et al. “Energetic proton generation in ultra-intense laser-solid interactions.” *Physics of Plasmas*, **8** (2001), pp. 542–549. doi:10.1063/1.1333697.

[6] T. E. Cowan et al. “Ultralow Emittance, Multi-MeV Proton Beams from a Laser Virtual-Cathode Plasma Accelerator.” *Physical Review Letters*, **92** (2004), p. 204801. doi:10.1103/PhysRevLett.92.204801.

[7] P. Sommer et al. “Laser-ablation-based ion source characterization and manipulation for laser-driven ion acceleration.” *Plasma Physics and Controlled Fusion*, **60** (2018), p. 054002. doi:10.1088/1361-6587/aab21e.

[8] F. Nürnberg et al. “Radiochromic film imaging spectroscopy of laser-accelerated proton beams.” *Review of Scientific Instruments*, **80** (2009), p. 033301. doi:10.1063/1.3086424.

[9] R. A. Snavely et al. “Intense high-energy proton beams from petawatt-laser irradiation of solids.” *Physical Review Letters*, **85** (2000), pp. 2945–2948. doi:10.1103/PhysRevLett.85.2945.

[10] J. Schreiber, P. R. Bolton, and K. Parodi. "Invited Review Article: "Hands-on" laser-driven ion acceleration: A primer for laser-driven source development and potential applications." *Review of Scientific Instruments*, **87** (2016), p. 071101. doi:10.1063/1.4959198.

[11] M. Borghesi et al. "Electric field detection in laser-plasma interaction experiments via the proton imaging technique." *Physics of Plasmas*, **9** (2002), pp. 2214–2220. doi:10.1063/1.1459457.

[12] L. Romagnani et al. "Dynamics of electric fields driving the laser acceleration of multi-MeV protons." *Physical Review Letters*, **95** (2005), pp. 4–7. doi:10.1103/PhysRevLett.95.195001.

[13] K. Quinn et al. "Laser-Driven ultrafast field propagation on solid surfaces." *Physical Review Letters*, **102** (2009), pp. 3–6. doi:10.1103/PhysRevLett.102.194801.

[14] M. Roth et al. "Bright Laser-Driven Neutron Source Based on the Relativistic Transparency of Solids." *Phys. Rev. Lett.*, **110** (2013), p. 44802. doi:10.1103/PhysRevLett.110.044802.

[15] P. K. Patel et al. "Isochoric heating of solid-density matter with an ultrafast proton beam." *Physical Review Letters*, **91** (2003), pp. 10–13. doi:10.1103/PhysRevLett.91.125004.

[16] J. C. Fernández et al. "Progress and prospects of ion-driven fast ignition." *Nuclear Fusion*, **49** (2009), p. 065004. doi:10.1088/0029-5515/49/6/065004.

[17] S. Busold et al. "Shaping laser accelerated ions for future applications - The LIGHT collaboration." *Nuclear Instruments and Methods in Physics Research, Section A: Accelerators, Spectrometers, Detectors and Associated Equipment*, **740** (2014), pp. 94–98. doi:10.1016/j.nima.2013.10.025.

[18] S. Bulanov et al. "Oncological hadrontherapy with laser ion accelerators." *Physics Letters A*, **299** (2002), pp. 240–247. doi:10.1016/S0375-9601(02)00521-2.

[19] S. D. Kraft et al. "Dose-dependent biological damage of tumour cells by laser-accelerated proton beams." *New Journal of Physics*, **12** (2010), p. 085003. doi:10.1088/1367-2630/12/8/085003.

[20] K. Zeil et al. "Dose-controlled irradiation of cancer cells with laser-accelerated proton pulses." *Applied Physics B*, **110** (2013), pp. 437–444. doi:10.1007/s00340-012-5275-3.

[21] A. Yogo et al. "Application of laser-accelerated protons to the demonstration of DNA double-strand breaks in human cancer cells." *Applied Physics Letters*, **94** (2009), p. 181502. doi:10.1063/1.3126452.

[22] F.-E. Brack et al. "Spectral and spatial shaping of laser-driven proton beams using a pulsed high-field magnet beamline." *Scientific Reports*, **10** (2020), p. 9118. doi:10.1038/s41598-020-65775-7.

[23] F. Kroll et al. "Tumor irradiation in mice with a laser-accelerated proton beam." *Under review in Nature Physics*.

[24] U. Linz and J. Alonso. "What will it take for laser driven proton accelerators to be applied to tumor therapy?" *Physical Review Special Topics - Accelerators and Beams*, 10 (2007), pp. 1–8. doi:10.1103/PhysRevSTAB.10.094801.

[25] A. Higginson et al. "Near-100 MeV protons via a laser-driven transparency-enhanced hybrid acceleration scheme." *Nature Communications*, 9 (2018), p. 724. doi:10.1038/s41467-018-03063-9.

[26] F. Wagner et al. "Maximum Proton Energy above 85 MeV from the Relativistic Interaction of Laser Pulses with Micrometer Thick CH2 Targets." *Physical Review Letters*, 116 (2016), p. 205002. doi:10.1103/PhysRevLett.116.205002.

[27] S. C. Wilks et al. "Absorption of ultra-intense laser pulses." *Physical Review Letters*, 69 (1992), pp. 1383–1386. doi:10.1103/PhysRevLett.69.1383.

[28] T. Esirkepov et al. "Highly Efficient Relativistic-Ion Generation in the Laser-Piston Regime." *Physical Review Letters*, 92 (2004), pp. 2–5. doi:10.1103/PhysRevLett.92.175003.

[29] A. P. L. Robinson et al. "Radiation pressure acceleration of thin foils with circularly polarized laser pulses." *New Journal of Physics*, 10 (2008), p. 013021. doi:10.1088/1367-2630/10/1/013021.

[30] A. P. L. Robinson et al. "Relativistically correct hole-boring and ion acceleration by circularly polarized laser pulses." *Plasma Physics and Controlled Fusion*, 51 (2009), p. 024004. doi:10.1088/0741-3335/51/2/024004.

[31] A. Macchi et al. "Laser Acceleration of Ion Bunches at the Front Surface of Overdense Plasmas." *Physical Review Letters*, 94 (2005), p. 165003. doi:10.1103/PhysRevLett.94.165003.

[32] T. Esirkepov, M. Yamagiwa, and T. Tajima. "Laser Ion-Acceleration Scaling Laws Seen in Multiparametric Particle-in-Cell Simulations." *Physical Review Letters*, 96 (2006), p. 105001. doi:10.1103/PhysRevLett.96.105001.

[33] A. Macchi, M. Borghesi, and M. Passoni. "Ion acceleration by superintense laser-plasma interaction." *Reviews of Modern Physics*, 85 (2013), pp. 751–793. doi:10.1103/RevModPhys.85.751.

[34] E. D'Humières et al. "Proton acceleration mechanisms in high-intensity laser interaction with thin foils." *Physics of Plasmas*, 12 (2005), p. 062704. doi:10.1063/1.1927097.

[35] R. Mishra, F. Fiuza, and S. Glenzer. "Enhanced ion acceleration in transition from opaque to transparent plasmas." *New Journal of Physics*, 20 (2018), p. 043047. doi:10.1088/1367-2630/aab8db.

[36] V. Vshivkov et al. “Nonlinear interaction of ultra-intense laser pulses with a thin foil.” *Physics of Plasmas*, 5 (1998), pp. 493–498. doi:10.1016/S0168-9002(98)00183-1.

[37] L. O. Silva et al. “Proton shock acceleration in laser-plasma interactions.” *Physical review letters*, 92 (2004), p. 015002. doi:10.1103/PhysRevLett.92.015002.

[38] D. Haberberger et al. “Collisionless shocks in laser-produced plasma generate monoenergetic high-energy proton beams.” *Nature Physics*, 8 (2012), pp. 95–99. doi:10.1038/nphys2130.

[39] F. Fiuza et al. “Laser-Driven Shock Acceleration of Monoenergetic Ion Beams.” *Physical Review Letters*, 109 (2012), p. 215001. doi:10.1103/PhysRevLett.109.215001.

[40] A. V. Brantov et al. “Synchronized Ion Acceleration by Ultraintense Slow Light.” *Physical Review Letters*, 116 (2016), p. 085004. doi:10.1103/PhysRevLett.116.085004.

[41] I. Göthel et al. “Optimized laser ion acceleration at the relativistic critical density surface.” *Under review in Plasma Physics and Controlled Fusion*. doi:arXiv:2110.01257.

[42] A. V. Kuznetsov et al. “Efficiency of ion acceleration by a relativistically strong laser pulse in an underdense plasma.” *Plasma Physics Reports*, 27 (2001), pp. 211–220. doi:10.1134/1.1354219.

[43] S. S. Bulanov et al. “Generation of GeV protons from 1 PW laser interaction with near critical density targets.” *Physics of Plasmas*, 17 (2010), p. 043105. doi:10.1063/1.3372840.

[44] T. Nakamura et al. “High-Energy Ions from Near-Critical Density Plasmas via Magnetic Vortex Acceleration.” *Physical Review Letters*, 105 (2010), p. 135002. doi:10.1103/PhysRevLett.105.135002.

[45] L. Willingale et al. “Collimated Multi-MeV Ion Beams from High-Intensity Laser Interactions with Underdense Plasma.” *Physical Review Letters*, 96 (2006), p. 245002. doi:10.1103/PhysRevLett.96.245002.

[46] Y. Fukuda et al. “Energy Increase in Multi-MeV Ion Acceleration in the Interaction of a Short Pulse Laser with a Cluster-Gas Target.” *Physical Review Letters*, 103 (2009), p. 165002. doi:10.1103/PhysRevLett.103.165002.

[47] J. Park et al. “Ion acceleration in laser generated megatesla magnetic vortex.” *Physics of Plasmas*, 26 (2019), p. 103108. doi:10.1063/1.5094045.

[48] A. Sharma and A. Andreev. “Effective laser driven proton acceleration from near critical density hydrogen plasma.” *Laser and Particle Beams*, 34 (2016), pp. 219–229. doi:10.1017/S0263034616000045.

[49] F. Sylla et al. “Development and characterization of very dense submillimetric gas jets for laser-plasma interaction.” *Review of Scientific Instruments*, 83 (2012), p. 033507. doi:10.1063/1.3697859.

[50] S. N. Chen et al. “Collimated protons accelerated from an overdense gas jet irradiated by a 1 µm wavelength high-intensity short-pulse laser.” *Scientific Reports*, **7** (2017), p. 13505. doi:10.1038/s41598-017-12910-6.

[51] M. H. Helle et al. “Laser-Accelerated Ions from a Shock-Compressed Gas Foil.” *Physical Review Letters*, **117** (2016), p. 165001. doi:10.1103/PhysRevLett.117.165001.

[52] T. Kluge et al. “Observation of Ultrafast Solid-Density Plasma Dynamics Using Femtosecond X-Ray Pulses from a Free-Electron Laser.” *Physical Review X*, **8** (2018), p. 31068. doi:10.1103/PhysRevX.8.031068.

[53] C. Danson et al. “Petawatt class lasers worldwide.” *High Power Laser Science and Engineering*, **3** (2015), p. e3. doi:10.1017/hpl.2014.52.

[54] I. Prencipe et al. “Targets for high repetition rate laser facilities: needs, challenges and perspectives.” *High Power Laser Science and Engineering*, **5** (2017), p. e17. doi:10.1017/hpl.2017.18.

[55] S. Göde et al. “Relativistic Electron Streaming Instabilities Modulate Proton Beams Accelerated in Laser-Plasma Interactions.” *Physical Review Letters*, **118** (2017), p. 194801. doi:10.1103/PhysRevLett.118.194801.

[56] M. Gauthier et al. “High repetition rate, multi-MeV proton source from cryogenic hydrogen jets.” *Applied Physics Letters*, **111** (2017), p. 114102. doi:10.1063/1.4990487.

[57] L. Obst et al. “Efficient laser-driven proton acceleration from cylindrical and planar cryogenic hydrogen jets.” *Scientific Reports*, **7** (2017), p. 10248. doi:10.1038/s41598-017-10589-3.

[58] L. Obst-Huebl et al. “All-optical structuring of laser-driven proton beam profiles.” *Nature Communications*, **9** (2018), p. 5292. doi:10.1038/s41467-018-07756-z.

[59] T. Ziegler et al. “Optical probing of high intensity laser interaction with micron-sized cryogenic hydrogen jets.” *Plasma Physics and Controlled Fusion*, **60** (2018), p. 074003. doi:10.1088/1361-6587/aabf4f.

[60] J. Fuchs et al. “Spatial Uniformity of Laser-Accelerated Ultrahigh-Current MeV Electron Propagation in Metals and Insulators.” *Physical Review Letters*, **91** (2003), p. 255002. doi:10.1103/PhysRevLett.91.255002.

[61] M. N. Quinn et al. “On the investigation of fast electron beam filamentation in laser-irradiated solid targets using multi-MeV proton emission.” *Plasma Physics and Controlled Fusion*, **53** (2011), p. 124012. doi:10.1088/0741-3335/53/12/124012.

[62] C. A. J. Palmer et al. “Rayleigh-Taylor Instability of an Ultrathin Foil Accelerated by the Radiation Pressure of an Intense Laser.” *Physical Review Letters*, **108** (2012), p. 225002. doi:10.1103/PhysRevLett.108.225002.

[63] J. Metzkes et al. “Experimental observation of transverse modulations in laser-driven proton beams.” *New Journal of Physics*, **16** (2014), p. 023008. doi:10.1088/1367-2630/16/2/023008.

[64] F. N. Beg et al. “High-Intensity-Laser-Driven Z Pinches.” *Physical Review Letters*, **92** (2004), p. 095001. doi:10.1103/PhysRevLett.92.095001.

[65] K. Quinn et al. “Weibel-Induced Filamentation during an Ultrafast Laser-Driven Plasma Expansion.” *Physical Review Letters*, **108** (2012), p. 135001. doi:10.1103/PhysRevLett.108.135001.

[66] H. Daido, M. Nishiuchi, and A. S. Pirozhkov. “Review of laser-driven ion sources and their applications.” *Reports on Progress in Physics*, **75** (2012), p. 056401. doi:10.1088/0034-4885/75/5/056401.

[67] K. Zeil et al. “The scaling of proton energies in ultrashort pulse laser plasma acceleration.” *New Journal of Physics*, **12** (2010), p. 045015. doi:10.1088/1367-2630/12/4/045015.

[68] S. A. Gaillard et al. “Increased laser-accelerated proton energies via direct laser-light-pressure acceleration of electrons in microcone targets.” *Physics of Plasmas*, **18** (2011), p. 056710. doi:10.1063/1.3575624.

[69] P. Mora. “Plasma Expansion into a Vacuum.” *Physical Review Letters*, **90** (2003), p. 185002. doi:10.1103/PhysRevLett.90.185002.

[70] J. Schreiber et al. “Analytical Model for Ion Acceleration by High-Intensity Laser Pulses.” *Physical Review Letters*, **97** (2006), p. 045005. doi:10.1103/PhysRevLett.97.045005.

[71] A. Macchi et al. “Theory and simulation of ion acceleration with circularly polarized laser pulses.” *C. R. Physique*, **10** (2009), pp. 207–215. doi:10.1016/j.crhy.2009.03.002.

[72] A. Stockem Novo et al. “Optimizing laser-driven proton acceleration from overdense targets.” *Scientific Reports*, **6** (2016), p. 29402. doi:10.1038/srep29402.

[73] C. A. J. Palmer et al. “Monoenergetic Proton Beams Accelerated by a Radiation Pressure Driven Shock.” *Physical Review Letters*, **106** (2011), p. 014801. doi:10.1103/PhysRevLett.106.014801.

[74] S. V. Bulanov et al. “Laser ion acceleration for hadron therapy.” *Physics-Uspekhi*, **57** (2014), pp. 1149–1179. doi:10.3367/ufne.0184.201412a.1265.

[75] Y. Sentoku et al. “High density collimated beams of relativistic ions produced by petawatt laser pulses in plasmas.” *Physical Review E - Statistical Physics, Plasmas, Fluids, and Related Interdisciplinary Topics*, **62** (2000), pp. 7271–7281. doi:10.1103/PhysRevE.62.7271.

[76] K. Nishihara et al. “High energy ions generated by laser driven Coulomb explosion of cluster.” In *Nuclear Instruments and Methods in Physics Research, Section A: Accelerators, Spectrometers, Detectors and Associated Equipment*, volume 464 (2001), pp. 98–102. doi:10.1016/S0168-9002(01)00014-6.

[77] E. Y. Echkina et al. “Ion Acceleration during the Coulomb Explosion of the Multispecies Clusters.” *31st EPS Conference on Plasma Phys. London*, 28 (2004), pp. P–2.032.

[78] S. Jinno et al. “Micron-size hydrogen cluster target for laser-driven proton acceleration.” *Plasma Physics and Controlled Fusion*, 60 (2018), p. 044021. doi:10.1088/1361-6587/aaafa8.

[79] S. Dobosz et al. “Observation of ions with energies above 100 keV produced by the interaction of a 60-fs laser pulse with clusters.” *Journal of Experimental and Theoretical Physics*, 88 (1999), pp. 1122–1129. doi:10.1134/1.558900.

[80] S. Grieser et al. “Nm-sized cryogenic hydrogen clusters for a laser-driven proton source.” *Review of Scientific Instruments*, 90 (2019), p. 043301. doi:10.1063/1.5080011.

[81] M. Protopapas, C. H. Keitel, and P. L. Knight. “Atomic physics with super-high intensity lasers.” *Reports on Progress in Physics*, 60 (1997), pp. 389–486. doi:10.1088/0034-4885/60/4/001.

[82] P. Gibbon et al. “Tree-code simulations of proton acceleration from laser-irradiated wire targets.” *Physics of Plasmas*, 11 (2004), pp. 4032–4040. doi:10.1063/1.1767096.

[83] S. Seuferling et al. “Efficient offline production of freestanding thin plastic foils for laser-driven ion sources.” *High Power Laser Science and Engineering*, 5 (2017), p. e8. doi:10.1017/hpl.2017.7.

[84] F. Cattani et al. “Threshold of induced transparency in the relativistic interaction of an electromagnetic wave with overdense plasmas.” *Physical Review E*, 62 (2000), pp. 1234–1237. doi:10.1103/PhysRevE.62.1234.

[85] F. F. Chen. *Introduction to Plasma Physics and Controlled Fusion*. Springer International Publishing (2016). doi:10.1007/978-3-319-22309-4.

[86] B. Quesnel and P. Mora. “Theory and simulation of the interaction of ultraintense laser pulses with electrons in vacuum.” *Physical Review E - Statistical Physics, Plasmas, Fluids, and Related Interdisciplinary Topics*, 58 (1998), pp. 3719–3732. doi:10.1103/PhysRevE.58.3719.

[87] T. Kluge et al. “Electron Temperature Scaling in Laser Interaction with Solids.” *Physical Review Letters*, 107 (2011), p. 205003. doi:10.1103/PhysRevLett.107.205003.

[88] S. C. Wilks and W. L. Kruer. “Absorption of ultrashort, ultra-intense laser light by solids and overdense plasmas.” *IEEE Journal of Quantum Electronics*, 33 (1997), pp. 1954–1968. doi:10.1109/3.641310.

[89] W. L. Kruer and K. Estabrook. “JxB heating by very intense laser light.” *Physics of Fluids*, **28** (1985), pp. 430–432. doi:10.1063/1.865171.

[90] F. Brunel. “Not-so-resonant, resonant absorption.” *Physical Review Letters*, **59** (1987), pp. 52–55. doi:10.1103/PhysRevLett.59.52.

[91] G. A. Mourou, T. Tajima, and S. V. Bulanov. “Optics in the relativistic regime.” *Reviews of Modern Physics*, **78** (2006), pp. 309–371. doi:10.1103/RevModPhys.78.309.

[92] P. Sprangle et al. “Propagation and Guiding of Intense Laser Pulses in Plasmas.” *Physical Review Letters*, **69** (1992), pp. 290–292. doi:10.1007/978-3-642-84910-7_88.

[93] W. Lu et al. “Generating multi-GeV electron bunches using single stage laser wakefield acceleration in a 3D nonlinear regime.” *Physical Review Special Topics - Accelerators and Beams*, **10** (2007), p. 061301. doi:10.1103/PhysRevSTAB.10.061301.

[94] J. R. Davies. “Laser absorption by overdense plasmas in the relativistic regime.” *Plasma Physics and Controlled Fusion*, **51** (2009), p. 014006. doi:10.1088/0741-3335/51/1/014006.

[95] L. Willingale et al. “Characterization of High-Intensity Laser Propagation in the Relativistic Transparent Regime through Measurements of Energetic Proton Beams.” *Physical Review Letters*, **102** (2009), p. 125002. doi:10.1103/PhysRevLett.102.125002.

[96] P. L. Poole et al. “Laser-driven ion acceleration via target normal sheath acceleration in the relativistic transparency regime.” *New Journal of Physics*, **20** (2018), p. 013019. doi:10.1088/1367-2630/aa9d47.

[97] S. Weber et al. “P3: An installation for high-energy density plasma physics and ultra-high intensity laser–matter interaction at ELI-Beamlines.” *Matter and Radiation at Extremes*, **2** (2017), pp. 149–176. doi:10.1016/j.mre.2017.03.003.

[98] T. Nakamura et al. “Interaction of high contrast laser pulse with foam-attached target.” *Physics of Plasmas*, **17** (2010), p. 113107. doi:10.1063/1.3507294.

[99] L. Fedeli et al. “Ultra-intense laser interaction with nanostructured near-critical plasmas.” *Scientific Reports*, **8** (2018), p. 3834. doi:10.1038/s41598-018-22147-6.

[100] A. Sgattoni et al. “Laser ion acceleration using a solid target coupled with a low-density layer.” *Physical Review E*, **85** (2012), p. 036405. doi:10.1103/PhysRevE.85.036405.

[101] H. Y. Wang et al. “Efficient and stable proton acceleration by irradiating a two-layer target with a linearly polarized laser pulse.” *Physics of Plasmas*, **20**. doi:10.1063/1.4773198.

[102] J. H. Bin et al. “Ion Acceleration Using Relativistic Pulse Shaping in Near-Critical-Density Plasmas.” *Physical Review Letters*, **115** (2015), p. 064801. doi:10.1103/PhysRevLett.115.064801.

[103] J. H. Bin et al. "Enhanced Laser-Driven Ion Acceleration by Superponderomotive Electrons Generated from Near-Critical-Density Plasma." *Physical Review Letters*, **120** (2018), p. 74801. doi:10.1103/PhysRevLett.120.074801.

[104] A. G. Krygier, D. W. Schumacher, and R. R. Freeman. "On the origin of super-hot electrons from intense laser interactions with solid targets having moderate scale length preformed plasmas." *Physics of Plasmas*, **21** (2014), p. 023112. doi:10.1063/1.4866587.

[105] W. J. Ma et al. "Laser Acceleration of Highly Energetic Carbon Ions Using a Double-Layer Target Composed of Slightly Underdense Plasma and Ultrathin Foil." *Physical Review Letters*, **122** (2019), p. 014803. doi:10.1103/PhysRevLett.122.014803.

[106] I. Prencipe et al. "Development of foam-based layered targets for laser-driven ion beam production." *Plasma Physics and Controlled Fusion*, **58** (2016), p. 034019. doi:10.1088/0741-3335/58/3/034019.

[107] D. Levy et al. "Laser-plasma proton acceleration with a combined gas-foil target." *New Journal of Physics*, **22** (2020), p. 103068. doi:10.1088/1367-2630/abbf6d.

[108] A. Henig et al. "Enhanced Laser-Driven Ion Acceleration in the Relativistic Transparency Regime." *Physical Review Letters*, **103** (2009), p. 045002. doi:10.1103/PhysRevLett.103.045002.

[109] S. Palaniyappan et al. "Dynamics of relativistic transparency and optical shuttering in expanding overdense plasmas." *Nature Physics*, **8** (2012), pp. 763–769. doi:10.1038/nphys2390.

[110] S. Steinke et al. "Efficient ion acceleration by collective laser-driven electron dynamics with ultra-thin foil targets." *Laser and Particle Beams*, **28** (2010), pp. 215–221. doi:10.1017/S0263034610000157.

[111] N. P. Dover et al. "Buffered high charge spectrally-peaked proton beams in the relativistic-transparency regime." *New Journal of Physics*, **18** (2016), p. 013038. doi:10.1088/1367-2630/18/1/013038.

[112] B. M. Hegelich et al. "Laser-driven ion acceleration from relativistically transparent nanotargets." *New Journal of Physics*, **15** (2013), p. 085015. doi:10.1088/1367-2630/15/8/085015.

[113] I. J. Kim et al. "Transition of Proton Energy Scaling Using an Ultrathin Target Irradiated by Linearly Polarized Femtosecond Laser Pulses." *Physical Review Letters*, **111** (2013), p. 165003. doi:10.1103/PhysRevLett.111.165003.

[114] D. Neely et al. "Enhanced proton beams from ultrathin targets driven by high contrast laser pulses." *Applied Physics Letters*, **89** (2006), p. 021502. doi:10.1063/1.2220011.

[115] T. Ceccotti et al. “Proton Acceleration with High-Intensity Ultrahigh-Contrast Laser Pulses.” *Physical Review Letters*, **99** (2007), p. 185002. doi:10.1103/PhysRevLett.99.185002.

[116] D. C. Carroll et al. “Carbon ion acceleration from thin foil targets irradiated by ultrahigh-contrast, ultraintense laser pulses.” *New Journal of Physics*, **12** (2010), p. 045020. doi:10.1088/1367-2630/12/4/045020.

[117] D. Jung et al. “Laser-driven 1 GeV carbon ions from preheadted diamond targets in the break-out afterburner regime.” *Physics of Plasmas*, **20** (2013), p. 083103. doi:10.1063/1.4817287.

[118] J. S. Green et al. “High efficiency proton beam generation through target thickness control in femtosecond laser-plasma interactions.” *Applied Physics Letters*, **104** (2014), p. 214101. doi:10.1063/1.4879641.

[119] A. J. Mackinnon et al. “Enhancement of proton acceleration by hot-electron recirculation in thin foils irradiated by ultraintense laser pulses.” *Physical Review Letters*, **88** (2002), pp. 2150061–2150064. doi:10.1103/PhysRevLett.88.215006.

[120] F. Dollar et al. “High contrast ion acceleration at intensities exceeding 1021 Wcm 2.” *Physics of Plasmas*, **20** (2013), p. 056703. doi:10.1063/1.4803082.

[121] L. Torrisi et al. “Ion acceleration from aluminium plasma generated by a femtosecond laser in different conditions.” *Contributions to Plasma Physics*, **60** (2020), p. e201900187. doi:10.1002/ctpp.201900187.

[122] L. Yin et al. “Monoenergetic and GeV ion acceleration from the laser breakout afterburner using ultrathin targets.” *Physics of Plasmas*, **14** (2007), p. 056706. doi:10.1063/1.2436857.

[123] B. Hegelich et al. “Experimental demonstration of particle energy, conversion efficiency and spectral shape required for ion-based fast ignition.” *Nuclear Fusion*, **51** (2011), p. 083011. doi:10.1088/0029-5515/51/8/083011.

[124] S. V. Bulanov and T. Z. Esirkepov. “Comment on “Collimated Multi-MeV Ion Beams from High-Intensity Laser Interactions with Underdense Plasma”.” *Physical Review Letters*, **98** (2007), p. 049503. doi:10.1103/PhysRevLett.98.049503.

[125] S. V. Bulanov. “Ion Acceleration in a Dipole Vortex in a Laser Plasma Corona.” *Plasma Physics Reports*, **31** (2005), p. 369. doi:10.1134/1.1925787.

[126] W. L. Zhang et al. “Monoenergetic ion beam acceleration from transversely confined near-critical plasmas by intense laser pulses.” *Physics of Plasmas*, **24** (2017), p. 093108. doi:10.1063/1.4999506.

[127] L. Willingale et al. “Reply to: Comment on "Collimated Multi-MeV Ion Beams from High-Intensity Laser Interactions with Underdense Plasma".” *Physical Review Letters*, **98** (2007), p. 049504. doi:10.1103/PhysRevLett.98.049504.

[128] N. Lemos et al. “Forward directed ion acceleration in a LWFA with ionization-induced injection.” *Journal of Plasma Physics*, **78** (2012), pp. 327–331. doi:10.1017/S0022377811000602.

[129] L. Willingale et al. “Longitudinal ion acceleration from high-intensity laser interactions with underdense plasma.” *IEEE Transactions on Plasma Science*, **36** (2008), pp. 1825–1832. doi:10.1109/TPS.2008.927357.

[130] S. S. Bulanov et al. “Helium-3 and helium-4 acceleration by high power laser pulses for hadron therapy.” *Physical Review Special Topics - Accelerators and Beams*, **18** (2015), p. 061302. doi:10.1103/PhysRevSTAB.18.061302.

[131] A. Yogo et al. “Laser ion acceleration via control of the near-critical density target.” *Physical Review E*, **77** (2008), p. 016401. doi:10.1103/PhysRevE.77.016401.

[132] K. Matsukado et al. “Energetic Protons from a Few-Micron Metallic Foil Evaporated by an Intense Laser Pulse.” *Physical Review Letters*, **91** (2003), p. 215001. doi:10.1103/PhysRevLett.91.215001.

[133] T. Schlegel et al. “Relativistic laser piston model: Ponderomotive ion acceleration in dense plasmas using ultraintense laser pulses.” *Physics of Plasmas*, **16** (2009), p. 083103. doi:10.1063/1.3196845.

[134] A. P. L. Robinson et al. “Hole-boring radiation pressure acceleration as a basis for producing high-energy proton bunches.” *Plasma Physics and Controlled Fusion*, **54** (2012), p. 115001. doi:10.1088/0741-3335/54/11/115001.

[135] S. Kahaly et al. “Detailed Experimental Study of Ion Acceleration by Interaction of an Ultra-Short Intense Laser with an Underdense Plasma.” *Scientific Reports*, **6** (2016), p. 31647. doi:10.1038/srep31647.

[136] A. Lifschitz et al. “Ion acceleration in underdense plasmas by ultra-short laser pulses.” *New Journal of Physics*, **16** (2014), p. 033031. doi:10.1088/1367-2630/16/3/033031.

[137] F. Sylla et al. “Short Intense Laser Pulse Collapse in Near-Critical Plasma.” *Physical Review Letters*, **110** (2013), p. 085001. doi:10.1103/PhysRevLett.110.085001.

[138] O. Tresca et al. “Spectral Modification of Shock Accelerated Ions Using a Hydrodynamically Shaped Gas Target.” *Physical Review Letters*, **115** (2015), p. 094802. doi:10.1103/PhysRevLett.115.094802.

[139] M. S. Wei et al. “Ion Acceleration by Collisionless Shocks in High-Intensity-Laser–Underdense-Plasma Interaction.” *Physical Review Letters*, **93** (2004), p. 155003. doi:10.1103/PhysRevLett.93.155003.

[140] K. Krushelnick et al. “Multi-MeV ion production from high-intensity laser interactions with underdense plasmas.” *Physical Review Letters*, **83** (1999), pp. 737–740. doi:10.1103/PhysRevLett.83.737.

[141] A. Flacco et al. "Persistence of magnetic field driven by relativistic electrons in a plasma." *Nature Physics*, **11** (2015), pp. 409–414. doi:10.1038/nphys3303.

[142] P. Antici et al. "Laser acceleration of high-energy protons in variable density plasmas." *New Journal of Physics*, **11** (2009), p. 023038. doi:10.1088/1367-2630/11/2/023038.

[143] M. Gauthier et al. "Investigation of longitudinal proton acceleration in exploded targets irradiated by intense short-pulse laser." *Physics of Plasmas*, **21** (2014), p. 013102. doi:10.1063/1.4853475.

[144] A. Pak et al. "Collisionless shock acceleration of narrow energy spread ion beams from mixed species plasmas using 1μm lasers." *Physical Review Accelerators and Beams*, **21** (2018), p. 103401. doi:10.1103/PhysRevAccelBeams.21.103401.

[145] M. Passoni et al. "Energetic ions at moderate laser intensities using foam-based multi-layered targets." *Plasma Physics and Controlled Fusion*, **56** (2014), p. 045001. doi:10.1088/0741-3335/56/4/045001.

[146] A. Zani et al. "Ultra-low density carbon foams produced by pulsed laser deposition." *Carbon*, **56** (2013), pp. 358–365. doi:10.1016/j.carbon.2013.01.029.

[147] L. Willingale et al. "High-power, kilojoule laser interactions with near-critical density plasma." *Physics of Plasmas*, **18**. doi:10.1063/1.3563438.

[148] S. Jiang et al. "Microengineering Laser Plasma Interactions at Relativistic Intensities." *Physical Review Letters*, **116** (2016), p. 085002. doi:10.1103/PhysRevLett.116.085002.

[149] D. Margarone et al. "Laser-Driven Proton Acceleration Enhancement by Nanostructured Foils." *Physical Review Letters*, **109** (2012), p. 234801. doi:10.1103/PhysRevLett.109.234801.

[150] O. Klimo et al. "Short pulse laser interaction with micro-structured targets: simulations of laser absorption and ion acceleration." *New Journal of Physics*, **13** (2011), p. 053028. doi:10.1088/1367-2630/13/5/053028.

[151] B. Aurand et al. "A multihertz, kiloelectronvolt pulsed proton source from a laser irradiated continuous hydrogen cluster target." *Physics of Plasmas*, **26** (2019), p. 073102. doi:10.1063/1.5093287.

[152] D. Margarone et al. "Proton Acceleration Driven by a Nanosecond Laser from a Cryogenic Thin Solid-Hydrogen Ribbon." *Physical Review X*, **6** (2016), p. 041030. doi:10.1103/PhysRevX.6.041030.

[153] J. Polz et al. "Efficient Laser-Driven Proton Acceleration from a Cryogenic Solid Hydrogen Target." *Scientific Reports*, **9** (2019), p. 16534. doi:10.1038/s41598-019-52919-7.

[154] S. D. Kraft et al. "First demonstration of multi-MeV proton acceleration from a cryogenic hydrogen ribbon target." *Plasma Physics and Controlled Fusion*, **60** (2018), p. 044010. doi:10.1088/1361-6587/aaae38.

[155] A. G. Krygier et al. "Selective deuterium ion acceleration using the Vulcan petawatt laser." *Physics of Plasmas*, 22 (2015), p. 053102. doi:10.1063/1.4919618.

[156] J. B. Kim, S. Göde, and S. H. Glenzer. "Development of a cryogenic hydrogen microjet for high-intensity, high-repetition rate experiments." *Review of Scientific Instruments*, 87 (2016), p. 11E328. doi:10.1063/1.4961089.

[157] R. A. C. Fraga et al. "Compact cryogenic source of periodic hydrogen and argon droplet beams for relativistic laser-plasma generation." *Review of Scientific Instruments*, 83 (2012), p. 025102. doi:10.1063/1.3681940.

[158] P. A. C. Jansson, U. Vogt, and H. M. Hertz. "Liquid-nitrogen-jet laser-plasma source for compact soft x-ray microscopy." *Review of Scientific Instruments*, 76 (2005), p. 043503. doi:10.1063/1.1884186.

[159] S. Garcia, D. Chatain, and J. P. Perin. "Continuous production of a thin ribbon of solid hydrogen." *Laser and Particle Beams*, 32 (2014), pp. 569–575. doi:10.1017/S0263034614000524.

[160] A. Tebartz et al. "Creation and characterization of free-standing cryogenic targets for laser-driven ion acceleration." *Review of Scientific Instruments*, 88 (2017), p. 093512. doi:10.1063/1.5001487.

[161] A. Huebl et al. "Spectral control via multi-species effects in PW-class laser-ion acceleration." *Plasma Physics and Controlled Fusion*, 62 (2020), p. 124003. doi:10.1088/1361-6587/abbe33.

[162] W. B. Leung, N. H. March, and H. Motz. "Primitive phase diagram for hydrogen." *Physics Letters A*, 56 (1976), pp. 425–426. doi:10.1016/0375-9601(76)90713-1.

[163] F. Henning and J. Otto. "Vapor-Pressure Curves and Triple Points in the Temperature Range from 14 to 90 Abs." *Physik Z*, 37 (1936), p. 633.

[164] R. B. Stewart and H. M. Roder. "Properties of normal and para-hydrogen." In *Technology and Uses of Liquid Hydrogen*. Elsevier (1964), pp. 379–404. doi:10.1016/B978-0-08-010779-0.50017-3.

[165] N. Grigor'ev and N. Rudenko. "Surface tension of liquid hydrogen isotopes and hydrogen-deuterium solutions." *Soviet Physics JETP*, 20 (1965), pp. 63–66.

[166] V. Blagoi, Yu P and Pashkov. "Surface Tension of Hydrogen Near the Critical Point." *Soviet Physics JETP*, 22.

[167] W. Keesom and G. Macwood. "The viscosity of liquid hydrogen." *Physica*, 5 (1938), pp. 745–748. doi:10.1016/S0031-8914(38)80196-8.

[168] M. Perera et al. "Refractive index measurements of solid parahydrogen." *Optics Letters*, 36 (2011), p. 840. doi:10.1364/OL.36.000840.

[169] H. M. McCarty, R D and Hord, J and Roder. *Selected properties of hydrogen (engineering design data). Final report*. U.S. Department of Commerce, National Bureau of Standards (1981).

[170] P. Sharma and T. Fang. "Breakup of liquid jets from non-circular orifices." *Experiments in Fluids*, **55** (2014), p. 1666. doi:10.1007/s00348-014-1666-z.

[171] J. B. Kim, C. Schoenwaelder, and S. H. Glenzer. "Development and characterization of liquid argon and methane microjets for high-rep-rate laser-plasma experiments." *Review of Scientific Instruments*, **89** (2018), p. 10K105. doi:10.1063/1.5038561.

[172] M. Kühnel et al. "Time-Resolved Study of Crystallization in Deeply Cooled Liquid Parahydrogen." *Physical Review Letters*, **106** (2011), p. 245301. doi:10.1103/PhysRevLett.106.245301.

[173] U. Zastrau et al. "Resolving Ultrafast Heating of Dense Cryogenic Hydrogen." *Physical Review Letters*, **112** (2014), p. 105002. doi:10.1103/PhysRevLett.112.105002.

[174] C. B. Curry et al. "Cryogenic Liquid Jets for High Repetition Rate Discovery Science." *Journal of Visualized Experiments*, **159** (2020), p. e61130. doi:10.3791/61130.

[175] A. V. Boukharov et al. "Dynamics of Cryogenic Jets: Non-Rayleigh Breakup and Onset of Nonaxisymmetric Motions." *Physical Review Letters*, **100** (2008), p. 174505. doi:10.1103/PhysRevLett.100.174505.

[176] R. Benattar, C. Popovics, and R. Sigel. "Polarized light interferometer for laser fusion studies." *Review of Scientific Instruments*, **50** (1979), pp. 1583–1586. doi:10.1063/1.1135764.

[177] Ö. Nordhage et al. "On the behavior of micro-spheres in a hydrogen pellet target." *Nuclear Instruments and Methods in Physics Research Section A: Accelerators, Spectrometers, Detectors and Associated Equipment*, **546** (2005), pp. 391–404. doi:10.1016/j.nima.2005.03.160.

[178] M. Rehwald. *Optische Charakterisierung eines festen Wasserstoffjets für die Laser-Protonenbeschleunigung*. Master's thesis. Technische Universität Dresden (2016).

[179] J. Eggers. "Nonlinear dynamics and breakup of free-surface flows." *Reviews of Modern Physics*, **69** (1997), pp. 865–930. doi:10.1103/RevModPhys.69.865.

[180] S. Ter-Avetisyan et al. "Quasimonoenergetic Deuteron Bursts Produced by Ultraintense Laser Pulses." *Physical Review Letters*, **96** (2006), p. 145006. doi:10.1103/PhysRevLett.96.145006.

[181] G. A. Becker et al. "Characterization of laser-driven proton acceleration from water microdroplets." *Scientific Reports*, **9** (2019), p. 17169. doi:10.1038/s41598-019-53587-3.

[182] T. Sokollik et al. "Directional laser-driven ion acceleration from microspheres." *Physical Review Letters*, **103** (2009), pp. 25–28. doi:10.1103/PhysRevLett.103.135003.

[183] M. Schnürer et al. "Ion acceleration with ultrafast laser driven water droplets." *Laser and Particle Beams*, **23** (2005), pp. 337–343. doi:10.1017/S0263034605050482.

[184] S. Busch et al. "Ion acceleration with ultrafast lasers." *Applied Physics Letters*, **82** (2003), pp. 3354–3356. doi:10.1063/1.1573363.

[185] T. Sokollik et al. "Laser-driven ion acceleration using isolated mass-limited spheres." *New Journal of Physics*, **12** (2010), p. 113013. doi:10.1088/1367-2630/12/11/113013.

[186] P. Hilz et al. "Isolated proton bunch acceleration by a petawatt laser pulse." *Nature Communications*, **9** (2018), p. 423. doi:10.1038/s41467-017-02663-1.

[187] T. M. Ostermayr et al. "Proton acceleration by irradiation of isolated spheres with an intense laser pulse." *Physical Review E*, **94** (2016), p. 033208. doi:10.1103/PhysRevE.94.033208.

[188] U. Weierstall et al. "Droplet streams for serial crystallography of proteins." *Experiments in Fluids*, **44** (2008), pp. 675–689. doi:10.1007/s00348-007-0426-8.

[189] A. Kacem et al. "Experimental investigations of planar water sheets flowing under gravity." In *WIT Transactions on Engineering Sciences*, volume 115 (2017), pp. 97–107. doi:10.2495/MPF170111.

[190] G. Taylor. "Formation of thin flat sheets of water." *Proceedings of the Royal Society of London. Series A. Mathematical and Physical Sciences*, **259** (1960), pp. 1–17. doi:10.1098/rspa.1960.0207.

[191] A. Watanabe et al. "A new nozzle producing ultrathin liquid sheets for femtosecond pulse dye lasers." *Optics Communications*, **71** (1989), pp. 301–304. doi:https://doi.org/10.1016/0030-4018(89)90012-6.

[192] B. Ha, D. P. DePonte, and J. G. Santiago. "Device design and flow scaling for liquid sheet jets." *Physical Review Fluids*, **3** (2018), p. 114202. doi:10.1103/PhysRevFluids.3.114202.

[193] G. Galinis et al. "Micrometer-thickness liquid sheet jets flowing in vacuum." *Review of Scientific Instruments*, **88** (2017), p. 083117. doi:10.1063/1.4990130.

[194] M. Ekimova et al. "A liquid flatjet system for solution phase soft-x-ray spectroscopy." *Structural Dynamics*, **2** (2015), p. 54301. doi:10.1063/1.4928715.

[195] Y. J. Choo and B. S. Kang. "The effect of jet velocity profile on the characteristics of thickness and velocity of the liquid sheet formed by two impinging jets." *Physics of Fluids*, **19** (2007), p. 112101. doi:10.1063/1.2795780.

[196] R. Li and N. Ashgriz. "Characteristics of liquid sheets formed by two impinging jets." *Physics of Fluids*, **18** (2006), p. 087104. doi:10.1063/1.2338064.

[197] K. M. George et al. “High-repetition-rate (kHz) targets and optics from liquid microjets for high-intensity laser–plasma interactions.” *High Power Laser Science and Engineering*, **7** (2019), p. e50. doi:10.1017/hpl.2019.35.

[198] D. L. Chubb et al. “Geometry of thin liquid sheet flows.” *AIAA Journal*, **32** (1994), pp. 1325–1328. doi:10.2514/3.12139.

[199] J. D. Koralek et al. “Generation and characterization of ultrathin free-flowing liquid sheets.” *Nature Communications*, **9** (2018), p. 1353. doi:10.1038/s41467-018-03696-w.

[200] M. Gauthier et al. “High-intensity laser-accelerated ion beam produced from cryogenic micro-jet target.” *Review of Scientific Instruments*, **87** (2016), p. 11D827. doi:10.1063/1.4961270.

[201] S. Assenbaum. *Characterization of a cryogenic hydrogen jet target in the low intensity regime to optimize laser proton acceleration*. Master’s thesis. Technische Universität Dresden (2020).

[202] T. Ziegler et al. “Proton beam quality enhancement by spectral phase control of a PW-class laser system.” *Scientific Reports*, **11** (2021), p. 7338. doi:10.1038/s41598-021-86547-x.

[203] U. Schramm et al. “First results with the novel petawatt laser acceleration facility in Dresden.” *Journal of Physics: Conference Series*, **874** (2017), p. 012028. doi:10.1088/1742-6596/874/1/012028.

[204] R. J. Gray et al. “Laser pulse propagation and enhanced energy coupling to fast electrons in dense plasma gradients.” *New Journal of Physics*, **16** (2014), p. 113075. doi:10.1088/1367-2630/16/11/113075.

[205] J. Psikal and M. Matys. “Dominance of hole-boring radiation pressure acceleration regime with thin ribbon of ionized solid hydrogen.” *Plasma Physics and Controlled Fusion*, **60** (2018), p. 044003. doi:10.1088/1361-6587/aaa7fa.

[206] L. Obst-Huebl. “Achieving optimal laser-proton acceleration through multi-parameter interaction control.” Ph.D. thesis, Technische Universität Dresden (2019).

[207] A. Jullien et al. “10ˆ10 temporal contrast for femtosecond ultraintense lasers by cross-polarized wave generation.” *Optics Letters*, **30** (2005), p. 920. doi:10.1364/ol.30.000920.

[208] M. Borghesi et al. “Measurement of highly transient electrical charging following high-intensity laser-solid interaction.” *Applied Physics Letters*, **82** (2003), pp. 1529–1531. doi:10.1063/1.1560554.

[209] L. Obst et al. “On-shot characterization of single plasma mirror temporal contrast improvement.” *Plasma Physics and Controlled Fusion*, **60** (2018), p. 054007. doi:10.1088/1361-6587/aab3bb.

[210] H. Kiriyama et al. "Experimental investigation on the temporal contrast of pre-pulses by post-pulses in a petawatt laser facility." *Optics Letters*, **45** (2020), p. 1100. doi:10.1364/ol.384759.

[211] T. Oksenhendler et al. "High dynamic, high resolution and wide range single shot temporal pulse contrast measurement." *Optics Express*, **25** (2017), p. 12588. doi:10.1364/OE.25.012588.

[212] T. Ziegler. "PW-class laser-driven proton acceleration optimization by spectral phase control." Ph.D. thesis, (working title, in preparation).

[213] C. Iaconis and I. A. Walmsley. "Self-referencing spectral interferometry for measuring ultrashort optical pulses." *IEEE Journal of Quantum Electronics*, **35** (1999), pp. 501–509. doi:10.1109/3.753654.

[214] M. Loeser et al. "Compact millijoule Yb 3+ :CaF 2 laser with 162 fs pulses." *Optics Express*, **29** (2021), p. 9199. doi:10.1364/OE.418319.

[215] C. Bernert. "Off-harmonic optical probing of high-intensity laser interaction with cryogenic hydrogen jet target." Ph.D. thesis, (working title, in preparation).

[216] F.-E. Brack. *Charakterisierung von Ionen aus Laserinduzierten Plasmen*. Master's thesis. Technische Universität Dresden (2016).

[217] Gafchromic. "User manual: Gafchromic dosimetry media, type EBT-3." Technical report.

[218] M. Roth et al. "Energetic ions generated by laser pulses: A detailed study on target properties." *Physical Review Special Topics - Accelerators and Beams*, **5** (2002), pp. 31–38. doi:10.1103/PhysRevSTAB.5.061301.

[219] J. Metzkes et al. "An online, energy-resolving beam profile detector for laser-driven proton beams." *Review of Scientific Instruments*, **87** (2016), p. 083310. doi:10.1063/1.4961576.

[220] M. Polyanskiy. "Refractiveindex.info." *https://refractiveindex.info (accessed: 2020-06-01)*.

[221] H. Burau et al. "PIConGPU: A Fully Relativistic Particle-in-Cell Code for a GPU Cluster." *IEEE Transactions on Plasma Science*, **38** (2010), pp. 2831–2839. doi:10.1109/TPS.2010.2064310.

[222] M. Bussmann et al. "Radiative signatures of the relativistic Kelvin-Helmholtz instability." In *Proceedings of the International Conference on High Performance Computing, Networking, Storage and Analysis*. ACM, New York, NY, USA (2013), pp. 1–12. doi:10.1145/2503210.2504564.

[223] B. Qiao et al. "Dominance of Radiation Pressure in Ion Acceleration with Linearly Polarized Pulses at Intensities of 10 21 Wcm-2." *Physical Review Letters*, **108** (2012), p. 115002. doi:10.1103/PhysRevLett.108.115002.

[224] H. W. Powell et al. "Proton acceleration enhanced by a plasma jet in expanding foils undergoing relativistic transparency." *New Journal of Physics*, **17** (2015), p. 103033. doi:10.1088/1367-2630/17/10/103033.

[225] C. Ruyer et al. "Growth of concomitant laser-driven collisionless and resistive electron filamentation instabilities over large spatiotemporal scales." *Nature Physics*, **16** (2020), pp. 983–988. doi:10.1038/s41567-020-0913-x.

[226] T. Bartal et al. "Focusing of short-pulse high-intensity laser-accelerated proton beams." *Nature Physics*, **8** (2012), pp. 139–142. doi:10.1038/nphys2153.

[227] J. C. Zier et al. "Magneto-Rayleigh-Taylor experiments on a MegaAmpere linear transformer driver." *Physics of Plasmas*, **19** (2012), p. 032701. doi:10.1063/1.3690088.

[228] M. R. Weis et al. "Coupling of sausage, kink, and magneto-Rayleigh-Taylor instabilities in a cylindrical liner." *Physics of Plasmas*, **22** (2015), p. 032706. doi:10.1063/1.4915520.

[229] N. R. Pereira, N. Rostoker, and J. S. Pearlman. "Z-pinch instability with distributed current." *Journal of Applied Physics*, **55** (1984), p. 704. doi:10.1063/1.333127.

[230] D. H. Kalantar and D. A. Hammer. "Observation of a stable dense core within an unstable coronal plasma in wire-initiated dense Z-pinch experiments." *Physical Review Letters*, **71** (1993), pp. 3806–3809. doi:10.1103/PhysRevLett.71.3806.

[231] J. Ruiz-Camacho et al. "Z-pinch discharges in aluminum and tungsten wires." *Physics of Plasmas*, **6** (1999), pp. 2579–2587. doi:10.1063/1.873529.

[232] F. N. Beg et al. "Optical and x-ray observations of carbon and aluminium fibre Z -pinch plasmas." *Plasma Physics and Controlled Fusion*, **39** (1997), pp. 1–25. doi:10.1088/0741-3335/39/1/001.

[233] D. D. Ryutov and M. K. Matzen. "The physics of fast Z pinches." *Reviews of Modern Physics*, **72** (2000), pp. 167–223. doi:10.1103/RevModPhys.72.167.

[234] M. G. Haines. "A review of the dense Z-pinch." *Plasma Physics and Controlled Fusion*, **53** (2011), p. 093001. doi:10.1088/0741-3335/53/9/093001.

[235] D. B. Sinars et al. "Measurements of Magneto-Rayleigh-Taylor Instability Growth during the Implosion of Initially Solid Al Tubes Driven by the 20-MA, 100-ns Z Facility." *Physical Review Letters*, **105** (2010), p. 185001. doi:10.1103/PhysRevLett.105.185001.

[236] S. V. Lebedev et al. "Coronal plasma behavior of the Z pinch produced from carbon and cryogenic deuterium fibers." *Physics of Plasmas*, **5** (1998), p. 3366. doi:10.1063/1.873050.

[237] V. Kaymak et al. "Nanoscale Ultradense Z-Pinch Formation from Laser-Irradiated Nanowire Arrays." *Physical Review Letters*, **117** (2016), p. 035004. doi:10.1103/PhysRevLett.117.035004.

[238] D. D. Ryutov et al. “Similarity criteria for the laboratory simulation of supernova hydrodynamics.” *The Astrophysical Journal*, **698** (2009), pp. 2144–2144. doi:10.1088/0004-637X/698/2/2144.

[239] J. J. Hester et al. “WFPC2 Studies of the Crab Nebula. III. Magnetic Rayleigh-Taylor Instabilities and the Origin of the Filaments.” *The Astrophysical Journal*, **456** (1996), p. 225. doi:10.1086/176643.

[240] D. D. Ryutov et al. “Magnetohydrodynamic scaling: From astrophysics to the laboratory.” *Physics of Plasmas*, **8** (2001), pp. 1804–1816. doi:10.1063/1.1344562.

[241] A. Stockem, M. E. Dieckmann, and R. Schlickeiser. “PIC simulations of the thermal anisotropy-driven Weibel instability: field growth and phase space evolution upon saturation.” *Plasma Physics and Controlled Fusion*, **51** (2009), p. 075014. doi:10.1088/0741-3335/51/7/075014.

[242] L. Gao et al. “Magnetic Field Generation by the Rayleigh-Taylor Instability in Laser-Driven Planar Plastic Targets.” *Physical Review Letters*, **109** (2012), p. 115001. doi:10.1103/PhysRevLett.109.115001.

[243] Y. Y. Lau et al. “Anisotropy and feedthrough in magneto-Rayleigh-Taylor instability.” *Physical Review E*, **83** (2011), p. 066405. doi:10.1103/PhysRevE.83.066405.

[244] A. Hauer and R. J. Mason. “Return-Current Heating and Implosion of Cylindrical CO2-Laser-Driven Targets.” *Physical Review Letters*, **51** (1983), pp. 459–462. doi:10.1103/PhysRevLett.51.459.

[245] M. A. Liberman et al. *Physics of High-Density Z-Pinch Plasmas*. Springer New York, New York, NY (1999). doi:10.1007/978-1-4612-1424-3.

[246] W. H. Bennett. “Magnetically Self-Focussing Streams.” *Physical Review*, **45** (1934), pp. 890–897. doi:10.1103/PhysRev.45.890.

[247] J. G. Linhart. “Dynamic Stability of a Conducting, Cylindrical Shell in a Magnetic Field.” *Journal of Applied Physics*, **32** (1961), p. 500. doi:10.1063/1.1736032.

[248] E. G. Harris. “Rayleigh-Taylor Instabilities of a Collapsing Cylindrical Shell in a Magnetic Field.” *Physics of Fluids*, **5** (1962), p. 1057. doi:10.1063/1.1724473.

[249] Rayleigh. “Investigation of the character of the equilibrium of an incompressible heavy fluid of variable density.” *Proceedings of the London Mathematical Society*, **s1-14** (1882), pp. 170–177. doi:10.1112/plms/s1-14.1.170.

[250] G. Taylor. “The instability of liquid surfaces when accelerated in a direction perpendicular to their planes. II.” *Proceedings of the Royal Society of London. Series A. Mathematical and Physical Sciences*, **202** (1950), pp. 81–96. doi:10.1098/rspa.1950.0086.

[251] M. Tatarakis et al. “Optical probing of fiber z-pinch plasmas.” *Physics of Plasmas*, **5** (1998), p. 682. doi:10.1063/1.872778.

[252] C. Thaury et al. “Self-generation of megagauss magnetic fields during the expansion of a plasma.” *Physical Review E - Statistical, Nonlinear, and Soft Matter Physics*, **82** (2010), pp. 3–6. doi:10.1103/PhysRevE.82.016408.

[253] M. E. Dieckmann et al. “PIC simulation of a thermal anisotropy-driven Weibel instability in a circular rarefaction wave.” *New Journal of Physics*, **14** (2012), p. 023007. doi:10.1088/1367-2630/14/2/023007.

[254] D. V. Romanov et al. “Self-organization of a plasma due to 3D evolution of the weibel instability.” *Physical Review Letters*, **93** (2004), pp. 19–22. doi:10.1103/PhysRevLett.93.215004.

[255] Y. Sentoku and A. J. Kemp. “Numerical methods for particle simulations at extreme densities and temperatures: Weighted particles, relativistic collisions and reduced currents.” *Journal of Computational Physics*, **227** (2008), pp. 6846–6861.

[256] S. Kar et al. “Guided post-acceleration of laser-driven ions by a miniature modular structure.” *Nature Communications*, **7** (2016), p. 10792. doi:10.1038/ncomms10792.

[257] W. Wang et al. “Efficient production of strong magnetic fields from ultraintense ultrashort laser pulse with capacitor-coil target.” *Physics of Plasmas*, **25** (2018), p. 083111. doi:10.1063/1.5000991.

[258] H. Ahmed et al. “Proton probing of laser-driven EM pulses travelling in helical coils.” *High Power Laser Science and Engineering*, **5** (2017), p. e4. doi:10.1017/hpl.2016.47.

[259] M. Borghesi et al. “Megagauss Magnetic Field Generation and Plasma Jet Formation on Solid Targets Irradiated by an Ultraintense Picosecond Laser Pulse.” *Physical Review Letters*, **81** (1998), pp. 112–115. doi:10.1103/PhysRevLett.81.112.

[260] A. S. Sandhu et al. “Laser-Generated Ultrashort Multimegagauss Magnetic Pulses in Plasmas.” *Physical Review Letters*, **89** (2002), p. 225002. doi:10.1103/PhysRevLett.89.225002.

[261] L. Yang. “Hybrid simulations of laser plasma interactions.” Ph.D. thesis, (working title, in preparation).

[262] A. McIlvenny et al. “Absolute calibration of microchannel plate detector for carbon ions up to 250 MeV.” *Journal of Instrumentation*, **14** (2019), pp. C04002–C04002. doi:10.1088/1748-0221/14/04/C04002.

[263] T. W. Jeong et al. “Experimental evaluation of the response of micro-channel plate detector to ions with 10s of MeV energies.” *Review of Scientific Instruments*, **87** (2016), p. 083301. doi:10.1063/1.4959187.

[264] K. Harres et al. “Development and calibration of a Thomson parabola with microchannel plate for the detection of laser-accelerated MeV ions.” *Review of Scientific Instruments*, **79** (2008), p. 093306. doi:10.1063/1.2987687.

[265] R. Prasad et al. “Calibration of Thomson parabola—MCP assembly for multi-MeV ion spectroscopy.” *Nuclear Instruments and Methods in Physics Research Section A: Accelerators, Spectrometers, Detectors and Associated Equipment*, **623** (2010), pp. 712–715. doi:10.1016/j.nima.2010.02.078.

[266] J. Ladislas Wiza. “Microchannel plate detectors.” *Nuclear Instruments and Methods*, **162** (1979), pp. 587–601. doi:10.1016/0029-554X(79)90734-1.

Danksagung

An dieser Stelle möchte ich allen herzlich danken, die mich bei der Verwirklichung der Doktorarbeit unterstützt haben und mir mit Rat und Tat zur Seite standen.
Zuerst den beiden Direktoren des Instituts für Strahlenphysik des HZDR, Tom Cowan und Ulrich Schramm. Ich bedanke mich für die vielfältigen Möglichkeiten an spannenden Experimenten im In- und Ausland teilzunehmen, auf diversen Konferenzen und Workshops Resultate und Ideen zu diskutieren sowie für die Betreuung während der gesamten Zeit am HZDR. An zweiter Stelle möchte ich dem kompletten Ionenteam für die durchweg angenehme Arbeitsatmosphäre danken. Ohne euren Einsatz - bis teilweise in die frühen Morgenstunden - wären so komplexe Experimente wie mit dem Wasserstoffjet nie möglich gewesen. Ganz besonders möchte ich Karl Zeil für das jahrelange Mentoring danken. Dass ich immer mit meinem wissenschaftlichen aber auch administrativen Fragestellungen und Problemen zu dir konnte, auf ein offenes Ohr gestoßen bin und du immer aufmerksam mitgedacht hast, hat mir sehr geholfen. Ein spezieller Dank geht auch an die anderen erfahrenen Experimentatoren, vor allem Josefine, die mir alle über die vielen Jahre seit meiner Bachelorarbeit alles beigebracht haben.
Tausend Dank an alle Doktoranden und Masteranden, mit denen man immer eine Diskussion auf gleichen Niveau führen konnte und auch abends nach der Arbeit noch etwas gemeinsam unternehmen konnte. Vor allem sollen an dieser Stelle Melanie, Florian Brack und Marco für einen guten Austausch während der gemeinsamen Master- und- Doktorarbeitszeit gedankt werden.
Im Speziellen bei Ilja und Thomas, aber auch beim gesamtem Simulationsteam, möchte ich mich für die vielen hundert Simulationen und dazugehörigen Diskussionen bedanken. Nur so konnten wir ein Verständnis der experimentellen Ergebnisse entwickeln. Danke, dass wir im Zweifel nicht einfach aufgehört haben, sondern uns noch die Zeit genommen haben eine neue Simulation zu starten und unsere Vermutung zu überprüfen.
René Gebhardt, Thomas Püschel, Stefan Bock und Uwe Helbig danke ich für die Pflege des Lasersystems und die vielen tausend Laserschüsse auf den Wasserstoffjet mit gleichbleibender Laserperformance. An der gleichen Stelle möchte ich außerdem Simon und Christoph für die vielen mechanischen und elektronischen Teile danken, die teilweise in Rekordzeit verschiedene Ideen ermöglicht haben. Andreas Wobst möchte ich für die Bereitstellung des flüssigen Heliums danken und dass sich im Zweifel auch immer noch eine Kanne gefunden hat. Allen Kollegen am Institut möchte ich für das positive Arbeitsklima und dem Elektronenteam unter Arie für den regen wissenschaftlichen Austausch danken. Ein Dank gilt außerdem meinen Kollegen im Büro: Lotti, Tim, Alex, Omid und Elias, die nicht nur meinen selten aufgeräumten Schreibtisch ertragen mussten, sondern auch immer bereit waren ihr Wissen zu teilen.

Neben den Kollegen am HZDR, wäre die Arbeit in dieser Form ohne externe Kollaborationen nicht möglich gewesen. Besonders möchte ich dabei Sebastian Göde für die Jahre der gemeinsamen Jetexperimente, Jetcharakterisierungsstrahlzeiten sowie Diskussionen zu diesem Thema danken. Danke, dass du mir die "Jetmagie" beigebracht hast und immer, wenn etwas mal nicht direkt funktioniert hat, auch spontan Zeit gefunden hast mit mir darüber zu diskutieren. Thank you Chandra, Maxence, Chris, Jongjin, Dan, Frederico and Siegfried for our joint experimental campaigns and the fruitful subsequent discussions.

Ich danke meinen Freunden Hannes, Corinna, Philipp, Franzi, Melle, Flo H., Flo B., Patty, Jan, Gregor, Robert und Jonas für die vielen schönen Unternehmungen und Momente in den über 10 Jahren seitdem wir gemeinsam unser Studium begonnen haben. Gerade neben den teilweise sehr kraftraubenden Experimenten war dieser Ausgleich unglaublich wichtig. Ich bin sehr froh, dass mich meine Familie durch die Zeit der Promotion unterstützt hat. Im Speziellen meinen Eltern bin ich dafür dankbar, dass sie meine Neugier und meinen Wissensdrang gefördert haben und in der gesamten Zeit bis zur Promotion immer für mich da waren. Die beiden wichtigsten Personen, denen ich Danke sagen möchte sind meine Frau Floria und mein Sohn Konrad. Gerade während der schwierigen Phasen habt ihr mir gezeigt, warum ich diesen Weg gehe. Danke Floria, dass du mich immer wieder motiviert hast, optmistisch warst, mir den Rücken frei gehalten hast und immer an meiner Seite standest.

Erklärung

Hiermit versichere ich, dass ich die vorliegende Arbeit ohne unzulässige Hilfe Dritter und ohne Benutzung anderer als der angegebenen Hilfsmittel angefertigt habe; die aus fremden Quellen direkt oder indirekt übernommenen Gedanken sind als solche kenntlich gemacht. Die Arbeit wurde bisher weder im Inland noch im Ausland in gleicher oder ähnlicher Form einer anderen Prüfungsbehörde vorgelegt.
Die Promotionsordnung, Technische Universität Dresden, Bereich Mathematik und Naturwissenschaften vom 23.02.2011 mit letzten Änderungen vom 23.05.2018 erkenne ich an.

Dresden, 09.12.2021

Martin Rehwald, M. Sc.

HELMHOLTZ ZENTRUM
DRESDEN ROSSENDORF

Bautzner Landstr. 400
01328 Dresden, Germany
Phone +49 351 260-2300
Fax +49 351 260-12300
Email m.rehwald@hzdr.de
http://www.hzdr.de